Investigation of pico-litre inkjet printing for nano-gram scale solid form screening of pharmaceuticals

Wathiq Al-Hachami (M.Sc.)

Thesis submitted to the University of Nottingham for the degree of Doctor of Philosophy

In the

Molecular Therapeutics and Formulation

School of Pharmacy

February 2018

Declaration

The work presented in this thesis is submitted to the University of Nottingham in support of my application for the degree of Doctor of Philosophy. No part has been submitted for any other degree at The University of Nottingham or any other institution. The work presented in this thesis has been carried out by myself.

Wathiq Al-Hachami

Abstract

The tendency of the majority of active pharmaceutical ingredients (APIs) to exist in different solid forms with keeping their chemical structures is called polymorphism. This phenomenon has gained a lot of interest in the pharmaceutical industry, hoping to avoid producing unexpected transformations of compounds during and after synthesis. The optimal way to avoid that is to subject the API, at the early stage of development, under various conditions in order to obtain an elegant (safe, effective, and stable) drug for the next formulation step. The aim of this thesis was to investigate some factors that affect the appearance of different polymorphs during screening of some APIs.

Four model drugs were selected: paracetamol; carbamazepine; mefenamic acid; and flufenamic acid. All have been well-characterised previously in terms of solid-state forms.

Piezoelectric, or 2D inkjet printing technique was used as a main technique in fabrication of nanoarrays of APIs onto predefined design on a solid tunable substrates because of its ability to control the delivered quantities of the the printed materials accurately, without any direct contact with the used substrate that may cause a sample cross-contamination. Light optical microscope was used to investigate the behaviour of the printed droplets during and after solvent evaporation and turn to dried spots, and to confirm the crystalline state of some spots by using the polarised light in the same microscope. Raman spectroscopy at low-wavenumber, or phonon region (40-400 cm^{-1}) was used for the first time to identify the resulted polymorphs after the printing process as its ability to probe the alterations that happen in the molecular skeleton inside the crystal lattice , in addition to molecular region (400-1800 cm^{-1}) to analyse the resulting spots.

In chapter three, the piezoelectric inkjet printing technique was successfully used for the first time to miniaturise, screen, and study the stability of the APIs at nano quantities in the range of (1-500 ng), about six-ordered magnification less than the reported studies. It was found that the variation in the printed quantities can produce different states and polymorphs. Stability with time was also studied for all the printed samples and it was noticed the variation in time for some printed drugs to convert from solid amorphous to crystalline state.

In chapter four, the advantage of the ability of the gold-coated slide to undergo further chemical modifications was exploited to create new substrates. Chemical modification of the gold substrates was carried out by treating them with two types of thiols to form self-assembly monolayers (SAMs) and use them as substrates in polymorph screening of some APIs. The new prepared SAMs were examined by preliminary tests like atomic force microscope (AFM) and water contact angle (WCA) measurements to investigate the texture of the new substrates before using them in printing process. It was found that changing the chemical structure of the substrate can lead to different polymorphs.

In chapter five, an attempt to create highly hydrophobic substrates was done to investigate whether it can affect the propensity of APIs for polymorphism. Fluorinated compounds were used in this chapter as they are considered more hydrophobic than the substrates used in the previous part of the work

The effect of the fluorinated substrates on appearance of new polymorphs was studied. Two fluorinated compounds were selected for preparation of high-water repellent surfaces and using them as substrates as they have the ability to limit the spreading of the printed droplets of the API, and allow the molecules to be constructed layer by layer and form a condense spot. The new fluorinated substrates were examined before using them in printing, and they exhibited high WCA. Another FLUF polymorph (VI) was investigated in addition to the two reference (I and III) polymorphs used in FLUF polymorphic screening. It was found that the intensity of the Raman peaks of the printed spots of APIs was good and clear to recognise when using fluorinated SAMs as a substrate, while the fluorinated substrate prepared from Flutec LE15 exhibited fluorescence effect due to the interactions between the glass and the drug's spot spectrum.

Acknowledgements

I would like to take a moment to thank my supervisor Dr Jonathan Burley for welcoming me and giving me the opportunity to work with him and his group, his advice, time and support. I am grateful to my co-advisor Prof. Morgan Alexander for his valuable suggestions within my first year in PhD and to my internal assessor Prof. Phill Williams for his precious advices which supported and enriched my thesis.

Also, I would like to thank Dr Andrew Hook, who kindly provided me the required training to use the microarray printer and I would like to express my appreciation to Dr Vincenzo Taresco for his help and support with valuable suggestions.

I am grateful for the assistance from my colleagues, Dr Mohammed Al-Qahtani, Dr Francessco Tress, Dr Ghaidaa Hamed, Dr Mohammed Al-Ameedi, Dr Majid Alani, Dr Saad Raoof, Dr Mustapha Al-Behadelli, Ali Al-Azzo, Mr Ahmed Al-Hachami, Dr Ghaith Al-Zubaidy, Dr Samer Al-Tameemi, and all my friends in Boots science building and room D19.

I would like to express a sincere acknowledgement to the school of pharmacy, University of Nottingham for providing me the opportunity to complete my PhD study. And I would like to express my great appreciation to the Iraqi ministry of higher education and scientific research and Iraqi cultural attaché for the financial support during four years.

Last but not least, there are no words to express my heartfelt gratitude to my beloved parents, brothers, sisters, and all my relatives and friends in Iraq for their support. Specially, I am deeply thankful of my lovely wife (Sarah) and my awesome son (Tariq) for their full support and encouragement.

Abbreviations

Abbreviation	Full form
APIs	Active Pharmaceutical Ingredients
BCS	Biopharmaceutics Classification System
GMP	Good manufacturing practices
HTS	High-Throughput Screening
XRPD	X-ray Powder Diffraction
DSC	Differential scanning calorimetry
DOD	Drop on demand
TIJ	Thermal inkjet printing
PET	Polyethylene Terphthalate
PLGA	Poly lactic-co-glycolic acid
ODFs	Orodispersible films
HPC	Hydroxypropyl cellulose
SEM	Scanning electron microscopy
HPLC	High performance liquid chromatography
NIR	Near infra-red
ATR-FTIR	Attenuated total reflectance Fourier transform infrared spectroscopy
DMSO	Dimethyl sulfoxide
DW	Distilled water
PAR	Paracetamol
CBZ	Carbamazepine
MEF	Mefenamic acid
FLUF	Flufenamic acid
SAM-CH_3	1-undecanethiol
SAM-CH_2-OH	11-mercapto-1-undecanol
SAMF	11-Mercaptoundecyl trifluoroacetate
AFM	Atomic Force Microscopy

PLM	Polarized Light microscope
WCA	Water contact angle
ST	Surface tension
RMS	Root mean square
LE15	Perfluoroper hydrophenanthrene oligomer

Table of Contents

List of Figures

List of Tables

Chapter one: Introduction

1.1. Pre-formulation and its importance in pharmacy

Pre-formulation, in pharmacy, can be defined as a group of studies that typically involves using qualitative and quantitative techniques to determine the physicochemical properties of a new drug candidate alone and when mixed with excipients [1]. This can enable the formulator to design a safe, effective, and stable dosage form on a commercial scale by establishing the compatibility of the new drug entity with common excipients, optimising the drug delivery by means of the physicochemical properties, determining the kinetic profile and stability, and providing ideas about how the newly formulated drugs should be stored [1].

Pre-formulation studies have witnessed tremendous developments since the late 1950s. Studies that are interested in the chemical structure of the drug candidate, including solid state properties, solubility, stability, and permeability studies, can be classified under fundamental pre-formulation. In contrast, the characterisation of flow properties, bulk density, compaction behaviour, and particle size and shape of the drug candidate can be listed as derived pre-formulation studies [1]. However, most pre-formulation studies focus on three main parts, as summarised in Figure 1.1.

The main parts that will be studied in the current work are polymorphism and crystallinity, due to their effect on producing an elegant (safe, effective, and stable) dosage form.

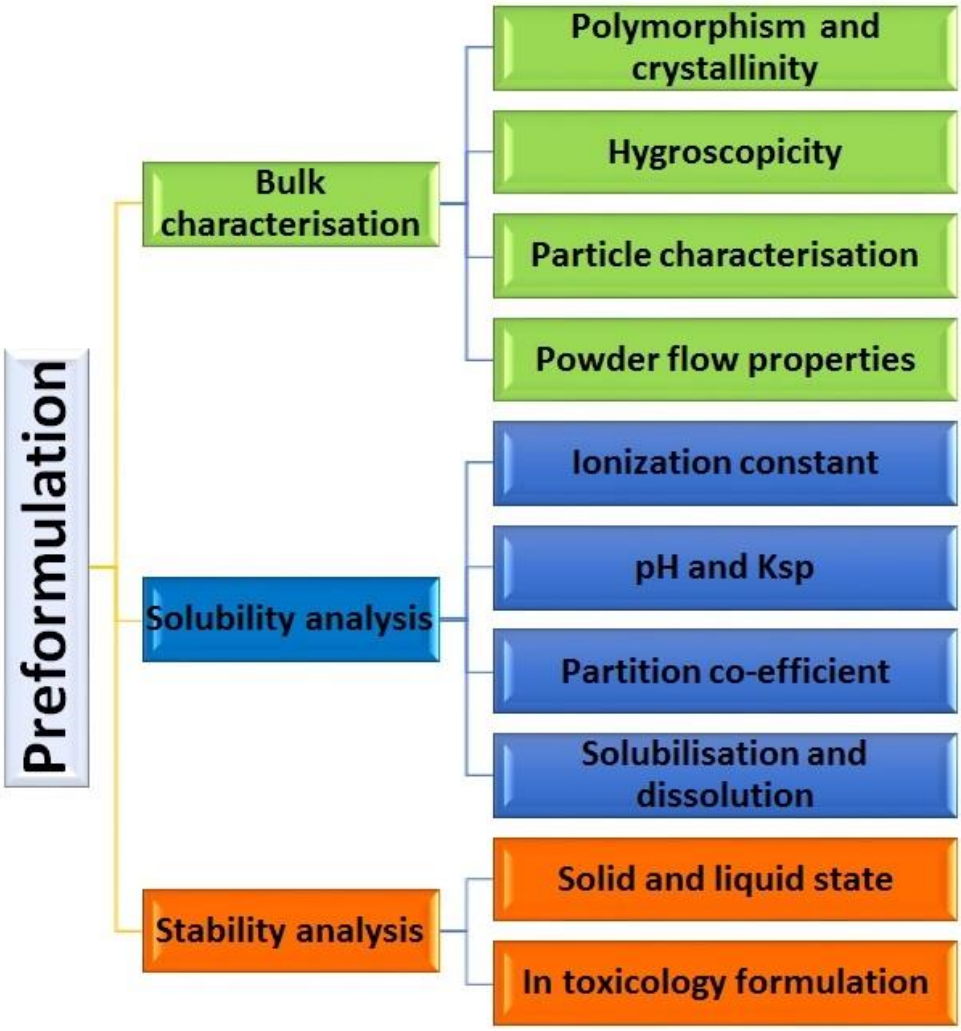

Figure 1.1. The main fields of preformulation studies [1]

1.2. Pharmaceutical solid forms

The majority of medicinal compounds can exist in different solid forms. These forms are divided into amorphous and crystalline solids. Crystalline forms can be subdivided into solvates, hydrates, polymorphs, and co-crystals. Each one of these forms has its own physiochemical characteristics, which affect the performance of the dosage form [2]. Figure 1.2 illustrates the representation of all the expected solid forms that can be found in medicinal compounds.

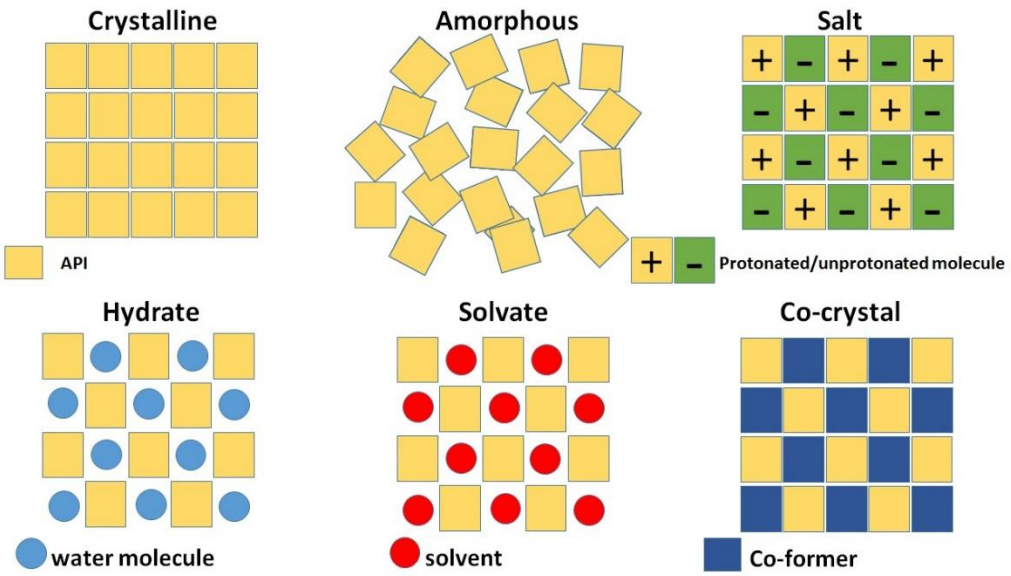

Figure 1.2. Types of solid dosage forms

An amorphous or non-crystalline solid is a solid that aggregates in a disorderly fashion, without regularly repeating three-dimensional structures [3]. Examples can be found in different industrial products, such as pharmaceuticals, polymers, and optical materials [4]. Crystal solids (e.g. diamonds and salts), unlike amorphous ones, can arrange in a consistent manner forming three-dimensional structures called crystal lattices [3]. In addition, an aggregation that takes place because of incorporation of an ion or a molecule of the solvent into the crystal lattice produces a crystal molecular compound called a solvate. A hydrate, which is a particular type of solvate, can be obtained by replacing the solvent with water [5]. Another type of solid forms is formed as a result of physical trapping of atoms or molecules within the crystal lattice of another substance [6].

In order to achieve the required dissolution-pH dependence of Active Pharmaceutical Ingredients (APIs), two or more chemically different molecules can be bound in the same crystal lattice via hydrogen bonding and van der Waals interactions to produce crystalline solid materials called co-crystals [7, 8].

1.3. Polymorphism

The tendency for a substance or compound to exist in multiple structures and to take different forms is called polymorphism. This definition includes different types of pharmaceutical, biological, and polymeric solid compounds [9].

Recent studies have begun to take into account this phenomenon due to its importance in many chemical and pharmaceutical industries and the variations

in physical properties such as melting point, hardness, compressibility, density, and solubility that can arise [10]. Researchers hope that studying polymorphism will limit the chances of unforeseen transformations of pharmaceutical products during and after synthesis [11].

Ritonavir, for example, which was believed to present as one polymorph (form I), demonstrates the impact of the existence of many structures of one compound in pharmaceutical manufacturing. It was temporarily pulled from the market after a new polymorph (form II) emerged, which led to major problems with the solubility of the final dosage form [12].

Differences in the characteristics of produced pharmaceutical forms are attributed to the possession of different molecular interactions, such as van der Waals forces and hydrogen bonding. Therefore, there are likely to be differences in the values of free energy [5].

Structurally, polymorphism can be classified into two categories, conformational and packing polymorphism, depending on formation of different crystalline lattice by means of two mechanisms. These mechanisms depend on the flexibility of the molecules producing those respective polymorphisms [5]. Conformational polymorphism arises as a result of folding flexible molecules into different conformations that can be packed into alternative 3D structures. Packing polymorphism refers to the existence of the molecules in a relatively rigid state which can be switched into various 3D structures with similar conformations [5].

Furthermore, solid form behaviour can be affected by a range of mechanical treatments for polymorphs, such as granulation and grinding [13], compression (tabletability), and freeze-drying. Paracetamol, for instance, has multiple forms and each one has its own procedure for tableting: form I requires some treatments with binding agents before compression, while form II does not [14-16]. Physical and chemical stability can also be affected by the solid form behaviour of polymorphs [17, 18].

Researchers in the pharmaceutical industry depend not only on the solubility but also on the permeability of drugs. Therefore, according to the Biopharmaceutics Classification System (BCS), active pharmaceutical ingredients can be divided into four categories (Figure 1.3): class (I) high solubility and permeability, class

(II) low solubility and high permeability, class (III) high solubility and low permeability, and class (IV) low solubility and permeability [19].

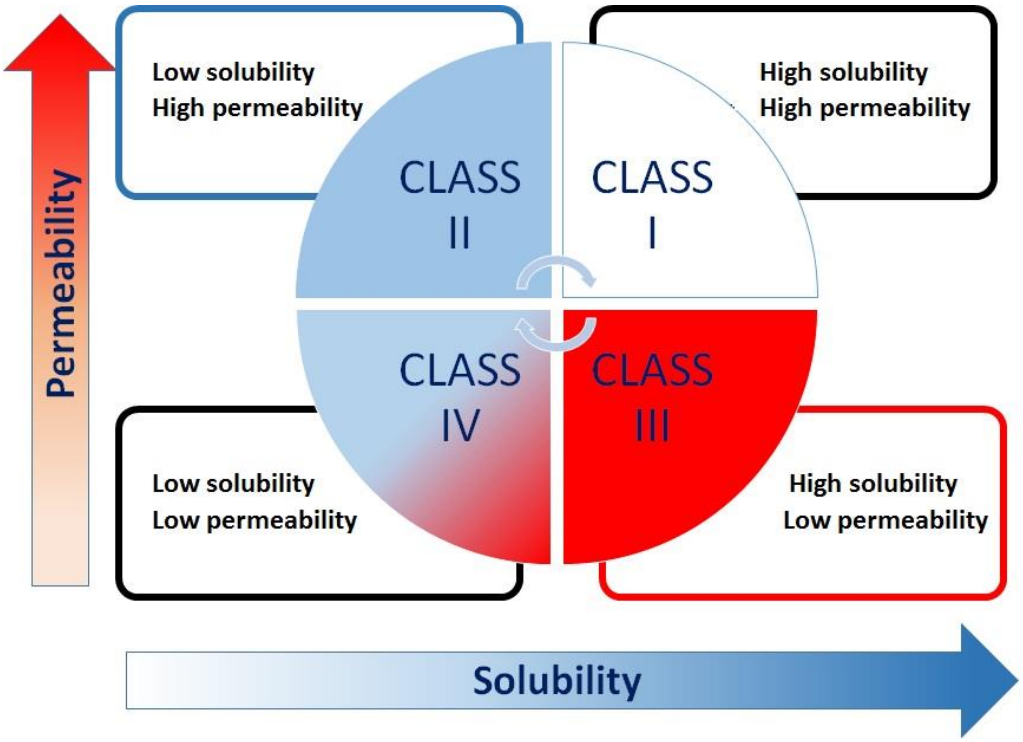

Figure 1.3. The biopharmaceutical classification system (BCS) [19].

Designing of the pharmaceutical dosage form has always been a challenge, especially drugs in class II, which is considered the most problematic class for scientists. Therefore, the activity, bioavailability, and dependability of solid forms on the rate of dissolution can be significantly influenced as a result of the variance in its physicochemical properties [20]. This point has been taken seriously by many researchers hoping to improve BCS class II drugs, which have high permeability and low solubility with dissolution-dependent bioavailability [21-24]. Figure 1.3 summarises the main characteristics of the Biopharmaceutics Classification System (BCS).

1.4. Solid form screening

Solid form screening is the identification of which solids are likely to form for a particular drug after typical manufacturing, processing, storage and use [9]. Although it was recognised at the beginning of the 19th century, increasing

attention is now being paid to the importance of solid form screening as a standard method for developing and improving the bioavailability and physical stability of the pharmaceutical compounds, due to the high percentage of active pharmaceutical ingredients that exhibit polymorphism, as seen in Figure 1.4 [25, 26].

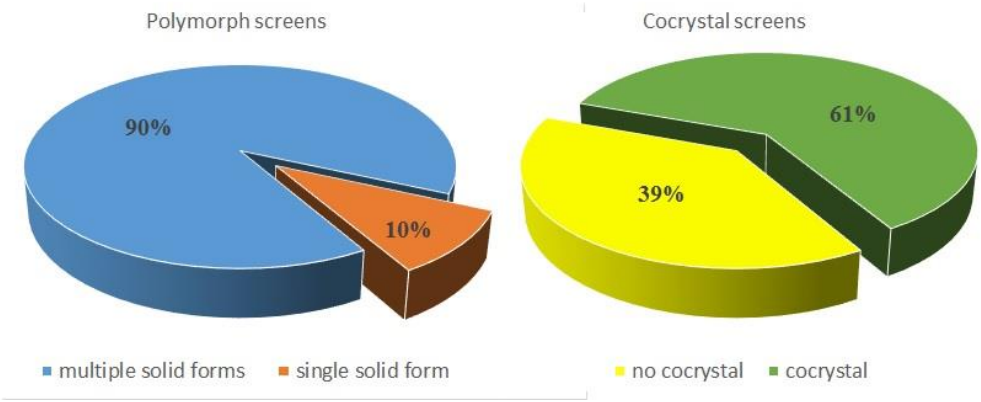

Figure 1.4. Diversity in different APIs solid forms [26]

The variation in the physical characteristics of some drugs, the failure to reach a satisfactory explanation for certain phenomena, such as nucleation [27, 28], and the sudden appearance of undesirable forms for some pharmaceuticals that have low dissolution rate and bioavailability (e.g. Ritonavir [22] and Neupro [29]) emphasise the importance of solid polymorph screening.

Pharmaceutical compounds can exist in many different forms. Each one of these forms has different physiochemical properties and hence different efficiencies in terms of dissolution rate and bioavailability, which are essential criteria needed to study how the medicine can be stored. Therefore, these properties must be monitored in a solid form to ensure safe and effective drug delivery [30].

The more preferable and stable pharmaceutical formulations do not significantly suffer from solid phase transformation [31, 32]. The differing properties observed in different solid forms are summarised in Table 1.1 [33].

Within the drug manufacturing steps, various screens can be carried out at different stages depending on the required aim of the screen [34]. Figure 1.5 illustrates the different screens that can be performed during the manufacturing process of an API.

Table 1.1. Physical characteristics of different solid forms [33]

Kinetic properties	Stability, solid state reaction rates, dissolution rate
Mechanical properties	Tabletability, compactability, flowability, tensile strength, hardness
Packing properties	Hydrogen bonding, refractive index, unit cell volume (crystalline forms only), hygroscopicity and density.
Surface properties	Interfacial tensions, contact angles, crystal habit, surface free energy.
Spectroscopic properties	Bonding type, colour, electronic transitions.
Thermodynamic properties	Entropy, enthalpy, free energy, melting point, solubility.

At early stages, small screening must be performed for the raw materials (as received) and other solid forms such as co-crystals, salts, and polymorphs [34]. It is also necessary to perform further screening tests at advanced stages of drug formulation to produce acceptable physicochemical properties [34].

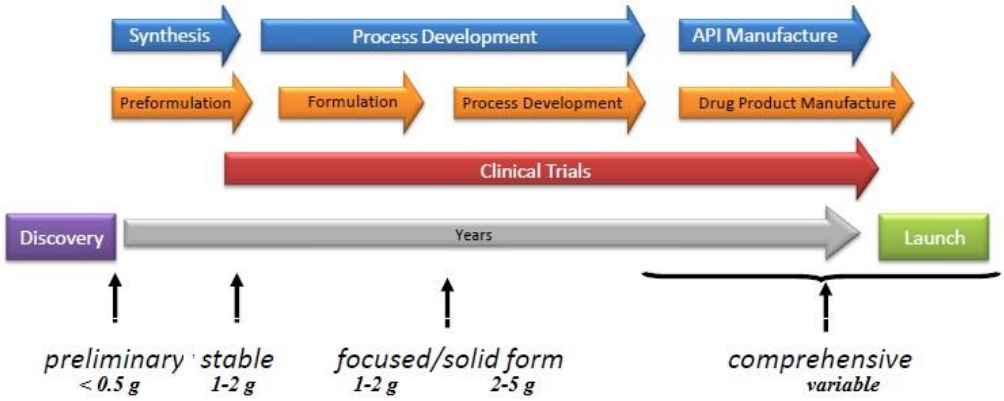

Figure 1.5. Types of polymorph screening at different stages of drug development. Adapted from [26]

At the early stage of the pharmaceutical development, a preliminary screening requires from 100 mg to 200 mg of materials to determine the propensity for polymorphism [26]. The next stage of polymorph screening aims to investigate the most thermodynamically stable form. It requires high quantities of materials, between 1g and 2g. The selected thermodynamically stable form can be subjected to a focused screening at the process development stage in order to confirm that the stable form will or will not be affected by impurities in good

manufacturing practices (GMP) conditions [26]. The final stage of polymorph screening is a comprehensive prediction of all the possible forms that can be found. It requires conducting many experiments with a maximum number of techniques, in addition to consuming high quantities of materials (2 g to 5 g), as seen in Figure 1.5 [26].

1.4.1. Traditional solid form screening

Solid forms screening techniques have been reviewed in many papers [5, 35, 36]. Figure 1.6 summarises the types of traditional solid form screening methods. Traditional polymorph screening methods that depend on crystallisation can be divided into two sections: manual and automated methods [34].

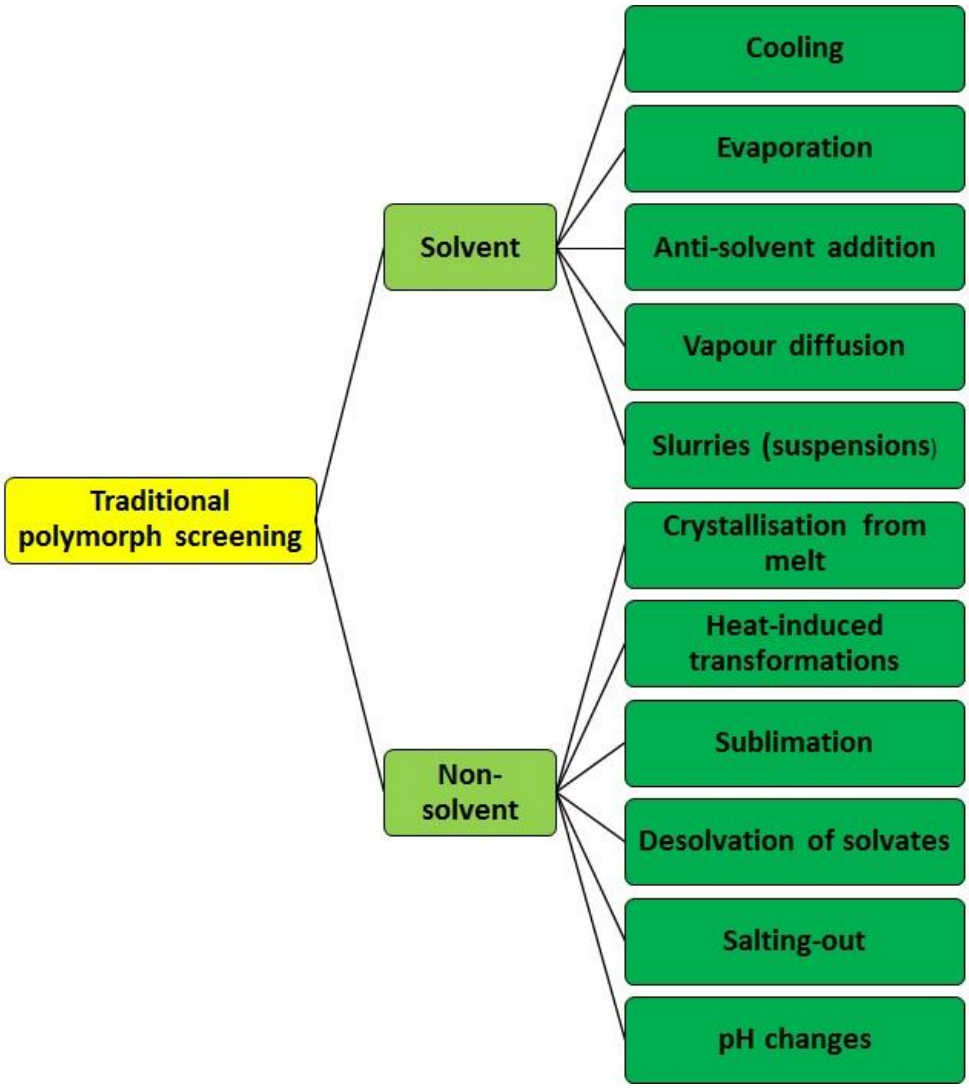

Figure 1.6. Traditional solid form screening strategies [34]

Manual crystallisation methods differ from automated methods in the used quantities of APIs and the time of screening. Manual crystallisation requires larger materials quantities (20 mg to 100 mg) per screen and longer times for achieving full screening than the automated methods, which use approximately 1mg to 3 mg of an API to run a successful screening within a short time [34].

1.4.2. High Throughput Screening

High-Throughput Screening (HTS) is one of the newest scientific approaches that has been widely used over the last two decades in the pharmaceutical industry [37]. In this approach, hundreds of thousands of samples with few milligrams (0.5 mg to 10.0 mg) can rapidly be identified by means of robotic automation, data processing software, and liquid handling devices [38, 39]. In order to choose the desirable drug candidate, it is necessary to develop the HTS strategies to be carried out at the early stages of development, while taking into consideration three main factors: the amount of the compound, resources, and time [40].

A high throughput polymorph screening system was developed by Peterson *et al.* [41] to evaluate different crystallisation conditions, such as concentration, temperature, and solvent for paracetamol polymorphs. This study was performed using 7,776 samples for 2,592 unique conditions. The newly developed screening system also involved robotics coupled with analytical measurements, including an X-ray diffraction pattern that identified the unstable form III a few hours before its conversion to form II [41].

A comprehensive identification of solid forms of the HIV protease ritonavir using the HTS system by way of cooling with four nominal concentrations was performed [38], in order to conduct more than 2,000 experiments using 24 different solvents, with a range of 1 mg to 10 mg for each single experiment. The authors discovered three new polymorphs in addition to the basic polymorphs I and II [38].

Recently, there have been new attempts to achieve fast and cheap in-vitro screening methods by miniaturising the APIs. These methods have enabled researchers to achieve fast identification of solubility-enhancing formulations using milligram or sub-milligram quantities of API [42].

Kojima *et al.* [43] presented a high-throughput screening approach for slurries containing 50 µl of indomethacin with 111 µl of 46 potential co-crystal formers. Highly efficient spectroscopic analysis techniques, such as ^{1}HNMR, Raman, XRPD and thermal analysis were used to characterise the prepared co-crystals. It was found that using this strategy can be time and cost saving [43].

A comparative study on some benzoic and benzamide derivatives was performed by Manin *et al.* [44]. They used two different co-crystal preparation techniques, namely the fast kinetic method and slow thermodynamic approach, to screen 18 binary systems of the used materials. It was found that six new co-crystals were obtained and confirmed by XRPD, and the thermal analysis by differential scanning calorimetry (DSC) provided valuable information about co-crystals, including melting point, thermal transition temperature, enthalpy of fusion, and hydrate or solvate formation. They consumed between 1.8 mg to 2.5 mg of the samples to run all the screening experiments [44].

However, the previous studies about HTS open the doors to scientists to start thinking about development new approaches which consume less materials and time than the conventional methods of screening in industry, especially in pharmaceutical fields. The current trend in the pharmaceutical industry is to use materials with high efficiency and quality that have the ability to ensure that the drug is accurately delivered. The active ingredients in progress must be delivered properly and in low quantities [45]. Therefore, looking for a powerful and dependable technique to produce pharmaceutical preparations with all of these specifications can be considered a renaissance in the pharmaceutical industry [46].

1.5. Inkjet printing technique

Although printing technologies are used in different life fields, their use in pharmaceutical research fields can be considered relatively novel. Some parts of the pharmaceutical industry are taking a long time and are inflexible, because there are several steps to gaining the required pharmaceutical production. Consequently, the quality control process for the resulting products is illogical due to the random sampling of these products using statistical methods [47].

All of these obstacles can be overcome by managing the size and quantity of the drug automatically. This control makes the process of drug preparation easier

and more accurate. Inkjet printing, in pharmaceutical fields, is a technique that involves the deposition of an API on a substrate to create a new pharmaceutical preparation. In this process the drug substance is jetted from the nozzle without coming into contact with the surface of the substrate. Additionally, this technique has the qualifications to be dependable in developed pharmaceutical industries.

Many reasons lie behind using this powerful technique. Firstly, from an economic perspective, it can assist in minimising expenses involved in the development of new medicines. Secondly, in order to strengthen the method of drug delivery, the inkjet printing technique can achieve distinct time profiles. Finally, some intractable problems such as overdosing can be avoided [46].

The importance of this technique has increased over the past few years because it plays an essential role in biomaterial applications [48, 49], drug delivery [50], genomics [51, 52], and life science [51, 53]. One of the benefits of this technique is that it can be employed to inject droplets of regular shape and volume, either in nanolitres or picolitres [54], and with a high degree of accuracy [51, 53]. This is because it has high productivity software and automation characteristics, which in turn can produce a homogenised form of the drug [55, 56].

Direct contact printing depends on transferring the pharmaceutical solution "ink" to a surface directly, using a high-precision robotic arm that determines the exact position for dotting [57]. Although it can be adapted to a broad range of solutions, and can be easily maintained and cleaned, the deposited droplet is not readily adjustable. Furthermore, there is the potential for surface damage that may result from direct contact between the pin and the substrate surface [58].

The inkjet printing technique (also known as the non-contact printing technique) operates in two modes: Drop-On–Demand (DOD) and Continuous. DOD is subdivided into the piezoelectric and thermal inkjet printing techniques. The piezoelectric inkjet printing technique is considered to be more suitable for several solvents. It relies on the setting of the voltage and pulse to generate electrical vibrations that lead to expand and contract the crystal inside the nozzle forcing ink to flow out of the nozzle in controllable quantities, as illustrated in Figure 1.7.

Thermal inkjet printing depends on the heating system to vaporise the ink and form bubbles. The expansion and contraction of these bubbles helps the printer to inject the ink out of the nozzle as a result of the collisions of these bubbles, producing a vacuum, which enhances the injection process. The thermal stability of active pharmaceutical ingredients and the limited number of solvents and substrates that can be used are the main disadvantages of the thermal inkjet printing technique [59].

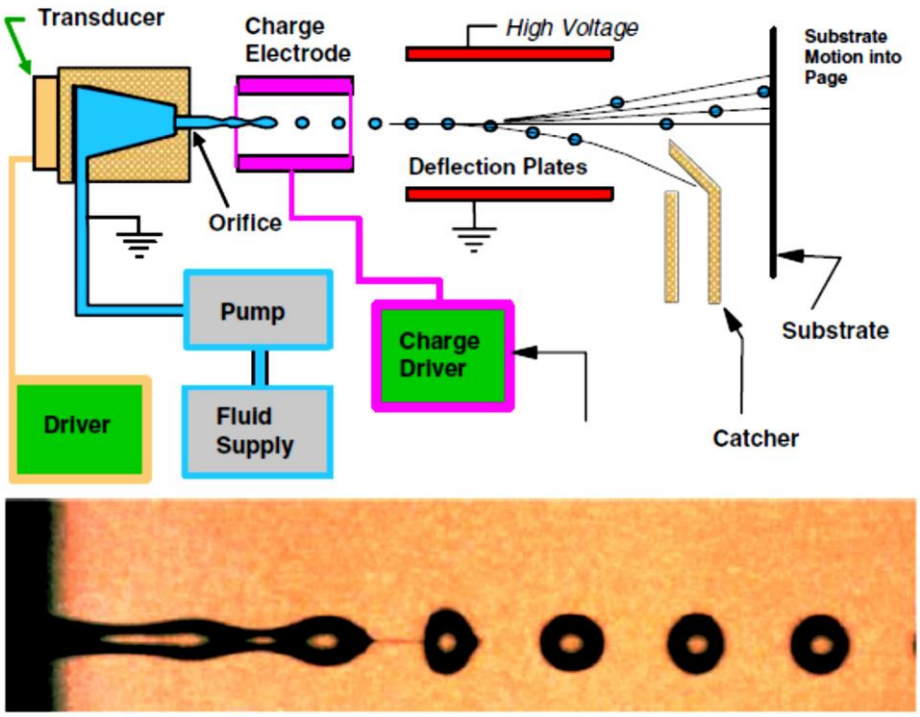

Figure 1.7. Effect of voltage manipulation on the shape of droplets in continuous mode of ink-jet printing technique [84]

Continuous inkjet printing is restricted to specific applications because of its expensive head costs and limited inkjet characteristics [60].

One of the most important things that should be taken into consideration when using this technique is the physicochemical properties of the used pharmaceutical ink, such as surface tension, viscosity, and the wettability behaviour of the nozzle material to ensure the smooth flow of the ink inside the nozzle (illustrated in Figure 1.8) and avoid blocking [61, 62].

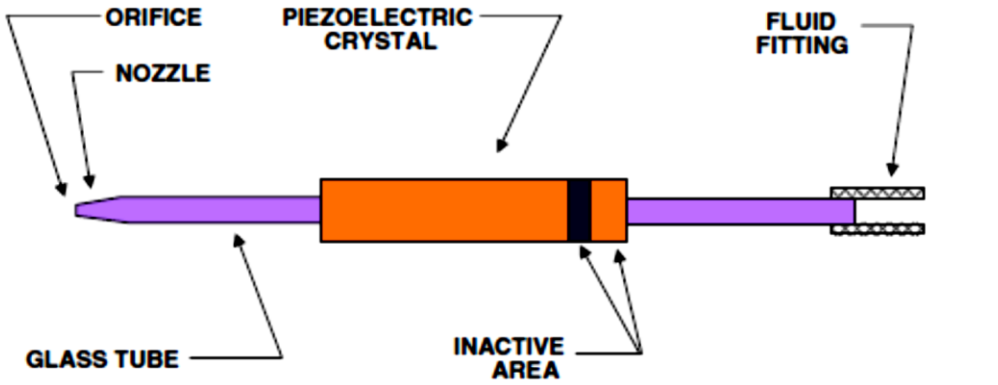

Figure 1.8. The composition of simple nozzle [85]

Viscosity and surface tension can play an important role in evaluation of the pharmaceutical inks. It is advisable for the viscosity to be lower than 20 mPa·s, as using highly viscous solutions can damage or block the printing nozzle (see Figure 1.8), while highly diluted solutions are not preferable as printing inks, as they may penetrate the nozzle glass capillary tube itself, which in turn affects its efficiency [47, 63].

Surface tension is another physical parameter that can be used to evaluate the property of the pharmaceutical solutions. It has been reported that surface tension in the range 30 $mN{\cdot}m^{-1}$ to 70 $mN{\cdot}m^{-1}$ is the optimal condition for achieving the printing process in a controllable way [63]. An important point that should be taken into consideration is that surface tension should be more than 30 $mN{\cdot}m^{-1}$ to avoid the ink dripping from the nozzle, and lower than 70 $mN{\cdot}m^{-1}$ to facilitate ink spreading over the surface [63]. Although there is a wide range of applications in many fields, inkjet printing technique can be considered as a cornerstone in recent pharmaceutical studies.

1.5.1. Pharmaceutical applications of inkjet printing techniques

The feasibility of using printing methods in designing a drug delivery system or device has been increasingly studied in the last few decades. Many researchers have used the inkjet printing technique to deposit drugs in solutions or suspensions on different types of substrates. The following review illustrates the importance of the inkjet printing technique in pharmaceutical fields.

The capture efficiency, a combination of active pharmaceutical ingredients with devices, of coated substrates has been discussed by Tarcha *et al.* [60], who used a stainless steel stent coated with a tetra non-polar polymer and

phosphorylcholine-linked methacrylate as a substrate for printing a fenofibrate and rapamycin derivative (ABT-578). The fenofibrate dose was assessed at the target of 100.0 µg ± 0.6 µg for a small stent, while printing of fenofibrate on the coated stent tubes produced 137.0 µg ± 1.8 µg dose with 100 % capture efficiency. It was concluded that this medicine maintains its stability [60].

Melendez *et al* [64] used the thermal inkjet printing (TIJ) technique in a preparation of a solid dosage form for prednisolone. After dissolving the pharmaceutical compound in a mixture of ethanol: water: glycerol (80:17:3), they tested two different approaches: TIJ cartridge with a personal printer and a micropipette to deposit the pharmaceutical ink on polytetrafluoroethylene-coated fibre glass film. The therapeutic dose that was obtained after 60 deposited layers was 8 mg. The crystallisation behaviour of these printable dots was investigated by spectroscopic analysis with Raman and XRPD measurements. It was found that there are two forms of predisosolone: Form (I) and (III). Form (I) is available in powder, while Form (III) is believed to be formed as a consequence of thermal treatment of the solvent system to remove residual solvent mixture.

The piezoelectric printing technique has been used to prepare calcium alginate microcapsules through deposition of a mixture of sodium alginate and rhodamine R-6G dye on a calcium chloride substrate [65]. It was noticed that the microcapsule dimensions play an important role in the kinetics of the rapid release of the drug studied [65].

The causative factors for the appearance of crystals include not only the heat treatment, but also the nature of the substrate that the printing process is done on [47]. Sandler and his co-workers tested three types of varying porosity substrates: uncoated paper, coated paper, and polyethylene terphthalate (PET), in a microscopic investigation of the crystallinity behaviour of some poorly water soluble medicines: theophylline, paracetamol, and caffeine. It was reported that drugs printed on the PET polymeric surface crystallised clearly, while they penetrated through the porous surface of the uncoated paper. Sandler *et al.* also noticed partial crystallisation of caffeine on the coated paper, which was attributed to the fact that a high concentration of caffeine was used [47].

Because of its high precision, piezoelectric printing technology has begun to play an important role in creating new pharmaceutical formulations used to regulate drug release. Scoutaris *et al.*[59] proposed improving the solubility of felodipine by adding various ratios of polyvinylpyrolidone as an excipient and using ethanol:DMSO as a solvent, the accepted formula of which has been confirmed by using microscopic and nanothermal analysis [59].

Buanz *et al.* [66] described a robust method based on the thermal inkjet printing technique to produce films for oral application containing salbutamol sulphate. They proposed printing of multiple layers of the drug-loaded ink on two different edible substrates (potato starch sheets and acetate films). They could produce different doses depending on the salbutamol concentration and also the changes in the physical dimensions of the printed dosage form. However, they could not obtain a linear relationship between the numbers of the printed layers with the amounts of the drug in the dosage form due to the shearing effect of the paper tray when feeding the substrate.

Pardeike *et al.* [67] introduced the feasibility of dispensing of 10 % of poorly soluble folic acid suspension with a very low particle size. They successfully used the inkjet printing technique to prepare a nanosuspension with low particle size (less than 500 nm) on an edible substrate. They demonstrated that the rate of dissolution of the prepared nanosuspension of folic acid within five minutes increased to 79% in comparison to the conventional suspension of folic acid, which exhibited 6% at the same interval.

Different formulations consisting of two poorly water soluble drugs, felodipine and hydrochlorothiazide, and two polymers, polyvinylpyrolidone and poly (lactic-co-glycolic acid), have been prepared using a piezoelectric microarray printer to create the optimal dosage form suitable for the patient's needs [68]. It was concluded that any improvements in the solubility of slightly water soluble drugs can be dependent on the consistency of the drug:polymer formula, which is needed to achieve the required stability for the medicine [68].

Lee *et al.* [69] demonstrated the design of well-defined and controlled geometrical structures, such as circles, grids, honeycombs, and rings from paclitaxel (PTX) and poly lactic-co-glycolic acid (PLGA) in *N*,*N*-dimethylacetamide using the piezoelectric inkjet printing technique and a glass slide as a substrate. They found that the dissolution rate of the resulting dosage

forms of PTX-PLGA depends on the surface area of the dosage form itself, with a descending rate order of honeycomb > grid > ring > circle.

A simple and rapid method for preparation of different sizes of alginate microparticles has been described, and the effect of particle volumes and the ejected volume of the pharmaceutical print solution on the rate of nanoparticle release was investigated [70]. According to microscopic analysis, the results show that the new synthesised nanoparticles are not affected by the drying process associated with printing, on the contrary, they retain their stable forms.

Many studies have dealt with the nature of the substrate and its role in obtaining appropriate pharmaceutical formulations. Genina *et al.* [71] have used chemical and microscopic analysis to evaluate three different model substrates used in inkjet printing drug delivery of a Parkinson's disease drug, rasagiline mesylate (RM). These models, porous copy paper sheets, orodispersible films (ODFs), and water-impermeable transparency films (TFs), were used as substrates for depositing multi-subsequent layers of (RM) using the thermal inkjet printer [71]. According to the microscopic results, it was found that there were no crystals on the surface of the copy paper substrate because of the penetration of the studied drugs inside the porous substrate. Statistically, this substrate produces a low standard deviation, in contrast to the other two model substrates, which prompted the researchers to conclude that all edible substrates that have the same properties of copy paper sheets are the best choice in drug delivery system preparation when using the thermal inkjet technique.

Genina *et al.* [72] used three commercially available edible icing sheets, in-house-produced edible hydroxypropyl cellulose (HPC) films, and PET film as a reference to study the behaviour of printed forms of loperamide and caffeine in the creation of personalised dosage forms. By controlling the printing parameters such as the drop spacing, the physical dimensions of the printed area, and the type of the used substrate, Genina and co-workers reported that loperamide is a good glass-forming compound as it was deposited in an amorphous state on all the used substrates, while caffeine exhibited recrystallization on all the used substrates.

Raijada *et al.* [73] also proposed another approach to enhance the dissolution rate for the printed dosage forms. They used a non-aqueous solvent (polyethylene glycol (PEG) 400/ethanol mixture) to dissolve the poorly-water

soluble drug (piroxicam). Printing of the drug-loaded ink on edible icing sheets was performed by using a piezoelectric inkjet printer. The resulting dosage forms were subjected to a visual characterisation using SEM, and quantitative analysis by means of HPLC [73]. In addition, they found that all the printed dosage forms exhibited high dissolution rates (more than 90%) within five minutes.

Vakili *et al.* [74] has fabricated orodispersible paediatric dosage forms, consisting of propranolol hydrochloride in a mixture of (water:glycerol 90:10 vol%). The drug solution was deposited with a colouring agent on three different edible substrates: icing sheets, rice paper, and hydroxypropyl cellulose (HPC), by the thermal inkjet printing technique on different squared fields: 1, 2, and 4 cm^2 with an amount range of (0.08 mg to 3.16 mg), followed by successful coating with a layer of saccharine. The effect of the printing on the used substrates was investigated by optical microscopic devices, and the content of the drug in the resultant spots was determined by a non-destructive colorimetric technique.

Varan *et al.* [75] recently investigated the behaviour of the prolonged release of a newly fabricated personalised drug, consisting of (anticancer) paclitaxel in cyclodextrin and (antiviral) cidofovir encapsulated in polycaprolactone nanoparticles printed onto adhesive film. It was found that the printed combination drug could be successfully used for treatment of HPV-related cervical cancer.

Wickström *et al.* [76] used a non-destructive colorimetric method for quality control of the printed doses of vitamin B on edible rice and sugar substrates. They used the TIJ technique to create (4 cm^2) doses of a multicomponent ink formulation with B1, B2, B3, and B6. This method was able to detect the doses up to the fifth and sixth layers. The results obtained were confirmed by liquid chromatography-mass spectrometer results.

Two oromucosal dosage forms, lidocaine hydrochloride and a combined drug, were prepared using the inkjet printing technique [77]. The single drug formulation of lidocaine hydrochloride was fabricated by deposition onto an electrospun and cross-linked gelatine substrate. The combined drug, consisting of lidocaine hydrochloride and piroxicam, was prepared using the incorporation of piroxicam with substrate fibres by electrospinning before printing lidocaine

hydrochloride onto them. The resulting dose of the printed drug was (2.0 mg to 3.0 mg) [77].

Vakili *et al.* [78] recently used the piezoelectric inkjet printing method for designing four different orodispersible dosage forms for levothyroxine and prednisolone in square shaped fields of 4 cm^2. The quantification assessment of the printed fields revealed the average amount of the printed drugs was between 0.15 mg to 0.90 mg for levothyroxine and 0.43 mg to 1.95 mg for prednisolone. The mechanical properties, stability, and disintegration behaviour of the new dosage forms were tested. They used the NIR spectral device to determine the drug quantities in printed formulations.

The inkjet printing technique has been used in solid form screening, taking advantage of its ability to produce small droplets with picolitres in volume. Chan and Kazarian [79] studied the printing of polymeric solutions of ibuprofen and nifedipine on a crystal of ZnSe by means of the TIJ technique under controllable humidity. The resulting printed spots were subjected to spectroscopic analysis using ATR-FTIR spectroscopy [79]. The method was rapid as it requires minimal quantities of a sample in the range of 0.1 µg to 1.0 µg and about three minutes for analysis of 100 samples. They proposed that it is possible to increase the number of the analysed samples either by depositing small droplets of the solution (less than 200 µm in diameter) or by extending the ZnSe crystal dimensions.

Further work by the group of Bradley [80] adopted this approach by printing an initial micro-array of polymer spots onto a glass slide with solvent at room temperature using inkjet printing, with the drug solution being dispensed onto these droplets to investigate the drug solid forms produced. Analysis was undertaken using polarised light microscopy and Raman spectroscopy, with XRPD also employed. The typical sample requirements here were 27 µg of each polymer and 6.5 mg of the selected drugs.

Miniaturisation of high throughput screening methods has recently gained a great interest. Taresco *et al.* [81] recently presented a rapid and miniaturised system for high-throughput screening of polymeric solutions of six drugs. They formulated different drug/polymer ratios with minimal amounts in the range (25-650 ng) using the piezoelectric inkjet printing technique. The crystallisation behaviour of the resulting dried spots was investigated by optical microscope

after the total evaporation of the solvent (DMSO). They observed that the drug nucleation depends on the drug/polymer ratio due to the incompatibility of the drug in the mixture [81].

The reason for using the non-contact piezoelectric inkjet printing technique in this study is its ability to create a regular droplet at any required size and volume, which provides the feasibility to use microgram or sub-microgram quantities for investigation and possibly preparation of dosage forms, use a wide range of solvents, and avoid any contamination between the print head and the used substrate. This can motivate performing a solid form screening for APIs at a very early stage in the pharmaceutical industry due to the ability of the printing technique to consume minimal amounts of materials to perform high-throughput screening at a short time.

1.6. Aims and objectives

The overall aim of this thesis is to investigate whether using printed micro-arrays is viable for small- molecule pharmaceuticals in the context of pre-formulation and solid form screening. If so, then to examine the effect of the selected experimental variables (especially substrate charachteristics) on this, with a focus on reducing sample quantities compared to current state of art.

In chapter three, the main aim is to investigate the effect of the printed quantities of some APIs on the appearance of new polymorphs. It is based on the previous studies of Kazarian *et al.* [79] and Bradley *et al* [80] recommending printing minimal amounts (milligrams or sub-milligrams) of drugs, while introducing the use of the gold-coated slide as a substrate for deposition of a pure drug from the DMSO solvent. This can allow screening of drug compound libraries at a very early stage in the pharmaceutical industry, which are typically kept as DMSO stock solutions.

The 2D piezoelectric inkjet printing technique is used, for the first time, to produce nano-arrays with pico-litre droplets of paracetamol and carbamazepine on a gold-coated slide. For physical behaviour, optical microscopy is used to monitor the printed droplets until all the solvent (DMSO or DW) has evaporated and turned to spots. In contrast, Raman microscopy is employed for analysing the dried spots in two spectral regions, the molecular region (400-1800 cm^{-1}), and the phonon region (40-400 cm^{-1}), which can be considered as an emerging tool for rapid and reliable identification of solid forms [82], including amorphous *vs* crystalline forms, and distinguishing between polymorphs.

In chapter four, the main aim is to investigate the effect of chemical modification of the gold-coated slide, which has an affinity to form self-assembled monolayers with thiols, on the behaviour of the nanoquantities of paracetamol and mefenamic acid that are printed onto it. Optical microscopy and Raman spectroscopy is used for monitoring and identification of the printed spots respectively.

The main aim in chapter five is to investigate the effect of the fluorinated substrates on the appearance of new polymorphs during APIs screening using the 2D inkjet printing technique to deposit nano-quantities of carbamazepine, flufenamic acid, and mefenamic acid on fluorinated substrates, and using optical microscopy and the low-wavenumber Raman spectroscopy to monitor and analyse the resulting spots.

Chapter Two: Materials and Methods

This chapter aims to give a straightforward description of all the materials and instruments used to achieve the objectives of the current work. It also gives reasonable justifications for choosing the different materials and the analytic techniques to characterize them.

2.1. Drugs

Four model drugs are selected: paracetamol; carbamazepine; mefenamic acid; and flufenamic acid. All have been well-characterised previously in terms of solid-state forms, and they therefore provide a good test set for our work.

2.1.1. Paracetamol

Paracetamol, or acetaminophen ($C_8H_9NO_2$); A7302, 98%, CAS no.: 103-09-2, M.wt.: 151.16 (Figure 2.1), is widely used as an antipyretic and analgesic medicine; however, it cannot be categorized as a non-steroidal anti-inflammatory drug like aspirin because it has only a low level of anti-inflammatory activity [83, 84]. It belongs to class III of the biopharmaceutical classification system (BCS) and is characterized by high water solubility and low permeability [85]. Paracetamol can exist in three different crystalline forms, I, II and III, in addition to an amorphous, stable solid state [15, 86-88] . The monoclinic form (form I), which has been considered the normal marketed form, was described in previous works [89, 90]. The orthorhombic form (form II) was prepared by recrystallization of the alcoholic solution of form I [91].The third polymorph of paracetamol (form III) which is unstable, was reported to exist over three decades ago. It was prepared by heating the monoclinic form (form I) at 169 ˚C then cooling the melted paracetamol between slide and cover slip at 53 ˚C [92, 93].

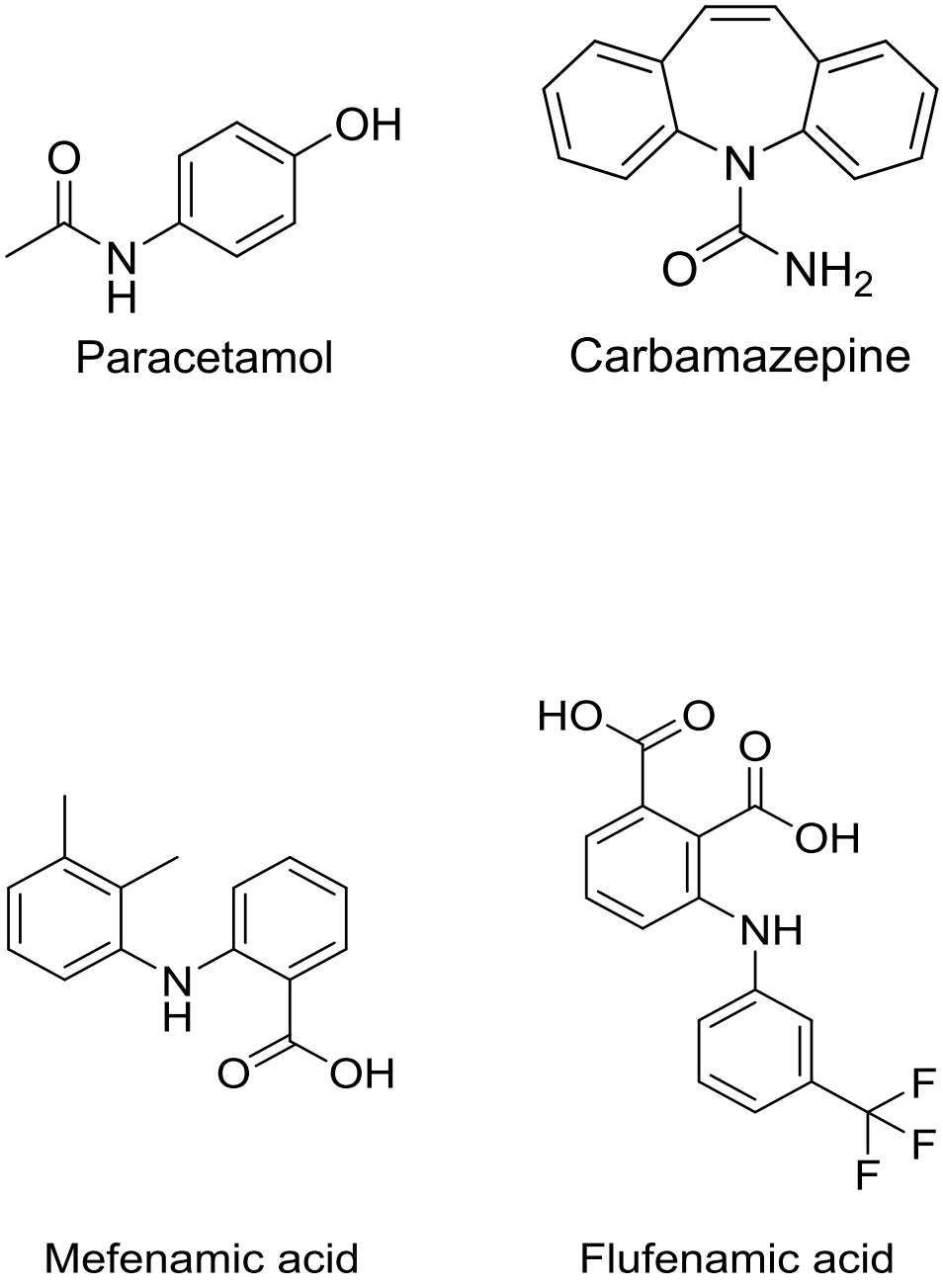

Figure 2.1. Chemical structures of paracetamol, carbamazepine, mefenamic acid and flufenamic acid

2.1.2. Carbamazepine

Carbamazepine, ($C_{15}H_{12}N_2O$), 153549, Lot no. M5827, CAS no.: 298-46-4, M.wt. 236.27 (Figure 2.1), is one of the most commonly used anticonvulsant drugs, which is prescribed for manic depression. It is used to treat neuropathic pains and seizure disorders [94]. It is characterized by low solubility and high intestinal permeability, and thus belongs to BCS class II. Three different anhydrous polymorphs (I, II and III) as well as one hydrated form have been reported in the literature [95].

2.1.3. Mefenamic acid

Mefenamic acid ($C_{15}H_{15}NO_2$), J62705, Lot. No. C07Z014, CAS no.: 61-68-7, M.wt.: 241.29, (Figure 2.1) is considered one of the most common drugs which belong to the fenamates group. The drug has analgesic and antipyretic effects, as well as being a non-steroidal anti-inflammatory agent [96]. It belongs to BCS class II and is characterized by low water solubility and high permeability[97]. According to the literature [98], two different polymorphs of mefenamic acid can be isolated: forms I and II. They show differences in physicochemical properties like stability and solubility. A new metastable polymorph of mefenamic acid (form III), which can be affected by variation in temperature to produce form II at high temperature and form (I) at low temperature, has been reported [99] .

2.1.4. Flufenamic acid

Flufenamic acid, ($C_{14}H_{10}F_3NO_2$) F9005, Lot BCBL8705, CAS n.: 530-78-9, M.wt.: 281.23, (Figure 2.1) is a non-steroidal anti-inflammatory drug which is used to treat musculoskeletal and joints illnesses [100]. It belongs to BCS class II. According to previous studies, nine forms of flufenamic acid have been investigated [11, 101].

2.2. Surfaces

Two different plain printing substrates have been used in this work: Gold coated microscope slides; 643203-5EA; Lot: MKBN5371V; layer thickness 100Aº; 99.999% (Au), were purchased from Sigma Aldrich. Another two gold-modified substrates have been used after treating the gold slides with two types of thiols to create self-assembled monolayers (SAMs).

2.2.1. Functionalized *n*-alkane thiols

The principles of thiol self-assembly monolayer formation will be described in Chapter Four. Three types of functionalized *n*-alkane thiols were used, one with a methyl-terminated group (1-undecanethiol), with a hydroxyl group (11-mercapto-1-undecanol), and with a CF_3-terminated group (11-mercaptoundecyl trifluoroacetate) (here abbreviated to SAM-CH_3, SAM-CH_2-OH, and SAMF respectively) (Figure 2.2). All the molecules have the same number of carbon atoms with a terminal thiol (SH) group which is expected to interact with gold [102]. These three molecules were used to prepare three clean and well-characterized substrates with different wettability, and this can give a chance to investigate the effect of the surface hydrophobicity on generating or triggering different polymorphic forms of APIs which have been printed on them.

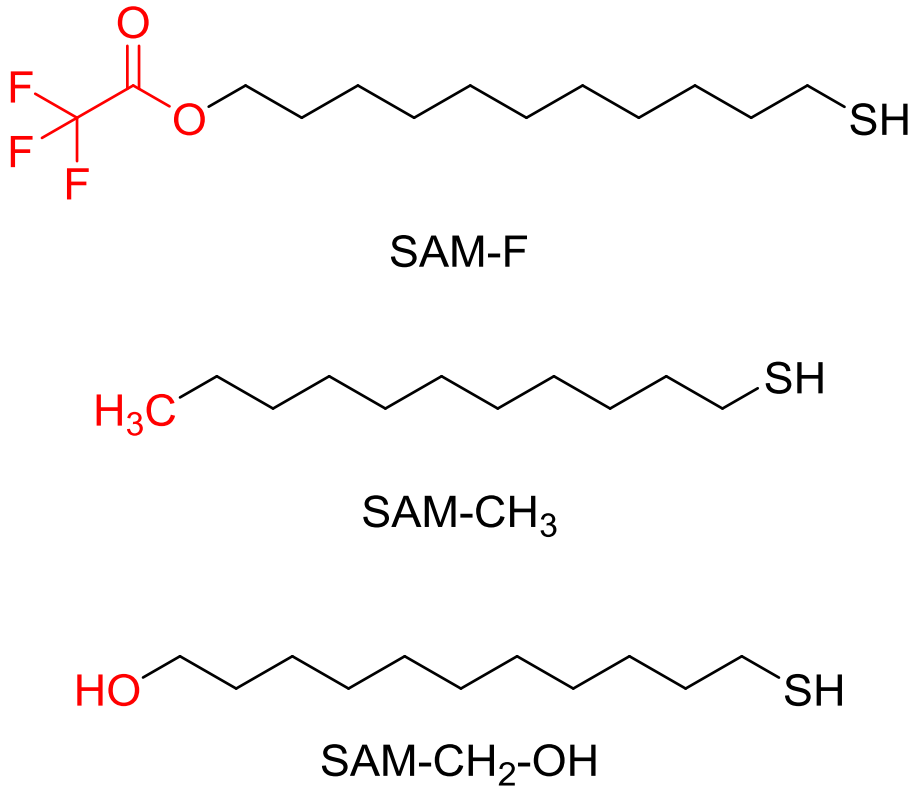

Figure 2.2. Chemical structures of 1-undecanethiol (SAM-CH_3), 11-mercapto-1-undecanol (SAM-CH_2-OH) and 11-mercaptoundecyl trifluoroacetate (SAM-F)

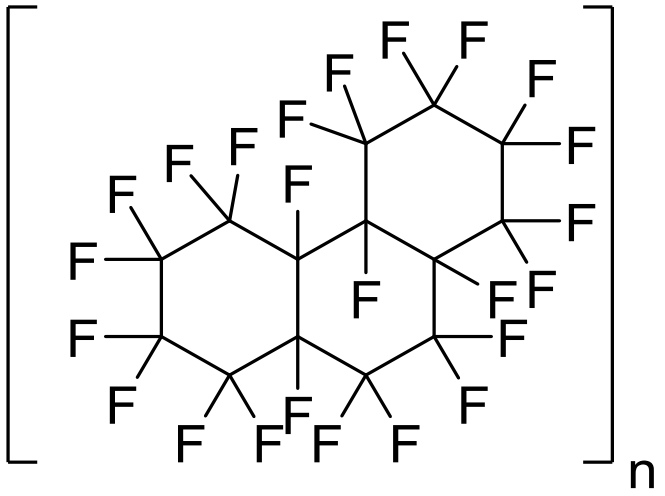

Figure 2.3. Chemical structure of perfluoroperhydrophenanthrene oligomer (Flutec LE15)

2.2.2. Perfluorocarbon fluid (Flutec LE15)

Perfluorocarbon fluid (Flutec LE15) was purchased from F2 chemicals (Lancashire, UK). It was used as a hydrophobising agent for the hydrophilic surface of the glass slides. Flutec LE15 has a low surface tension of 11.5 $mN \cdot m^{-1}$, viscosity of 0.656 mPa·s, density of 1.7 $g \cdot cm^{-3}$, and high water contact-angles between 99-102 [103] (Figure 2.3).

2.3. Instrumentations

2.3.1. Inkjet printing technique

A non-contact piezoelectric depositing system (Sciflexarryer S5, Scienion) was used in this work (Figure 2.4).

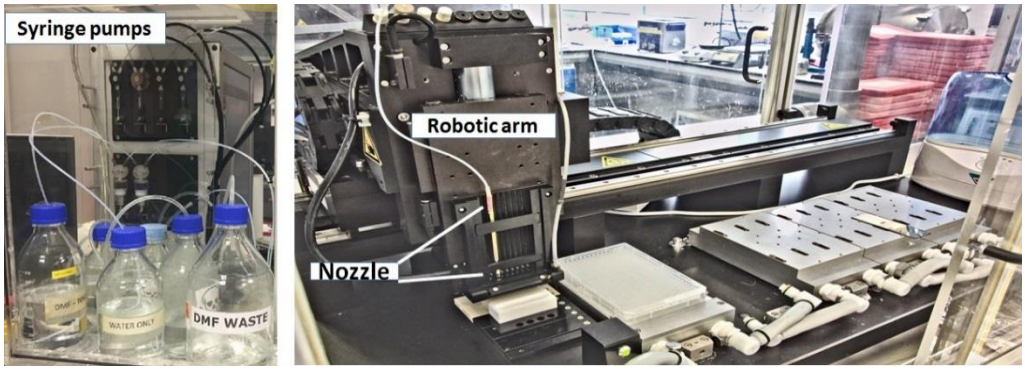

Figure 2.4. Microarray or 2D inkjet printer

This system is provided with a dispenser head, which comprises a nozzle connected with an automated arm which enables the nozzle to move in different directions with high flexibility and accuracy. A syringe pump is the second part of the hardware, which is connected to the nozzle and uses suction for taking samples and also for circulating the solvents for washing the nozzle and the whole system before and after the printing process.

Many precautions need to be taken into consideration when a microarray printer is used. All the hardware parts are embedded in a plastic chamber kept under controlled temperature and humidity and stored in a glass box to prevent contamination, and the substrates should be fixed carefully to the holder in order to avoid attaching and breaking the nozzle head.

The hardware parts are operated by integrated software, which manages all the printing steps. It can control the voltage and the electrical pulse can be easily tuned to regulate printed droplet size. Moreover, through the software it is also

possible to design the microarray fields by managing the droplet spacing (Figure 2.5 and Figure 2.6).

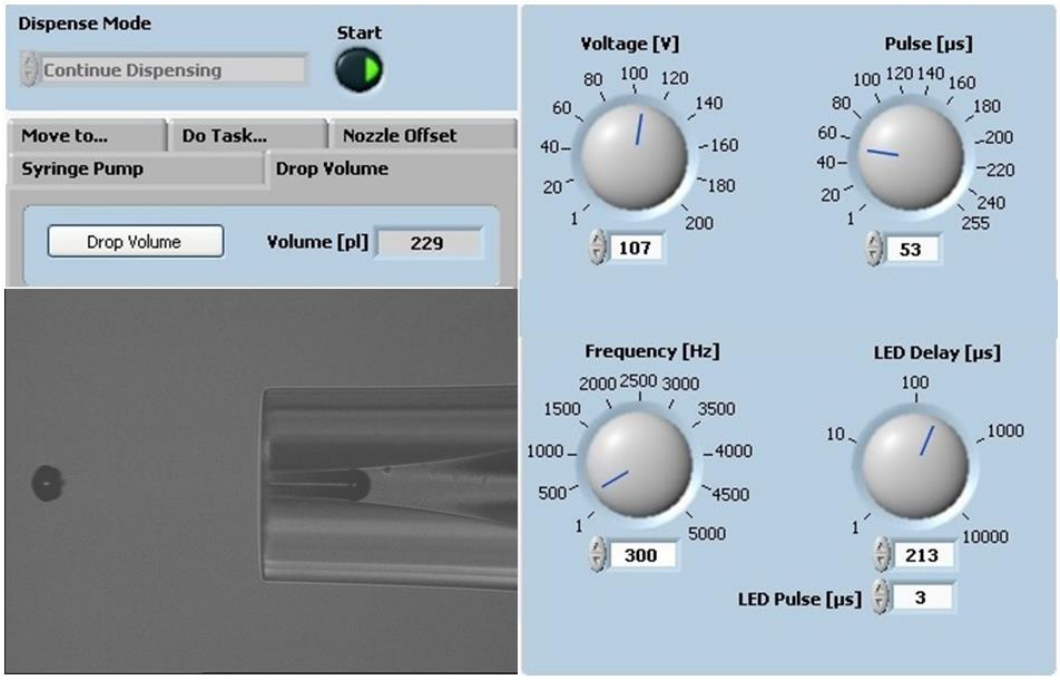

Figure 2.5. Droplet optimization via adjusting voltage and pulse

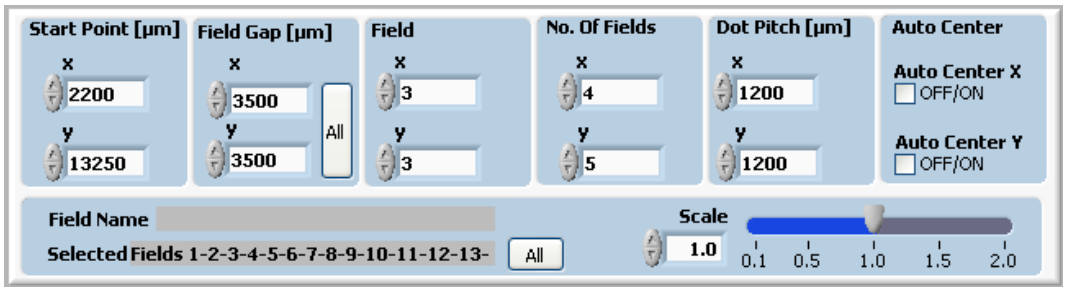

Figure 2.6. Parameters of setting the microarray

2.3.2. Raman spectroscopy

Although inelastic scattering was theoretically discovered in 1923, its effect, called Raman scattering, was observed and reported in 1928 by Sir Chandrasekhara V. Raman [104]. He won the Nobel Prize in Physics in 1930 as a reward for his observations. Nevertheless, applications of Raman scattering did not appear until the invention of the laser in the 1960s [105].

Raman spectroscopy has some disadvantages: there is the possibility of decomposition of samples due to high excitation intensities, and overlapping high levels of fluorescence, which may be caused by impurities[106]. However, due to the high stability of Raman peaks, it is considered a good choice for

analysis and identification of samples. When a molecule absorbs radiation, two types of scattering events happen: elastic and inelastic scattering. In the first type, both the incident and scattered photons have the same energy. This event is known 'Rayleigh scattering'[106].

Alternatively, the energy of the scattered photons may increase or decrease compared to the incident photons, which is known as 'Raman scattering'. There are two possible ways in which this absorbed radiation can be emitted. When a sample is irradiated by monochromatic radiation, the potential energy of a molecule is increased, and photons will move to a high level of energy then relax again to the ground state by emitting photons. These photons have the same as the absorbed light frequency; however, if the energy of the scattered photons is lower than the incident photons, it is known as 'Stokes Raman scattering' and if it is higher than that of the incident photons, it is called 'Anti-Stokes Raman scattering', as illustrated in Figure 2.7.

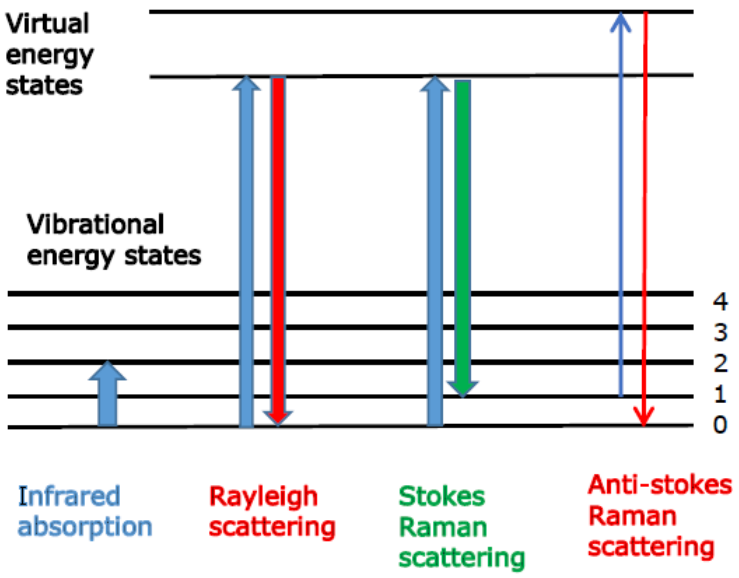

Figure 2.7. Schematic representation of the theory of Raman spectroscopy

With regard to chemical characterization of organic compounds, two main regions can be used in recognition of different crystal modifications, the molecular region from 400 cm^{-1} to 2000 cm^{-1} and phonon (lattice vibrations) region from 40 cm^{-1} to 400 cm^{-1}. The low-wavenumber bands include a strong contribution from phonon-mode vibration and other low energy movements such as torsional and twisting *etc*. These interactions can be easily observed in

Raman spectrum, which makes the identification of the different forms of APIs easier than the high wavenumber region, i.e. different solid forms have different inter-molecular interactions, therefore, low-wavenumber mode is quite sensitive to these differences [107].

The low-wavenumber vibrations are directly related to the physiochemical properties of polymorphs and offers useful information to deduce the acceptable method to determine the different solid forms. This is because it can be used to clearly observe the molecular structural distortion, librations and translations in vibrational frequencies below 400 cm^{-1} [108].

Two types of peaks are observed at low wavenumber: broad and sharp peaks. In amorphous forms, there is a broad peak as a consequence of the disordered nature of the molecular environment in the amorphous state, where intermolecular vibrations are not quantized [109]. Conversely, in crystal material, due to the regular periodic arrangement of molecules which arise from the quantized nature of the lattice vibration, sharp peaks can appear [109]. Hédoux *et al.* [110] presented the ability of Raman spectroscopy to investigate the amorphous and crystalline solid forms at phonon region. Caffeine was used as a model for studying the polymorphic transitions from liquid amorphous to solid crystalline state. Caffeine has two crystal forms, each one with a different peak in the low-wavenumber region. They used these two crystal forms in addition to the liquid state to compare the resulting peaks in the phonon region. The liquid state of caffeine exhibits a broad peak in the phonon region as illustrated in Figure 2.8. Distinctive peaks can be seen in the same region which indicate the crystalline form of caffeine form I and II [110].

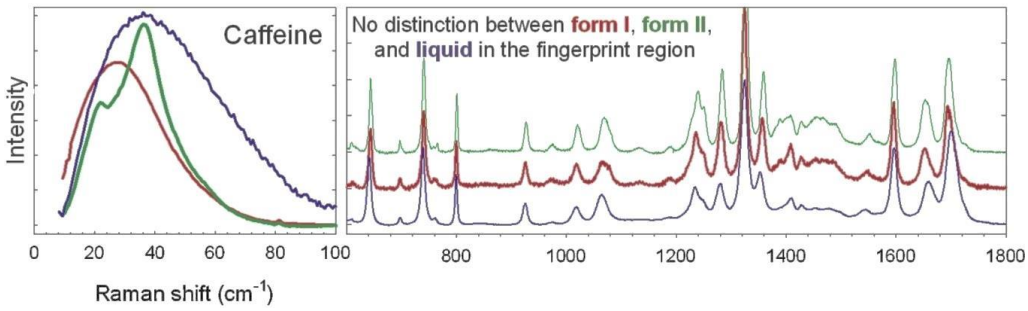

Figure 2.8. Raman spectra of amorphous, crystalline and liquid Caffeine [110]

One of the earliest studies, that was conducted to identify the polymorphs at low frequencies, was presented by Bellows *et al.* [111]. They could recognise two anhydrous forms with trihydrate form of ampicilline, and they also studied the effect of solvents, such as chloroform and benzene, on the appearance of the crystal structure of griseofulvin [111].

Al-Dulaimi *et al.* [112] presented a rapid and non-invasive solid form analysis using low-frequency Raman spectroscopy to analyse milligram quantities of paracetamol, flufenamic acid, and imipramine. It was found that there is an increasing in Raman peak intensity at low wavenumber region in comparison with those appear at molecular region, this is because of the high sensitivity of the low wavenumber peaks to the intermolecular interactions [112].

2.3.3. Confocal Raman Microscopy

A confocal Horiba-Jobin-Yvon LabRAM system (Horiba-Jobin-Yvon Ltd., Middlesex, UK), (Figure 2.9), was used in this work. It is provided of four different laser excitation capabilities: UV (325 nm), green (532 nm), red (660 nm), and NIR (785 nm). Illumination of all the samples in this work was done by using a 785 nm laser. The detector is a 1024-pixel silicon charge-coupled device detector (CCD), which has the ability to detect the Raman signals in one acquisition. It also has a motorized stage that can move in the x, y and z directions and can be used to carry out fast and extensive mapping and depth profiling of various samples including pharmaceuticals such as tablets [113].

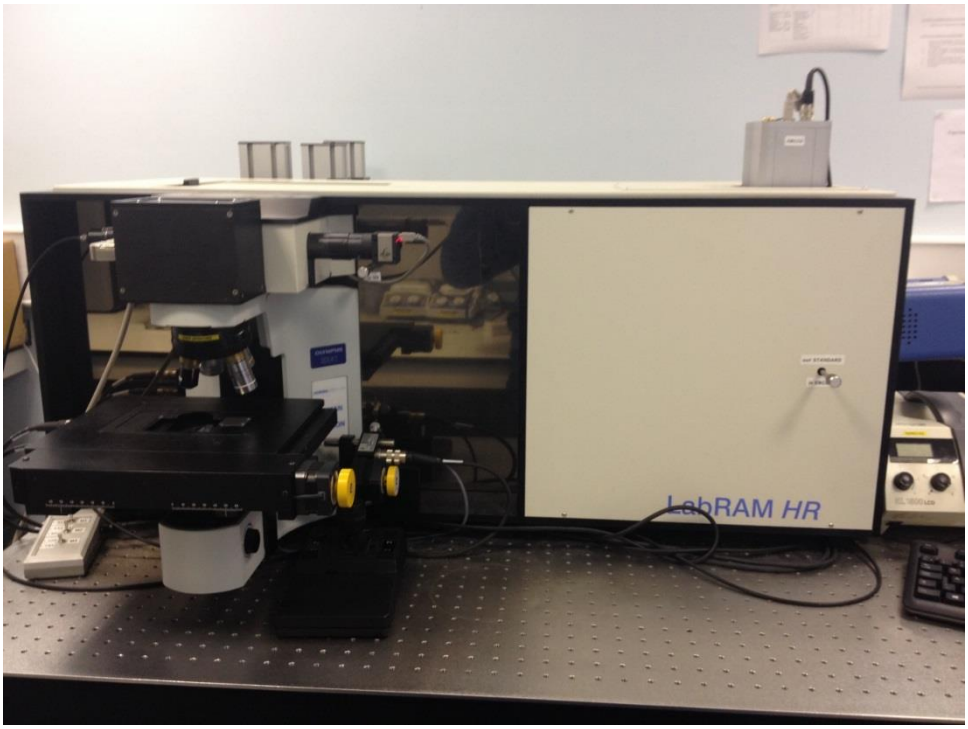

Figure 2.9. Raman spectrophotometer

The Raman spectrophotometer was also attached to an Olympus BX41 microscope provided with four objective lenses (10×, 40×, 50× and 100×). Smaller magnification was used for detecting dry spots on the different surfaces and larger magnification for Raman acquisition. Visualizing and focusing of the area of interest for analysis was performed by a video camera fixed over the sample holder.

2.3.4. Atomic Force Microscopy

This is an extremely versatile method for imaging and force/mechanical measurements at the nano and micro scales. It was invented in 1986 by Binnig, Quate and Gerber [114]. Figure 2.10 illustrates a schematic diagram of an AFM apparatus, which consists of a cantilever, typically made from silicon or silicon nitride, which is fixed in a location over the sample with the tip pointing down. The system also includes a laser source, a scanner, a quartered photodiode and a photosensitive detector. All these components are controlled by a software (NanoScope Analysis 1.7).

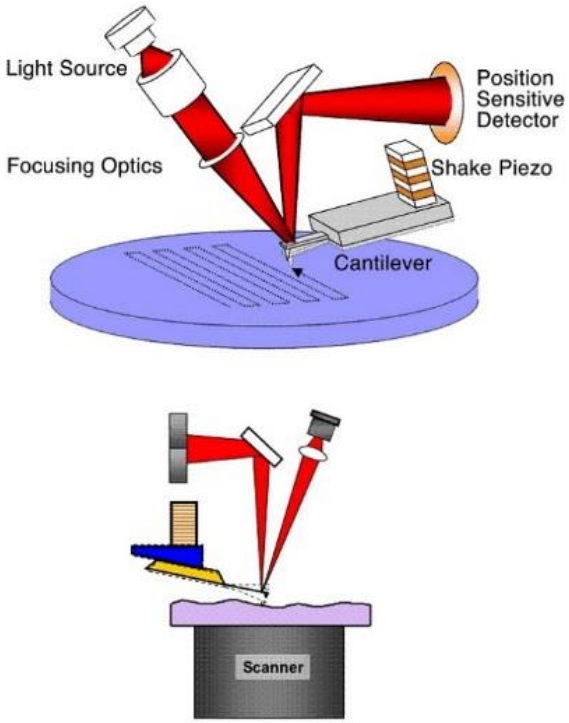

Figure 2.10. The schematic diagram of Atomic force microscope AFM

The scanner can be either fixed in the base or in the head of the AFM and moves in x, y, and z directions. Generally, there are two different modes for AFM imaging: tapping/contact mode and non-contact mode. In tapping mode, the cantilever oscillates at a certain frequency which makes the tip tapping the top of the sample, reducing the possibility of tip damaging by decreasing the large lateral force induced by scanning. The tapping mode was used in imaging the surfaces of the prepared substrates in this work. The laser beam is focused on the back of the cantilever; when the tip comes close to the surface, the cantilever starts moving up and down, and contacts with the sample surface intermittently, producing interactions between the tip and the sample surface. The generation of the topographic image can be achieved as a result of changes in the scanner height. The deflected laser can be probed by the quartered photodiode and the difference in light intensities between lower and upper photodetector quadrants is measured by the photodetectors[115].

2.3.5. Polarized Light microscope (PLM)

This is a simple technique which involves illumination of a sample by a polarized light. PLM can probe the birefringence resulting from an anisotropic sample, like a crystalline material, due to its interaction with the polarized light

causing a contrast with the background [116]. However, any amorphous sample does not show any birefringence due to its isotropic nature, which leads to a similar colour to the background being shown. In this work, the resulting dots were investigated by means of an Advanced Polarizing Microscope (HS1; Prior LuxPOLTM) with a 12V and 30W halogen lamp with variable brightness control (Figure 2.11).

Figure 2.11. Polarized Light microscope (PLM)

2.3.6. Evaluation of substrate surface and pharmaceutical solutions by means of water contact angle (WCA) and surface tension (ST) measurements

The KSV CAM 200 (Figure 2.12) is a computer-controlled and user-programmable video-based instrument designed for the measurement of water contact angle (WCA) and surface tension (ST). In this work, the KSV CAM200 was used to measure the WCA to evaluate the roughness and the wettability of the prepared solid substrates depending on the side observation of the drop; then, the contact angle was able to be determined by measuring the angle between the tangent of the drop surface at the contact line and the surface [117].

Also, it was used to calculate the interfacial ST for the drugs solutions using the pendant drop method, which is one of the most suitable methods to determine ST [117]. The pendant is suspended from a needle in a bulk liquid or gaseous phase. The shape of the drop results from the relationship between the surface tension or interfacial tension and gravity. In the pendant drop method, the surface tension or interfacial tension is calculated from the shadow image of the pendant drop using drop shape analysis [117]. Both water contact angle and surface tension can be calculated according to Young's equation [117]

$$\gamma_{lv} \cos\theta = \gamma_{sv} - \gamma_{sl}$$

Where: γ_{lv} is the liquid-vapor interfacial tension, γ_{sv} is the solid-vapor interfacial tension, γ_{sl} represent, solid-liquid, and θ is the contact angle.

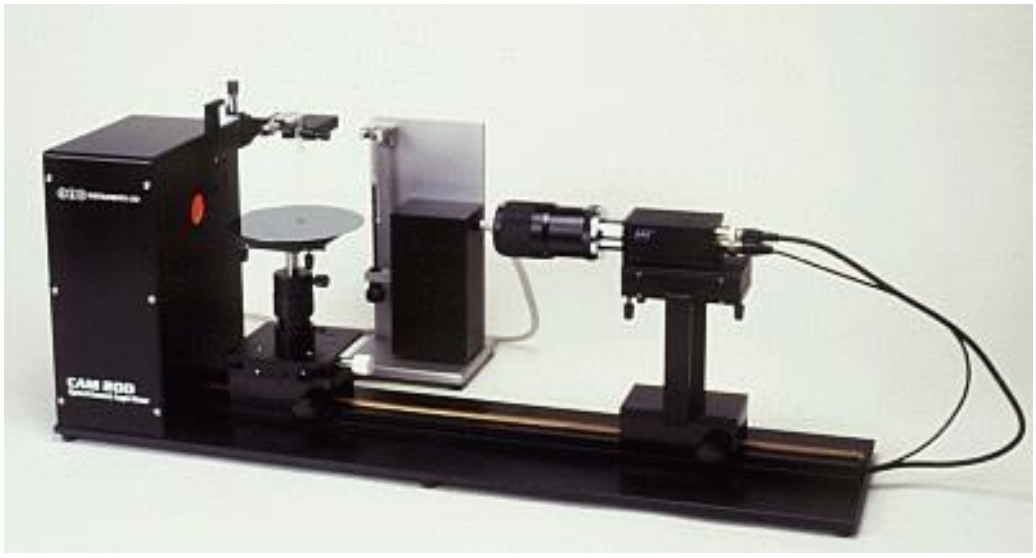

Figure 2.12. Water contact angle and surface tension apparatus

2.3.7. Dip Coating

Dip coating (referred to sometimes in the literature as vertical deposition) (Figure 2.13) can be considered one of the earliest commercialized coating techniques. It was presented for the first time in 1939 [118]. It is a low-cost and practical method that does not require special equipment. The dip-coating technique is based on five technical steps: immersing the surface in the solution at a fixed speed, the time of the immersion inside the solution, deposition of the material on the surface, draining the excess solution from the substrate and the evaporation [119]. Dip coating technique was successfully used to fabricate thin film substrates in this work.

Figure 2.13. Dip-coating unit

Chapter Three: Miniaturisation of API solid form screening using the 2D inkjet printing technique

3.1. Introduction

Many new drug candidates are hydrophobic and exhibit low solubility, which leads to inadequate oral bioavailability. This is one of the most crucial challenges facing the pharmaceutical industries [120]. For a drug substance to be active *in vivo*, it needs to be dissolved in water. The importance of dissolution in determining bioavailability is often considered in the context of the Biopharmaceutical Classification System (BCS) [21], which classifies drugs according to their solubility and gastro-intestinal permeability. Many drugs in development pipelines are BCS class II (low-solubility, high permeability) and their efficacy (or lack thereof) is largely determined by the solubility of that drug in its formulation [21]. The design of the pharmaceutical dosage form has always been difficult, especially drugs with BCS class II (high permeability and low solubility), which is considered the most problematic class for scientists [21-24]. Economically, the formulation of a suitable form with acceptable physical and chemical properties can take a great deal of time, resources and human efforts. There is, therefore, a pressing need to improve screening tests to obtain a rapid evaluation of a formulation designed for increasing solubility using small quantities of pharmaceutical compounds [42].

In addition to solubility challenges, the majority of medicinal compounds can exist in different solid forms. These forms are divided into amorphous and crystalline solids. An amorphous or non-crystalline phase is when a solid is arranged in a disorderly fashion without a regularly repeating three dimensional structure [3]. Examples can be found in different industrial products, such as pharmaceuticals, polymers and optical materials [4]. Unlike amorphous solids, a crystalline solid, such as diamond or graphite, is arranged in a consistent manner, forming three dimensional structures called crystal lattices [3], see Chapter One for details.

Due to the differences in dissolution rates and solubility, the bioavailability of amorphous solids differs to that of crystalline solids. Novobiocin, for example, does not have high bioavailability in its crystalline phase. In contrast, its

amorphous form exhibits an effective therapeutic concentration [121]. Thus, dissolution has to be monitored in a solid form to ensure safe and effective drug delivery [30].

The tendency for a substance or compound to exist in multiple solid structures and to take different forms is called polymorphism [9]. This phenomenon might induce changes in physical properties such as melting point, density and solubility [10]. It has been gained a great interest by researchers hoping to prevent happening unexpected products during and after synthesis. Ritonavir for example, which was believed to present as one polymorph (Form I), demonstrates the impact of the existence of many structures of one compound in pharmaceutical manufacturing. It was temporarily pulled from the market after a new polymorph (Form II) emerged that led to major problems with the dissolution rate of the final dosage form (see Chapter one) [12].

Solid form screening is the identification of which solids are likely to form for a particular drug after typical manufacturing, processing, storage and use [9]. Although it was recognised at the beginning of the nineteenth century, increasing attention is now being paid to the importance of solid form screening as a standard method for improving the bioavailability and physical stability of the pharmaceutical compounds, due to the high percentage of active pharmaceutical ingredients that exhibit polymorphism [25, 26].

For high-value materials, such as pharmaceuticals, the availability of samples for a solid-form screen can be problematic. For example, lead compounds might only be available in sub-milligram quantities, and for hit compounds taken forward in development the various biological assays (e.g. toxicity) can consume the majority of the compound synthesised, leaving little available for any preliminary formulation studies.

Current industrial approaches to miniaturisation typically involve scaled-down versions of bulk solvent-based crystallisation methods. For example well-plate technologies may use temperature profiles, evaporation, salting out, *etc*. to induce the crystallisation of drug into multi-well plates. While these approaches can reduce sample requirements to as low as a few milligrams, they introduce complexity into the sample analysis. Crystallisation or precipitation does not necessarily occur at an identical location in each well, which adds complexity to the analysis of the screen [34, 42].

Therefore, there is currently an opportunity to develop a solid form screening method that both employs minimal amounts of sample and also produces a readily addressable experimental layout. This opportunity was first realised for solid forms by the group of Kazarian [79] who employed a heated "droplet on demand" system to deposit between 0.1 µg to 1 µg of drug/polymer melt directly onto an FTIR-ATR diamond focal plane array to produce a solid dispersion micro-array for analysis. A controlled humidity cell was also employed, which allowed spectroscopy measurement of the response of polymer:drug spots to water.

Further work by the group of Bradley [80] adopted this approach by printing an initial micro-array of polymer spots into a glass slide from solvent at room temperature using ink-jet printing, with drug solution being dispensed onto these polymeric dry spots to investigate drug solid forms produced. Analysis was undertaken using polarised light microscopy and Raman spectroscopy, with XRPD also employed. The typical sample requirements for the whole screening process were 27 µg of each polymer and 6.5 mg of the selected drugs [80].

Taken into account both Kazarian *et al* [79] and Bradley *et al* [80] methods and the crucial understanding of the solid form in pharmaceutical pre-formulation. However, the main advantage of using 2D inkjet printing technique to deposit milligrams or sub-milligrams of materials in previous studies gives a motivation to use the same technique to miniaturise the used quantities of APIs at nano-scales (pico-litres) to achieve solid form screening at the primary stage in pharmaceutical industries.

It has been adopted the use of 2D inkjet printing technique, for the first time, for deposition of pure drug from (DMSO) solvent on a gold-coated slide which is used as an insoluble chemically tunable surface. This also potentially allows the method to be readily transferred to allow screening of drug compound libraries in pharmaceutical industry, which are typically kept as DMSO stock solutions. In addition, further miniaturisation of the sample quantities required were investigated, again with a view to pharmaceutical application. For analysis of solid form, low-wavenumber Raman microscopy was employed, which is an emerging tool for rapid and reliable identification of solid forms, including amorphous *vs* crystalline and distinguishing between polymorphs. Three model drugs were selected: paracetamol (PAR), carbamazepine (CBZ), and mefenamic

acid (MEF). All of these have been well-characterised previously in terms of solid-state forms, and they therefore provide a good test set for the current work.

3.2. Experimental design

Paracetamol PAR (Acetaminophen 98%) was purchased from Sigma-Aldrich (France); it was used as received and there was no need for purification. Raman spectrum analysis confirmed that it was of form I. It was also found to melt at 169-170 °C [14, 122]. Carbamazepine CBZ was purchased from MP Biomedical, was used as received and there was no need for purification. Raman spectrum and literature confirmed that it was of form III [123]. It was also found to melt at 177°C [124]. The two used polymorphs of CBZ were confirmed by XRPD measurements, see (Figure A. 1). Mefenamic acid MEF ($C_{15}H_{15}NO_2$), was purchased from Alfa Aesar, A Johnson Matthey Company. Raman spectrum confirmed that it was of form II. It was also found to melt at 230-231 °C [125]. Analytical, Dimethyl sulfoxide (DMSO), (C_2H_6OS) 99.5%, was purchased from Sigma-Aldrich and Gold coated microscope slides with layer thickness 100Å; 99.999% (Au).

3.2.1. Preparation of polymorphs of the selected drugs

PAR (as received) was confirmed by Raman spectrophotometer as polymorph I and used to compare the resulting polymorphs. CBZ I was prepared by heating an amount of the CBZ powder (as received) for 48 hour at 170 C˚ and then verifying the identity of the product by Raman spectroscopy [126]. Two polymorphs for MEF were prepared to be additional references with what we found in previous study to identify the resulting polymorph after printing, MEF II was prepared by heating an amount of the MEF (as received) for 48 hour at 160 C˚ and then verifying the identity of the product by Raman spectroscopy [96].

These abovementioned drugs were used as models compound in this study as they have all been well-characterised previously in terms of solid-state forms, and they therefore provide a good test set for this study. [95, 98, 127, 128].

3.2.2. Preparation of pharmaceutical solutions

A solution of 6 mg·mL^{-1} of PAR was prepared by dissolving 30 mg in 5 ml of distilled water (DW) as it is freely soluble in water. Preparation of 6 mg·mL^{-1} of CBZ and MEF were performed by dissolving 30 mg of each drug separately in 5 mL of dimethyl sulfoxide (DMSO) due to their poorly solubility in water. Table 3.1 shows the actual solubility of the studied drugs in distilled water and DMSO.

Table 3.1. The solubility in (mg/ml) of the studied drugs in distilled water and DMSO [128]

Drug	Solubility in D.W	Solubility in DMSO
Paracetamol	13.4	1133
Mefenamic acid	Scarcely soluble	48
Carbamazepine	Scarcely soluble	47

After preparation of the pharmaceutical solutions, the printing process was conducted by depositing different volumes of these solutions on a gold coated glass microscope slide used as a substrate. Images of the printed droplets were then taken over time using an optical microscope to investigate the solvent evaporation and re-crystallization of the drugs in the dry spots, and Raman spectroscopic identification was then used for the resulting spots, see Figure 3.1.

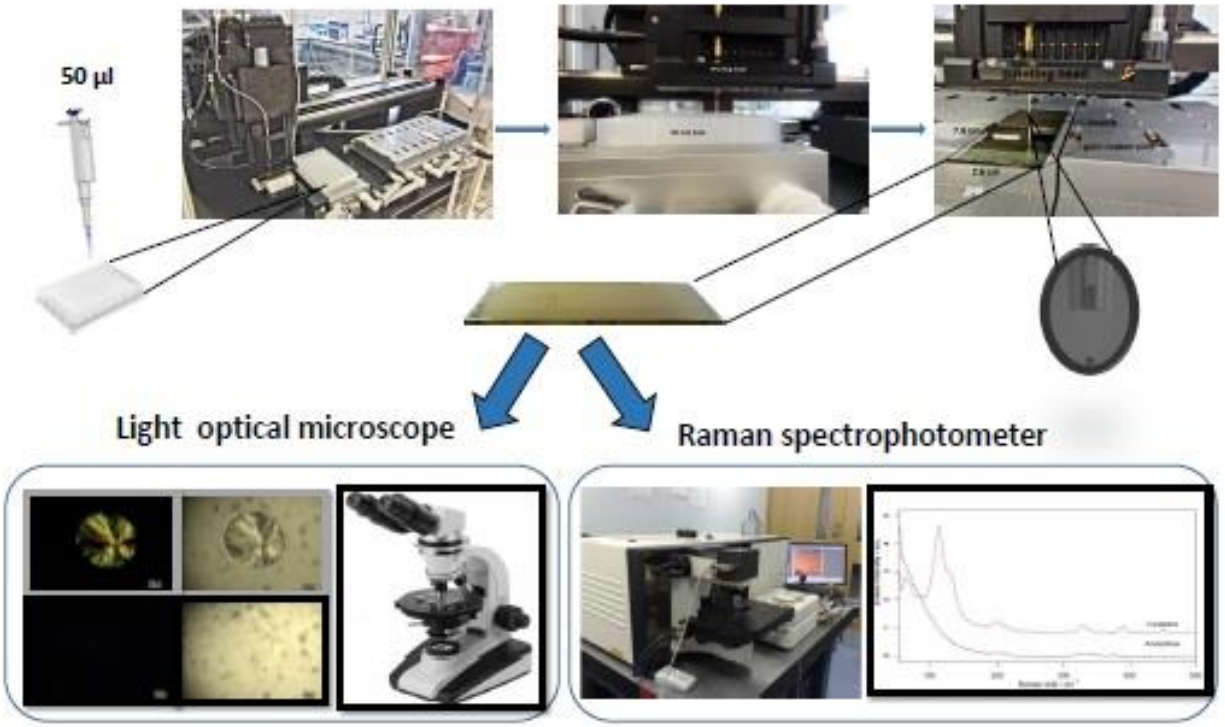

Figure 3.1. The steps of printing and identification of different volumes of drug on gold-coated microscope slide.

3.2.3. Fabrication of APIs microarray

PAR, CBZ, and MEF, were deposited on the gold-coated under ambient conditions (RH=52%, T=21˚C) by using a 90 µm orifice nozzle on a non-contact piezoelectric depositing system (Sciflexarryer S5, Scienion). The droplet size and shape were controlled by adjusting the values of the firing voltage and the electrical pulse at 85V and 48 µs respectively to obtain a regular droplet shape with volume of (232±3) pL for PAR in DW, and (248±2) pL for PAR, CBZ, and MEF, in DMSO.The printed array was designed by producing four main fields one for PAR in DW and three for the whole drugs in DMSO, the gaps between each field and the droplet spacing were 3500 and 1200 µm respectively. Each field consists of six clusters with (3×3) replicates representing the six different quantities; 1, 10, 50, 100, 250, and 500 ng, see Figure 3.2.

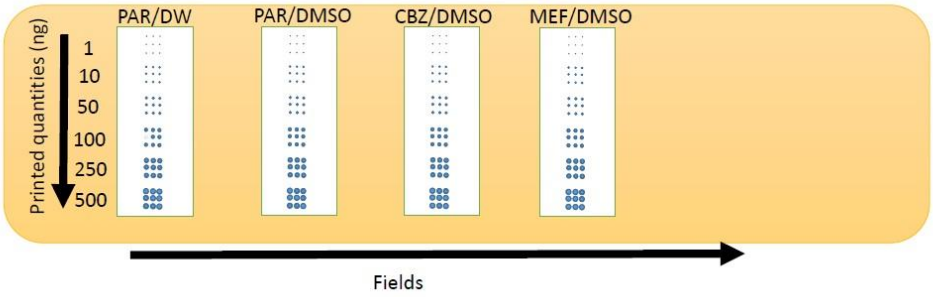

Figure 3.2 Schematic representation of APIs microarrays on gold-coated slide

The details of printing conditions are summarised in Table 3.2

Table 3.2.The number of droplets and the printed quantities of 6mg·mL^{-1} of the selected drugs.

Theoretical quantities of solute (ng)		1	10	50	100	250	500
PAR, CBZ, and MEF, and in DMSO Vol. = (248±2 pL)	**Actual printed quantities (ng)**	1.48	10.42	50.59	99.69	249.98	499.96
PAR / D.W, Vol. = (232±3 pL)		1.39	9.74	50.11	100.22	250.56	499.72

The printed gold slide was then transferred directly to the light optical microscope to investigate the behaviour of the droplets during and after solvent evaporation, and pictures of the final dried spots were taken at regular intervals. They were then kept in a desiccator at room temperature.

3.2.4. Optical microscopy

The resulted dots were subjected to Advanced Polarising Microscope (HS1 microscope), Prior LuxPOLTM with 12V and 30W halogen lamp and with variable brightness control using only (10×) magnification to investigate the crystalline behaviour of the printed spots with time. The bright-field and cross-polarised images were recorded by means of a camera fixed to the top of the microscope and connected to a computer. The acquired data was processed via Q-capture^{TM} software to manipulate the brightness and the light exposure time in order to get an image with high quality.

3.2.5. Raman spectroscopy

As mentioned in Chapter Two, this confocal Raman spectrophotometer has four different laser excitation capabilities: UV (325 nm), green (532 nm), red (660 nm) and NIR (785 nm). Only the NIR (HeNe, 785 nm) laser was used with 600 lines/mm of grating, 300 µm of confocal hole and spectral range between 40 and 1800 cm^{-1}. It was also connected to an Olympus BX41 microscope provided with four objective lenses (10×, 40×, 50× and 100×). Three objective lenses were used, 10× for selecting the spots, 50× for calibration and 100× for focusing the small printed spots of the drug. The obtained Raman data was processed by means of the LabSpec 5 software.

3.3. Results

3.3.1. Properties of ink formulation

PAR, CBZ, and MEF were chosen to be models for this study as they have a wide range of well-characterised polymorphs [95, 128, 129] that can be used to compare the resulting polymorphs that form during and/or after the printing process.

A gold-coated slide was selected as a substrate in this chapter as it has an acceptable WCA of 52.8°± 0.5, which prevent the rapid spreading of the drug droplets after they attach to the substrate, and therefore, a visual characterization

is simple. Beside its chemical inertia and ability to magnify the Raman signals [130, 131], gold has been chosen as a starter surface platform, because it can undergo further modifications (as seen in the following chapter) to evaluate the drug behaviour once the latter is in contact with different chemical environment [130]. Coated surfaces may also affect the molecular mobility of the printed droplets, which may affect the stability of these materials [132].

DMSO was selected in this study because it can play important roles in pharmaceutical industries as it can be used as a solvent during synthesis of the drug components, work as a co-solvent for stabilising the formulation products, and be used as a cryoprotector and drug carrier [133].

The prepared pharmaceutical solutions should have specific physical properties in order to achieve a successful printing. Viscosity and surface tension can play an important role in evaluation of the pharmaceutical inks. It is advisable for the viscosity to be lower than 20 mPa·s as using highly viscous solutions can damage or block the printing nozzle (Figure 1.8), while highly diluted solutions are not preferable as printing inks as they may penetrate the nozzle wall itself, which in turn affects its efficiency [47, 63].

Surface tension is another physical parameter that can be used to evaluate the property of the pharmaceutical solutions. It has been reported that the surface tension in the range 30 $mN \cdot m^{-1}$ to 70 $mN \cdot m^{-1}$ is the optimal condition for achieving the printing process in a controllable way [63]. An important point that should be taken into consideration that surface tension should be more than 30 $mN \cdot m^{-1}$ to avoid the ink dripping from the nozzle, and lower than 70 $mN \cdot m^{-1}$ to facilitate ink spreading over the surface [63]. Table 3.3 illustrates the physical properties of the two selected solvent used in this study. It is evident that the viscosity and the surface tension of DW and DMSO are within the acceptable range for using them as solvents in this study. It is also expected that the evaporation time of DMSO will take longer than DW because of the high boiling point of DMSO [63].

Table 3.3. Physical properties of the used solvents [63]

Solvent property	Solvent	
	DW	DMSO
Boiling point (°C)	100.0	189.0
Vapour pressure (mmHg at 20 °C)	17.5	0.1
Surface tension ($mN \cdot m^{-1}$)	72.8	43.5
Viscosity (mP·s at 20°C)	1.0	2.0

The surface tension and the contact angles of all the prepared solutions on the gold-coated slide were measured. Table 3.4 shows the experimental values of surface tension and contact angle for PAR, CBZ, and MEF at room temperature.

Table 3.4. Surface tension and contact angle (on gold-coated slide) for the used drugs

Drug	Solvent	Surface tension ($mN \cdot m^{-1}$) (n=6)	Contact angle (°) (n=9)
PAR	DW	75.6 ± 0.4	52.8°± 0.5
PAR	DMSO	42.3 ± 0.2	25.2°± 0.2
CBZ	DMSO	43.1 ± 0.4	26.2°± 0.5
MEF	DMSO	43.2 ± 0.1	24.3°± 0.5

According to Young's equation (see Chapter two), the contact angle proportional increases with the surface tension of the used solution [72].

Aqueous PAR droplets, for example, show a CA of 52.8°± 0.50, whereas PAR droplets prepared using DMSO exhibit 25.20°± 0.20. The difference in CA values can be attributed to the variance in surface tension values of DW and DMSO, see Table 3.3 [63]. Also, the low surface tension values of PAR, CBZ, and MEF make the spreading of their droplets over the gold substrate rapid, which is exemplified by their low CA values, see Table 3.4.

In the current work, we initially investigated the kinetics of crystallisation of the printed spots by using optical microscope with 10× magnification. In order to achieve additional polymorph information, we employed Raman spectrometer to differentiate the drug crystallization. The phonon region from 40 cm^{-1} to 400

cm^{-1} was particularly taken into account as it can be considered as a fingerprint for the identification of different polymorphs and solid states [109].

3.3.2. The behaviour of the printed droplets of the used APIs on the gold substrate

Figure 3.3 shows the evaporation time of different printed volumes of PAR, CBZ, and MEF on gold substrate. Figure 3.4 illustrates the relationship between the volume of the printed droplets with the time to full evaporation (time to dryness). The high CA of PAR/DW of 52.80°± 0.50 (Table 3.4) suggested that it may take a long time for evaporation compare to the PAR/DMSO droplets, which exhibits low CA of 25.20°± 0.20, indicating that it would evaporate rapidly. They both showed behaviour different to this, however. It can be seen that PAR droplets prepared using DW evaporated faster than those prepared with DMSO, the volume of 56 nL of PAR/DW required only three minutes to turn into a solid spot, while 72 minutes was required to evaporate the same volume of PAR/DMSO droplets (Figure 3.3 and Figure 3.4).

The hydrophobicity behaviour of the printed droplets of PAR, CBZ, and MEF on gold-coated slide was presented in (Figure A. 2).

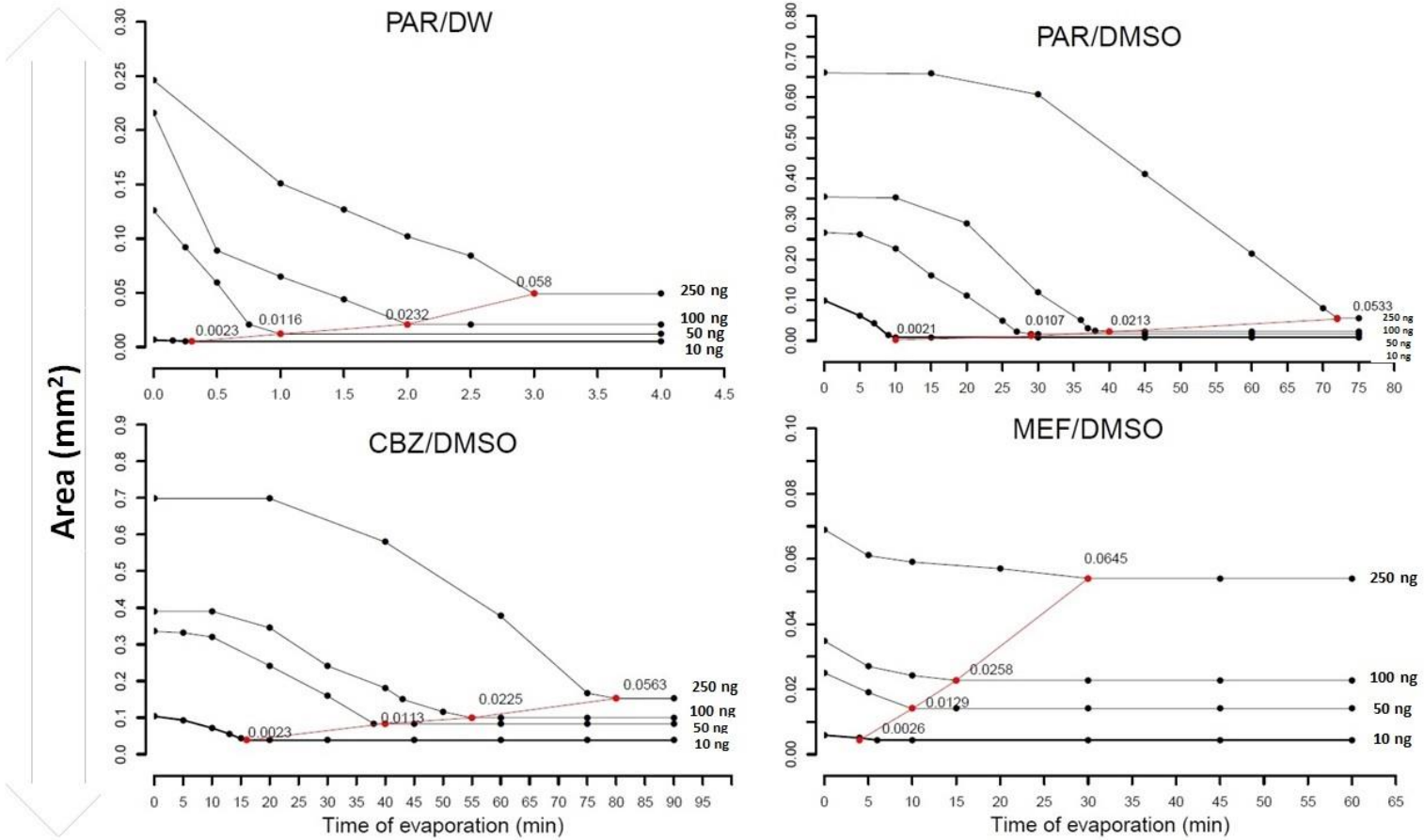

Figure 3.3. The evaporation time of different printed quantities of the selected APIs on gold-coated slide . The red points reveal the volume of each printed quantity which is clearly demonstrated in the next figure

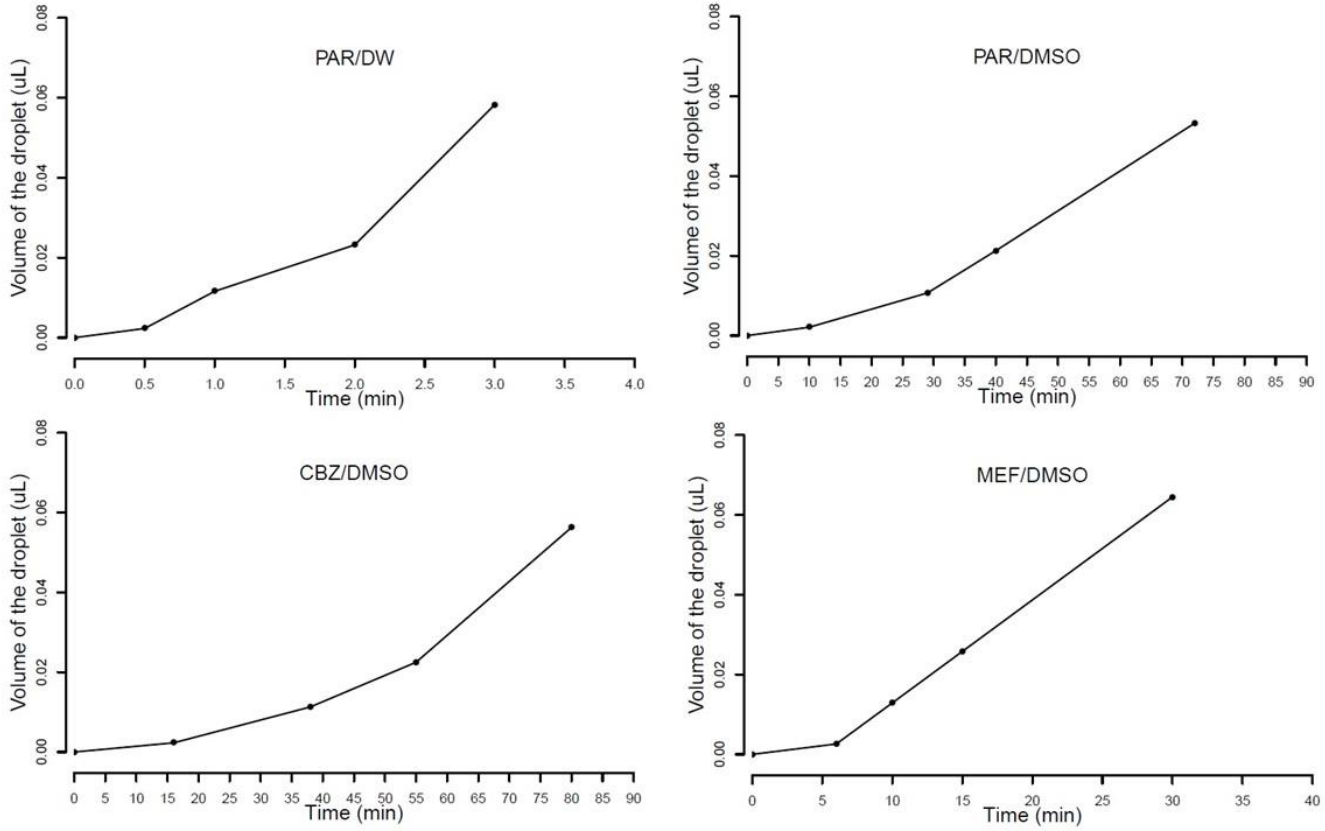

Figure 3.4. The time to full evaporation of different printed volumes of the selected APIs on gold-coated slide

This huge difference in evaporation time was attributed to the variety in boiling point and vapour pressure of DW and DMSO (Table 3.3). The high boiling point and the low vapour pressure values of DMSO can delay the evaporation time of PAR/DMSO droplets up to 72 minutes (Figure 3.4) [63]. The behaviour of CBZ and MEF droplets on gold slide were investigated (Figure 3.4). It can be noticed that 60 nl of CBZ and MEF in DMSO required 80 and 30 minutes respectively to remove all the DMSO and turn to solid spots. As mentioned above, the reason of the long evaporation time is attributed to the vapour pressure of DMSO (Table 3.3) which delays the evaporation process [63]. The evaporation time *vs* the area relationship of the different printed volumes of FLUF/DMSO was presented in (Figure A. 3).

3.3.3. Investigation of the PAR spots behaviour on the gold-coated slide

Optical microscopic identification can provide the visual confirmation of the events occurring during the transformation from one state or form to another. The printed gold coated slides were transferred onto the optical microscope to investigate the drug spots crystallisation behaviour over time by means of 10× magnification for all the printed amounts. The aqueous and DMSO solutions of PAR were printed on gold slide with six different quantities, as shown previously in experimental section (Figure 3.2). Later, the printed gold-coated slide was transferred onto the optical microscope to examine the crystallisation habit of the PAR droplets over the time by means of 10× lens for all the printed amounts (Figure 3.5).

The microscopic investigation revealed that all the printed quantities of PAR/DMSO solidified in the shape of the droplets with relatively smooth and transparent surface, and did not give any birefringence when exposed to the polarised light, which indicated the amorphous state of these droplets.

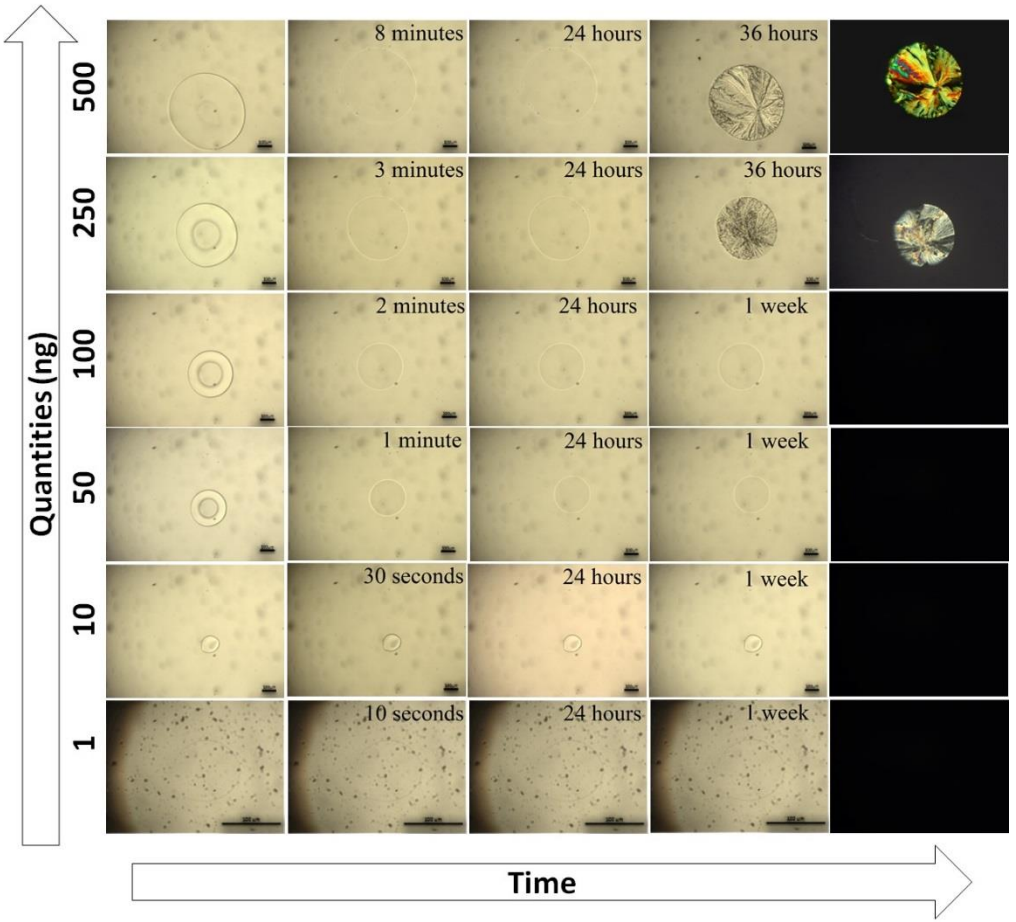

Figure 3.5. The bright-field and cross-polarised images of different printed quantities of PAR/DW , (scale bar 0.1 mm)

This was not the final physical state for some of these printed quantities, however. Two days later, the big printed spots (250 ng and 500 ng) had changed in appearance to a crystal form. The conversion from solid amorphous to crystal state for these big printed quantities required more than 36 hours, while the printed amounts below 100 ng did not exhibit any change in their amorphous state, see (Figure 3.5).

The behaviour of PAR droplets prepared using DMSO is shown in Figure 3.6. The bright-field images revealed that all of the printed quantities underwent a decrease in size due to DMSO evaporation followed by solidification with a relatively transparent surface, indicating the amorphous state of all of the droplets. The cross-polarised images confirmed the amorphicity of the PAR/DMSO spots. The physical state of PAR spots had not changed so far (Figure 3.6).

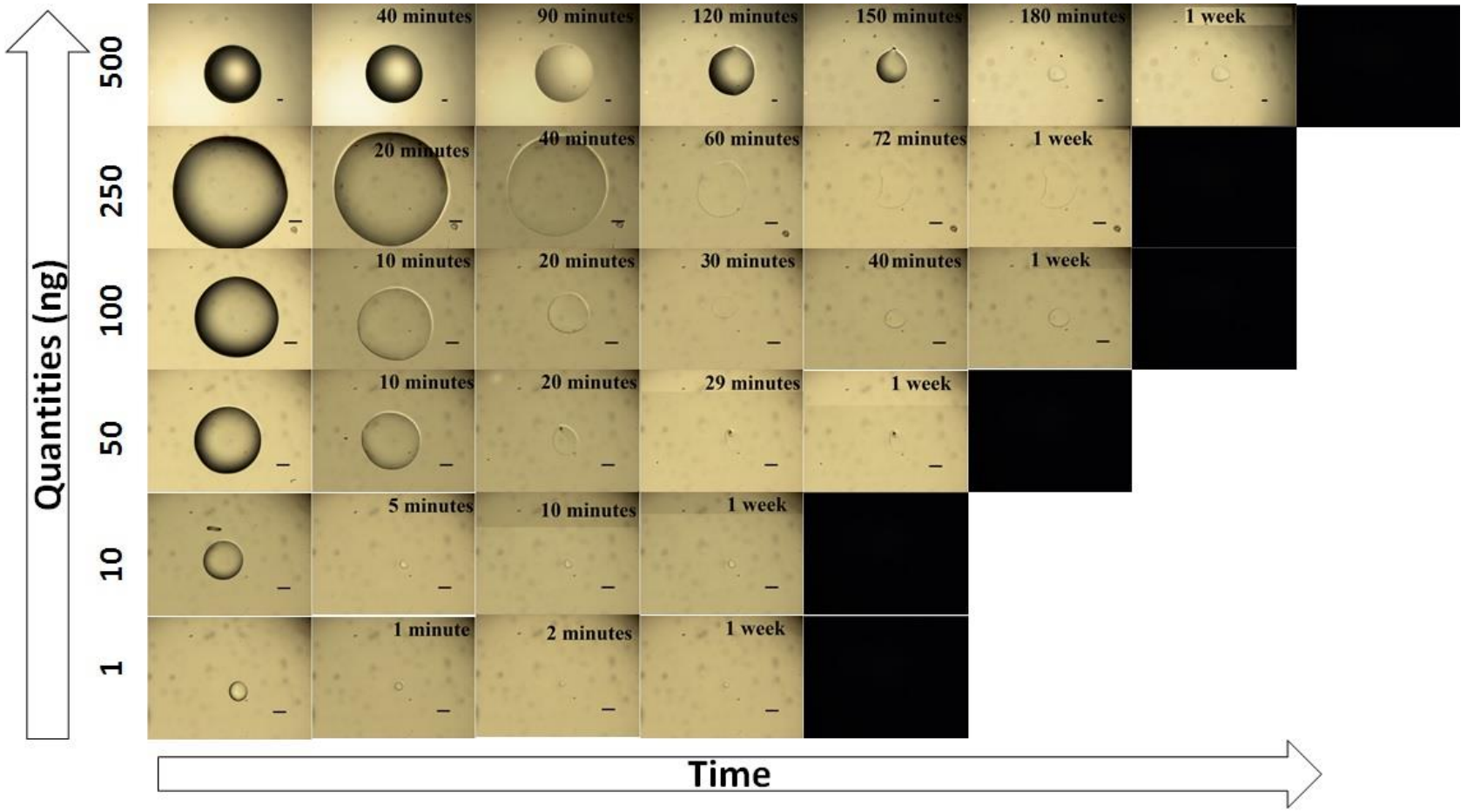

Figure 3.6. The bright-field and cross-polarised light images of different printed quantities of PAR/DMSO (scale bar 0.1mm)

Raman single point analysis was performed to confirm the physical states of the printed dots that were previously observed by light optical microscope.

Figure 3.7 Figure 3.8 present the Raman spectra in the phonon and molecular regions of the printed spots of PAR that resulted from aqueous and organic solvents evaporation. As described before, the low printed quantities of PAR (in both DW and DMSO) showed an amorphous state. Due to the phonon region (40 cm^{-1} to 400 cm^{-1}), or low wavenumber region being considered as a fingerprint of any polymorph, it can show the effect of the intermolecular vibrations that take place in this region. Spots of 1ng,10 ng, 50 ng, and 100 ng of PAR/DW exhibited broad and continuous peaks in the wavelength range between 40 cm^{-1} and 400 cm^{-1}, while two distinct peaks at ~ 122 cm^{-1} and 140 cm^{-1} can be seen in the high printed quantities (250 ng and 500 ng, Figure 3.7).

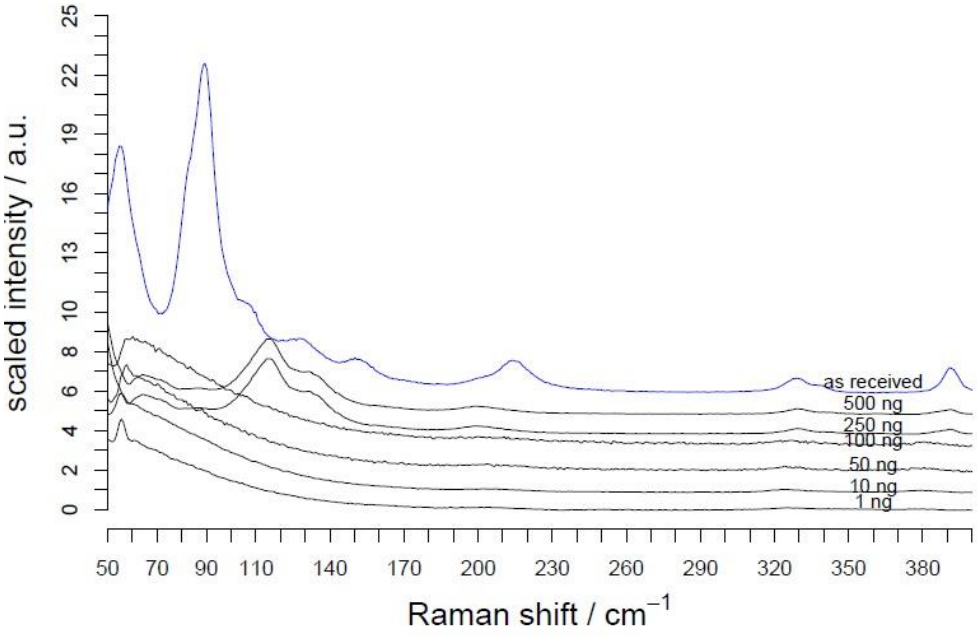

Figure 3.7. Raman spectra in phonon region for different printed quantities of PAR in DW, with reference spectrum (blue).y-axis offsets were employed for presenting the differences between panels.

In the molecular region, the amorphous behaviour of the low printed amounts of PAR/DW spots (1ng to 100 ng) was confirmed by two apparent features. First, a characteristic peak at ~ 1600 cm^{-1} can be noticed only in low printed quantities spectra, which indicates the unorganised nature of these spots producing amorphous state [112]. Second, it can be seen there is a sharp single peak at ~ 1650 cm^{-1} in the high printed quantities (250 ng and 500 ng) and in PAR (as

received) spectra that does not appear in the low quantities' spectra. This suggest that only crystal forms exhibit this peak [112] (Figure 3.8).

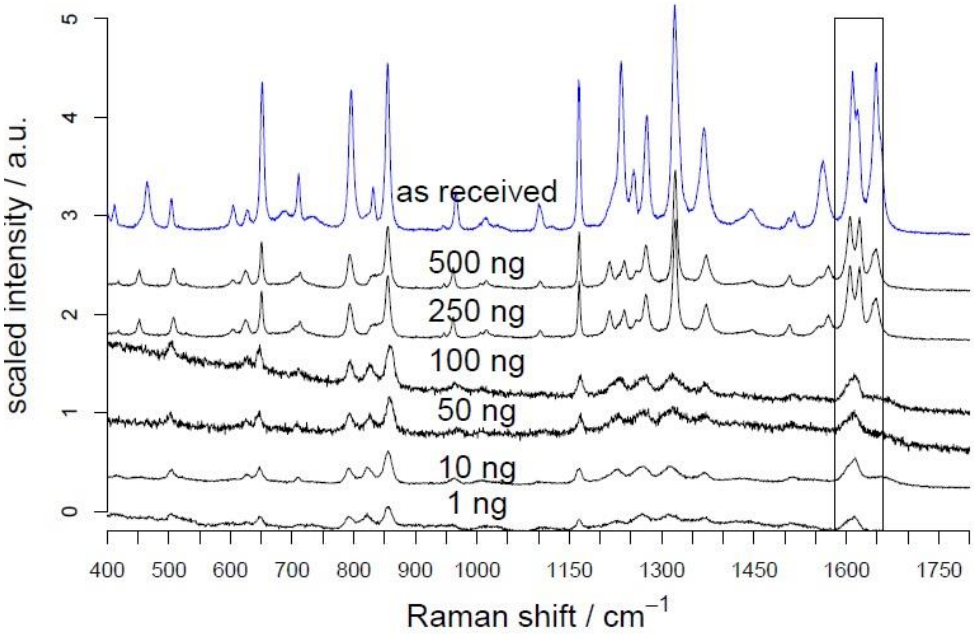

Figure 3.8. Raman spectra in molecular region for different printed quantities of PAR in DW , with reference spectrum (blue).y-axis offsets were employed for presenting the differences between panels. The region inside the bar reveal the unorganised nature of the small printed quantities (1 ng to 100 ng) comparing to the crystal nature of the big spots (250 ng and 500 ng)

The PAR/DMSO spots, on the other hand, exhibited only amorphous state for all the printed quantities. These results were compared with reference spectra in literature to identify the different polymorphs. The Raman spectra of all the printed quantities confirmed that the amorphous state is the predominant for PAR/DMSO droplets. The resulting figure is completely in accordance with what was presented in literature [112] (Figure 3.9 Figure 3.10).

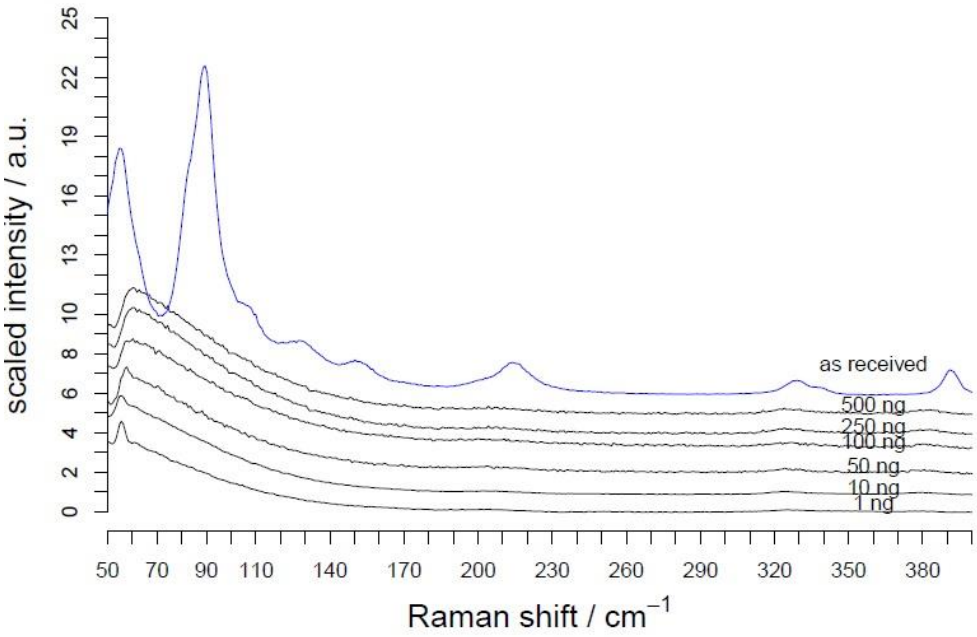

Figure 3.9. Raman spectra in phonon region for different printed quantities of PAR in DMSO, with reference spectrum (blue).y-axis offsets were employed for presenting the differences between panels.

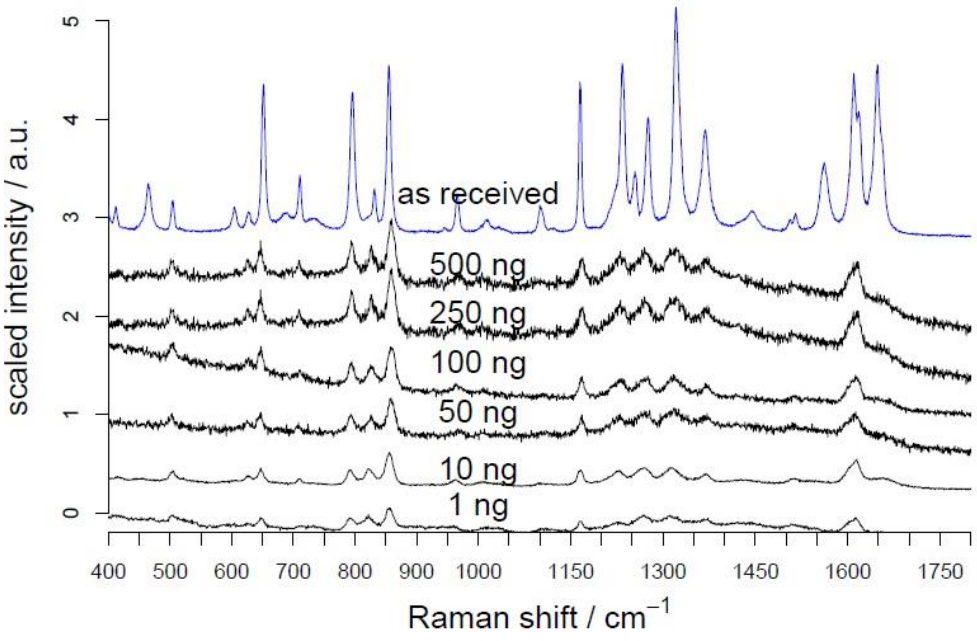

Figure 3.10. Raman spectra in molecular region for different printed quantities of PAR in DMSO , with reference spectrum (blue).y-axis offsets were employed for presenting the differences between panels.

Overall, it can be noticed that PAR droplets prepared by DW showed a different behaviour as they exhibited an amorphous state at quantities low than 250 ng, and crystalline form (II) at high printed amounts more than 250 ng after more than 36 hours. While the PAR droplets made by DMSO did not exhibit change in amorphous state for all the printed quantities after full DMSO evaporation.

3.3.4. Investigation of the MEF spots behaviour on the gold-coated slide

Figure 3.11 shows the bright-field images of different quantities of MEF printed on gold-coated slide. It can be seen that all the printed quantities of MEF, from 10 to 500 ng, underwent a slight decrease in size due to DMSO evaporation followed by direct crystallisation, as all the MEF polymorphs exhibit a crystal state. At high quantities (500 ng), the droplets required around 62 minutes to remove DMSO and turn directly into a crystal state, while the lower printed quantity (10 ng) needed only five minutes to achieve full DMSO evaporation and turn to crystal form (Figure 3.11).

Because of the birefringent characteristic of the crystal materials such as MEF spots, they exhibit an interference effect when putting them under polarised light microscopic mode, this destructive interference with the white light can cause a spectrum of colours [5, 134].

Figure 3.12 Figure 3.13 show the Raman spectra in the phonon and molecular regions for different quantities of MEF printed on gold slide. Two reference spectra were used as references for comparison to the acquired spectra: MEF (as received) that was previously characterised as polymorph I (red), and polymorph II ,which was previously prepared and identified (blue) [123, 135].

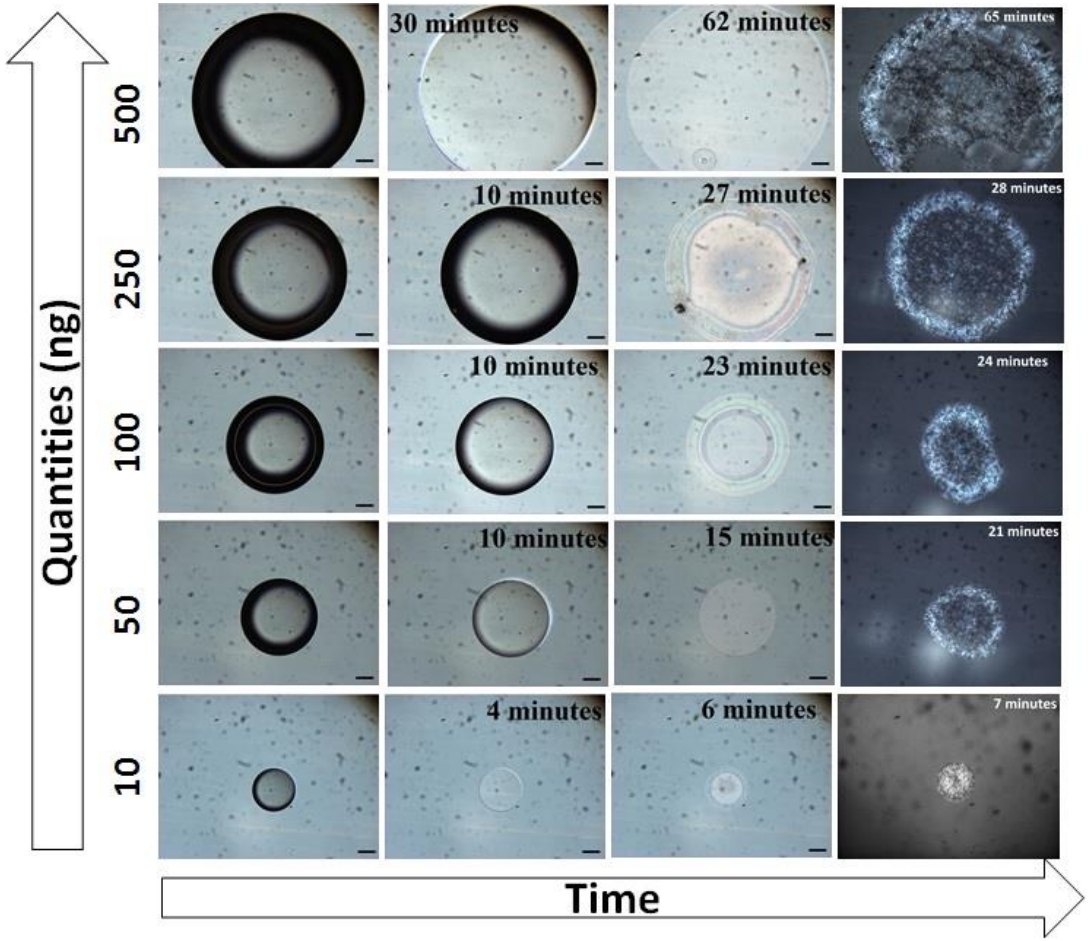

Figure 3.11. The bright-field and cross-polarised light images of different printed quantities of MEF in DMSO , (scale bar 0.1 mm)

In the phonon region, it can be seen that all the printed spots and the reference spectra exhibit multiple peaks due to the variation in intermolecular vibrations for these samples. The Raman spectra acquired from the printed spots from 1 ng to 250 ng of MEF show characteristic features at ~ 50 cm^{-1}, a single sharp peak at ~ 152 cm^{-1}, and three broad peaks between 80 cm^{-1} and 110 cm^{-1}, see Figure 3.12. It was found that these characteristic peaks (in the box), after comparing with the reference spectra and literature, are close in features to MEF II [123].

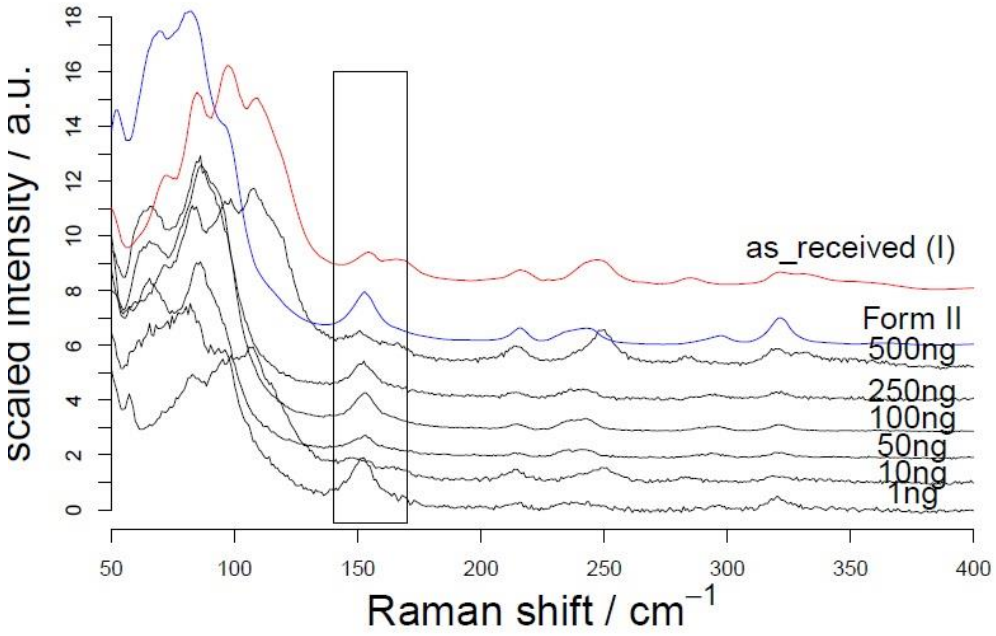

Figure 3.12. Raman spectra in phonon region for different printed quantities of MEF in DMSO , with reference spectra (blue and red).y-axis offsets were employed for presenting the differences between panels.

For the high amounts of MEF printed on gold substrate (500 ng), the Raman single point measurements exhibited a different spectrum, which was close to MEF I [123].

In the molecular region, further distinguishable differences, demonstrated inside the boxes, can be used as an additional confirmation of the identity of the printed spots of MEF (Figure 3.13.). The change in peaks position between 750 cm^{-1} and 810 cm^{-1}, and the peak shapes between 1240 cm^{-1} and 1245 cm^{-1}can be used to differentiate between MEF polymorphs. A single broad peak at 1515 cm^{-1} can be easily seen in 500 ng spot spectrum that does not appear in the low printed

quantities, indicating that the 500 ng spot of MEF exhibit polymorph I [135, 136].

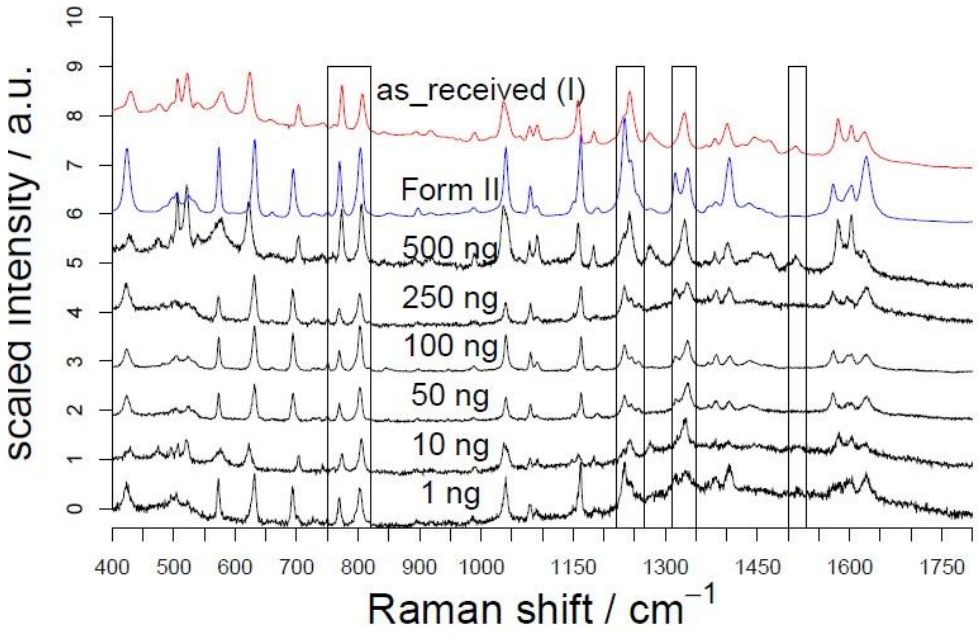

Figure 3.13 Raman spectra in molecular region for different printed quantities of MEF in DMSO , with reference spectra (blue and red).y-axis offsets were employed for presenting the differences between panels. The entire bars represent the differences of the Raman spectra at these selected regions

Finally, the Raman single point measurements acquired from 500 ng spot of MEF exhibit single sharp peak at ~ 1345 cm^{-1}, which can be assigned to MEF I, while the other quantities' spectra exhibited a mix of Raman features for both form I and II. It can be noticed also two distinct peaks between 1330 and 1340 cm^{-1} in 250 ng spectrum, which can be attributed to the dimeric nature of MEF II [135, 136].

3.3.5. Investigation of the CBZ spots behaviour on the gold-coated slide

The CBZ droplets required 48 to 72 hours to become crystallised. They also underwent a decrease in size as a result of DMSO evaporation, producing solid amorphous spots in 10, 48, 72, 98, and 240 minutes for 10 ng, 50 ng, 100 ng, 250 ng, and 500 ng respectively. One day later, the CBZ amorphous spots started to turn into a crystal state, depending on the printed quantity (Figure 3.14).

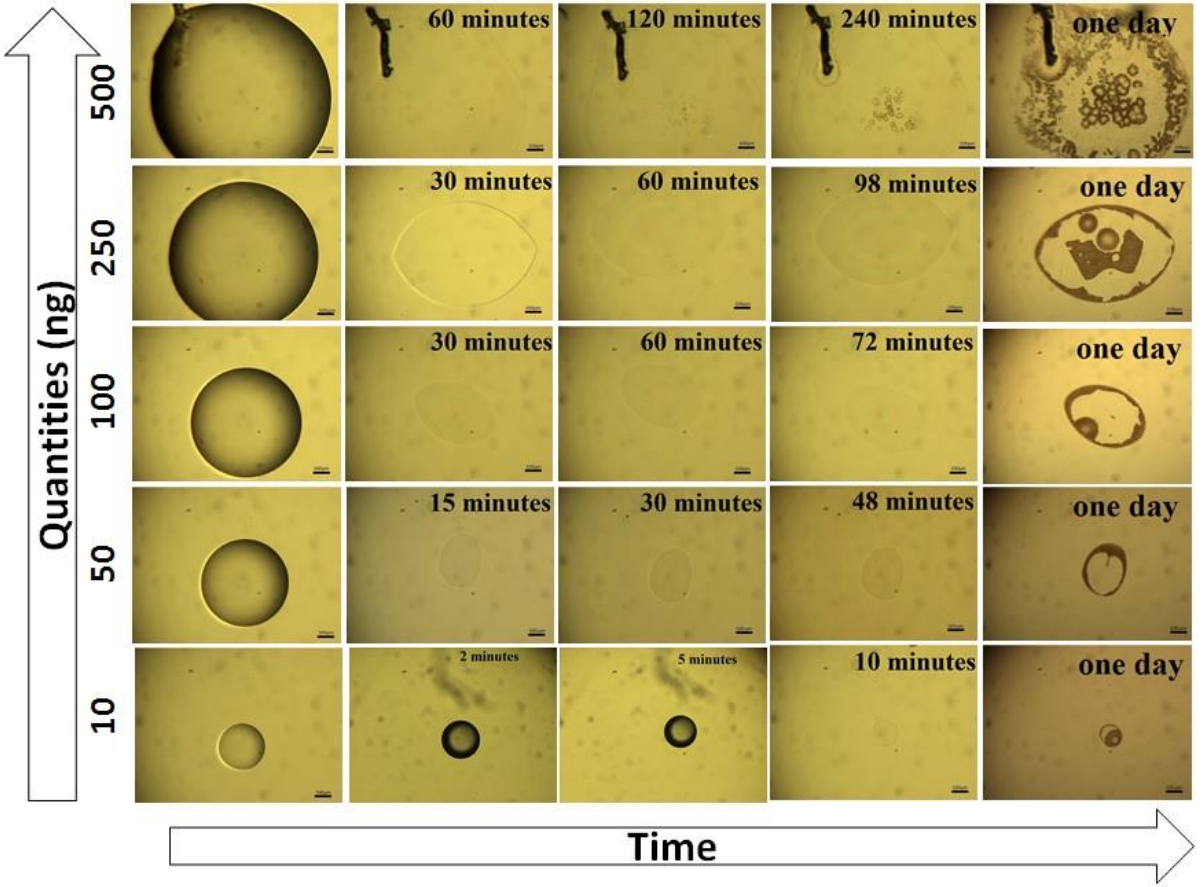

Figure 3.14 The bright-field images of different printed quantities of CBZ in DMSO (scale bar 0.1mm)

Figure 3.15 and Figure 3.16 show the Raman spectra in the phonon and molecular regions for different quantities of CBZ printed on gold slide. Two reference spectra were used as references to compare the acquired spectra: CBZ (as received) that was previously characterised as polymorph III (blue) and polymorph I which was previously prepared and identified (red) [123, 126].

In the low wavenumber region between 40 cm^{-1} and 400 cm^{-1}, many differences, demonstrated between boxes, can be characterised between the two reference spectra of CBZ I and III. It can be also noticed that all the printed quantities exhibited two distinct peaks at 52 cm^{-1} and 110 cm^{-1} with a shoulder at 125 cm^{-1}, and two broad peaks at (60-64) cm^{-1} and (160-180) cm^{-1} regions were also characterised. These characterised peaks were closer in features to CBZ I rather than to III [123] (Figure 3.15).

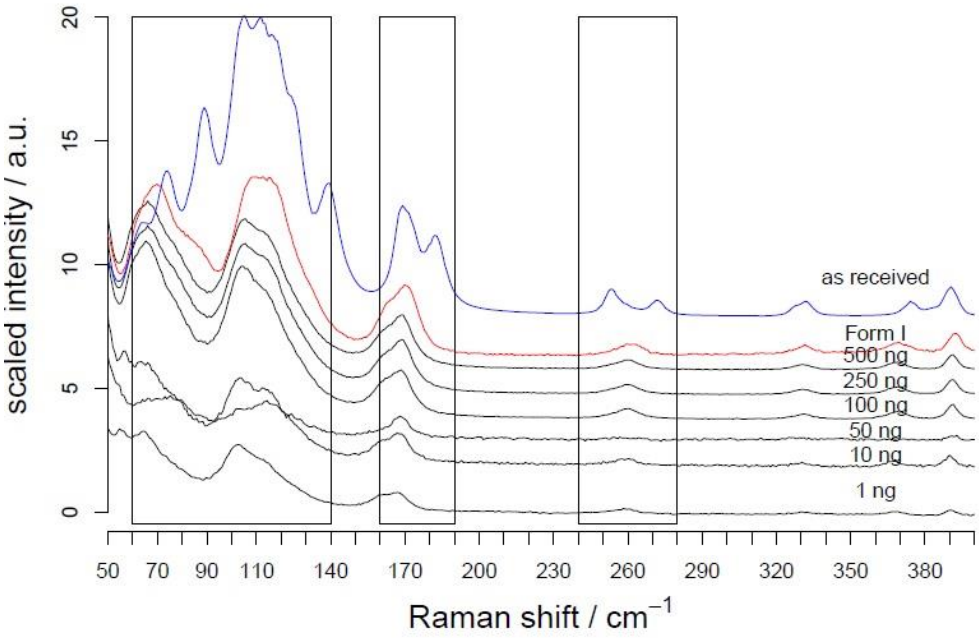

Figure 3.15. Raman spectra in phonon region for different printed quantities of CBZ in DMSO, with reference spectra (blue and red).y-axis offsets were employed for presenting the differences between panels. The entire bars represent the differences of the Raman spectra at these selected regions

The appearance of two single broad peaks between (160 cm^{-1} and 170 cm^{-1})and 250 cm^{-1} and 270 cm^{-1} regions in all the CBZ spots' spectra confirmed that all the resulting spots exhibited polymorph I, as CBZ III exhibited multiple peaks in the same areas [123], see Figure 3.15.

In the high wavenumber region (400 cm^{-1} to 1800 cm^{-1}, three characteristic differences, is demonstrated between the boxes, can be seen in Figure 3.16. the

difference in the height of the two sharp peaks at 1025 cm^{-1} and 1040 cm^{-1} was the first differentiation between CBZ polymorphs [137]. The C-H bending (non-aromatic) mode exhibited a sharp single peak at 1309 cm^{-1} in CBZ III and 1305 cm^{-1} in CBZ I [137, 138]. Furthermore, the shifting of the three sharp peaks between 1550 cm^{-1} and 1625 cm^{-1}provides a clear differentiation between CBZ polymorphs [138]. These characteristics features provide evidence that all the printed quantities exhibit polymorph I.

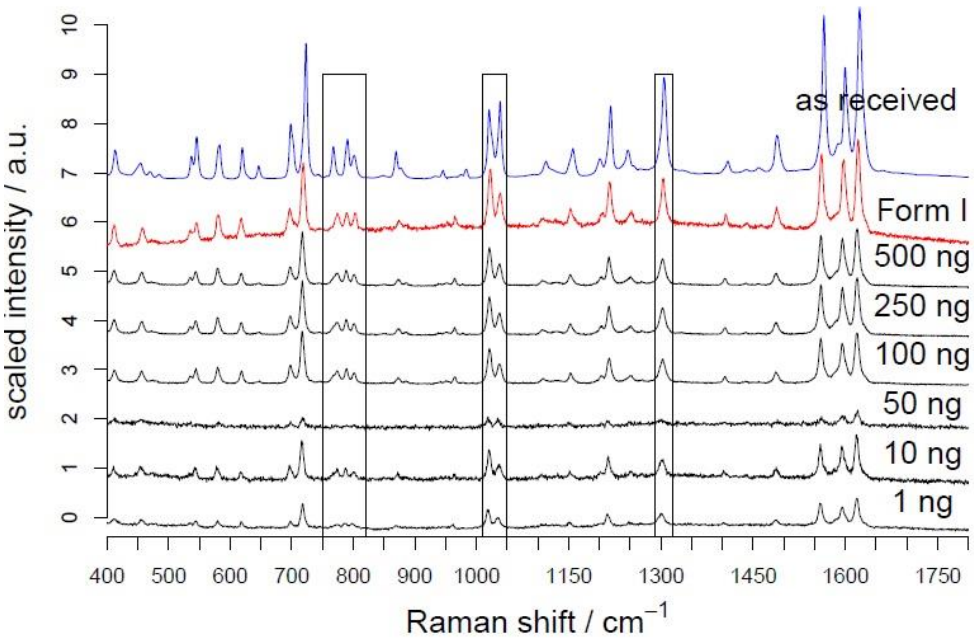

Figure 3.16. Raman spectra in molecular region for different printed quantities of CBZ in DMSO with reference spectra (blue and red).y-axis offsets were employed for presenting the differences between panels. The entire bars represent the differences of the Raman spectra at these selected regions

The optical observations and the Raman spectra, at the phonon and molecular region, of the printed quantities of FLUF on gold-coated slide were shown in ().

3.4. Conclusions

The current study has shown for the first time the viability of using printed nano-arrays with pico-litres of small-molecule pharmaceuticals in the context of pre-formulation, and solid form screening. Pharmaceutical polymorph investigations of PAR, MEF and, CBZ can be, in principle, conducted by manipulating the quantities of these drugs by using the 2D inkjet printing technique, and using subsequent spectroscopic and microscopic analyses. The novelty of using 2D inkjet printing technique in APIs polymorphic screening based on previous studies [79, 80]. The group of Kazarian adopted a heated "droplet on demand" system to print drug quantities in the range (0.1 µg to 1.0 µg) [79], while Bradley's group adopted 2D inkjet printing technique to perform APIs polymorph screening using 6.5 mg of the selected drug[80].

In this chapter, it can be found that the quantity factor can play an important role in appearance of different states and polymorphs. It was therefore concluded that manipulating in the APIs printed quantities on gold-coated slide can produce different forms when using distilled water (for PAR only) and DMSO as solvents. PAR/DW, for example, shows an amorphous state for the printed quantities less than 250 ng, while a crystalline form II was obtained after increasing the printed amounts over than 250 ng. PAR/DMSO spots on the gold-coated slide did not show any change in physical state for all the printed quantities, indicating there is only an amorphous state could be obtained after PAR/DMSO droplets evaporation. MEF exhibited form I at high quantities 500 ng, while MEF II exhibited at 250 ng. It can be noticed the alterations in the Raman spectra for the quantities less than 250 ng, they exhibited a mixture in the Raman features of forms I and II at quantities less than 250 ng, indicating that there is a mixture of two polymorphs can be obtained at these printed amounts. It can be achieved an API polymorph screening at six-order magnification less than the reported quantities in the abovementioned works in literature [79, 80] by depositing between 1 ng to 500 ng of an API by means of 2D inkjet printing technique.

It can also be concluded that time factor has an impact on the printed dots. It was found that the conversion from amorphous to crystal solid state in PAR/DW

requires more than 36 hours at 250 ng and 500 ng only, while two hours or more was enough to recrystallize all the printed dots of MEF and CBZ respectively.

This can be linked with Baird *et al*. [139] study, which included an assessment of the ability of vitrification of molecules during cooling, or, which called glass-forming ability, of CBZ, PAR, and 49 other small molecules. They classified these molecules into three main classes; class I molecules showed crystallisation under cooling, class II molecules exhibited crystallisation after reheating, and class III molecules which did not exhibit any crystallisation activity upon cooling, or heating.

CBZ was classified under class I, which undergoes crystallisation upon cooling. That observation contradicts the obtained results of the printed spots of CBZ which exhibited crystallisation at room temperature. PAR also was reported as class II molecule, which exhibit crystallisation after reheating, however, the printed droplets of PAR made from DW and DMSO exhibited crystalline and amorphous state, respectively at room temperature without any effects of thermal conditions.

The effect of moisture also needs to be taken into consideration. Therefore, all the printed slides were stored in the air to help increasing of the molecular mobility of the printed material on the substrate via plasticization [140].

Finally, the low frequency Raman spectra of the different quantities of printed dots of the selected drugs reveal that the bands below 400 cm^{-1} exhibit higher intensity then the conventional Raman spectra, and clearly differentiated between the amorphous *vs* crystalline states.

In order to improve the resulting Raman signal of the printed spots, it is necessary to improve the hydrophobicity of the substrate to obtain a thick spot that allows the Raman laser beam to make a deep contact with the spot contents before touching the substrate. Also, because the capacity of the substrate to control the selective growth of polymorphs has been reported in previous studies [141-143], attempts will be made in the next chapter to modify the gold-coated slide. This will take advantage of its ability to undergo further modifications with thiols and produce highly-ordered and organised self-assembled monolayers that can be used as new substrates to investigate the viability of the appearance of new polymorphs on these new substrates.

Chapter four: Self-assembled monolayers (SAMs) as new substrates for nanoscale screening of APIs

In this chapter, the solid form screening of APIs is extended. Despite the emergence of different forms and states of PAR, MEF, and CBZ through the printing of different amounts on gold-coated slides, the change in the chemistry of the substrate can produce a templet for monitoring the behaviour of the deposited materials and investigate the variation in the ionic or hydrogen bonding interactions between the printed drugs and the substrate itself which may or may not drive different polymorph recrystallization [144]. Therefore, it is suggested, in this chapter, to use self-assembled monolayers SAMs as templets (substrates) for investigating the behaviour of the deposited pico-litres droplets of some APIs. After using the plain gold-coated slide as a substrate to deposit the nano-quantities of PAR and MEF by means of the 2D inkjet printing technique (in Chapter three), the gold slide was chemically modified by treating with two types of thiols to create new self-assembled monolayers (SAMs), and using them as substrates for the inkjet printing of the APIs. This may allow the method to be transferred readily to allow screening of drug compound libraries in industry.

4.1. Introduction

Studies of thin layer systems started in the 18^{th} century, specifically in 1774 with Franklin's team study of the behaviour of an oil layer on water surfaces [145]. Further studies and investigations were performed at the end of the 19^{th} century on some prepared monolayers of immiscible liquid at air-water interfaces [146-149].

In the last century, many systematic studies were carried out in the field of thin organic films, a new monolayer model was presented by Langmuir [150]. This model created monolayers of amphiphilic molecules (with both strong and weak affinity for attaching the substrate) on a water surface. As a result, he was awarded the Nobel Prize in 1932. Three years later, a new system based on Langmuir's model was presented by Blodgett [151]. These monolayers, which were named Langmuir-Blodgett films, were created by depositing some fatty

acids onto solid substrates [151]. This new model was the first technique which allowed the fabrication of thin ordered organic films. In the 1940s, another common model for creating such a monolayer, called the self-assembly technique, appeared, becoming one of the most important methods in fabrication of organic monolayers [152]. A self-assembly monolayers (SAMs) are molecular aggregates with a high degree of orientation that are spontaneously formed by adsorption of an active surfactant from a solution or gas phase onto the substrate. SAMs are created by chemisorption of long-chain amphiphilic molecules in substrates producing an activated surface with highly ordered patterns [153, 154].

As detailed in the literature, many SAMs models have been created so far: organosilane compounds, such as R-$SiCl_3$, R-SiH_3 and R-$Si(OCH_3)_3$, condense with hydroxylated surfaces like Al_2O_3 and SiO_2 to produce a thin layer of polysiloxane [155-157]; alkanethiol compounds (R-SH) form an ordered thin organic monolayer on metals like, gold, silver and copper [158-160], dialkyl sulfides (RSR´) and disulfides (RS-SR´) can make SAMs on gold [130, 161] and alkanoic acids can also make SAMs on aluminium oxide and silver [162, 163].

In addition to be the standard substrate that was used in the previous chapter, gold was selected because it has many advantages will be mentioned in next section.

4.2. Self-assembled monolayer

SAMs usually consist of three main units (Figure 4.1). The first is the sulfur head group, which spontaneously attaches to the gold substrate, producing strong covalent or ionic bonds [164]. Next, the spacer, consists of the alkyl moiety (variable-length chain) that connects the head group to the functional group (see below [164]. The length of the alkyl chains can play an essential role in the configuration and stability of SAMs. Preparation of SAMs using molecules with long alkyl chains (more than 10 carbons) allows generation of more Van der Waals interactions between the alkyl chains, forming more stable SAMs than those with short chains [165].

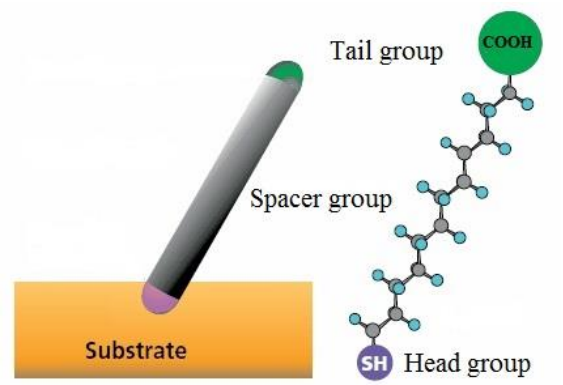

Figure 4.1. Main parts of a thiol molecule

Finally, the tail, or end group can play an important role in tailoring the physical properties of the solid surface of the new monolayer [164]. For example, carboxylic acid-terminated alkanethiolates [$COOH(CH_2)_nSH$] turn the SAM surface to hydrophilic due to the polarity of the tail group (carboxyl group). On the contrary, SAMs created from non-polar methyl-terminated alkanethiolates [$CH_3(CH_2)_nSH$] are hydrophobic [166]. Figure 4.2 illustrates the steps of SAMs preparation by immersing a gold-coated slide onto ethanoic solution of a thiol.

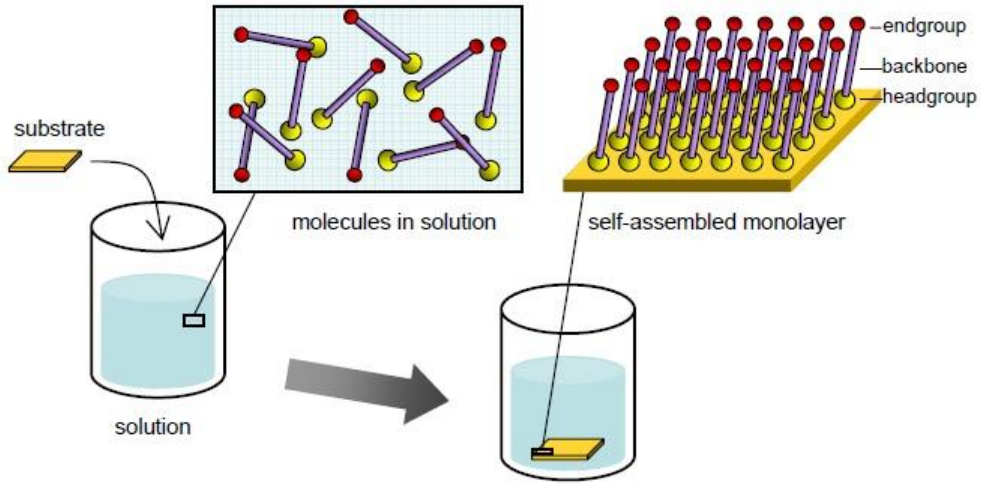

Figure 4.2: Schematic presentation for SAM preparation and the main units of the resulted SAM molecule [167]

Metals such as copper, silver and palladium can provide similar SAM systems. Technically, copper can be used as a solid substrate during SAM formation due to its ability to connect and seed layers of new SAMs. However, it is highly sensitive to atmospheric oxygen [159]. Silver has been more studied in fabrication of SAMs than copper. It can offer more highly ordered SAMs than gold; however, it cannot be used because of its rapid oxidation [159].

To date, gold has been the standard in studies of SAMs. It has a number of useful properties that lend it unique importance as a substrate for SAMs [130]. First, gold can be obtained easily not only as a colloid but also as thin films. Second, gold surface is chemically inert because it does not undergo any changes upon exposure to atmospheric oxygen and does not oxidise at temperatures below its melting point [130]. Third, gold has a high affinity to bind to *n*-alkanethiols, forming a very interesting and strong S–Au bond, producing highly ordered and well-characterised SAMs [154].

4.2.1. Mechanism and kinetics of SAMs

Adsorption of thiol molecules onto gold surface can be performed by two methods: gas-phase monolayer formation and liquid-phase monolayer formation.

4.2.1.1. Gas-phase monolayer formation

The kinetics of the assembly of thiolates on gold using the gas-phase adsorption method is clear and easy, since it can neglect the effect of the solvent interactions and also makes sure the investigation of the cleanness of the substrates, using an in-situ surface analysis technique, is precise.

A study of gas-phase deposition of C10-SAM on gold was performed by Schreiber and his co-workers [168]. They used X-ray photoelectron spectroscopy (XPS), low-energy helium atom diffraction (LEAD) and grazing incidence X-ray diffraction (GIXD) to prove the occurrence of the full-coverage phase. It was found that the phase can be carried out in two steps: the first step involves a rapid formation of an ordered layer of *n*-alkanethiol molecules called the striped phase, which is lying flat on the gold surface (Figure 4.3). This rapid step is believed to be an intermediate stage before nucleation and subsequent growth of the higher-coverage structures that make up SAMs. The second step, which is ~500 times slower than the first, involves an arrangement of the molecules nearly perpendicular to the gold surface [168].

Further evidence for the mechanism of C10-SAM on gold was presented by the STM study [169]. Poirier successfully investigated the two above-mentioned steps in addition to other intermediate phases [169].

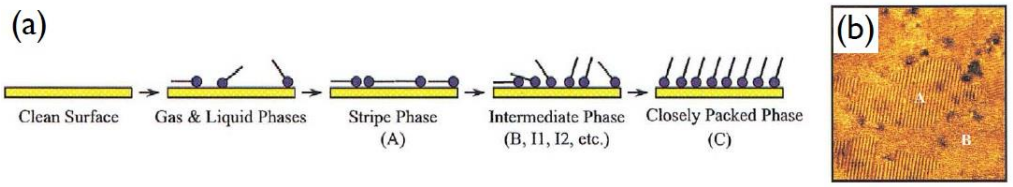

Figure 4.3. a) Steps of gas-phase deposition of an alkanethiol on a clean gold surface to form a high-organised SAM, b) a (107 nm x 107 nm) STM image of the striped phase [168]

4.1.1.2 Liquid-phase monolayer formation

The kinetic of the assembly of *n*-alkanethiols onto gold using solution phase has been monitored by different surface analysis techniques, such as surface plasmon resonance (SPR) [170], ellipsometry [166], second harmonic generation (SHG) measurements [171], mass spectrometry [172], sum frequency generation (SFG) [173] and helium atom diffraction [174].

Like the gas-phase monolayer system, the kinetic of the SAM formation in the liquid-phase monolayer system has been extensively studied. Most of these studies have proposed that formation of SAMs occures in two steps: the first step (fast regim), is rapid, where 80-90% of the monolayer is formed within seconds to a few minutes.The second step (slow regim) needs a long time (from minutes to hours) to build up the highly-organised SAMs [170, 174-176].

4.2.2. Factors affecting the structure of SAMs

Many different factors can influence the formation of SAMs: solvent, concentration of the solution, cleanliness of the substrate, temperature and immersion time.

4.2.2.1. Solvents

One of the most commonly used solvents for preparing SAMs is ethanol. It has many advantages that make it a preferable choice including high purity, low toxicity and ability to dissolve a wide range of alkanethiols [166].

The choice of solvent can affect the solvent-substrate and solvent-adsorbate interactions. However, the effect of the selection of a suitable solvent on the mechanism of SAM formation is complicated and still poorly understood [166]. This has been a motivation for some researchers to study the effect of using different types of solvents on the structure of SAMs.

Solvent–substrate interaction can impede the adsorption mechanism of alkanethiols from the solution because the solvent molecules have to be displaced from the surface before thiol adsorption [166]. The molecular structure and the polarity of the solvent have an essential role in SAMs formation, it has been found that using non-polar solvents like heptane and hexanes rather than ethanol can increase the rate of SAM formation [170, 177]. However, using long-chain hydrocarbons as solvents can produce less organised SAM than that formed in ethanol [177].

Furthermore, using long-chain hydrocarbons (more than 10 carbons) as solvents can decrease the SAMs formation rate because of the high interaction between the solvent and adsorbate, which can hinder the arrangements of alkanethiol molecules to create SAMs [177].

This is corroborated by the findings of water contact angle (WCA) and electrochemistry studies [166, 170, 177, 178]. It has been found that SAMs produced from solutions of thiols in non-polar solvents are less-ordered than those produced using ethanol.

4.2.2.2. Thiol concentration and time of immersion

Concentration of the solution and immersion time can play an important role in formation of SAMs. The concentration of the adsorbent (*n*-alkanethiol) is inversely related to the immersion time [166, 179], which in turn affects the density of the formed SAM.

Typically, in order to obtain a highly-ordered SAM, a concentrated solution of thiol with mM range is preferable [166].It has been found that immersion of a gold-coated slide in a thiol solution of 1mM for 12 to 18 hour is enough to achieve a maximum coverage of the gold surface with a density of ~ 4.5×10^{14} molecule·cm^{-1}. Using highly diluted concentrations (1 µM or less) requires long immersion time, days or maybe weeks, in order to obtain an organised monolayer [167, 180]. However, imperfect monolayers have been investigated [166]. Using very highly concentrated solutions may cause thiol disruption and, as a consequence, a greater amount of contaminants will be produced. These impurities in turn may have high affinity for gold with respect to the desired species [166].

4.2.2.3. Impurities

Another point that should be taken into consideration is that the existence of impurities and other sulfur-containing compounds in diluted solutions can make the process of SAMs formation difficult [166].

In practice, it has been suggested that 5% of disulfides, common impurities derived from *n*-alkanethiols, do not significantly affect the structure of the resulting SAM [166, 181].

4.2.2.4. Oxygen dissolved in solution

Oxygen dissolved in solution can play a negative role in the rate of formation and the structure of the resulting SAM because O_2 has the ability to produce ozone, a powerful oxidant, which readily oxidises or reacts with the surface species, which in turn affects the production of highly-ordered SAMs [157]. Furthermore, it is important to avoid oxidation of thiols to sulfonates and other oxygenated species. Therefore, it has been suggested that removing oxygen from the solution by means of an inert gas, like argon or nitrogen, is the best way to achieve a SAM with high quality [157].

4.2.2.5. Temperature

It is worth noting the importance of temperature in the formation of SAMs of organosulfur derivatives. Most SAMs are created and kept at room temperature. Increasing temperature, like increasing concentration, can help to enhance the first kinetic adsorption step and reduce, at the same time, the defects in the resulting SAMs in a shorter time [154].

4.2.2.6. Cleanness of the substrates

A further essential parameter which is required for a high-quality SAM is the cleanness of the gold surface, which has a significant effect on the formation and structuration of SAMs. It is not easy to control the cleanness of the gold substrate because it rapidly attracts contaminants and impurities once exposed to atmosphere. These impurities, which include hydrocarbon pollutants, can cause a certain delay at the beginning of the adsorption process, which in turn impacts on SAM growth [166].

Therefore, in order to obtain a clean gold substrate, it has been suggested to immerse the surface in strong oxidising agents such as "Piranha solution" (H_2SO_4:H_2O_2) or expose it to ozone plasmas beforehand [154].

4.3. Aims and Objectives

The main objective of this chapter is to understand the PAR and MEF recrystallization behaviour not only by printing different amounts but also studying the effect of the new created substrates. Neither of these two previous studies investigated the crystallisation behaviour of pure drugs, however. Kazarian [79] specifically printed a solid drug:polymer dispersion, while Bradley [80] printed the drug solutions directly onto the pre-printed polymer spots using the solvent from which the polymers had been printed, thereby introducing the strong possibility of re-dissolution of polymer into the drug-containing droplet prior to total evaporation. The hypothesis of using SAMs as substrates in this chapter because they tend not to re-dissolve because of their robustness, and if they do, the amounts will be extremely small as there is only a molecular mono-layer.

For the use of insoluble chemically tuneable surfaces for deposition we employ SAMs on gold-coated glass slides as substrates for printing pure drugs from dimethyl sulfoxide (DMSO) solvent. This also potentially allows the method to be transferred more readily to allow screening of drug compound libraries in industry, which are typically kept as DMSO stock solutions. We also investigate further miniaturisation of the sample quantities required, again with a view to pharmaceutical application. For analysis of solid form we employ low-wavenumber Raman microscopy, which is an emerging tool for rapid and reliable identification of solid forms, including amorphous *vs*. crystalline and distinguishing between polymorphs.

4.4. Experimental design

4.4.1. Materials

Paracetamol PAR and mefenamic acid MEF were used as received and there was no need for purification. Raman spectrum analysis confirmed that they were both form I. These two drugs were selected as models because they exhibit a wide range of well-characterised polymorphs [129]. DMSO (99.5%) was used as a solvent. Two types of functionalised *n*-alkane thiols with the same number of methylene groups and different terminating groups were used for the current study, one with a methyl-terminated group (1-undecanethiol) (b.p =103-104 °C) and the other with a hydroxyl group (11-mercapto-1-undecanol) (m.p= 33-

37 °C) (Here abbreviated to SAM-CH_3 and SAM-CH_2-OH respectively). Choosing long-chain alkane thiols can help to produce a highly-ordered SAM which has the ability to resist penetration of active oxidant species in the close SAM structure due to the strength of the Au-S bond [182]. Also, it is important to mention that CBZ and FLUF were used in this chapter and all the related data (microscopic and spectroscopic analysis) were presented in (Appendix B).

4.4.1.1. Preparation of samples and thiols solutions

Solutions of 6 mg·mL^{-1} of PAR and MEF were prepared separately by dissolving 30 mg of the APIs in 5 ml of DMSO. MEF form II was prepared by heating an amount of the pure MEF as received for 48 hours at 160°C [96] and then verifying the identity of the product by Raman spectroscopy. The prepared polymorph of MEF (II) was adopted as a bulky reference to compare with the spectra of the resulting dots of MEF, and it did not print on the used substrates anymore. Two types of thiol stock solutions were prepared separately by dissolving 0.045 ml and 40.8 mg of 1-undecanethiol and 11-mercapto-1-undecanol respectively in 100 ml of 99.00% ethanol (final concentration 2.0 mM) at room temperature and under deoxygenated environment.

4.4.1.2. Preparation of SAMs

Two types of SAMs were prepared by immersing the gold slides in the thiol solutions under inert environment for ~18 hrs. Then they were removed from the solution, washed with a small volume of ethanol to remove the unreacted molecules of thiol and dried with nitrogen [183].

4.4.2. Methods

4.4.2.1. Surface analysis

In this work, the KSV CAM200 was used to measure the water contact angle (WCA) to evaluate the wettability of the prepared solid substrates depending on the side observation of the drop. Then, the contact angle was able to be determined, i.e. by measuring the angle between the tangent of the drop surface at the contact line and the surface.

4.4.2.2. Atomic force microscopy

The roughness and the topography of the used substrates were studied at the nanoscale level using Bruker's Dimension FastScan AFM system. In this work, the tapping mode was used in imaging the topography of all the surfaces with

high resolution. AFM measurements were carried out at five to eight different areas throughout the selected substrates using an aluminium reflective coating tip MPP-12120(TAP150A) with 30×30 μm^2 scanning area and resolution of 256 x 256 points. The obtained topographical images of all the solid surfaces were processed using Nano Scope Analysis, version 1.7.

4.4.2.3. Printing drugs solutions on the prepared substrates

The printing of PAR and MEF was performed under ambient conditions (RH=50.5%, T=25˚C). Pharmaceutical solutions were deposited onto the prepared surfaces by using a 90µm orifice nozzle on a non- contact piezoelectric depositing system (Sciflexarryer S5, Scienion). The droplet size was controlled depending on the value of the firing voltage around (90V) and electrical pulse (around 50 µs). The obtained droplet volume was 225±3 pL. The printing process was performed by depositing different volumes of paracetamol solution onto the two prepared surfaces. The printed array was designed by producing four main fields one for each quantity, the gap between each field and the droplet spacing were 3500 µm and 1200 µm respectively. Each field was created by printing one quantity with nine replicates (3×3). The different quantities deposited were 10, 50, 100 and 250 droplets, equivalent to 13.5 ng, 67.5 ng, 135.0 ng and 270.0 ng respectively (Figure 4.4). The printed slides were directly moved to the light optical microscope to investigate the behaviour of the droplets during and after DMSO evaporation and pictures of the final dried spots were taken at regular intervals. Then they were kept in a desiccator at room temperature.

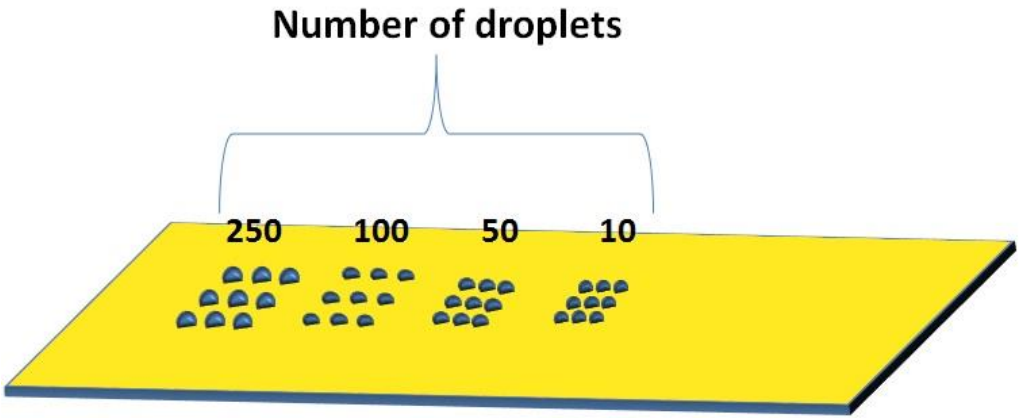

Figure 4.4. PAR and MEF microarray fabrication with four different quantities and nine replicates

4.4.2.4. Microscopic investigation of the printed droplets

The resulting dots were examined by means of an Advanced Polarizing Microscope (HS1; Prior LuxPOL^{TM}) with a 12 V and 30 W halogen lamp with variable brightness control using only one nominal magnification (10×) for sample focusing. The bright-field and cross-polarised images were recorded by means of a camera fixed to the top of the microscope and connected to a computer. The acquired data was processed via Q-capture^{TM} software to manipulate the brightness and the light exposure time in order to get an image with high quality.

4.4.2.5. Raman spectroscopy

A confocal Horiba-Jobin-Yvon LabRAM system (Horiba-Jobin-Yvon Ltd, Middlesex, UK) was used to perform Raman spectrophotometric measurements on single printed spots. The NIR (HeNe, 785 nm) laser was used with 600 lines/mm of grating, 300 µm of confocal hole and spectral range between 40 and 1800 cm^{-1}. As mentioned in chapter two, it was also connected to an Olympus BX41 microscope provided with four objective lenses (10×, 40×, 50× and 100×). Three objective lenses were used, 10× for selecting the spots, 50x for calibration and 100× for focusing the small printed spots of the drug. The obtained Raman data was processed by means of the LabSpec 5 software.

4.5. Results

4.5.1. Characterization of the new SAM substrates

Preliminary tests were carried out to investigate the characteristics of the prepared substrates before printing the drug solution. As described above, two different solid substrates were used in this study, chemical modified gold substrates with 1-undecanethiol (SAM-CH_3) and 11-mercapto-1-undecanol (SAM-CH_2OH) in addition to a plain gold-coated slide. These substrates were subjected to preliminary examinations, such as, investigation of the topographic nature by means of atomic force microscope (AFM) and of the wettability by water contact angle measurements (WCA). Figure 4.5 shows (30×30) μm^2 AFM topographical images of all the selected and prepared substrates as described in chapter two. The AFM image was taken for the plain gold-coated slide to compare with those of the resulted SAMs. It can be observed that AFM images of plain gold and SAM-CH3slides exhibit quite smooth topography with no

aggregates, while a few aggregates can be seen in SAM-CH2OH slide. These observations were close in description to those whom presented by Faucheux *et al*. [184].

The root mean square RMS roughness values of these surfaces were calculated automatically.

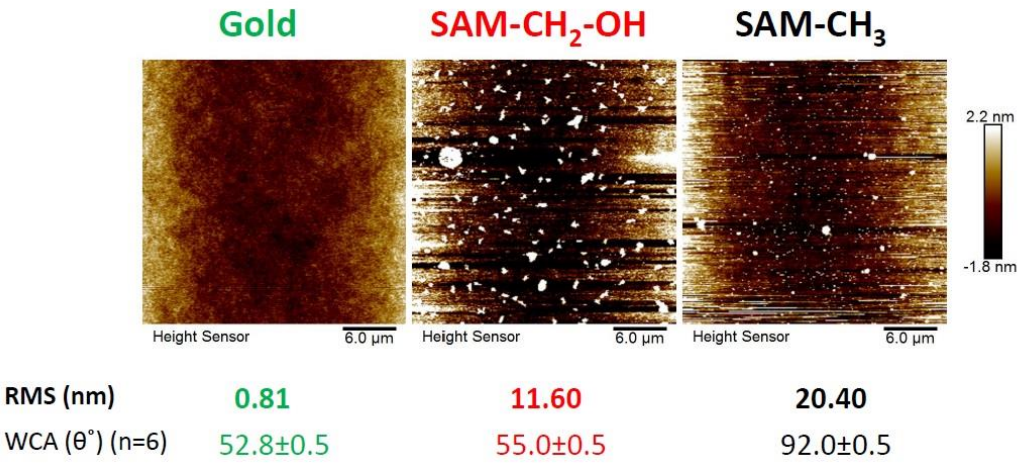

Figure 4.5. AFM topographic images, WCA and RMS values for the prepared SAMs slides compared with the plain gold coated slide

In this study, roughness are being controlled with constant texture. Statistically, roughness of a surface can be expressed by root mean square (RMS), which is a good way to provide an understanding about surfaces' roughness when they have the same surface texture. In this study, three different surfaces were used, namely gold-coated, (SAM-CH_3) and (SAM-CH_2OH) slides. It was important to know the degree of roughness of these substrates before using them as printing substrates.

As can be seen, the plain gold surface appears to be smooth, with an RMS value of 0.81nm. The apparent WCA for the plain gold-coated slide was 52.8˚±0.5˚. Although the RMS roughness of SAM-CH_2OH is around ten times greater than that of the plain gold substrate, it has approximately similar WCA value (55.0˚±0.5˚). This in turn indicates the similarity in the wettability of both surfaces. Also, it is apparent from the AFM image of SAM-CH_2OH there is a lot of agglomerations, due to formation of intermediate products (dithiols) as a result of thiol exposing to atmospheric oxygen, which give indications that the covering of the gold-coated slide with the thiol was not totally completed. On

the contrary, the modified gold substrate with 1-undecanethiol exhibits a different behaviour towards water retardation. It produced a hydrophobic substrate with high values of WCA and RMS roughness, 92.0˚±0.5˚ and 20.40 nm respectively (Figure 4.5).

A stability test for the prepared SAMs was performed to check their resistance against the solvents and make sure that they were not affected after extended exposure to solvents. 1-undecanethiol (SAM-CH_3) and 11-mercapto-1-undecanol (SAM-CH_2OH) slides were immersed in two different solvents, distilled water (DW) and DMSO, for one hour, and the contact angle was checked as a function of time. Figure 4.6 compares the values of the WCA of SAM-CH_3 and SAM-CH_2OH after immersion in two different solvents, DW and DMSO, over a one-hour period because it is the maximum time required for evaporation of DMSO in the bigger printed droplets. As can be seen, the WCA values of SAM-CH_3 remained fairly stable between 89º and 92º. These values are convergent to those of SAM-CH_3 before immersion.

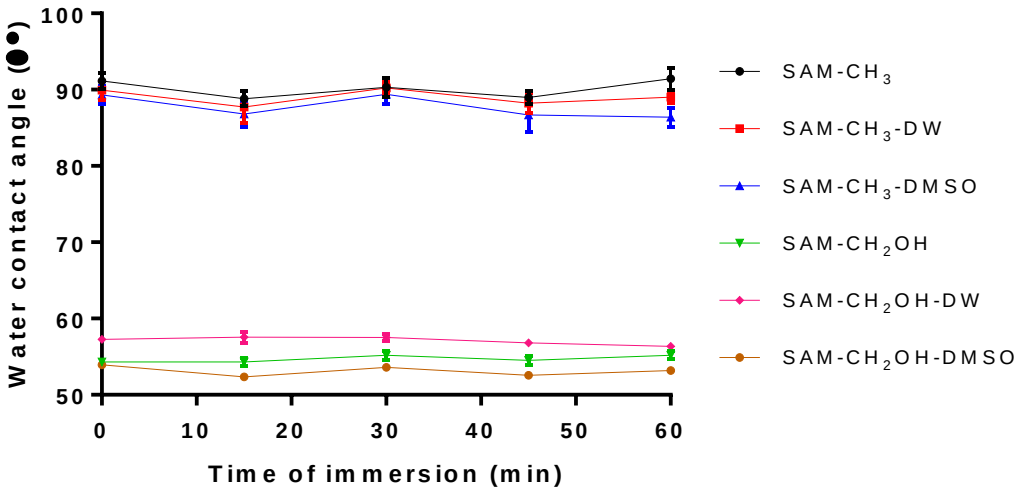

Figure 4.6. Stability of the prepared SAMs against DMSO and DW

The SAM-CH_2OH slides show the same behaviour in relation to the solvents. Keeping the slides inside two separated solvents for different times does not show a significant change in WCA values, which fluctuate around 55º. That indicates the robustness of the prepared SAMs against the solvents. That will

support the idea of using SAM as a solid and stable substrate for nano-polymorphic screening of APIs.

4.5.2. The behaviour of the printed droplets on the used substrates

The behaviour of the printed droplets on the used substrates was investigated. Figure 4.7 shows the evaporation time of different printed volumes of PAR/DW on gold-coated, SAM-CH_2-OH, and SAM-CH_3 slides. The red points represent the volume of each printed quantity. Figure 4.8 illustrates the relationship between the volumes of printed droplets of PAR in DW with time to full evaporation (dryness) on the used slides. It can be seen that PAR droplets on the gold and SAM-CH_2-OH slides evaporate faster than those deposited on the SAM-CH_3 slide. The PAR droplet volume of 55 nL shows different evaporation time depending on the substrate that is printed on, it takes around two and three minutes to remove all the DW on the SAM-CH_2OH and gold-coated slides respectively, while the hydrophobic substrate of the SAM-CH_3 slide delays the water evaporation of the same volume to 10 minutes.

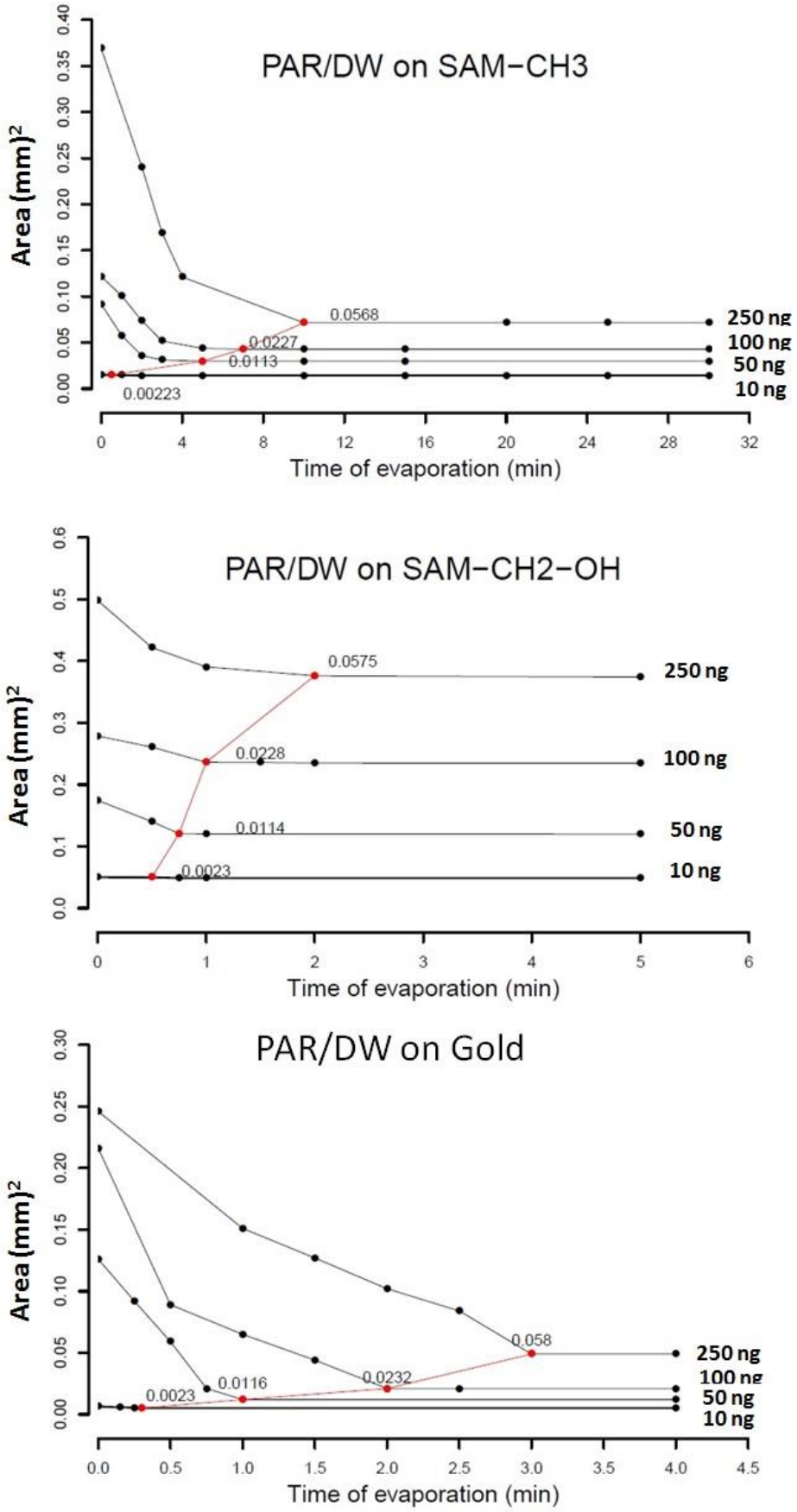

Figure 4.7. The evaporation time of different printed quantities of PAR/DW on different substrates

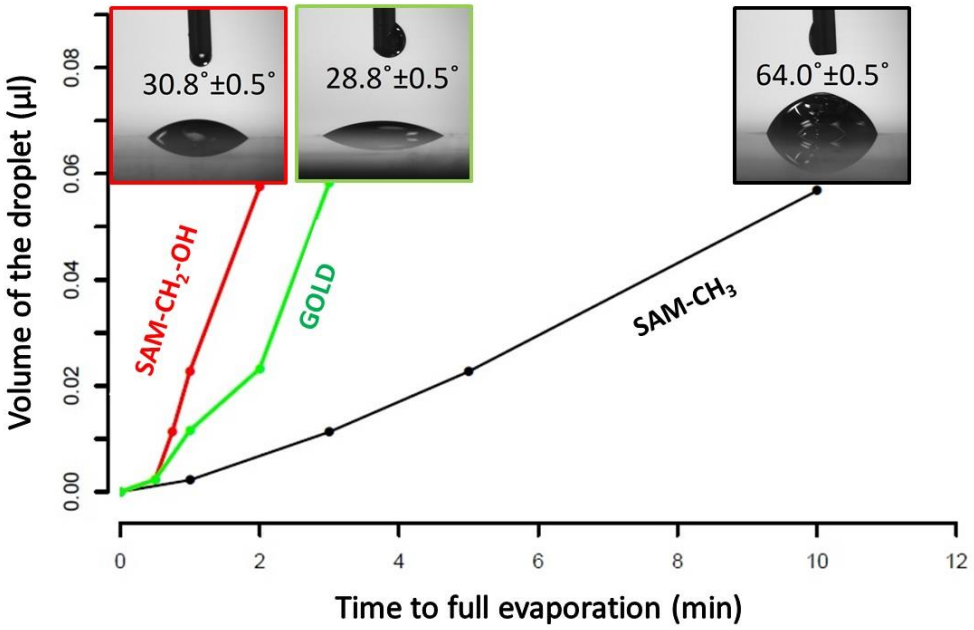

Figure 4.8: The time of full evaporation of different printed volumes of PAR/DW droplets on different substrates

As expected, a substrate with low contact angle, of both the gold and SAM-CH_2OH slides, has high wettability because of high spreading rate and the droplet surface becomes thin. As the liquid layer becomes thinner, heat transfer from the solid to liquid-vapour interface is enhanced. Spreading of the droplet also increases the heat transfer area. Both these effects contribute to a faster evaporation rate [185]. Furthermore, it should be noticed that all the data related to the evaporation time, the behaviour, the microscopic investigation, and the Raman spectra of the CBZ, MEF, and FLUF printed droplets on SAM-CH_3 and SAM-CH_2OH slides were presented in (Appendix B).

4.5.3. Effect of printing different quantities of paracetamol on the crystallinity behaviour

Optical microscopic identification can provide visual confirmation of events occurring during the transformation from one state or form to another. The DMSO solution of PAR was deposited on the prepared slides with four different quantities: 13.5 ng, 67.5 ng, 135.0 ng and 270.0 ng, which they are represented in Figure 4.9, to investigate the effect of printed quantities of APIs on appearing new polymorphs. The printed slides were transferred onto the optical

microscope for investigating the crystallisation behaviour of the drug droplets with time by means of 10× magnification for all the amounts.

The optical micrographs of all the quantities of printed dots of paracetamol on the SAM-CH3 slides are shown in Figure 4.9. These dots were investigated within successive time intervals by means of light optical microscopy analysis to study the effect of time on their physical state. The microscopic analysis revealed that all the printed droplets underwent decreases in size and solidified in the shape of the droplets with relatively smooth surface. It can be noticed that all the paracetamol dots appeared to be smoothly transparent indicating an amorphous state. Also, there was no change in the amorphous state throughout the days after and the slide was kept at room temperature.

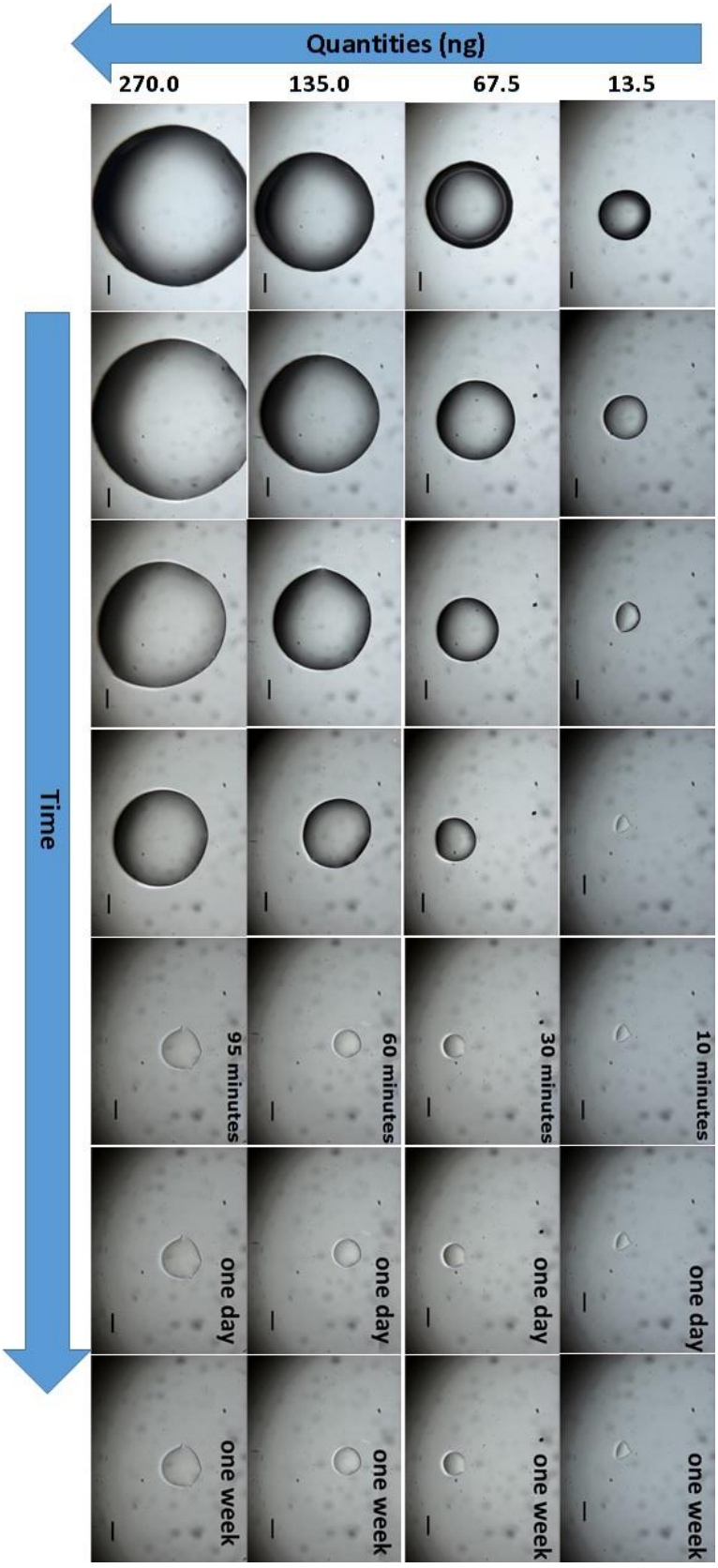

Figure 4.9: The optical micrographs of all the quantities of the printed dots of paracetamol on SAM-CH_3 slide , scale bar: 0.1 mm

In order to confirm the physical state of PAR spots on SAM-CH_3 slide, Raman spectroscopy was employed to investigate the identity of the resulting spots.

The Raman spectra of the standard powder (as received), which was previously identified as polymorph I [112] and the printed quantities of paracetamol from 10 cm^{-1} to 1800 cm^{-1} are shown in Figure 4.10. The spectra are a composite of two main zones, the intra-molecular region (400 cm^{-1} to 1800 cm^{-1}) and the low frequencies region (10 cm^{-1} to 400 cm^{-1}) which corresponds to the lattice mode vibrations.

In Figure 4.10, the Raman spectra of PAR (as received) are characterised by sharp bands and a good signal-to-noise ratio. In the phonon region, the spectra of all the printed paracetamol spots on the SAM-CH_3 slide exhibit broad and continuous peaks in the phonon region due to the irregular arrangement of molecules in amorphous state. These results were compared with reference spectra in the literature to identify the amorphous state [186]. In the molecular region between 400 and 1800 cm^{-1}, three characteristic peaks, demonstrated inside the box, can be seen between 1550 and 1650 cm^{-1} in the crystal form I of PAR (as received) spectrum, while the unorganised nature of the amorphous paracetamol can be noticed in broader peaks around 1600 cm^{-1} at all the printed spots of PAR SAM-CH3 slide, see Figure 4.10 [112].

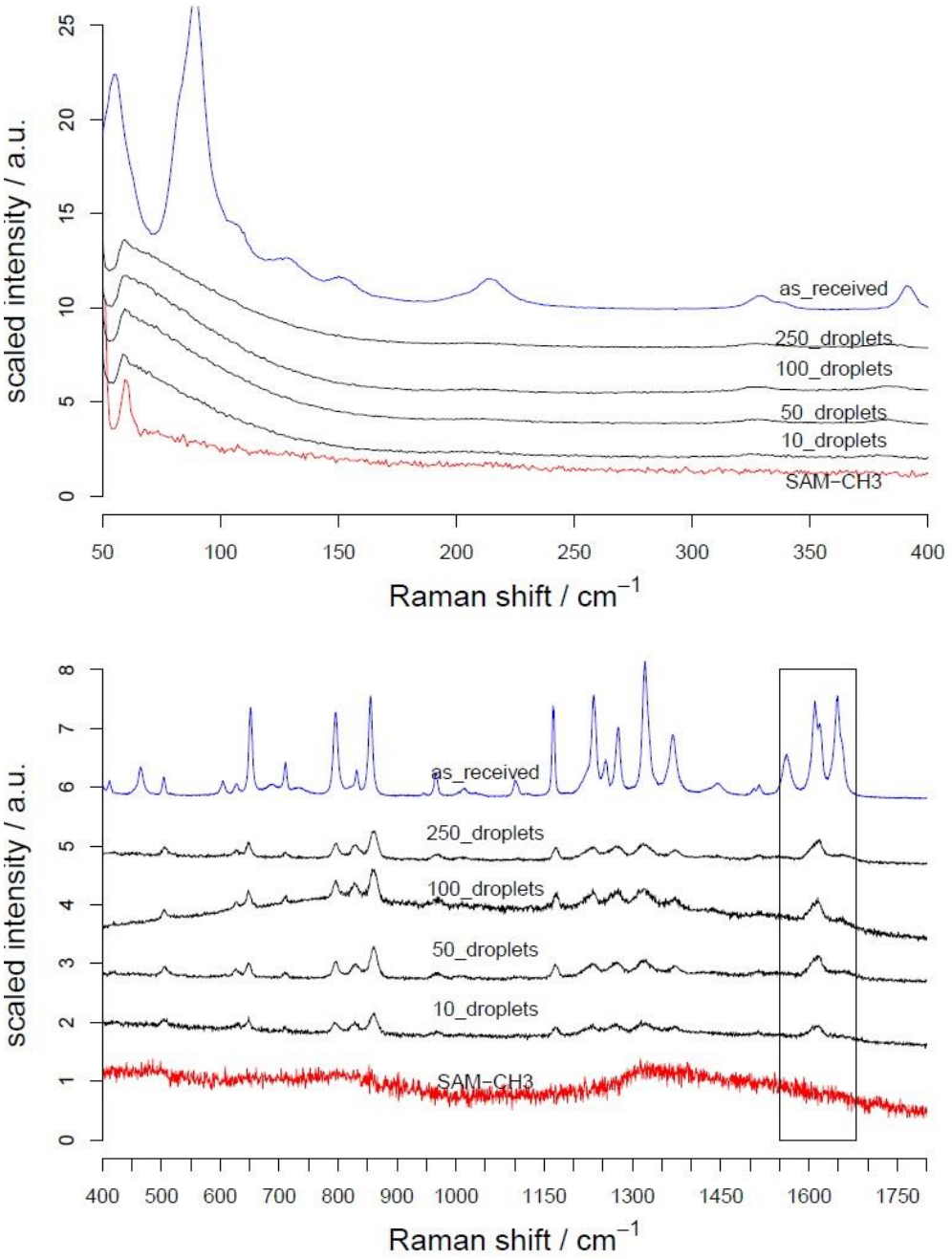

Figure 4.10: Raman spectra for phonon region (top) and molecular region (bottom) of different printed quantities of paracetamol printed on SAM-CH_3 ,with reference spectra of PAR (as received) (blue) and the prepared substrate (red).y-axis offsets were employed for presenting the differences between panels. The entire bar in the molecular region (bottom) represent the differences of the Raman spectra at these selected regions

The behaviour of paracetamol droplets on the SAM-CH_2OH slide was not the same as on SAM-CH_3.

Figure 4.11 shows the light optical micrograph and cross-polarised images of all the paracetamol droplets and dots on the SAM-CH_2OH slide. As can be seen, all the printed quantities underwent decreases in size and solidified with abnormal shape due to the heterogeneity of the prepared substrate (SAM-CH_2OH), resulting from the partial formation of dithiol as an intermediate product because of exposing to oxygen, which makes the spreading of the printed droplets with different thickness. Consequently, there will be differences in evaporation time within the same droplet depending on the area thickness, producing irregular droplet shape.

The evaporation time of the 13.5 ng droplet of PAR was eight minutes, to obtain a glassy spot indicating amorphous state, while the high quantity of 270 ng droplet required one hour to become free of DMSO and transfer to a glassy dot. However, it was not the final physical state for any of these amorphous spots. The next day, all of them had changed in appearance to a crystal form. For further visual detection, a polarised light microscope was used to monitor the change in physical state of the PAR spots from a glassy appearance that refers to amorphicity to a reflective appearance, which indicates the crystallinity of the spots, see Figure 4.11.

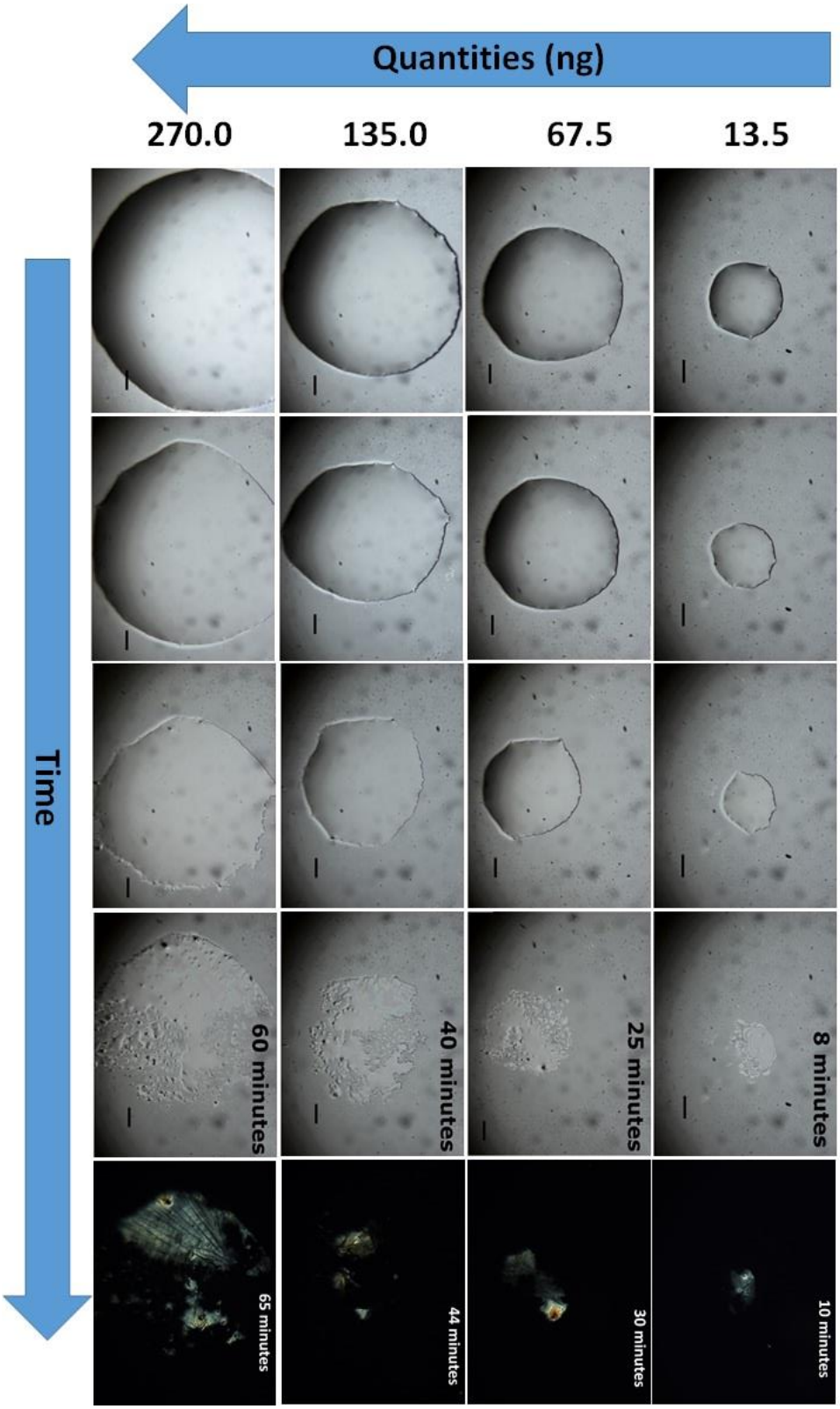

Figure 4.11: The optical micrographs of all the quantities of the printed dots of PAR/DMSO on SAM-CH_2OH slide , scale bar: 0.1 mm

Raman analysis was used to support the light optical microscopy observations. In the low-frequencies region, which corresponds to the lattice vibrations, a distinct peak at ~122 cm^{-1} can be noticed in the spectra of all the printed spots of PAR, while it does not exist in the reference spectrum, which refers to polymorph I (Figure 4.12). That intense peak was reported by Kachrimanis *et al*. [187], when they developed a rapid method for quantification of PAR polymorphs I and II using FT-Raman spectroscopy. They found that the orthorhombic form of PAR, which in turn refers to polymorph II exhibits that intense peak at ~122 cm^{-1}.

In the high-wavenumber region, three characteristics differences can be recognised to differentiate between the spectra of the PAR reference and all the printed spots of PAR on SAM-CH_2OH slide. The first difference can be noticed in the spectral region between 1200 cm^{-1} and 1260 cm^{-1}. Szelagiewicz *et al*. [122] described the variation in the spectra of PAR polymorphs via quantitative study by means of hot-stage Raman microscope. They found that spectrum of polymorph I exhibits two distinct peaks at the range of spectra from 1233 $cm^{-1}$to 1238) and from 1254 cm^{-1} to 1258 cm^{-1}, while these peaks underwent shifting to left at 1242 cm^{-1} and from 1218 cm^{-1} to 1219 cm^{-1} in the spectrum of polymorph II, which is quite similar to those peaks that existed in the spectra of the printed spots of PAR on SAM-CH_2OH slide.

Another difference in spectra can be noticed at the beginning of the molecular region between 450 cm^{-1} and 470 cm^{-1}, where the reference (as received) spectrum of PAR, which is refers to polymorph I, exhibited a distinct peak in the spectral range from 460 cm^{-1} to 466 cm^{-1}, while a slight shift took place to that peak in the spectra of all the printed spots at 451 cm^{-1} -452 cm^{-1}. These variations in peaks were characterised by Szelagiewicz *et al*. [122]. They found that distinct peak at the spectral region from 451 cm^{-1} to 452 cm^{-1} belongs to polymorph II. As a result, the variation in that spectral range was used later for identification and spectroscopic determination of PAR polymorphs in mixtures [188]. Finally, there is a noticeable difference in the spectral range from1600 cm^{-1} to 1625 cm^{-1}, where one sharp peak appears in the spectrum of the reference PAR (polymorph I), while two distinct peaks can be noticed at the same spectral range in the spectra of all the printed spots. That is due to the effect of the vibrations of the amide carbonyl group and the aromatic hydrogen as reported

in literature [187]. Polymorph II in the normal state is difficult to make as it is prepared by slow cooling of about 2 g to 3 g of melted polymorph I in silica tube under evacuated atmosphere (10^{-3} Pa). Therefore, printing of PAR on SAM-CH_2OH slide can lead to appear polymorph II.

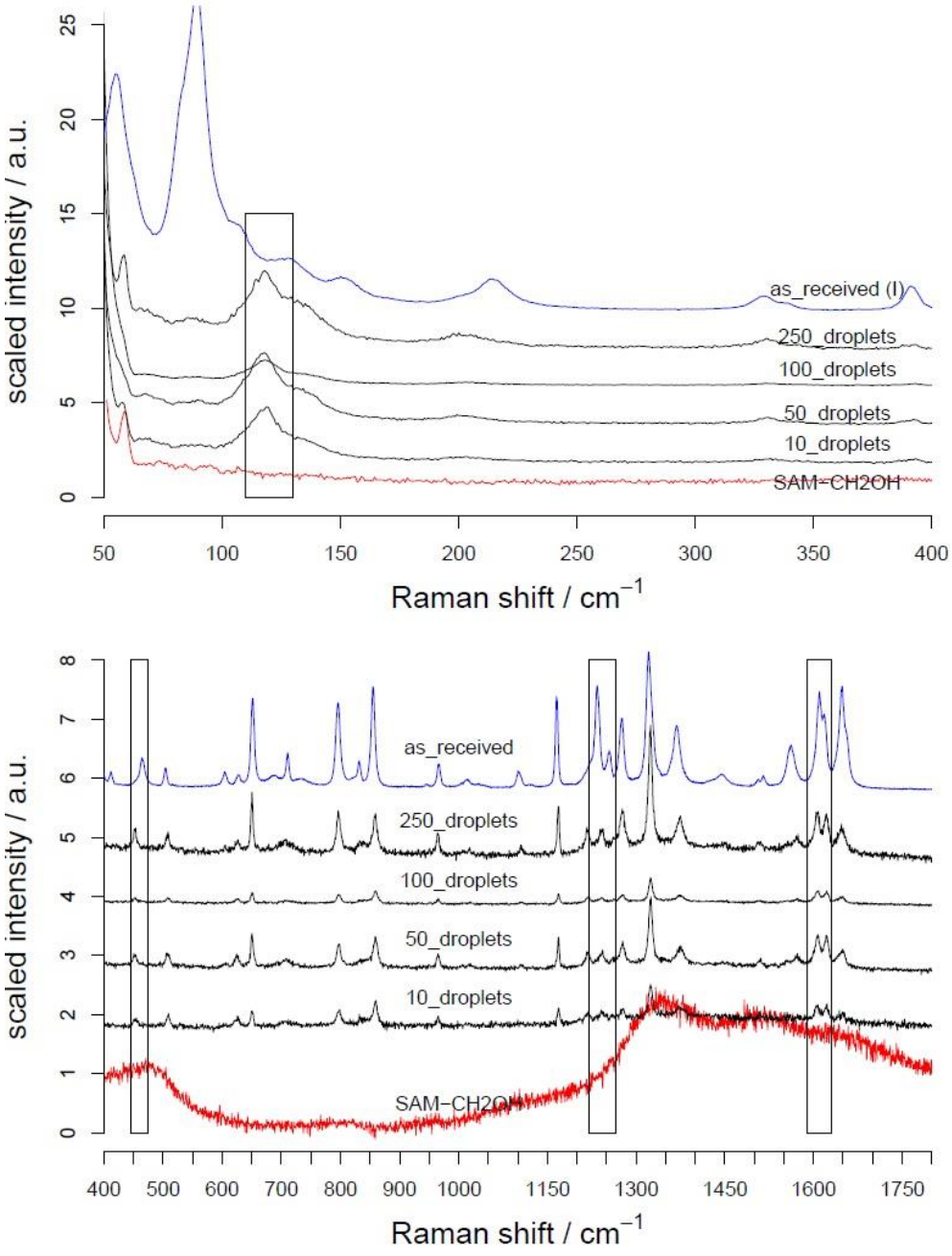

Figure 4.12: Raman spectra for phonon region (top) and molecular region (bottom) of different printed quantities of PAR/DMSO printed on SAM-CH_2OH , with reference spectra of PAR (as received) (blue), and the prepared substrate (red). The entire bar in the molecular region (bottom) represent the differences of the Raman spectra at these selected regions

4.5.4. Investigation of MEF crystallisation on different substrates

The possibility of obtaining a new solid form from another by modifying the chemical nature of the substrates was also investigated. MEF was selected as a model for this study because it has more than one well-characterised crystal form [96]. Printing of MEF on gold was described earlier in chapter three but it was done again to compare the same printed quantity with, SAM-CH_3 and SAM-CH_2OH slides. The process was performed under the same laboratory conditions as those used for creating the paracetamol microarray; only, for the quantity of MEF 100 droplets which equivalent to 135 ng was chosen to facilitate the monitoring of evaporation process of DMSO.

4.5.4.1. Optical observations of MEF on gold-coated slide

The change in visual appearance of the MEF droplet on gold slide is presented in Figure 4.13. The 135 ng droplet was deposited within few seconds, and the printed droplet was transferred to the light optical microscope to start monitoring the spot's behaviour during and after DMSO evaporation. The 135 ng droplet of the MEF was investigated and the micrograph images were taken at regular intervals. The low value of MEF contact angle on gold slide (24.31˚±0.50˚) see Table 4.1, shows the high wettability of the used surface, that makes the MEF droplets spreading over large area and then increase the possibility to remove the DMSO quickly within 30 minutes.

It can be observed that MEF droplets on gold-coated slide underwent DMSO evaporation and then rapid transformation to crystal state. The polarised light microscope confirmed forming bright crystals of MEF on gold slide after evaporation process, see Figure 4.13.

Table 4.1. Contact angles of a solution of MEF in DMSO on different substrates

Substrate	Gold	SAM-CH_2OH	SAM-CH_3
Contact angle (θ˚) (n=9)	24.31˚±1.50˚	26.10˚±1.50˚	60.01˚±1.50˚

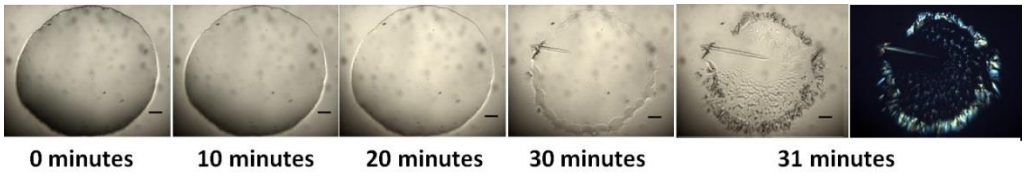

Figure 4.13: MEF on gold slide , scale bar: 0.1 mm

4.5.4.2. Optical observations of MEF on SAM-CH_2OH slide

The crystal habit of MEF droplets on SAM-CH_2OH slide is presented in Figure 4.14. The printing of 135 ng of MEF took few seconds, and the monitoring of the droplets was directly performed after printing process by means of light optical microscope. Figure 4.14 reveals the decreasing in droplet size with time due to the evaporation of DMSO. The crystal state of MEF spot appears after 25 minutes when all the DMSO was removed, and the polarised light microscope confirmed the reflective appearance of MEF spot.

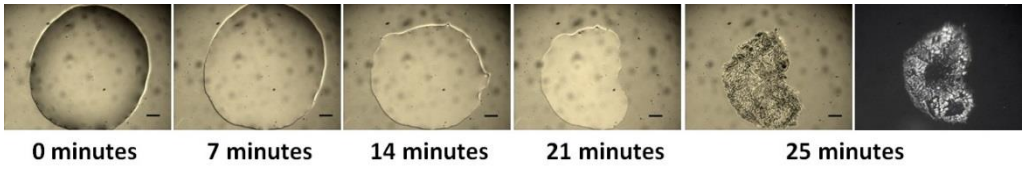

Figure 4.14: MEF on SAM-CH_2OH , scale bar: 0.1 mm

4.5.4.3. Optical observations of MEF on SAM-CH_3 slide

The behaviour of 135 ng droplet of MEF on SAM-CH_3 was slightly different, see Figure 4.15. The MEF droplet started decreasing in size due to DMSO evaporation. The high contact angle of MEF droplets on the SAM-CH_3 slide (60.01˚±0.50), see Table 4.1, gives an indication of the low wettability of the used substrate, which in turn increases the droplet evaporation time from few seconds to around 38 minutes, see Figure 4.15. Since then, the dry spot has been directly changed to crystal state, and the polarised light microscope confirmed the birefringent appearance of the dried spot.

Effect of contact angles on droplet evaporation rate was studied [185]. Low WCA means spreading the droplet over a large area on the surface forming a thin liquid layer which in turn enhance the heat transfer from the solid surface to liquid-vapour interface and increase the evaporation rate.

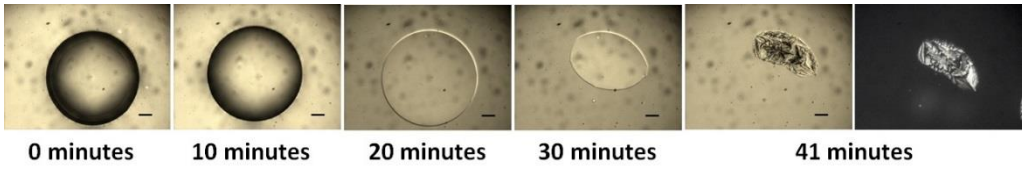

Figure 4.15: MEF on SAM-CH_3, scale bar: 0.1 mm

Using both optical and polarised light microscopic modes in monitoring the MEF spots provides the ability to investigate the crystallised parts in the spots. Because of the birefringent characteristic of the crystal materials such as MEF spots, they exhibit an interference effect when putting them under polarised light microscopic mode, this destructive interference with the white light can cause a spectrum of colours [5, 134].

The optical microscopic investigation did not give any idea about the identity of the resulting crystal dots, therefore, Raman spectroscopy was a good supportive technique to investigate the identity of the produced polymorph on the used substrates.

4.5.4.4. Raman analysis of MEF spots on the gold-coated, SAM-CH_2OH, and SAM-CH_3 slides

Figure 4.16 illustrates Raman spectra of the resulting spots of MEF on the gold, SAM-CH_3 and SAM-CH_2OH slides. The Raman data results were compared with those of MEF (as received) and the prepared polymorph II in addition to the spectra found in the literature [135]. Phonon region from 50 cm^{-1} to 400 cm^{-1} can be considered the finger print of any polymorph. It can show the effect of intermolecular vibrations that take place in this zone. Although MEF has more than two crystalline polymorphs, the distinct peaks of all these forms in the phonon region can be recognise easily [123].

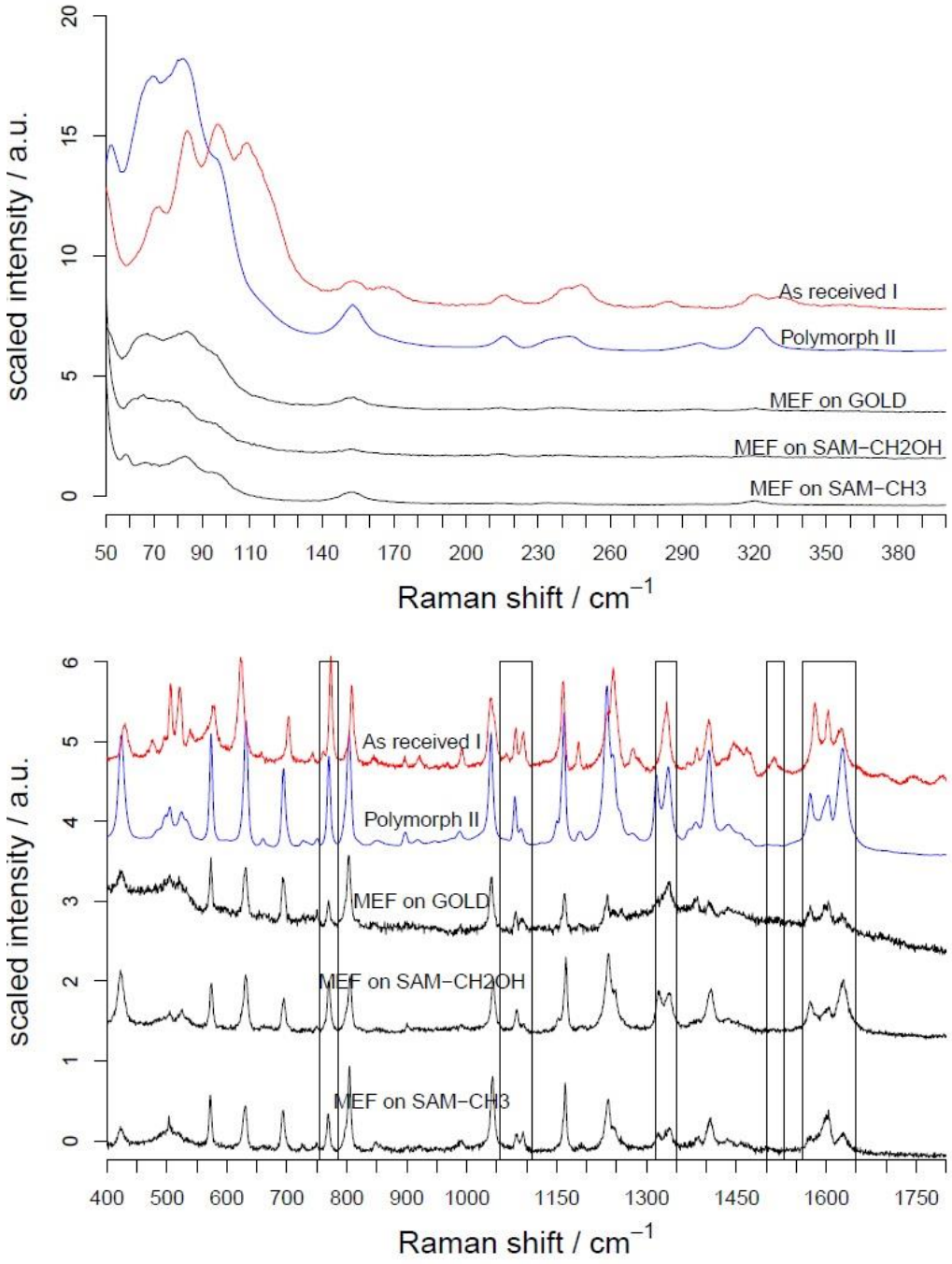

Figure 4.16: Raman spectra at phonon region (top) and molecular region (bottom) for 100 droplets of MEF on SAM-CH_3, SAM-CH_2OH, and gold-coated slide ,with reference spectra of MEF (as received) (red) and MEF (polymorph II) (blue).y-axis offsets were employed for presenting the differences between panels. The entire bars represent the differences of the Raman spectra of the printed MEF at these selected regions

In phonon region (Figure 4.16), it is difficult to recognise the peaks at ~ 33 cm^{-1} which indicates polymorph I because of the overlapping with the peaks of gold slide. Nevertheless, a distinct peak at ~ 48 cm^{-1} can be noticed in the spectrum of MEF on the gold slide to confirm the identity of polymorph I.

The Raman spectra acquired from the MEF spots on the SAM-CH_3 and SAM-CH_2OH slides contain characteristics peaks associated with polymorph II at ~ 52 cm^{-1} and with several broad scattering peaks in the 68-84 cm^{-1} region compared to the MEF I as reported in literature [135].

In the high wavenumber zone (400 cm^{-1} to 1800 cm^{-1}), three remarkable differences can be noticed to distinguish the MEF polymorphs. Due to the dimeric structure of MEF II [135], two distinct peaks in the (1330 cm^{-1} and 1340 cm^{-1}) region are shown in the spectra of MEF spots on the SAM-CH_3 and SAM-CH_2OH slides. These peaks are assigned to the (O-H bending) while only one sharp peak, relating to form I at ~ 1345 cm^{-1} , can be noticed in the spectrum of MEF on the gold slide.

A small single peak can also be seen at around 1515 cm^{-1} in the spectrum of the pure MEF previously confirmed to be form I. This peak can be clearly noticed in the spectrum of the MEF on gold-coated slide, while it does not exist in the spectra of MEF spots on the SAM-CH_3 and SAM-CH_2OH slides, which indicates that MEF spots on both on the SAM-CH_3 and SAM-CH_2OH slides exhibit polymorph II.

A sharp peak , which attributed to the deformation of the ring [189], can be noticed in the reference spectrum (as received) which refers to polymorph I and the spectrum of MEF spots on gold-coated slide at 773 cm^{-1}, and at 767 cm^{-1} in the spectrum of MEF II and the spectra of MEF spots on both the SAM-CH_3 and SAM-CH_2OH slides.

Finally, three intense peaks between 1550 cm^{-1} and 1700 cm^{-1} region can be easily noticed, assigned to N-H bending and the stretching of the aromatic ring. The differences in the height of these peaks can be recognised to differentiate the polymorphs I and II of MEF [135].

Another point that should be taken into consideration is that the spectrum of MEF on the gold slide exhibits some noise and the peaks are not very intensive due to a bad signal-to-noise ratio. However, intensive and clear peaks can be noticed in the spectra of the drug on SAM-CH_3 and SAM-CH_2OH. This is attributed to the better signal-to-noise ratio.

4.6. Conclusions

The aim of this chapter was employing stable and solid substrates in APIs polymorph screening. The novelty of using newly prepared substrates arises from Bradley's group study [80]. They used soluble substrates (polymers) for polymorph screening of APIs, introducing the strong possibility of re-dissolving the polymer into the drug-containing droplet prior to total evaporation.

Throughout this chapter, the newly prepared SAMs were successfully used as substrates for nanoscale polymorph screening of APIs. The new substrates were found to be stable and robust against prolonged exposure to solvents, indicating that the printed drug solution does not affect the texture of these surfaces. In this study, the 2D inkjet printing technique was successfully used to deposit the APIs on the gold-coated, SAM-CH_2OH, and SAM-CH_3 slides.

Light optical microscopy and Raman spectroscopy were complementary techniques that used to evaluate the physical state of the printed quantities of APIs on the used substrates. They were able to provide clear ideas about the crystal habits of the printed quantities of APIs although these drugs were deposited in a nano-quantities about 13 ng, about six-order magnification less that was reported in literature [79, 80]. This may help to enhance the screening of the drug compound libraries in pharmaceutical industry because it can save time, resources, and human efforts.

The new SAMs can control the evaporation time of the printed droplets. The roughness of SAM-CH_3 slide, for example, can retard the spread rate of the droplets and decrease the wettability. This, in turn, thickens the droplet surface and increases evaporation time.

Only an amorphous state could be observed after printing different quantities of paracetamol in DMSO on the SAM-CH_3 slide. The physical state (amorphous) of PAR spots on SAM-CH_3 has not changed so far, while one crystal modification was investigated in a 24 hours after deposition of paracetamol solution on the SAM-CH_2OH slide. This crystal state was identified by polarised light microscope, and the crystal modification was confirmed to be polymorph II by Raman spectroscopy, and in accordance with reference spectra and previous studies.

Changing the chemical nature of the substrate can also help to obtain a different crystalline form of MEF. Optical microscopy was not enough to characterise the identity of the produced polymorph, because MEF has two or more crystal modifications. Therefore, comparing the resulted Raman spectra of the printed MEF spots with the reference spectra of MEF and what was found in literature can help to identify the polymorph that formed on the used substrates.

Polymorph II can be observed after modifying the gold-coated slide with two types of thiols, 1-undecanethiol (SAM-CH_3) and 11-mercapto-1-undecanol (SAM-CH_2-OH), while the MEF spots on the gold slide exhibit polymorph I. this difference may be attributed to the effect of the functional group on the substrate which may change alteration in torsion angles of the MEF molecules producing a new conformation.

Furthermore, improving the hydrophobicity of the substrate can help to obtain an intense spectrum with high signal-to-noise ratio, which makes the differentiation between the polymorphs easier in the molecular region. In the phonon region the identification of peaks was imperfect because of the overlapping of the spectrum of the MEF with the gold signal. The next chapter attempts to create substrates using fluorinated compounds as they are considered more hydrophobic than the substrates used in this part of the work, promoting avoidance of the gold signals and the obtaining of better signals in phonon region to differentiate between the polymorphs.

Chapter five: The effect of fluorinated substrates on the crystalline behaviour of some APIs

The overall aim of this thesis, as mentioned in Chapter One, was to achieve a clear nanogram solid form screening method for the APIs by using of the 2D inkjet printing technique and with help of the light optical microscope and Raman spectroscopy. In chapter four, it was found that changing in the chemistry of the gold-coated slide plays a critical role in obtaining different solid forms. PAR droplets exhibited different behaviour on the two prepared SAMs substrates. On SAM-CH_3, PAR spots keep their amorphous state even after full evaporation of DMSO, while polymorph II could be obtained when PAR droplets deposited on SAM-CH_2-OH slide. MEF droplets exhibited different polymorphs when deposited on SAM-CH_3, on SAM-CH_2-OH, and gold-coated slides. MEF I could be obtained after printing on gold-coated slide, while MEF II was identified on the new prepared SAMs slides.

That work encouraged continuing investigation of the effect of surface modification on the appearance of new polymorphs after printing process, taking the advantage of using the gold substrate, which has the ability to undergo further modifications with thiols producing high-organised self-assembled monolayers (SAMs) with different WCA and topography than the original gold substrate. The Raman single spot analysis confirmed that changing in the chemistry of the gold substrate can produce new polymorphs.

These results encouraged thinking in another factor that may affect the solid form (amorphous *vs* crystal) nature of the APIs, this factor related to the hydrophobicity of the used substrate. Therefore, fluorinated hydrocarbons were suggested to create high-water repellent surfaces as they have high hydrophobicity in comparison of hydrogenated analogues, which can limit the spreading of the printed droplets and giving the chance to condense the droplet content in a small area that can facilitate the analysis of the droplet contents easily.

5.1. Introduction

Interest in and applications for fluorine chemistry have significantly advanced since 1886 when Henri Moissan prepared and isolated molecular elemental

fluorine gas (F_2) [190]. The preliminary studies in the field of fluorine chemistry were focussed on fluorenes; the first aliphatic fluorinated hydrocarbons that were reported and fully characterised were carbon tetrafluoride, hexafluoroethane and tetrafluoroethylene [191]. Increasing attention has being paid to the importance of fluorinated compounds after the discovery of Teflon® in 1938 [192]. Since then, fluorinated materials have played an essential role in different technological developments[190].

5.1.1. Why fluorine is important?

The main reason for the particularity of fluorinated compounds is that they contain fluorine, which has the highest electronegativity of all the elements, and also has high reactivity with most other elements even heavy noble gases like krypton, xenon and radon[190].

Incorporation of fluorine atom in an organic compound may change the physicochemical properties of that compound, because fluorine has the ability to react easily with most other atoms to form a very strong bond. The bond between the carbon and fluorine atom (C-F), for example, is 113 $kJ{\cdot}mol^{-1}$ stronger than a (C-Cl) bond (Table 5.1). The high value of dissociation energy (D.E) can be attributed to the electrostatic attraction between $C^{\delta+}$ and $F^{\delta-}$ rather than normal covalent bond with electron sharing [192, 193]. Furthermore, the substitution of hydrogen atom with fluorine atom can play an essential role in changing the steric hindrance of the molecule. This is due to the length of the C-F bond (1.38 Å) in comparison to the 1.09 Å length of C-H bond, and the different values of Van der Waals volumes of both C-F and C-H bonds, 42.6 and 16.8 $Å^3$ respectively [194]. One of the most interesting properties of fluorinated compounds is the high hydrophobicity in comparison to hydrogenated analogues, because of the weaker effect of Van der Waals forces between adjacent molecules due to low polarizability [195].

Table 5.1. Dissociation energy (D.E) of various C-X bonds [193]

Bond	C-F	C-H	C-O	C-C	C-Cl	C-N
D.E ($kJ{\cdot}mol^{-1}$)	441.0	410.0	351.5	348.0	328.4	292.0

The hydrophobicity of a surface describes its ability to be unwettable by water. This behaviour is attributed to many factors, such as surface energies of both the

water and the solid surface, and factors related to the surface itself, such as roughness, porosity, and chemical reactivity [196]. This chapter will focus on the roughness of the solid substrates and its effect on achieving a solid form screening for the APIs.

5.1.2. Methods of roughening the surfaces

Many strategies for making rough surfaces have been reported [197]. They are simple in general, and can be performed in a one-step process. However, the fabrication of hydrophobic or super-hydrophobic surfaces requires the creation of a rough surface, followed by modification with low-surface energy materials see Figure 5.1 [197].

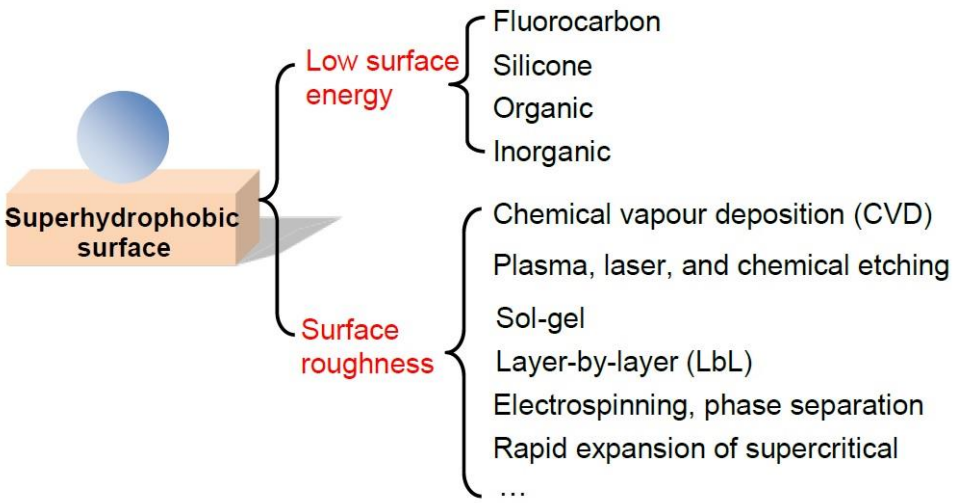

Figure 5.1. Strategies for obtaining super-hydrophobic surface

5.1.2.1. Chemical vapour deposition (CVD)

A hydrophobic surface can be chemically created by depositing a thin film of some materials onto a heated substrate via chemical reaction in the gaseous phase [198]. This versatile process, which is called chemical vapour deposition (CVD), uses chemical solutions to change the character of the substrates by depositing solid metals and oxides [198].

Liu *et al.* [199] reported that ZnO films were introduced as models for creation substrates with tuneable wettability by exposing them to external parameters such as, light illumination, heat treatment and dark storage. They used super hydrophobic films with an original WCA of 110.6º see Figure 5.2 [199] . The authors changed the ZnO film's wettability from hydrophobic (WCA=110.6º) to hydrophilic (WCA=0º) after UV-irradiation. The hydrophobicity of the same

surface could be recovered with a higher WCA of 164º either by heating or storing in darkness [199].

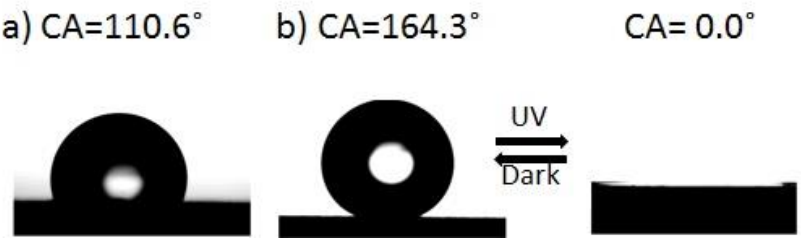

Figure 5.2. WCA of a) initial hydrophobic surface and b) after heating of storing in darkness [199]

5.1.2.2. Plasma etching

Etching is an efficient and simple method to create rough surfaces. Oxygen plasma etching can provide a clean and rough surface. Because of the availability and low cost of oxygen O_2, it is commonly used in plasma cleaning technology. Incorporating the O_2 source in a plasma system can generate oxygen plasma. Using this kind of plasma has been discussed in previous studies [200, 201]. One of these studies was Teshima's team's study [201]. They successfully fabricated a transparent ultra-water repellent substrate via two dry processing techniques: formation of nano-texture on a poly ethylene terephthalate (PET) substrate via treatment with oxygen plasma, followed by either plasma enhanced chemical vapour deposition (PECVD) or low-temperature (CVD) using tetramethylsilane (TMS) as a precursor for providing hydrophobic functional groups onto the nano-texture surfaces, see Figure 5.3. The resulting surface showed a WCA greater than 150º [201].

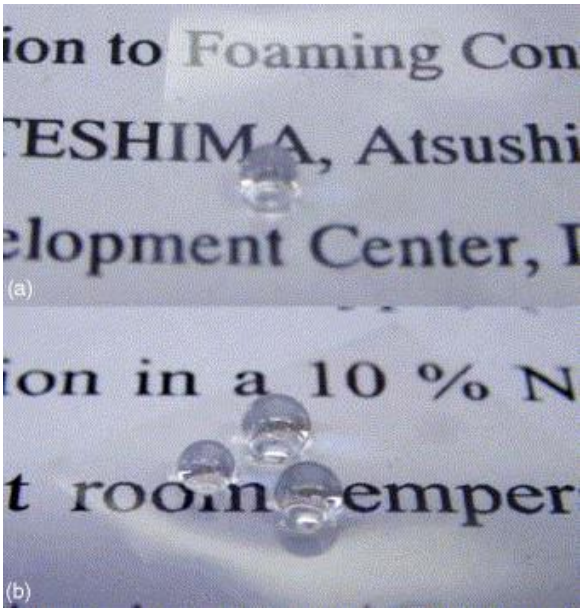

Figure 5.3. Images of water droplets on the Nano textured PET substrates covered with a) Low-temperature CVD layer using FAS and b) PECVD layer using TMS [201]

A super-hydrophobic surface can also be obtained by the formation of micro or nano-grooves textured by laser treatment, see Figure 5.4 [202]. Poly dimethyl-siloxane (PDMS), for example, was treated with laser (532 nm) to produce micro-, sub-micro and nano-composite structured PDMS substrates [202]. The resulting ultra-water repellent surface had a WCA as high as 160º.

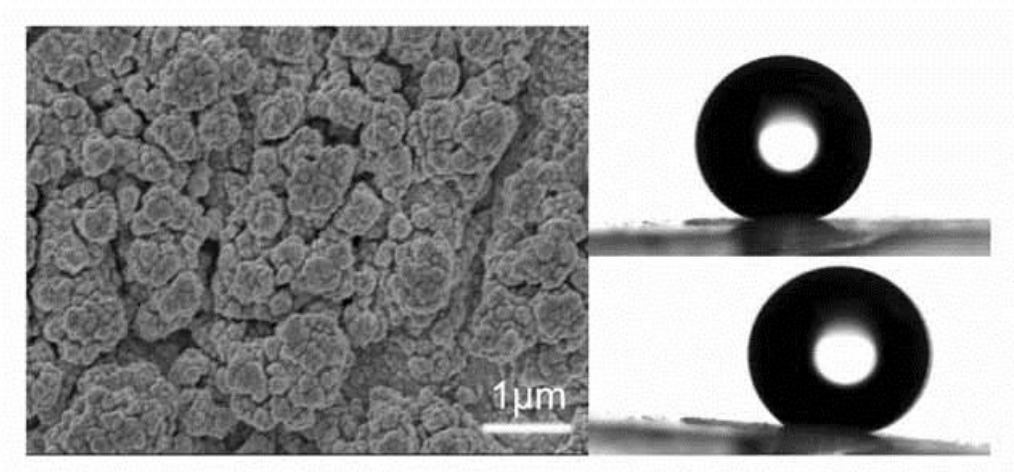

Figure 5.4. SEM image (Left) and WCA and sliding angle of rough polydimethylsiloxane (PDMS) surface [202]

Chemical compounds can also affect the texture of the surfaces and turn them hydrophobic. This process called chemical etching, which consists of two steps together: chemical treatment followed by low surface-energy materials treatment. Polycrystalline metals, like zinc, aluminium, and copper, were

chemically treated by dislocation etching in HCl, HCl and HF, and HCl and CH_3COOH respectively see Figure 5.5 [203]. Afterwards, a subsequent functionalisation with a low-surface free energy like fluoroalkylsilanes, was performed. The resulting surface showed super-hydrophobic character with a WCA greater than 150º [203].

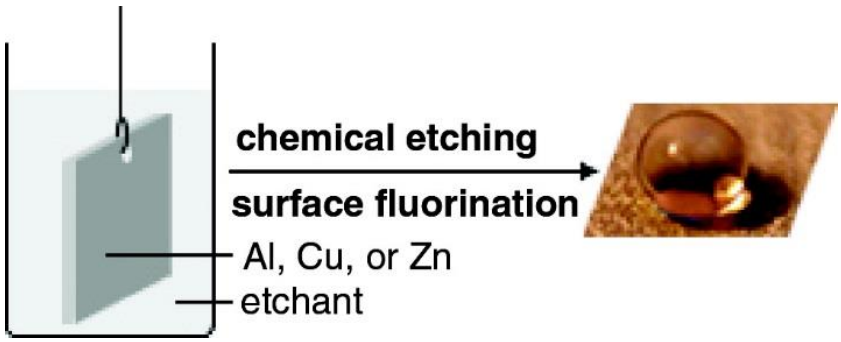

Figure 5.5. Creation super-hydrophobic surface by chemical etching [203]

5.1.2.3. Layer-by-layer (LbL) method

Layer-by-layer (LbL) is a simple, flexible, cost effective and pervasive method to fabricate highly-ordered nanostructured thin films as well as controlling the film thickness [204]. The principle of LbL depends on the sequential adsorption of oppositely charged molecules on a surface, with washing steps between the deposition of each molecule (Figure 5.6) using electrostatic interactions, hydrogen bonds, cation dipole interactions and bio-specific interactions [205, 206].

Many different approaches can be used to operate LbL assembly, including dipping, spin-assisted, and spray-assisted LbL assembly [207]. The principle of each method was reviewed by Li and his co-workers [207]. Figure 5.6 shows the simple scheme for all these techniques.

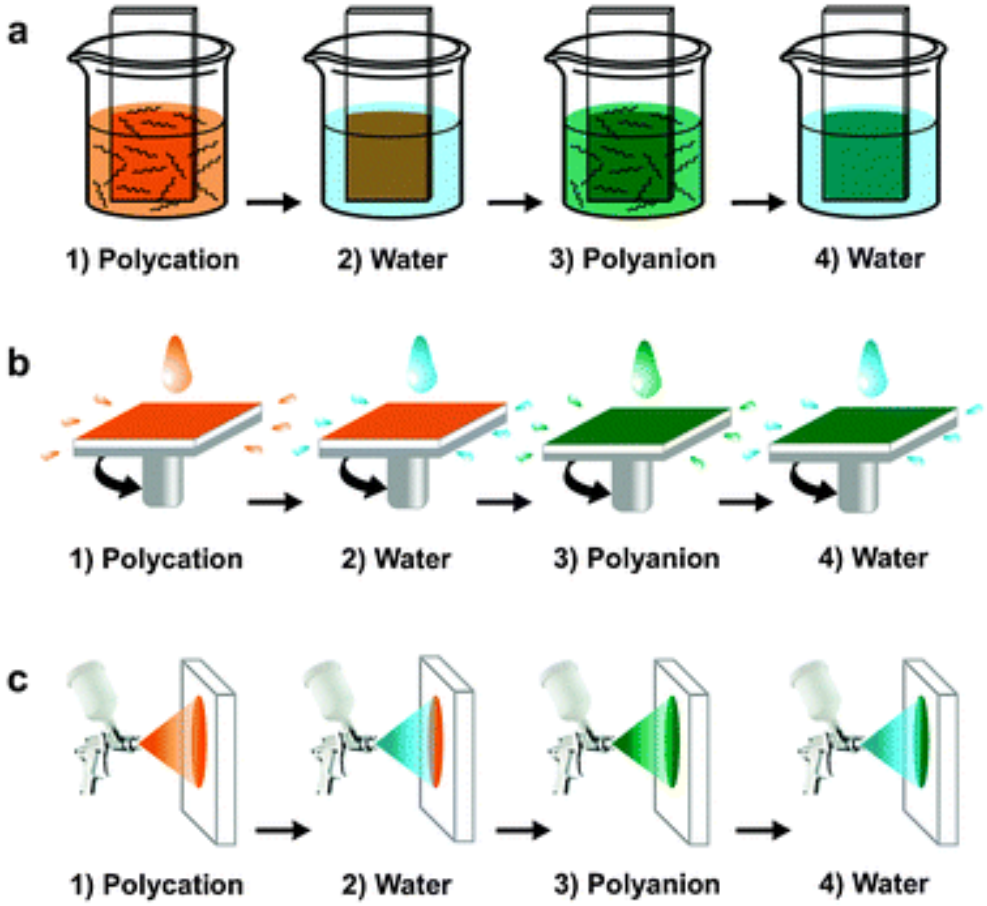

Figure 5.6. Approaches of Layer-by-layer method [207]

Zhai et.al. [208] used this technique to produce a honeycomb-like hydrophobised polyelectrolyte multilayer substrate with a WCA of 172º after acidic treatment of polyallylamine hydrochloride (PAH) and poly acrylic acid (PAA) followed by overcoating with silica nanoparticles (Figure 5.7) [208].

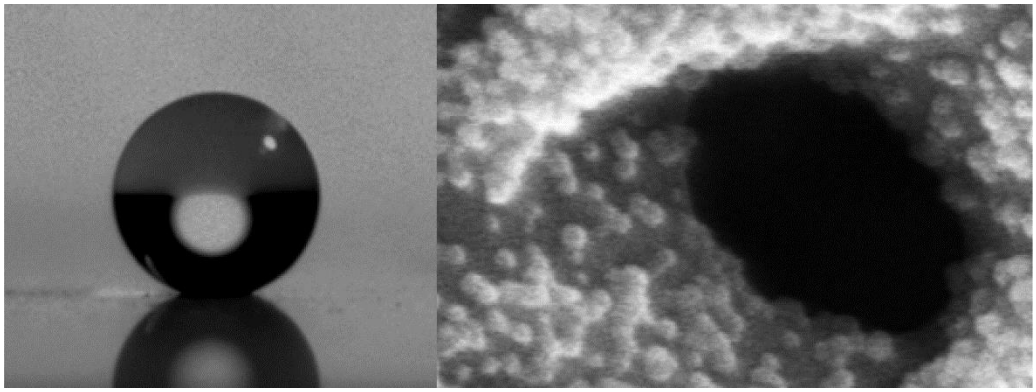

Figure 5.7.WCA and SEM image of honeycomb-like hydrophobised polyelectrolyte multilayer surface created by LBL method [208]

5.1.2.4. Sol-gel method

The sol-gel process is a chemical route involving the transition in phases from liquid "sol" to semi-solid "gel" phase at relatively low temperature near to the temperature of glass transition T_g of the used material [209]. The sol-gel method depends on wet chemistry that comprises preparing the solution then removing the liquid and turning it to gel after drying and heat treatment, It can be considered a versatile method for creating hydrophobic surfaces [209].

There have been a number of studies describing how to create super-hydrophobic surfaces using sol-gel technique. One of these was conducted by Hikita and his team [210]. Colloidal silica particles and fluoroalkylsilane were used to manage the surface energy and roughness of the prepared film; the degree of hydrophobicity of the resulting surface depends on the optimisation of the amounts of starting materials [210]. It was found that the new film exhibited repellency to both to both water and oil, see Figure 5.8.

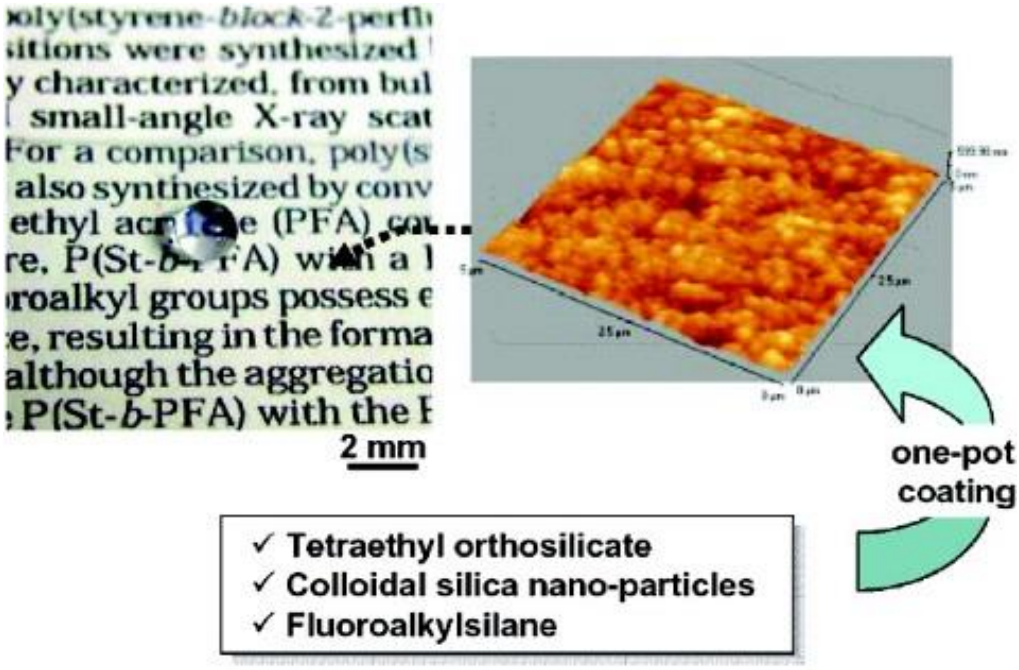

Figure 5.8.Image of water droplet (Left) and 3D-AFM (Right)for a fabricated PET film with sol-gel method [210]

In addition to using SAM technique (see Chapter four), a simple and cheap LbL approach was adapted in this chapter using dip-coating unit to create super-hydrophobic coating on a glass substrate.

5.1.3. Roughening the surface of low surface energy materials

5.1.3.1. Silicones

Poly dimethylsiloxane (PDMS) can be considered one of the most common organosilicon compounds used in fabrication of super-hydrophobic surfaces, due to its intrinsic deformability and hydrophobic properties [211]. A series of studies was carried out by Jin *et al.* [202] and Khorasani *et al.* [212] by using laser etching, Ma *et al.* [213] using electrospinning, and Zhao *et al.* [214] using block copolymer micellar solution in order to illustrate the importance of using PDMS in creation ultra-water repellent surfaces with very high WCA (Figure 5.9).

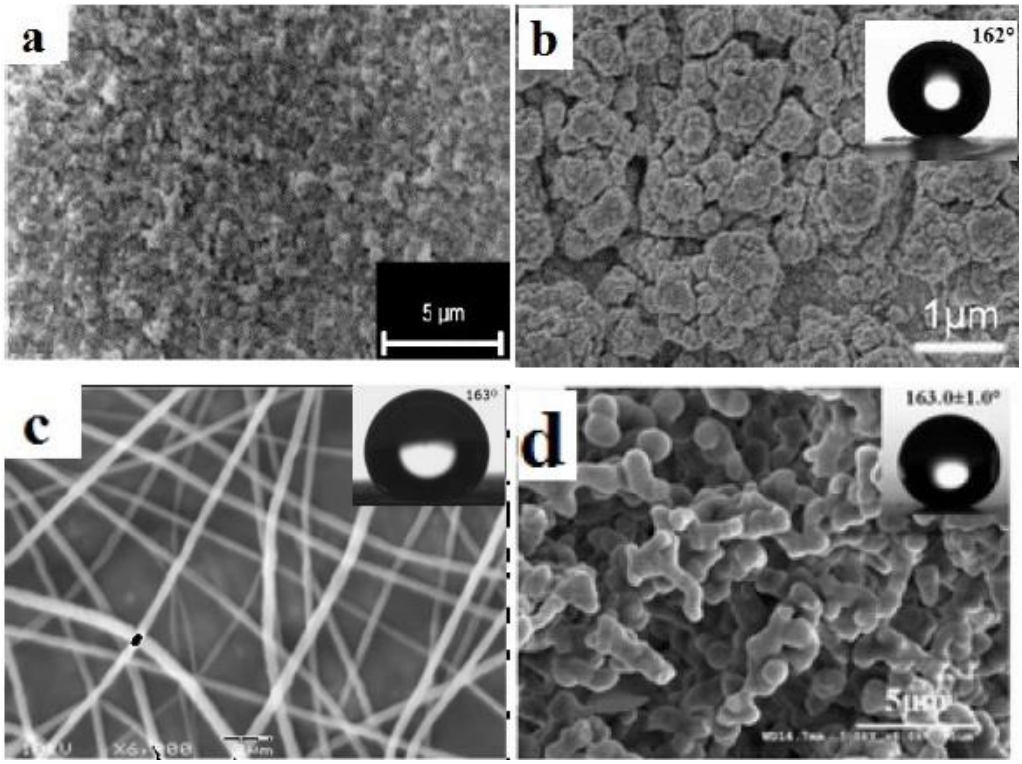

Figure 5.9.SEM images for treated PDMS with a) and b) Laser etching, c) electrospinning, and d) block co-polymer micellar solution [202, 212-214]

5.1.3.2. Fluorocarbons

There is increasing interest in the fabrication of super-water repellent surfaces by using fluorinated hydrocarbons, due to their extremely low surface energy [215]. Because of their limited solubility, fluorinated materials may be linked to or blended with other materials rather than used directly [216]. A stretching

method can be used to fabricate a super-hydrophobic surface [217]. Zhang and co-workers created a super-hydrophobic poly tetrafluoroethylene (Teflon) film by converting it into fibrous crystals. They stretched it at different ratios producing a large fraction of void space in the surface, which was believed to be responsible for the low wettability (WCA=165º) and high hydrophobicity, (Figure 5.10) [217].

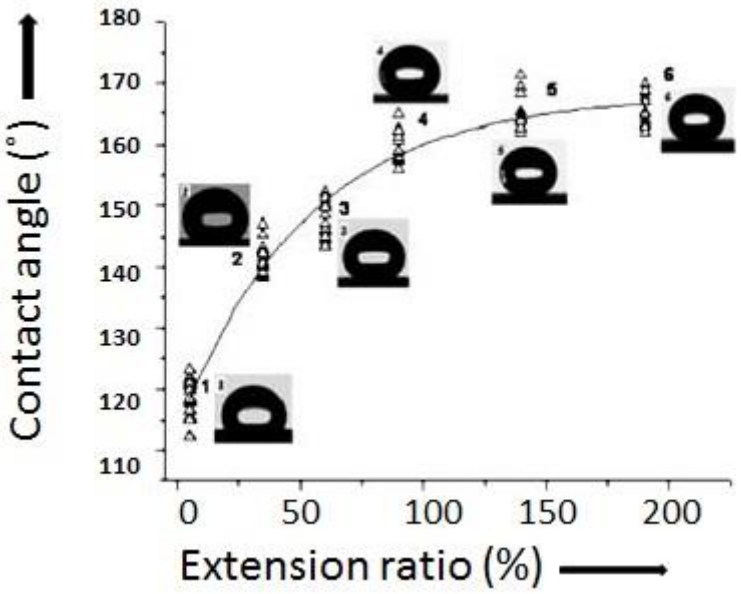

Figure 5.10.WCA of Teflon at different stretching ratios [217]

Another approach was adopted by Shiu *et al.* [216]. They observed that oxygen plasma treatment on a Teflon film can produce a rough surface with a high WCA of 168º, see Figure 5.11[216].

A fluorinated block co-polymer, consisting of equimolar fluorinated acrylate and methyl methacrylate, was used to prepare a super-hydrophobic honeycomb-like porous structure under humid environment (relative humidity ~60% at room temperature) [218]. In this study, the super-hydrophobic porous structure produced could easily be controlled by manipulating the casting volume of co-polymer solution [218]. The resulting honeycomb film was observed with 1.6 µm pores and high WCA of 170º, see Figure 5.11[218].

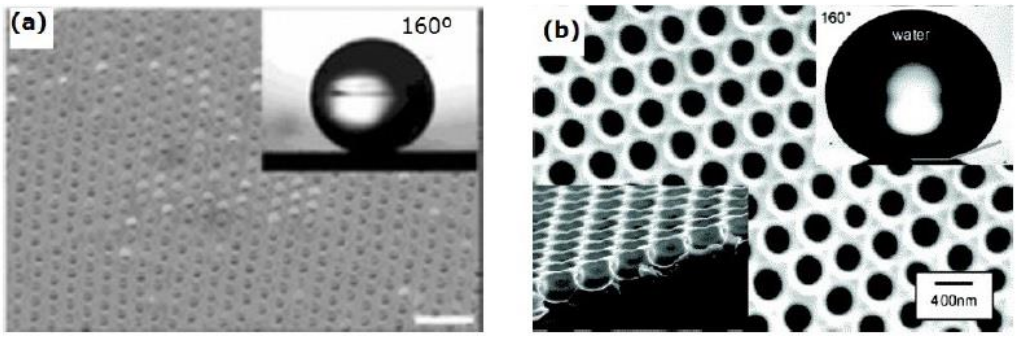

Figure 5.11.SEM images of honeycomb-like porous structure with WCA on this film [216] [218]

Hydrophobicity cannot only be obtained using silicones and fluorocarbons, but also by using organic materials (low-density poly ethylene (LDPE) [219] and polystyrene (PS) [220]) and inorganic materials (metal oxides such as ZnO [221]).

The purpose of reviewing the methods of roughening the surface is to have an idea about the technique or approach that will be used in this chapter. LbL is selected for fabrication high hydrophobic substrate because it is cheap and simple approach that can be used in a short time.

5.2. Aim

The aim of this chapter is to investigate the role of surface hydrophobicity on the APIs polymorph screening, by changing the roughness of the used substrates using SAMs and LbL approaches to create high-water repellent substrates, such as fluorinated SAMs and fluorohydrocarbones, for polymorph screening of nano quantities of carbamazepine, mefenamic acid and flufenamic acid.

5.3. Experimental design

5.3.1. Materials

Carbamazepine CBZ ($C_{15}H_{12}N_2O$), was purchased from MP Biomedical, was used as received and there was no need for purification. Compared to the literature available, it was confirmed that it was form III [123]. It was also found to melt at 177°C [124]. Mefenamic acid MEF ($C_{15}H_{15}NO_2$), was purchased from Alfa Aesar, A Johnson Matthey Company. Raman spectrum confirmed that it was of form II. It was also found to melt at 230-231 °C [125]. Flufenamic acid FLUF ($C_{14}H_{10}F_3NO_2$), was purchased from Fluka Analytical. Raman spectrum

confirmed that it was of form I [127]. It was also found to melt at 133-134 °C [222]. These drugs were selected as models because they exhibit wide ranging and well characterised polymorphs [95, 99, 101]. Dimethyl sulfoxide (DMSO), 99.5%, was purchased from Sigma-Aldrich. Two types of fluorinated compounds were used in this study. One is functionalized *n*-alkane thiols with a CF_3-terminated group (11-Mercaptoundecyl trifluoroacetate), here abbreviated to SAMF. This was purchased from Sigma-Aldrich. Flutec fluid (perfluoroperhydrophenanthrene oligomer), here abbreviated to LE15, was purchased by F2 chemicals (Lancashire, UK). Gold-coated microscope slides were purchased from Sigma-Aldrich with layer thickness 100Å and 99.999% (Au).

5.3.1.1. Preparation of samples and thiol solutions

Solutions of 6 $mg \cdot mL^{-1}$ of CBZ, MEF and FLUF were prepared separately by dissolving 30 mg in 5 mL of DMSO. Due to the slight water-solubility of the APIs that used in this study, DMSO was used in this chapter as it has effective roles in pharmaceutical industries. Besides being a solvent during synthesis of the drug components, it works as a co-solvent for stabilising the formulation products, and is used as a cryoprotector and drug carrier [133]. MEF form (II) was prepared by heating an amount of the pure MEF as received for 48 hour at 160 C˚[96] and then verifying the identity of the product by Raman spectroscopy. The prepared polymorph of MEF (II) was adopted as a bulk reference to compare with the spectra of the resulting dots of MEF. FLUF form (III) was prepared by adding an amount of FLUF (as received) in 10 mL of refluxing methanol, the hot solution was recrystallised by adding cold water, and then the resulting crystals were filtered then kept at room temperature [96]. The Raman spectrum of FLUF (III) was used as a reference to compare with the spectra of the resulting dots of FLUF without printing it on the used substrates. Thiol stock solution was prepared by dissolving 0.0142 mL of 11-Mercaptoundecyl trifluoroacetate in 25 ml ethanol 99.00% (final concentration of 2.0 mM) at room temperature and under deoxygenated environment by using inert nitrogen gas [157].

5.3.1.2. Preparation of substrates

Two types of fluorinated slides were prepared to be substrates for the subsequent APIs printing. SAMF slides were prepared by immersing the gold slides in the thiol solutions in an inert environment for ~ 18 hr. Then they were removed from the solution, washed with a small volume of ethanol and dried with nitrogen. Flutec, or LE15 slides were prepared by dipping the glass slides into and subsequent removing from Flutec solution. The dipping process was performed within 60 minutes and then it was left to dry at room temperature overnight.

5.3.2. Methods

5.3.2.1. Evaluation of the prepared substrates

As described in chapter four, the roughness and the wettability of the prepared surfaces were investigated by means of the AFM and KSV CAM200 instrument for determining the RMS and WCA respectively. The CA was measured with ~ 2.5 µl water droplet at ambient temperature, and on different areas of the fluorinated substrates. All WCA measurements of both SAMF and LE15 slides were within ± 0.5ºC of the averages. AFM measurements were also carried out on five to eight different areas throughout the selected substrates using aluminium reflective coating tip MPP-12120(TAP150A) with 30 µm × 30 µm scanning area and resolution of 256×256 points. The obtained topographical images of all the solid surfaces were processed using Nano Scope Analysis, version 1.7.

5.3.2.2. Printing drugs solutions on the prepared substrates

Deposition of CBZ, MEF, and FLUF on the prepared fluorinated substrates was performed under the same laboratory conditions described in chapter four. The solutions of the selected drugs were deposited onto the substrates by means of 90 µm orifice nozzle on a non- contact piezoelectric depositing system (Sciflexarryer S5, Scienion). Adjusting firing voltage to around (85V) and electrical pulse to around (48 µs) can produce a regular droplet shape with a volume of 220 ± 2 pL. Fabrication of the printed microarrays was performed creating three main fields, one for each drug. Each field was sub-divided into four (3×3) clusters representing the four quantities that were deposited on the

fluorinated substrates; 10, 50, 100 and 250 droplets which in turn equivalent to 13, 66, 132, and 330 ng respectively (Figure 4.4). Each printed slide was moved to the light optical microscope to monitor the behaviour of the droplets during and after DMSO evaporation, and pictures of these droplets were captured at a regular intervals. The slides were then kept in a desiccator at room temperature.

5.3.2.3. Microscopic observations of the printed droplets

Later, the microscopic investigations of the resulting dots were conducted using the polarising microscope with the same specifications mentioned in chapter three. The bright-field and cross polarised images were recorded by means of a camera was fixed on the top of the microscope and connected to a computer. The acquired data was processed via a Q-capture^{TM} software to manipulate the brightness and the light exposure time in order to get a high-quality image.

5.3.2.4. Raman spectroscopy

A confocal Horiba-Jobin-Yvon LabRAM system (Horiba-Jobin-Yvon Ltd Middlesex U.K.) was used to perform Raman spectrophotometric measurements on single printed spots. A NIR (HeNe, 785nm) laser was used to with 600 lines/mm of grating, 300 µm of confocal hole and a spectral range between 40 and 1800 cm^{-1}. It is also, as mentioned in chapter two, connected to an Olympus BX41 microscope provided with four objective lenses 10×, 40×, 50× and 100×. Three objective lenses were used, 10× for getting the spots, 50x for calibration and 100× for focussing the small printed spots of the drug. The obtained Raman data of APIs spots were processed by means of LabSpec 5 software.

5.4. Results

5.4.1. Characterization of the solid surfaces

The chemically modified gold-coated slide with 11-mercaptoundecyl trifluoroacetate (SAMF) and the glass slide coated with Flutec (LE15) were subjected to preliminary tests to evaluate their texture using AFM and WCA measurements.

Figure 5.12 shows 30 µm × 30 µm 2D and 3D AFM topographical images, WCA and RMS values of gold coated slide, SAMF and LE15. It is obvious, as described before in chapter three, that long-time immersion of a gold coated

slide in an ethanoic solution of a thiol can change the texture of the gold slide. Keeping the gold slide in an alcoholic solution of 11-mercaptoundecyl trifluoroacetate for 18 hours produces a low wettability surface with high WCA of 85.33˚±0.50˚ see Figure 5.12.

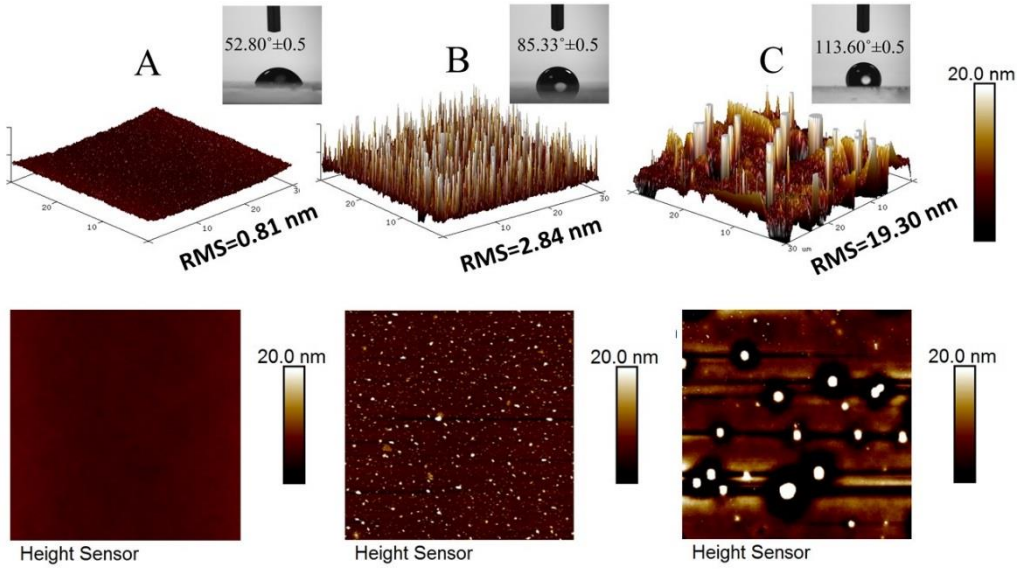

Figure 5.12.WCA, 2D and 3D AFM images of a) gold-coated, b) SAMF and c) LE15 slides

Another parameter were taken into consideration during AFM measurements was the roughness of the prepared substrates that was automatically measured and expressed by means of root mean square (RMS). As described in chapter three, the smoothness of gold slide surface gives high wettability (low WCA=52.80˚±0.50˚) and RMS of 0.81 nm. The topography of the gold slide has changed as a result of being immersed for 18 hours in ethanoic 11-mercaptoundecyl trifluoroacetate. The resulted surface reveal a uniform distribution of needle-like shaped in all the sample (Figure 5.12) which makes the surface hydrophobic with WCA of 85.33˚±0.50˚ and RMS of 2.84 nm.

Also, time of dipping of glass slide onto the fluorocarbon solution (Flutec LE15) was examined to decide which time of dipping can produce a highly hydrophobic substrate can change the nature of the glass slide. Flutec required around 60 minutes to be deposited on the microscope slide to create a highly water repellent surface with a WCA of 113.60˚±0.50˚ see Figure 5.13.

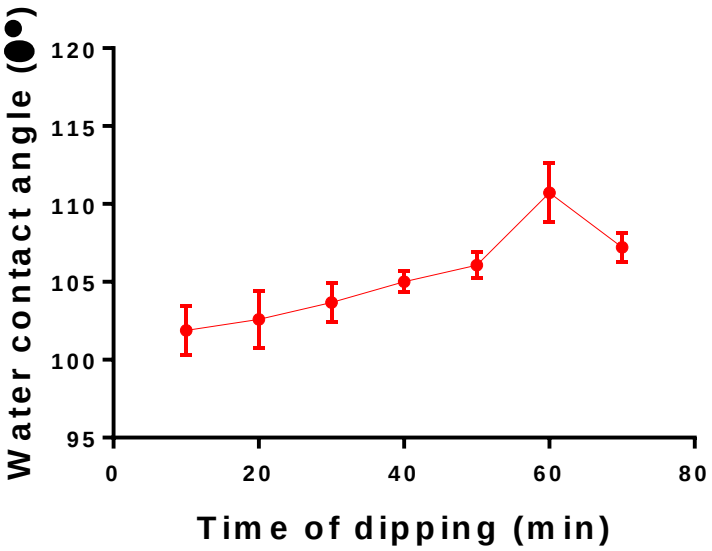

Figure 5.13. WCA of different prepared LE15 slides with different time of dipping

The surface of glass slide was covered with Flutec LE15 by dipping for one hour, producing non-uniform features which make the resulted surface more hydrophobic with high WCA of 113.60˚±0.50˚ and RMS of 19.30 nm.

5.4.2. The behaviour of the printed carbamazepine, flufenamic acid, and mefenamic acid droplets on the used substrates

Figure 5.14 shows the behaviour of different printed quantities of the CBZ, FLUF, and MEF droplets behaviour on both LE15 and SAMF slides. Figure 5.15 illustrates the time required to full evaporation of the printed droplets of the used APIs. It can be seen that the time of evaporation of the selected drugs quantities printed on LE15 is greater than that of the same drugs on SAMF.

The small deposited quantity (13 ng) of CBZ, FLUF, and MEF shows different evaporation time on both the used substrates; it takes 19(5), 23(5), and 16(6) minutes for CBZ, FLUF, and MEF on LE15 (and SAMF) respectively.

While the high printed quantity (330 ng) of the same used drugs shows time of evaporation as follow; 112(60), 126(50), and 110(37) minutes for CBZ, FLUF, and MEF on LE15 (and SAMF) respectively.

Also, it is evident from Figure 5.14 that the occupied area of the high printed quantity spot (330 ng) of CBZ, FLUF, and MEF, exhibit different values on both the two substrates used. It occupies 0.04 (0.07), 0.10 (0.05), and 0.05 (0.17) mm^2 for CBZ, FLUF, and MEF on both LE15 (and SAMF) slide respectively.

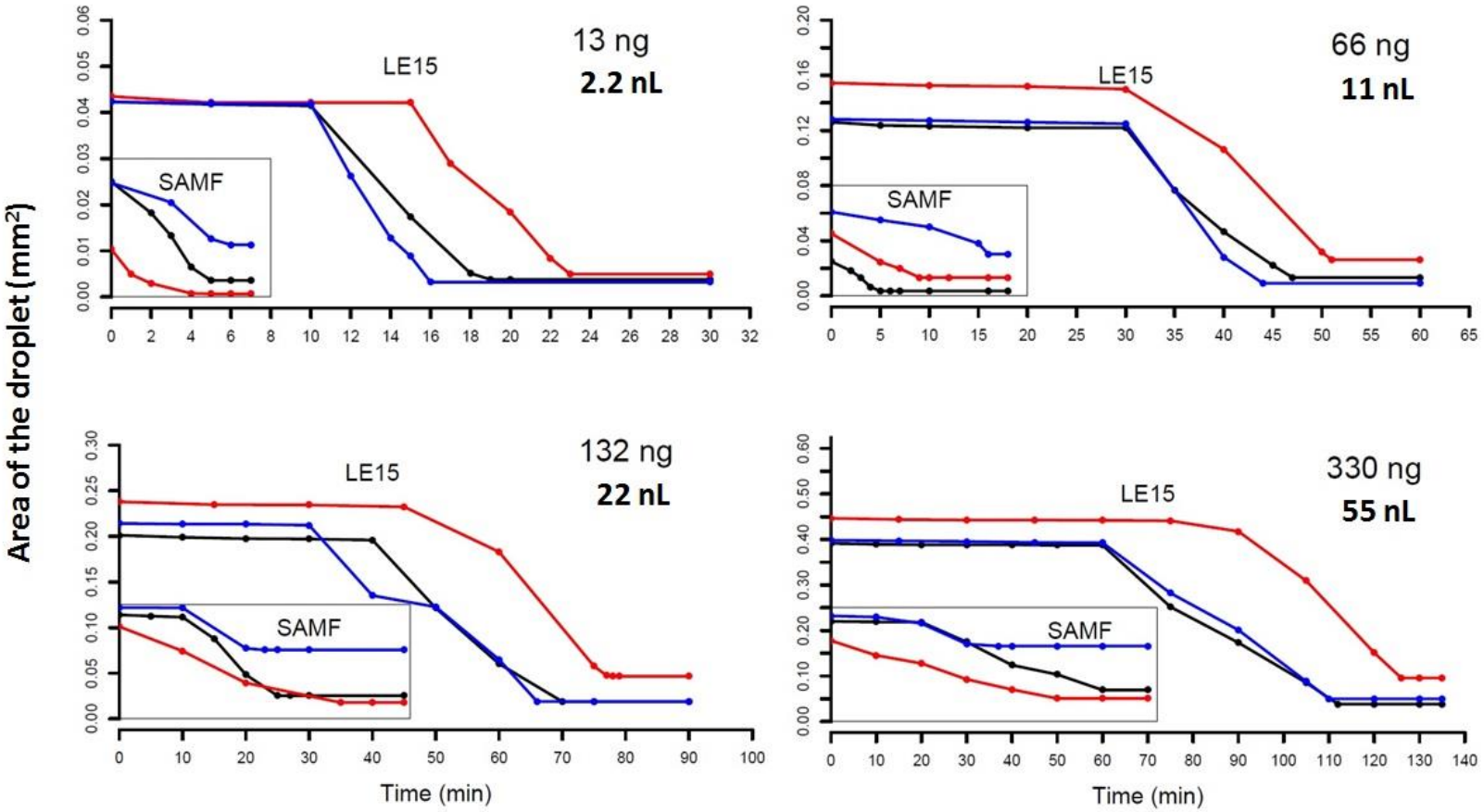

Figure 5.14. The behaviour of different printed quantities/volumes of CBZ (black), FLUF (red), and MEF (blue) on SAMF and LE15 substrates

That observation gives a good proof about the high hydrophobicity of LE15 slide, in comparison with the SAMF slide, which makes the droplet surface thick. Consequently, it takes longer time to complete the evaporation of DMSO [185]. The evaporation time *vs* the area of the different printed droplets of PAR/DMSO on LE15 relationship was presented in (Figure C. 1).

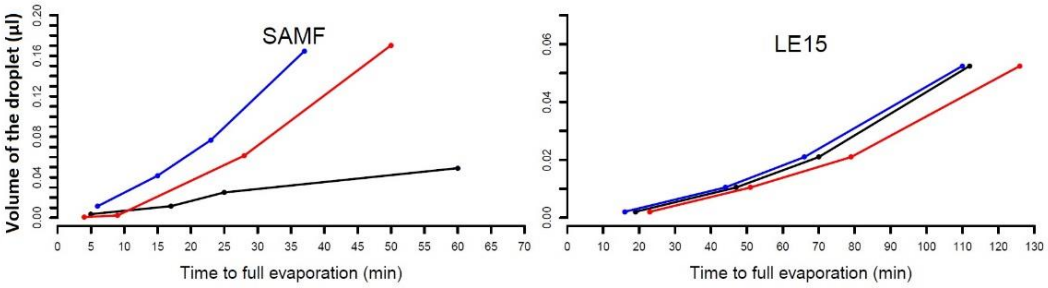

Figure 5.15. time of full evaporation of different printed quantities of CBZ (black), FLUF (red), and MEF (blue)on the two used fluorinated slides

5.4.3. Observation of the printed droplets of carbamazepine, flufenamic acid, and mefenamic acid on different substrates

Visual confirmation of events occurring during the transformation from liquid droplets to solid spots can be observed by optical microscopic investigation to monitor effect of various printed quantities on the appearance of new polymorphs on the used substrates. As the volume of the single droplets is 0.22 nL, containing 1.32 ng of drug, the exact printed quantities of CBZ, FLUF, and MEF were deposited on SAMF and LE15 slides with four different number of droplets; 10, 50, 100, and 250 were equivalent to 13, 66, 132, and 330 ng respectively.

As described in previous two chapters, the printed slide was transferred onto the light optical microscope to start investigating the droplets evaporation and the crystallisation behaviour, with time using 10× magnification for all the printed spots.

The optical micrographs of all CBZ printed quantities on the SAMF slide are shown in Figure 5.16 . The optical observations revealed that all the printed droplets underwent decreases in size and solidified in the shape of the droplets with relatively smooth surface. The evaporation of DMSO in the printed quantities of CBZ required 5, 17, 25, and 60 minutes for 13, 66, 132, and 330 ng

respectively. It can be noticed that all the dried spots of CBZ appeared to be smoothly transparent showing an amorphous state directly after full DMSO evaporation. The resulting spots were investigated continuously to monitor their crystallisation behaviour. It can be noticed that CBZ spots start turning to crystalline state 24 hours after DMSO evaporation. (Figure 5.16).

The same behaviour was observed in the FLUF droplets on SAMF, the small printed quantity (13 ng) needed only five minutes to remove the DMSO, while the (330 ng) droplet required 50 minutes for completing evaporation process. Like CBZ, all the FLUF droplets underwent change in their physical state, i.e. they changed in appearance to crystal form 5 to 10 minutes after full evaporation (Figure 5.17).

The MEF droplets on SAMF also underwent crystallisation after evaporation of DMSO. As can be seen, 330 ng required about 37 minutes to start turning to a crystal form directly while the small printed quantity (13 ng) needed only six minutes to remove all the solvent (Figure 5.18).

From the above data, it can be said that CBZ droplets undergo changing in the physical state with two steps mechanism, first turning from solution to amorphous solid state, which takes between 5 to 60 minutes, and the second step which include changing from amorphous solid state to crystalline that needs about 24 hours.

While the behaviour of FLUF and MEF droplets was followed the same mechanism, which include two steps, one required from (5 to 50) and (6 to 37) minutes for both FLUF and MEF, respectively to turn from solution to amorphous solid state, followed by fast step to change to crystalline state within 2-3 minutes.

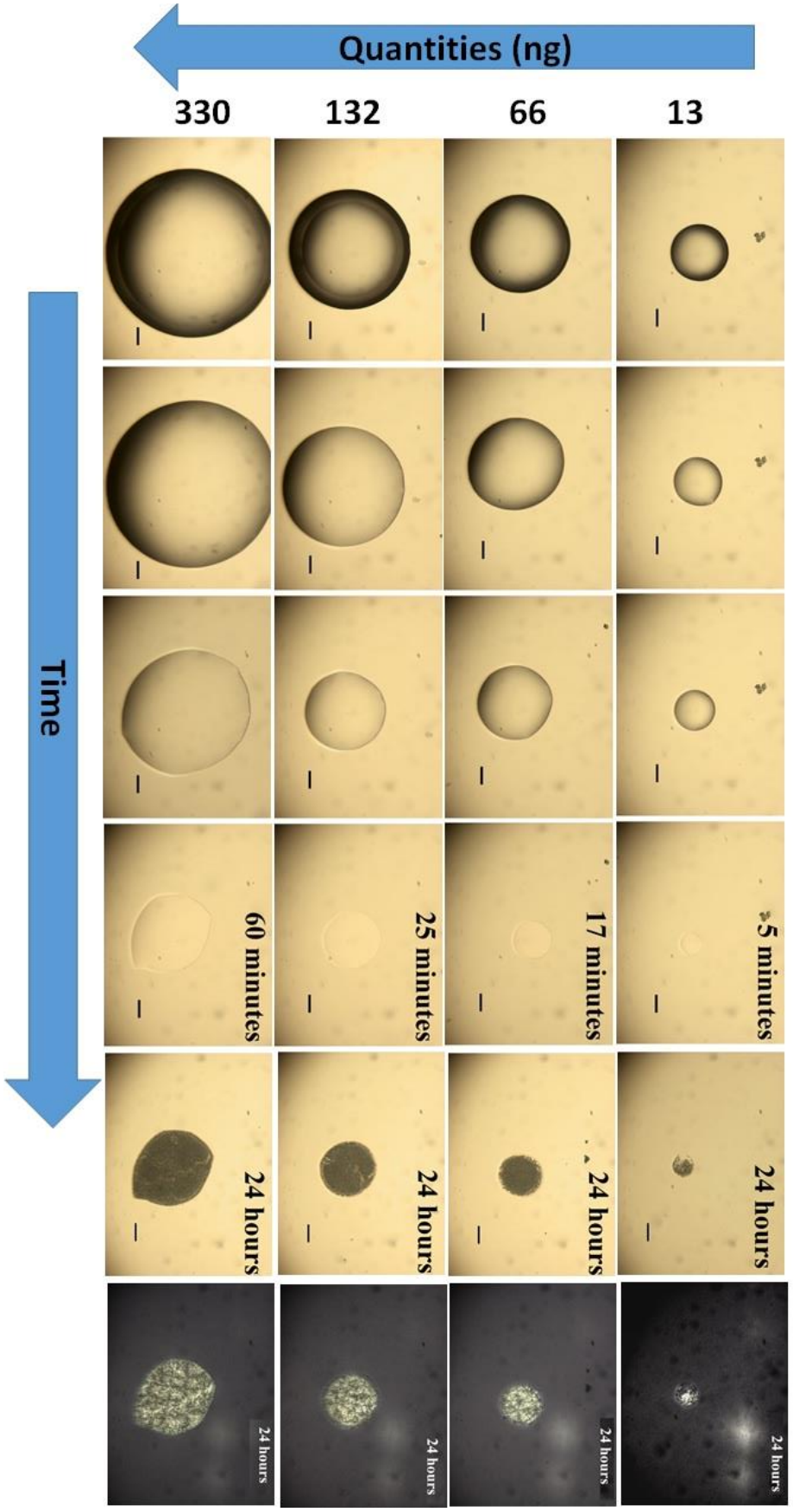

Figure 5.16. Bright-field and cross-polar micrographs of carbamazepine in DMSO SAMF , scale bar: 0.1mm

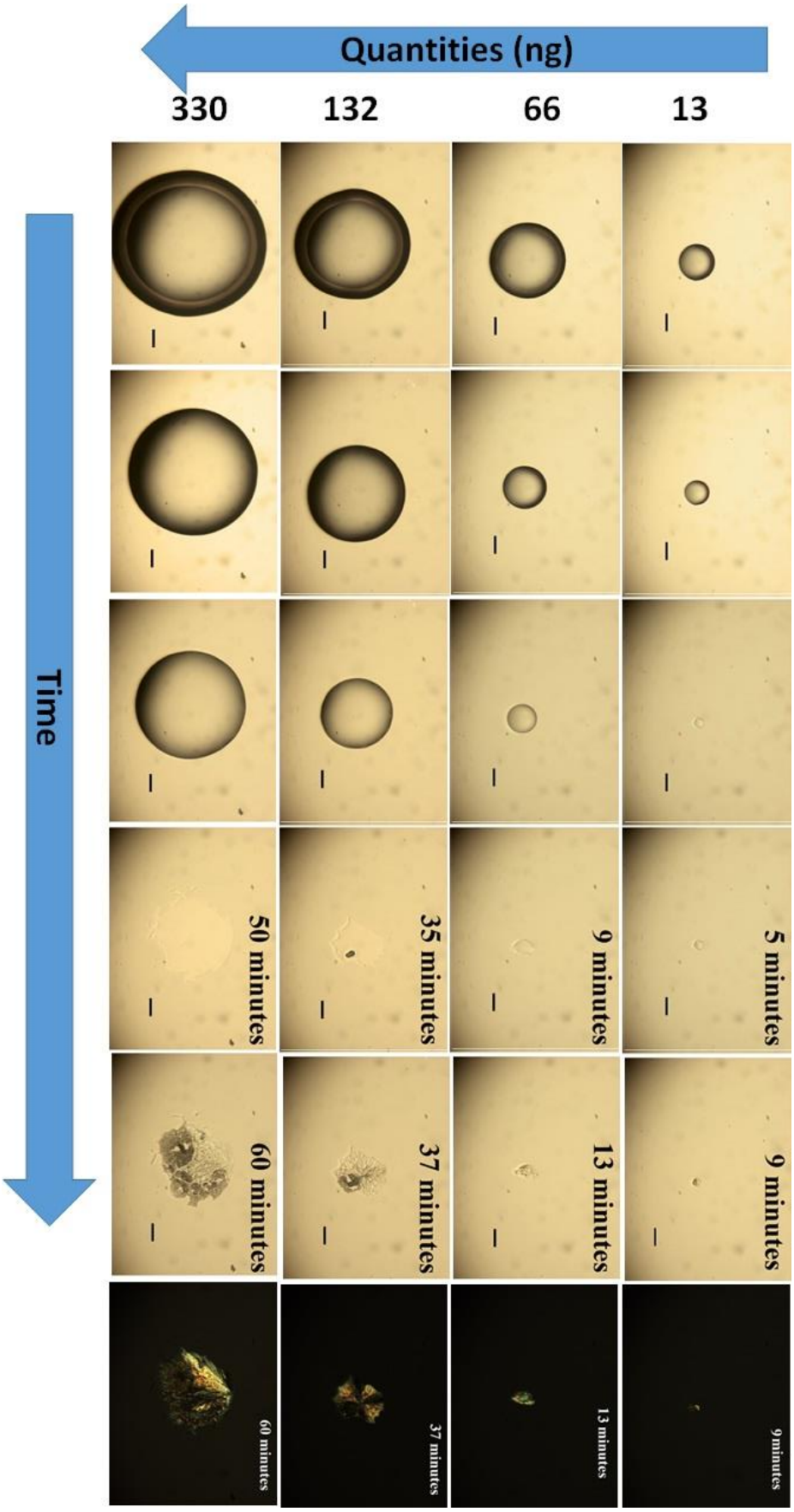

Figure 5.17. Bright-field and cross-polar micrographs of flufenamic acid in DMSO on SAMF , scale bar: 0.1mm

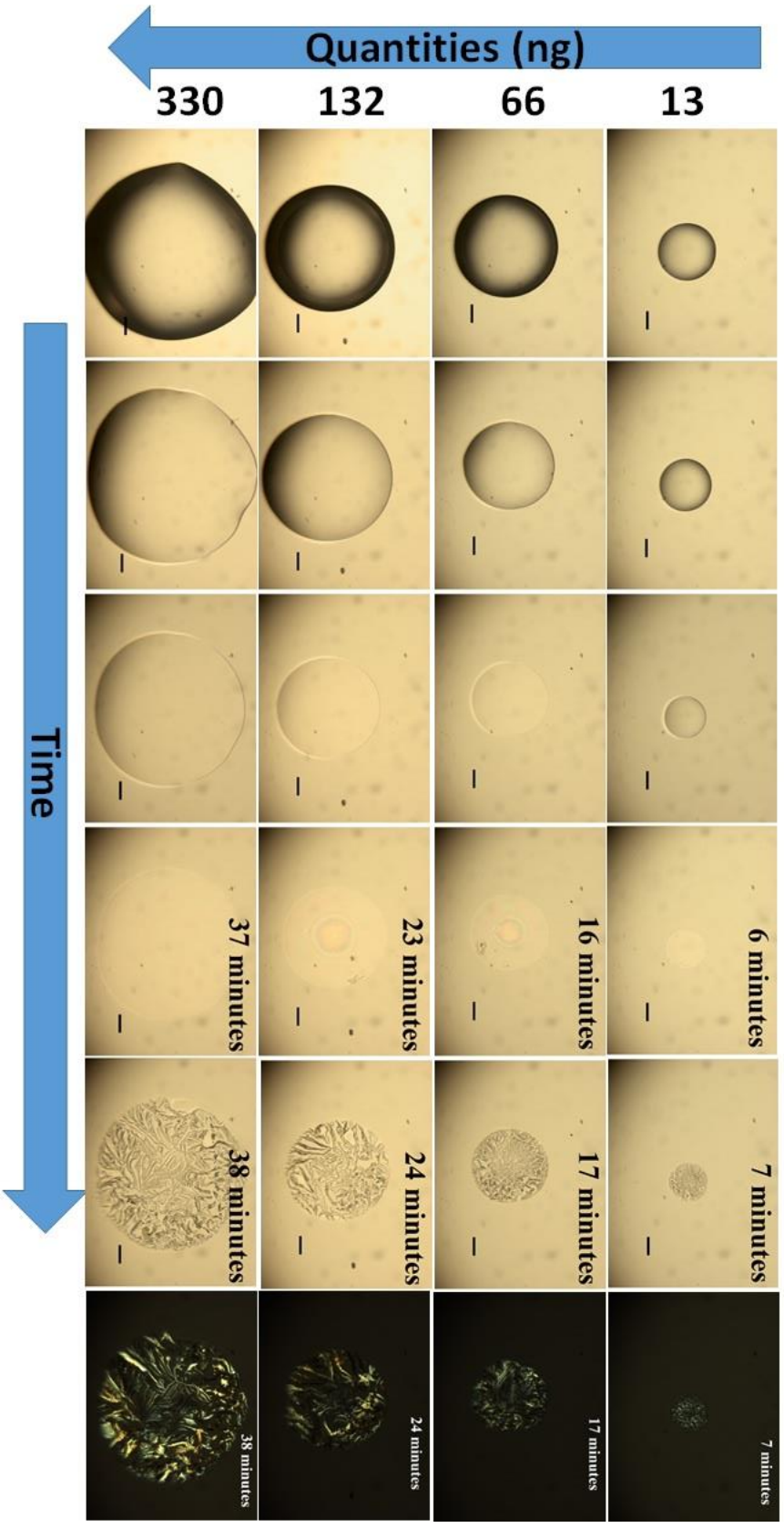

Figure 5.18. Bright-field and cross-polar micrographs of mefenamic acid in DMSO on SAMF , scale bar 0.1mm

The CBZ, FLUF, and MEF droplets on LE15 slide exhibited essentially the same behaviour as those on SAMF. Figure 5.19,Figure 5.20, and Figure 5.21 show the optical micrograph of different printed quantities of CBZ, FLUF, and MEF respectively on LE15. Generally, all the printed droplets underwent decreasing in size due to the DMSO evaporation that consumed longer time than their counterparts on SAMF.

In CBZ printed quantities, 13 ng droplet required 19 minutes to remove the DMSO and turn to amorphous solid form, while 115 minutes was enough to for DMSO evaporation from 330 ng droplet. The resulting amorphous solid form was not the final physical state, it underwent slow changing to crystalline state 24 hours after the full DMSO evaporation (Figure 5.19).

The optical micrographs of all FLUF printed quantities on LE15 slide are shown in Figure 5.20. The evaporation of DMSO required 25, 53, 79, and 130 minutes for 13, 66, 132, and 330 ng droplets respectively (Figure 5.20).

Finally, the microscopic investigation of the MEF droplets on LE15 slide is shown in Figure 5.21, it shows that MEF exhibits the same behaviour as CBZ and FLUF. Compared with the MEF droplets on SAMF, the MEF droplets took longer time to remove the DMSO as they required 16, 44, 66, and 112 minutes for 13, 66, 132, and 330 ng droplets respectively (Figure 5.21).

It can be noticed that CBZ printed quantities underwent different mechanism than FLUF and MEF to obtain the final solid state. The resulting crystalline state of all printed quantities of CBZ required two steps, one for transferring from liquid droplet to solid amorphous state which consumed from 20 to 120 minutes to complete the DMSO evaporation, and long-time step, 24 hours after the full DMSO evaporation, to turn from solid amorphous to crystalline state.

The mechanism of obtaining crystalline state in the all different FLUF and MEF quantities are the same. It consists of two steps, the first one consumed long time for DMSO evaporation and transferring from a liquid droplet to solid amorphous state, it takes from 15 to 130 minutes. While the second step required about 3 to 4 minutes for turning to crystalline state.

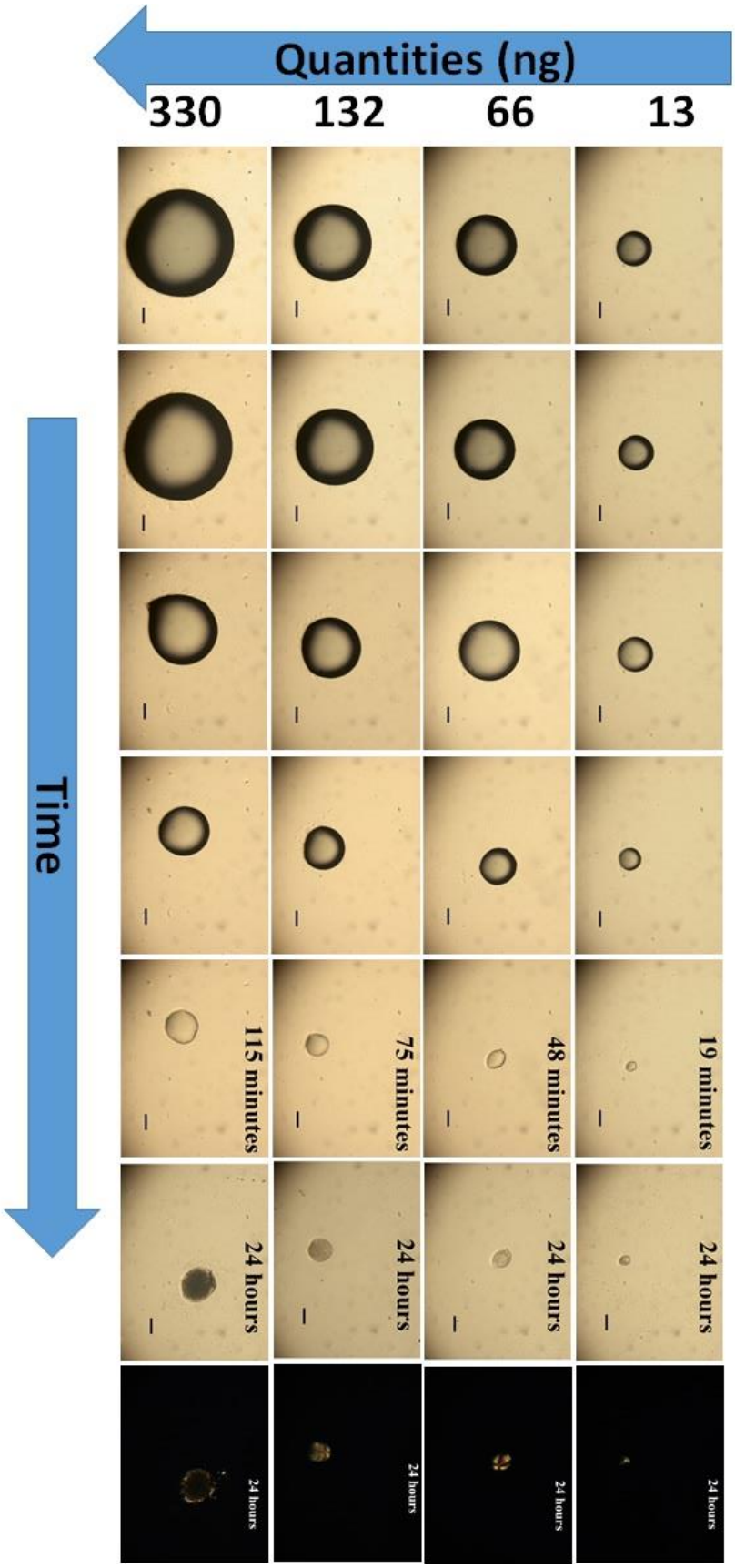

Figure 5.19. Bright-field and cross-polar micrographs of carbamazepine in DMSO on LE15 , scale bar: 0.1mm

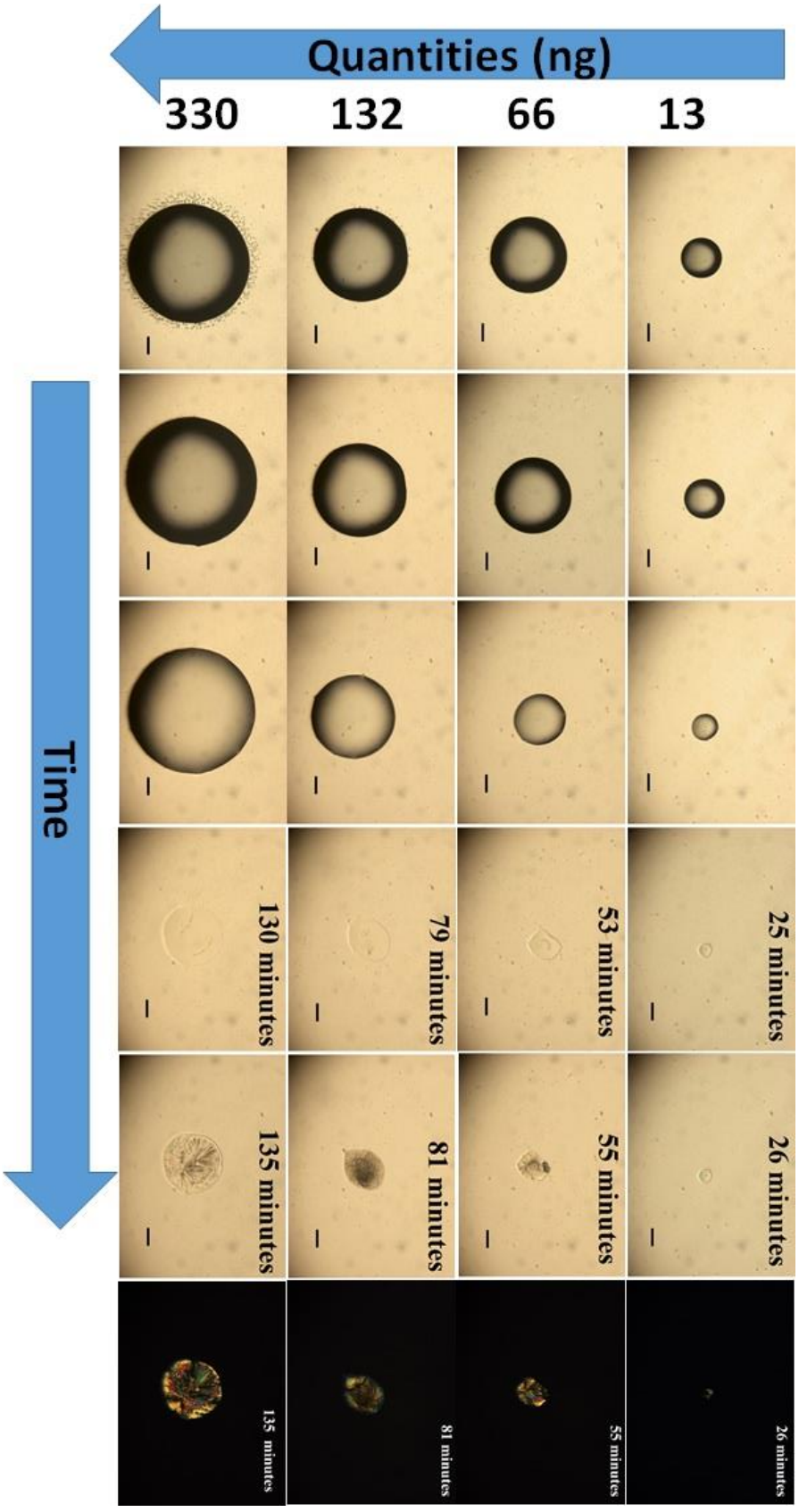

Figure 5.20. Bright-field and cross-polar micrographs of flufenamic acid in DMSO on LE15 , scale bar: 0.1mm

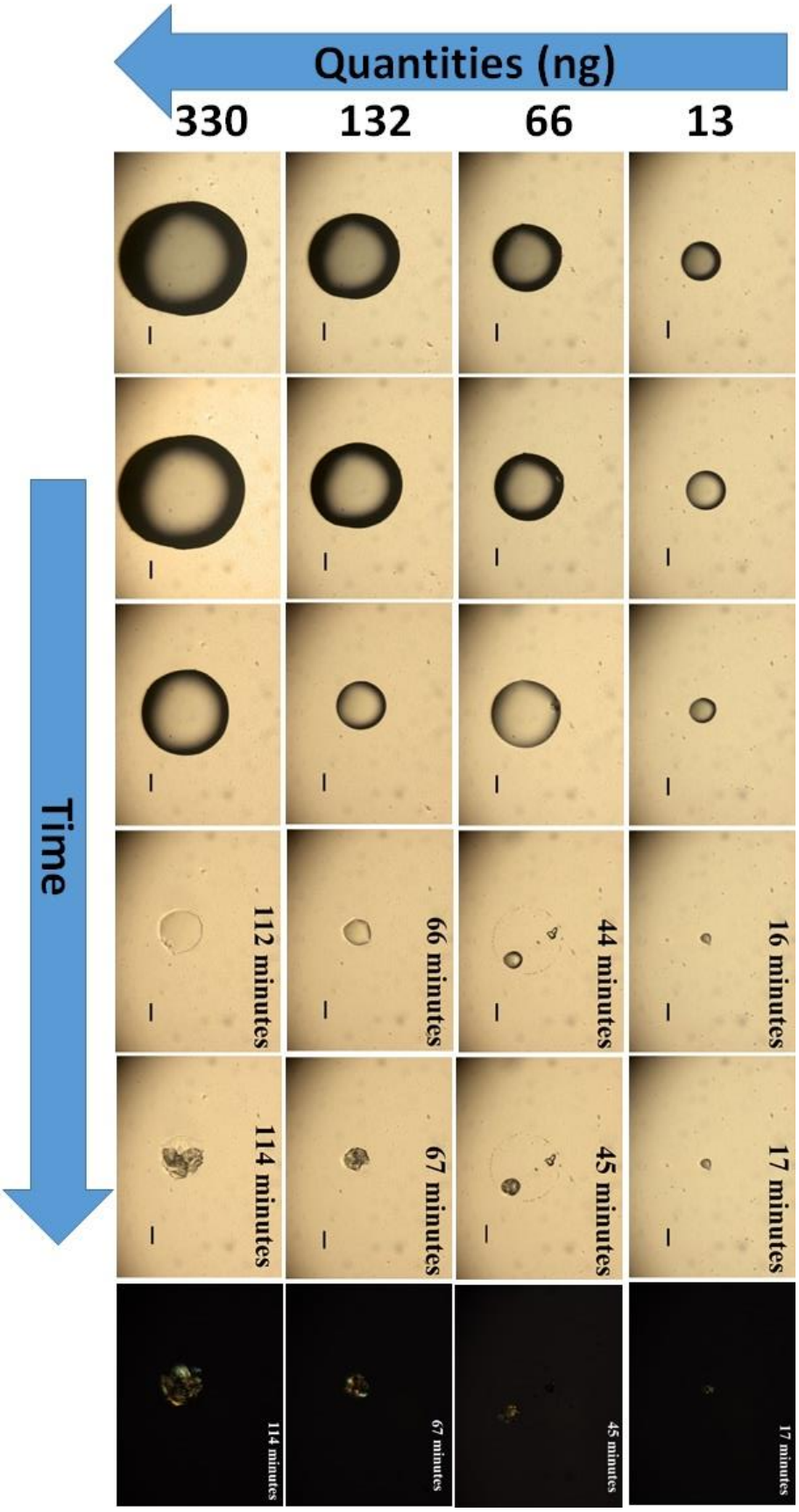

Figure 5.21. Bright-field and cross-polar micrographs of mefenamic acid in DMSO on LE15 , scale bar: 0.1mm

The evaporation process for CBZ, FLUF, and MEF can be attributed to the hydrophobic nature of the LE15 slide, which retards the spreading of the droplets over the substrate, and then causes the droplet surface to become thick. This, in turn, requires a long time to evaporate the solvent [185]. Meanwhile, the evaporation process for these drugs droplets was faster on SAMF because it is less hydrophobic than LE15, which makes the spreading of the droplet easy, producing at the same time a thin droplet wall with high surface area (Figure 5.14), which in turn can be in direct contact with air, which enhances the evaporation of DMSO [185].

5.4.4. Raman investigation of carbamazepine, mefenamic acid, and flufenamic acid on different substrates

5.4.4.1. Raman identification of carbamazepine on SAMF

Figure 5.22 Figure 5.23 show the phonon and molecular region spectra for the CBZ (as received) that was previously identified as polymorph III [123] and polymorph I which was prepared and previously identified [126] in addition to the spectra of the different printed spots of CBZ on SAMF.

It is evident from the above mentioned figures that there are many distinct differences between the two reference spectra, polymorph III and I, of CBZ.

In low wavenumber (phonon) region between 40 cm^{-1} and 400 cm^{-1}, dramatic differences can be identified between the two references spectra of CBZ (Figure 5.22). CBZ (I) exhibits two distinct peaks at 52 cm^{-1} and 110 cm^{-1}, and there is a shoulder at 125 cm^{-1} on the 110 cm^{-1} peak. Also, two broad peaks at (60-64) cm^{-1} and (160-180) cm^{-1} areas are characterised.

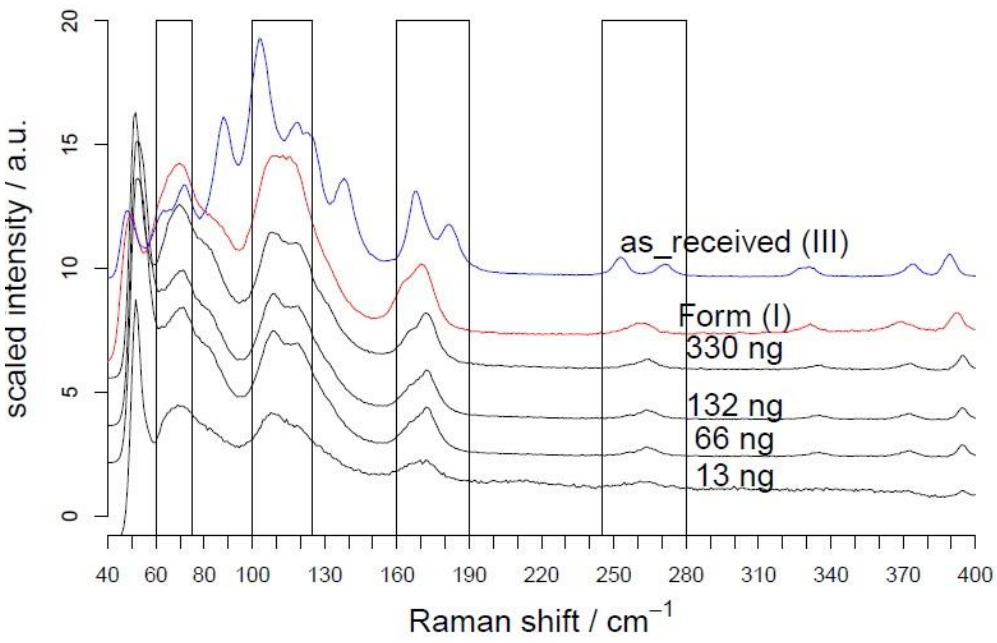

Figure 5.22. Raman spectra in phonon region for different printed quantities of CBZ on SAMF ,with reference spectra of CBZ (as received) (blue) and CBZ (form I) (red).y-axis offsets were employed for presenting the differences between panels. The entire bars represent the differences of the Raman spectra of the printed CBZ at these selected regions

In contrast, CBZ (III) exhibits well-identified Raman peaks at the same studied region 40 cm^{-1} to 200 cm^{-1} [123]. CBZ (III) shows a short distinct peak at 41cm^{-1}, a broad peak at 72 cm^{-1} with a shoulder at 62 cm^{-1}, two distinct peaks between 80 cm^{-1} and 110 cm^{-1}, a broad peak at 120 cm^{-1} with a weak shoulder at 125 cm^{-1}, and a distinct peak at ~ 138 cm^{-1}.

Furthermore, CBZ (III) can be distinguished by the appearance of two peaks at the region between 160 cm^{-1} and 170 cm^{-1}, while only one broad peak can be found in CBZ (I) (Figure 5.22).

Another marked difference between the reference spectra of CBZ is identified between 250 cm^{-1} and 270 cm^{-1}. A low-intensity broad peak in CBZ (I) spectrum can be seen, while two distinct peaks can be seen in CBZ (III). By comparing the spectra of the printed dots of CBZ on SAMF with the reference spectra of CBZ (I and III) and literature [123], It can be found that all the printed quantities of CBZ exhibit polymorph I.

In the high wavenumber (molecular) region between 400 cm^{-1} and 1800 cm^{-1}, three marked differences can be recognised to identify the CBZ reference spectra (Figure 5.23).

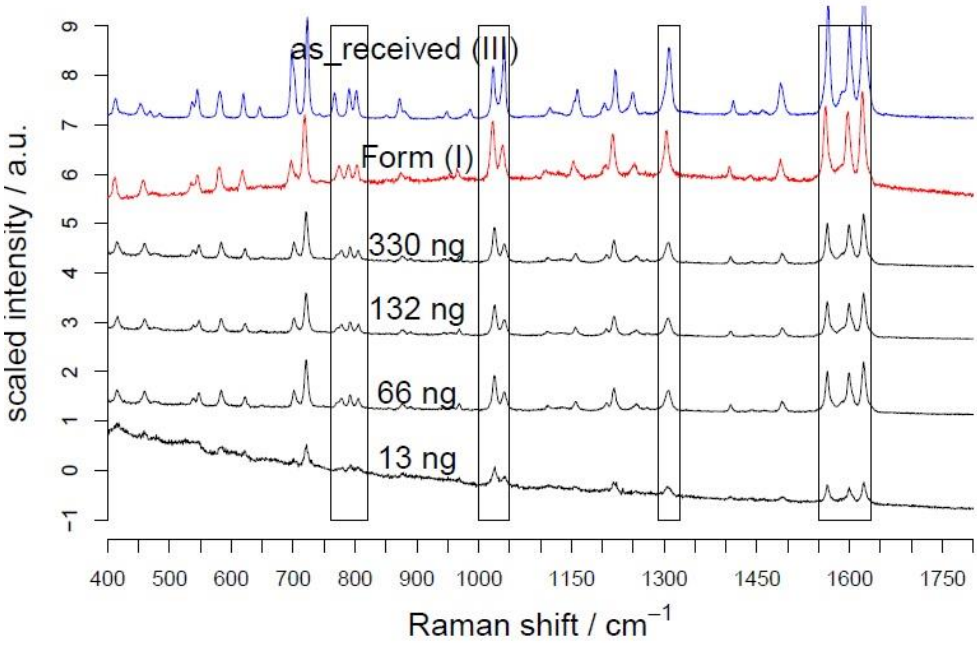

Figure 5.23. Raman spectra in molecular region for different printed quantities of CBZ on SAMF , with reference spectra of CBZ (as received) (blue) and CBZ (form I) (red).y-axis offsets were employed for presenting the differences between panels. The entire bars represent the differences of the Raman spectra of the printed CBZ at these selected regions

O'Brien *et al* [137] reported the isothermal conversion of CBZ (III) to (I) at (1000-1050) cm^{-1} zone, they could recognise CBZ polymorphs by monitoring the changes in intensities of the two sharp peaks at 1025 cm^{-1} and 1040 cm^{-1}, which were assigned to two C-H bending modes [137]. The differences in the heights of the peaks can be used to differentiate the CBZ polymorphs (I and III). Furthermore, a sharp single peak, which was assigned to C-H bending (no-aromatic) mode can be noticed at 1309 cm^{-1} in CBZ(III) and 1305 cm^{-1} in CBZ (I) [137, 138]. It can also be seen that when shifting the three sharp peaks at the (1550-1625) cm^{-1} zone, CBZ (III) exhibits high intensity peaks at (1567-1624) cm^{-1} zone. In the CBZ (I) spectrum, however, these peaks have shifted back to the (1562-1622) cm^{-1} zone (Figure 5.23). The change in peaks' positions provides clear recognition between CBZ polymorphs (I and III) [138]. It can be noticed that all the printed quantities of CBZ exhibited spectra close in features to polymorph I.

5.4.4.2. Raman identification of flufenamic acid on SAMF

Figure 5.24 Figure 5.25 show the phonon and molecular region spectra for the FLUF (as received), which was previously identified as polymorph I and polymorph III which was prepared and previously identified [127] in addition to the spectra of the different printed spots of CBZ on SAMF.

Polymorph I and III of FLUF exhibit different Raman spectra in the phonon region due to lattice vibrational modes, which make the identification of crystalline and amorphous materials easy (Figure 5.24). Two broad peaks at 62 and 78 cm^{-1} can be noticed in FLUF (I) spectrum, whereas only one distinct clear peak appears around 60 cm^{-1} in FLUF (III).

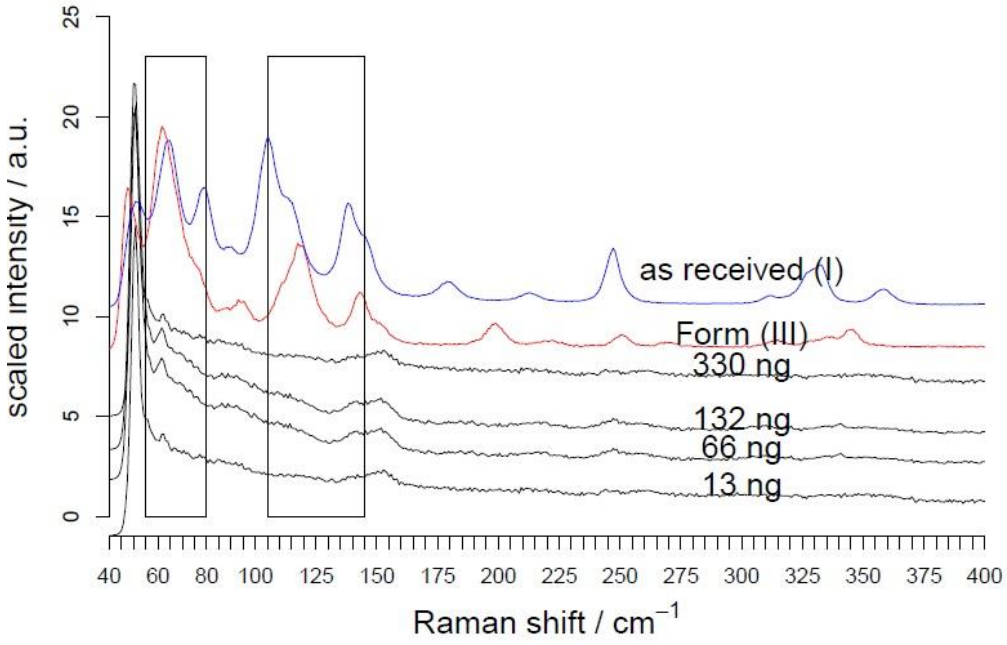

Figure 5.24. Raman spectra in phonon region for different printed quantities of FLUF on SAMF , with reference spectra of FLUF I (as received) (blue) and FLUF (form III) (red).y-axis offsets were employed for presenting the differences between panels. The entire bars represent the differences of the Raman spectra of the printed FLUF at these selected regions

FLUF (I) can be distinguished easily due to appearance of two broad peaks: 105 cm^{-1} with a weak shoulder at 113 cm^{-1} and at 138 cm^{-1} with a weak shoulder at 145 cm^{-1}. In FLUF (III), however, they appear at 118 cm^{-1} and 142 cm^{-1} respectively (Figure 5.24). The change in the peaks' positions provides good differentiation between FLUF polymorphs [112].

In the molecular region, many distinguished peaks between the two reference spectra of FLUF can be seen (Figure 5.25), FLUF (I) shows two small broad

peaks at ~ 420 cm^{-1} and 450 cm^{-1}, while only one distinct peak at 440 cm^{-1} with a broad shoulder at 450 cm^{-1} can be recognised in FLUF (III).

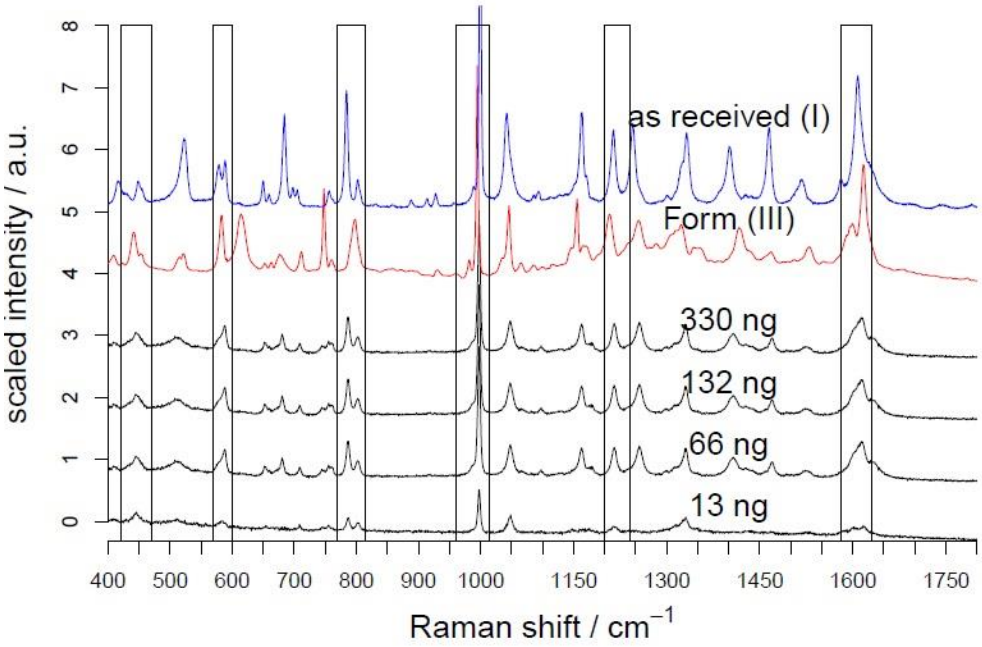

Figure 5.25. Raman spectra in molecular region for different printed quantities of FLUF on SAMF , with reference spectra of FLUF I (as received) (blue) and FLUF (form III) (red).y-axis offsets were employed for presenting the differences between panels. The entire bars represent the differences of the Raman spectra of the printed FLUF at these selected regions

Another marked difference can be noticed between the FLUF reference spectra. Only one sharp peak appears in FLUF (III) at ~ 800 cm^{-1}, while two distinct peaks appear between 780 cm^{-1} and 805 cm^{-1} in FLUF (I). A slightly shifting back can be observed at 1004(995) cm^{-1} and 1220(1210) cm^{-1} for polymorph I (and III) respectively (Figure 5.25). These apparent differences in FLUF I and III spectra can be used as references with literature to compare with the Raman spectra of the resulting spots of FLUF on SAMF.

As shown in Figure 5.24 and Figure 5.25, all the spots of the printed quantities of FLUF exhibit the same spectra as the FLUF (III) spectrum [96] except two peaks at ~ 590 cm^{-1} and 1620 cm^{-1}, which are totally different to the peaks on FLUF I and III. These two peaks were characterised by Matzger and his co-workers when they described and prepared all the possible polymorphs of FLUF (especially FLUF has eight polymorphs [127]), and identified them using Raman spectroscopy [101]. They found that these characterised peaks (at ~ 590 cm^{-1} and 1620 cm^{-1}) were closer in features to FLUF (VI) which was prepared as a

result of thermal treatment for polymorph IV which in turn underwent a solid-solid transformation at ~ -130 ºC .This indicates that polymorph (VI) in addition to polymorphs I and III might appear during the evaporation of DMSO from the FLUF printed droplets.

5.4.4.3. Raman identification of mefenamic acid on SAMF

The Raman spectra in phonon and molecular regions of MEF (as received), which was previously identified as polymorph I and polymorph II, which was prepared and previously identified [123, 135] in addition to the spectra of the different printed spots of MEF on SAMF are shown in Figure 5.26 Figure 5.27. It is evident from Figure 5.26, that the recognition of the two MEF reference spectra is easy. Because of the overlapping with the gold peaks of the modified gold-coated slide with the peaks of MEF in low wavenumber region, however, it is difficult to recognise the peak at ~ 33 cm^{-1}. It can be seen that all the printed spots of MEF exhibit the same peaks as the MEF (I) dots after comparing with the reference spectra and literature [123].

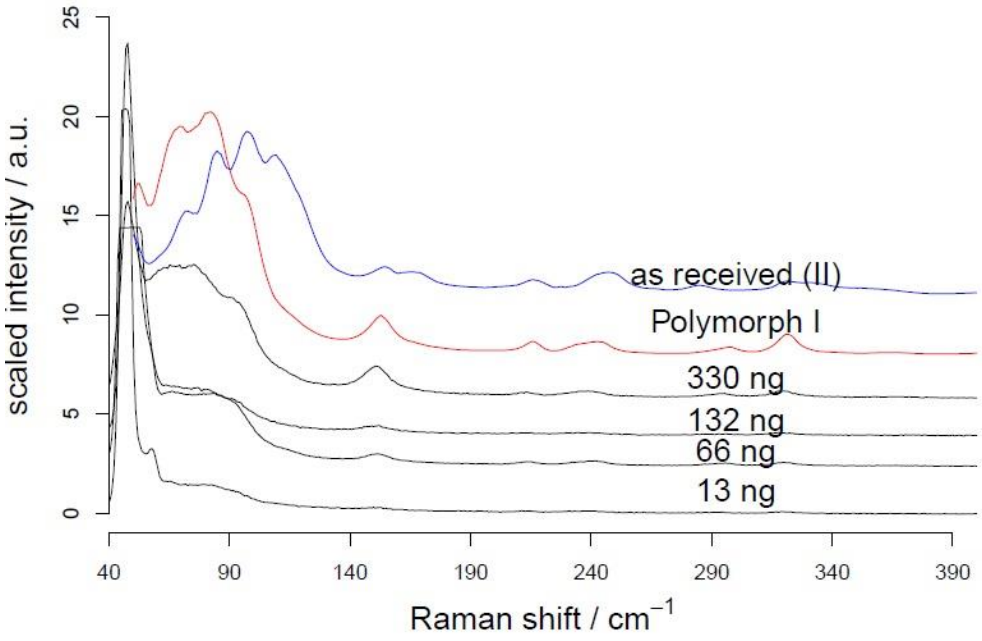

Figure 5.26. Raman spectra in phonon region for different printed quantities of MEF on SAMF , with reference spectra of MEF II (as received) (blue) and MEF (polymorph I) (red).y-axis offsets were employed for presenting the differences between panels

Another distinguishable difference can be seen at ~ 48 cm^{-1} in the MEF (I) spectrum that does not appear in MEF (II). A single sharp peak at ~ 152 cm^{-1} appears in MEF (I), while two weak broad peaks appear between 150 cm^{-1} and 170 cm^{-1} in MEF (II). Three broad peaks can be found between 80 cm^{-1} and 110

cm^{-1} in MEF (I), while the MEF (II) spectrum exhibits several broad scattering peaks at (40-80) cm^{-1} region (Figure 5.26). Changing in peaks' positions can be used to recognise the different MEF polymorphs [123]. It can be seen that all the printed spots of MEF on SAMF exhibit the same peaks as MEF (I) does.

In molecular region, the change in peaks' intensities and shapes can be used to recognise the two reference spectra [137]. Two sharp peaks from 750 cm^{-1} to 810 cm^{-1} region, and single peak at around 575 cm^{-1}, can be noticed in different intensities in both the MEF I and II spectra (Figure 5.27). Furthermore, one sharp peak at 1245 $cm^{-1}$with broad shoulder at 1240 cm^{-1} appears in MEF (II), while the same peak appears in opposite shape at 1240 cm^{-1} with broad shoulder at 1245 cm^{-1}.

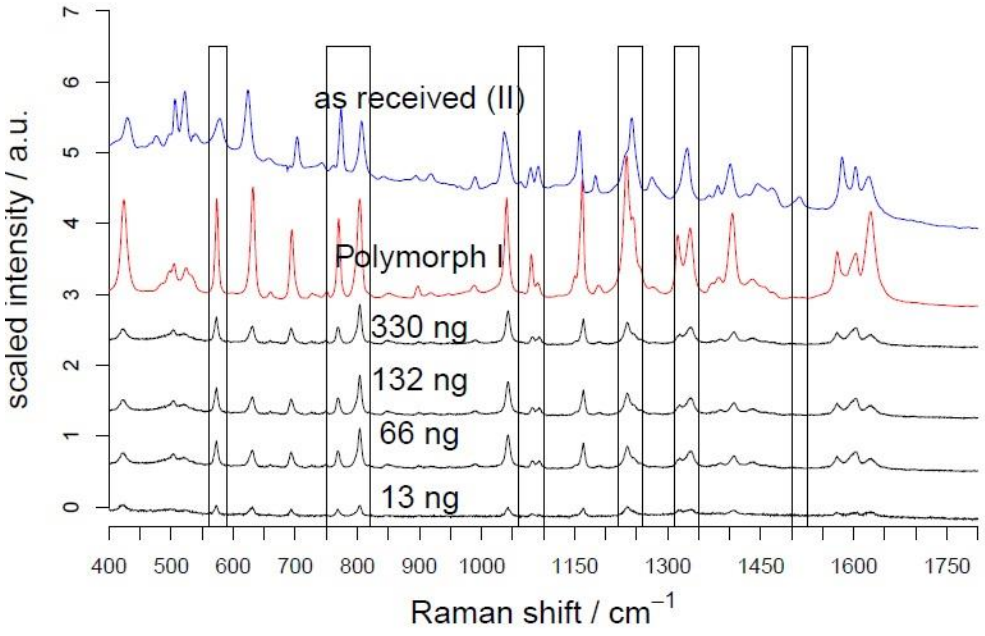

Figure 5.27. Raman spectra in molecular region for different printed quantities of MEF on SAMF , with reference spectra of MEF II (as received) (blue) and MEF (polymorph I) (red).y-axis offsets were employed for presenting the differences between panels. The entire bars represent the differences of the Raman spectra of the printed MEF at these selected regions

Three intense peaks between 1550 cm^{-1} and 1700 cm^{-1}, attributed to the effect of N-H bending mode and the stretching of aromatic ring, can also be easily identified (Figure 5.27) [135]. All these marked differences can make the characterisation of MEF polymorphs easy.

The MEF (II) spectrum shows two distinct peaks between 1330 cm^{-1} and 1340 cm^{-1} region which are attributed to the dimeric structure of MEF (II) [135], whereas only a single sharp peak can be clearly seen in MEF (I) at ~ 1345 cm^{-1} (Figure 5.27).

Finally, a single broad peak can be observed at around 1515 cm^{-1} in MEF (I), while it does not exist in MEF (II). The spectra of the different printed quantities (13 ng,66 ng,132 ng, and 330 ng) of MEF do not exhibit this peak, which indicates that all of these printed spots exhibit polymorph I [135].

5.4.4.4. Raman identification of carbamazepine on LE15

Figure 5.28 Figure 5.29 show the phonon and molecular region spectra for the CBZ (as received) which was previously identified as polymorph III [123] and polymorph I which was prepared and previously identified [126] in addition to the spectra of the different printed spots of CBZ on LE15 slide.

In the phonon region, the spectra of the printed spots exhibit the same features as CBZ (I) does (Figure 5.28).

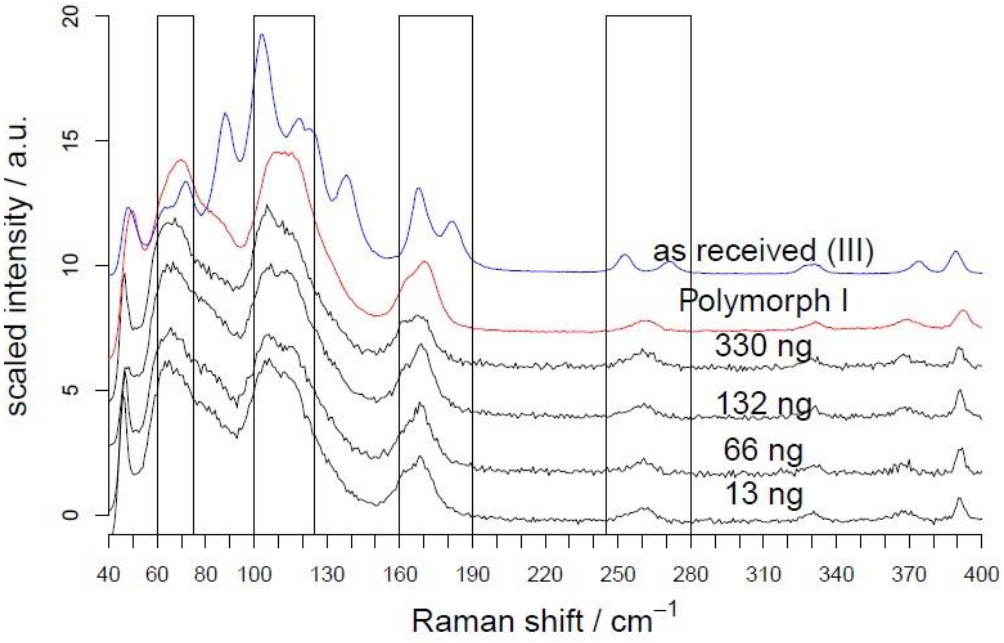

Figure 5.28. Raman spectra in phonon region for different printed quantities of CBZ on LE15 , with reference spectra of CBZ III (as received) (blue) and CBZ (polymorph I) (red).y-axis offsets were employed for presenting the differences between panels. The entire bars represent the differences of the Raman spectra of the printed CBZ at these selected regions

It can be noticed that all the printed quantities of CBZ on LE15 slide exhibited the same spectral features, in both phonon and molecular region, of their counterparts printed on SAMF. Differentiation between CBZ polymorphs at low-wavenumber region was performed by Roy *et al*. [123]. They could identify the characteristic peaks that can be considered as fingerprint for CBZ and nine other APIs. After comparing with the reference spectra and the data in literature, it is evident from Figure 5.28 and Figure 5.29 that all the spectra show only one polymorph for CBZ which is I.

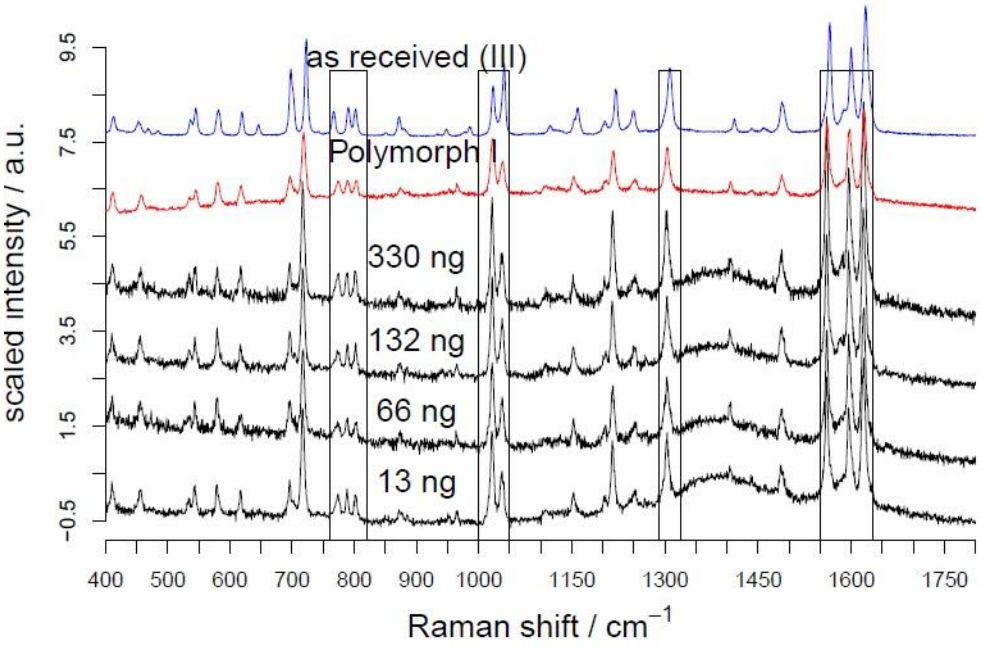

Figure 5.29. Raman spectra in molecular region for different printed quantities of CBZ on LE15 , with reference spectra of CBZ III (as received) (blue) and CBZ (polymorph I) (red).y-axis offsets were employed for presenting the differences between panels. The entire bars represent the differences of the Raman spectra of the printed CBZ at these selected regions

5.4.4.5. Raman identification of Flufenamic acid on LE15

Figure 5.30 Figure 5.31 show the phonon and molecular region spectra for the FLUF powder which was previously identified as polymorph I [127] and polymorph III which was prepared and previously identified [96] in addition to the spectra of the different printed spots of FLUF on LE15 slide.

Although the small diameter of the printed droplets allows the molecules to be constructed nucleation and form a condense spot, the laser beam that passes through the spot could not produce a clear scattering peak in phonon region due to the effect of fluorescence resulting from the substrate itself.

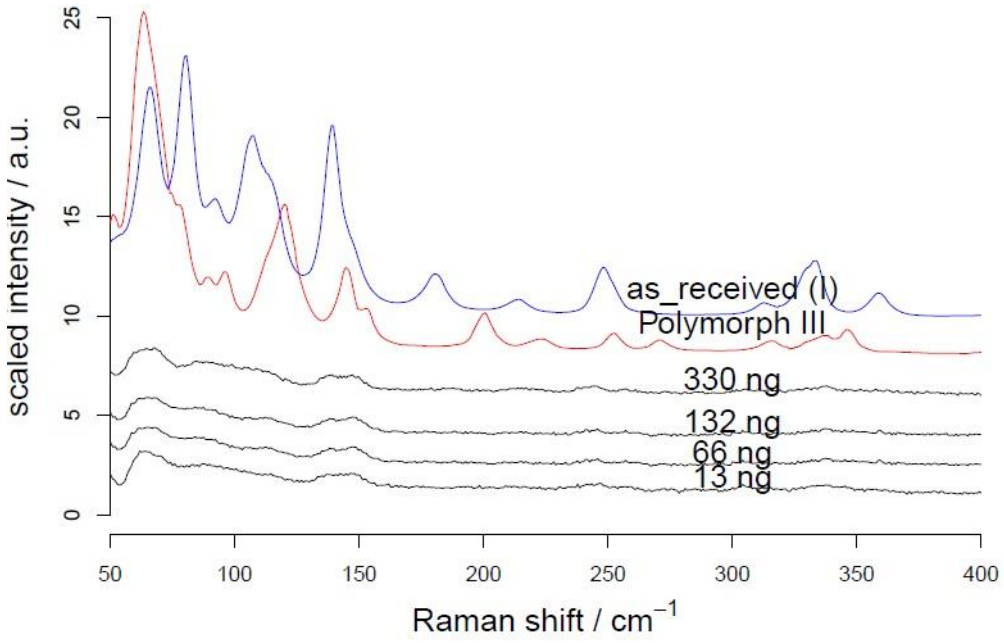

Figure 5.30. Raman spectra in phonon region for different printed quantities of FLUF on LE15 , with reference spectra of FLUF I (as received) (blue) and FLUF (III) (red)

In the high wavenumber region, the Raman spectra of all quantities of FLUF spots show characteristic features of FLUF (I) [223] (Figure 5.31). The main noticeable difference was from 780 cm^{-1} to 810 cm^{-1} and ~ 590 cm^{-1}, there were three distinct peaks that could be seen in the spectra of all the printed spots, which do not appear in FLUF (III) [223].

It can be seen that the features of the spectra of all the printed quantities of FLUF close to polymorph III. These resulting spectra were compared with the literature presented by Matzger *et al*. [101] who prepared and identified all the possible FLUF polymorphs by Raman spectroscopy.

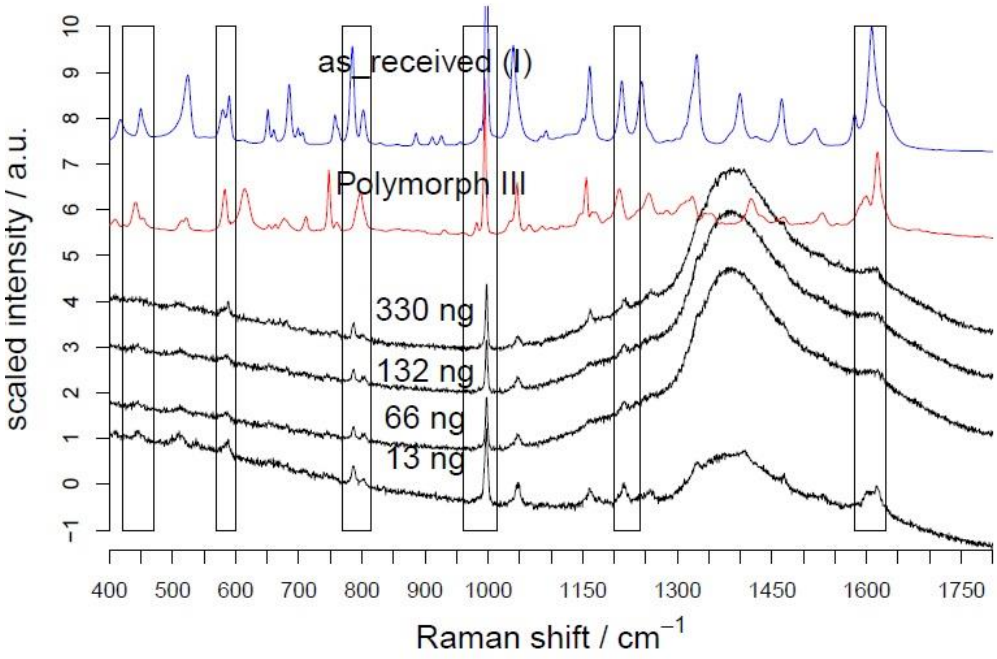

Figure 5.31. Raman spectra in molecular region for different printed quantities of FLUF on LE15 , with reference spectra of FLUF I (as received) (blue) and FLUF (polymorph III) (red).y-axis offsets were employed for presenting the differences between panels. The entire bars represent the differences of the Raman spectra of the printed FLUF at these selected regions

5.4.4.6. Raman identification of mefenamic acid on LE15

Figure 5.32 Figure 5.33 show the phonon and molecular region spectra for the MEF on LE15 slide. The printed spots of MEF on LE15 exhibit distinct peaks with high intensities in molecular region.as described in Figure 5.14, the printed droplets of the MEF on LE15 slide produced a small diameter spots with high thickness. Because the thickness has been reported as one of most important factors that affect the absorption of the Raman scattered photons by the sample itself, which can be called self-absorption [224], a study has been published by Wang *et al* [225], it has been found that Raman signal intensity can be affected by decreasing or increasing the sample particle size and/or thickness [225].

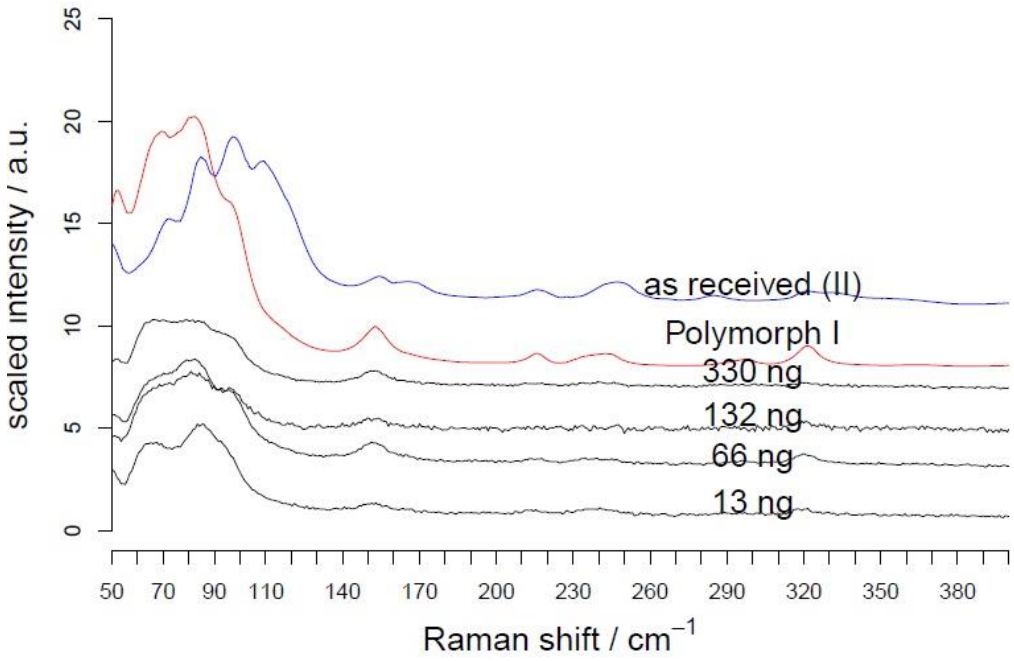

Figure 5.32. Raman spectra in phonon region for different printed quantities of MEF on LE15 ,with reference spectra of MEF II (as received) (blue) and MEF (polymorph I) (red).y-axis offsets were employed for presenting the differences between panels

It can be noticed there is a kind of fluorescence effect due to the nature of the substrate. The differences in the spectra of MEF I and II was illustrated with details before (Figure 5.32). It is evident that all the printed quantities of MEF on LE15 exhibit polymorph I after comparing with the reference spectra and literature. Identification of MEF polymorphs by Raman spectroscopy in phonon region was studied by Roy et.al [123].

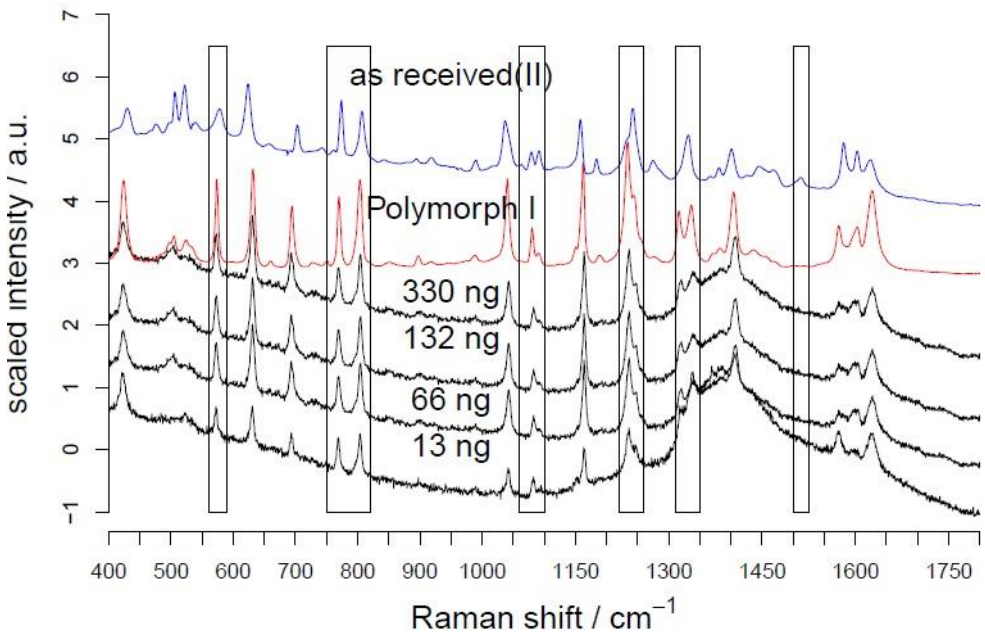

Figure 5.33. Raman spectra in molecular region for different printed quantities of MEF on LE15 ,with reference spectra of MEF II (as received) (blue) and MEF (polymorph I) (red).y-axis offsets were employed for presenting the differences between panels. The entire bars represent the differences of the Raman spectra of the printed MEF at these selected regions

It can be noticed that there is a strong broad peak between 1300 cm^{-1} and 1500 cm^{-1} in all the spectra of CBZ, FLUF, and MEF spots on LE15 slides, this is attributed to the normal absorbance of the silica of glass slide as it considered an amorphous solid having no periodic re-arrangements. This broad peak was found also by Cochain *et al*. [226], when they presented a simple method to estimate the Fe II/Fe III ratio in borosilicate glasses.

In addition, two weak broad peaks can be observed at ~ 490 cm^{-1} and 605 cm^{-1} which interfere with the drugs spectra. These weak peaks were characterised by Hemley *et al*. [227], when they studied the Raman spectra behaviour of SiO_2 glass at very high pressure.

Also, it should be noticed that the Raman spectra of the different printed quantities of PAR/DMSO on both SAMF and LE15 substrates were presented in (Appendix C).

5.5. Conclusions

The aim of this chapter was to investigate the role of surface modification by fluorinated compounds on the nanogram solid form screening of the APIs .The work presented earlier described the effect of the chemical modifications of the substrates that used in the APIs polymorphic screening. Chemical modifications of the gold-coated slide with thiols and producing SAMs to use them as deposition substrates (in Chapter four) was the basic idea which encourages to investigate the effect of the surface hydrophobicity on the appearance of different states or polymorphs.

This study has shown, for the first time, the viability of obtaining nanogram solid form screening for some APIs deposited on two different types of fluorinated substrates, one with chemical modification of the gold-coated slide with fluorinated thiol to create fluorinated SAM, and the second with roughening the glass slide with a fluorinated hydrocarbon by dipping coating method.

In this chapter, CBZ, FLUF, and MEF were used as models for rapid solid form screening at nano-scales. This was performed using piezo inkjet printing technique. APIs were deposited on two types of fluorinated substrates to investigate the behaviour of these drugs droplets.

The printing of CBZ, FLUF, and MEF was performed successfully on the new substrates as regular droplet shapes were formed in a consistent style which made the optical observation easy, and the printed droplets showed different evaporation times depending on the roughness of the substrate. The printed drugs on SAMF evaporated faster than those on LE15 due to the difference in hydrophobicity and wettability.

Optical microscopic observations for these printed droplets confirmed that the amorphous state of all the spots was temporary, and they started crystallising once the evaporation of the DMSO was complete. The optical observations revealed two types of mechanisms in order to obtain crystal forms. The first one consists of two long-time steps which was observed clearly in CBZ droplets. They required between 15 to 130 minutes (depends on the printed quantity) to turn to the solid amorphous state, and followed by 24 hours to change to crystalline state. While the behaviour of FLUF and MEF droplets showed differences in the time of these two steps, the showed that the first step which

include turning the droplet to solid amorphous state taking long time (from 5 to 130 minutes) over the second step which consumed only 2 to 3 minutes to obtain crystal form.

The resulting crystal modifications were placed under a Raman microscope to investigate whether new polymorphs appear after printing on the fluorinated substrates. It can be concluded that all the printed drugs exhibit the same polymorphs on both the substrates CBZ (I), and MEF (I) except FLUF which exhibited FLUF (VI) in addition to FLUF (III). That is can be attributed to the strong intermolecular interactions that happen between the SAMs substrate and the drug molecule leading to control the arrangement of the drug molecule to produce a different polymorph [228].

The Raman spectra of the selected APIs on SAMF show clear and good intense peaks that can easily be used to identify the differences in polymorphism, especially in phonon region 40 cm^{-1} - 400 cm^{-1}. It can be noticed that there is an effect of broad band in the Raman spectra of APIs on LE15 due to an interaction between the SiO_2 in glass and the spot spectrum.

Finally, it can be concluded that although the high WCA of the LE15 slide and the simplicity of observing the resulting droplets of it, SAMF can be considered better choice for fluorinated substrates for solid form screening as it can minimize the time of droplet evaporation and for its ability to show clear and distinct Raman peaks at both phonon and molecular region which makes recognition of the solid forms easy. The identification of peaks in the phonon region can easily be done, however.

Chapter six: Conclusions and future work

6.1. Conclusions

This thesis has investigated, for the first time, the viability of using 2D inkjet printing technique in fabricating nano-arrays with pico-litres of small-molecule pharmaceuticals in the context of pre-formulation and solid form screening, and the effect of modifying the used substrates underneath the deposited samples.

Chapter Three studied the development of a novel approach to the solid form screening of APIs, with the aim of miniaturising the used quantities on the nanogram scale by means of a 2D inkjet printing technique to produce these trace amounts.

In Chapter Three, the viability of using a 2D inkjet printing technique for miniaturising, screening, and investigating the APIs' stability before introducing into any formulation process was studied. A gold-coated slide was selected to be a deposition substrate due to its unique properties. The variation in the printed quantities leads to the appearance of new forms rather than the starting forms. PAR, for example, shows an amorphous state at quantities below 250 ng, while it exhibits crystal form II at quantities higher than 250 ng. MEF also shows two different crystal modifications as a result of the variation of the printed quantities: MEF II with low quantities (less than 250 ng) and polymorph I with high amounts (more than 250 ng). It can be achieved an API polymorph screening at a six-order magnification less than the reported quantities in Bradley *et al.*'s study (6.5 mg) [80] and Kazarian *et al.*'s study (0.1 µg -1 µg) [79]. This can offer, from an economic point of view, use of lower material quantities and human efforts.

The effect of the time factor was also studied. It could be noticed that the conversion of PAR/DW spots from a solid amorphous state to a crystalline state required more than 36 hours (for amounts more than 250 ng), while two and four hours were enough to recrystallize all the printed dots of MEF and CBZ respectively.

Raman spectroscopy was successfully used to differentiate between the resulting polymorphs, especially in the low wavenumber region (40 cm^{-1} - 400 cm^{-1}), which can be considered a fingerprint for any polymorph due to the intermolecular vibrational effects.

Using soluble substrates (polymers) for polymorphic screening of APIs, a previous study [80] introduced a strong thought that the polymer may be re-dissolved into the drug-containing droplet to achieve total evaporation. This belief encourages using solid and stable substrates to avoid any chance of re-dissolving the substrates with the droplet content and to ensure an API polymorphic screening.

In Chapter Four, a gold-coated slide was modified, taking advantage of its ability to undergo further chemical modifications with two types of thiols to create new SAMs. The new prepared SAMs were successfully used as substrates in nanogram polymorph screening of APIs after testing their stability against prolonged exposure to solvents. The physical state of the printed quantities of APIs on SAMs and even a plain gold substrate were evaluated by means of both light optical microscopy and Raman spectroscopy. Printing of different amounts of PAR/DMSO onto the newly prepared SAMs exhibits an amorphous state on SAM-CH_3 and polymorph II on SAM-CH_2OH.

A specific quantity of MEF (135 ng) was chosen to be a model for investigating the crystal habits on the newly prepared SAMs and the gold-coated slide. It could be noticed that MEF droplets show different crystal modifications on the used substrates. The Raman spectroscopy was used to confirm that differentiation. MEF dots that were printed onto SAM-CH_3 and SAM-CH_2OH exhibited polymorph II, while the MEF spots on the gold-coated slide exhibited polymorph I. This indicates the important role of the substrate chemistry in the appearance of different polymorphs.

In Chapter Five, the chemical modifications of the used substrates with fluorinated compounds was taken into consideration when applying the APIs' solid form screening. The chemical modifications of the gold-coated slide with thiols and producing SAMs to use them as deposition substrates (in Chapter Four) was the basic idea that encouraged investigation of the effect of the surface modification on the appearance of different states or polymorphs. Further, it was an attempt to improve the signal of the acquired Raman spectra of the printed spots using high water repellent surfaces, based on a previous study conducted by Wang *et al.* [225].

In order to achieve the above, two types of fluorinated compounds were used: functionalised *n*-alkane thiols with a CF3-terminated group (11-Mercaptoundecyl trifluoroacetate; SAMF), and Flutec fluid (perfluoroperhydrophenanthrene oligomer) or LE15, to create high-water repellent substrates for nanogram polymorph screening of APIs.

Fluorinated substrates were subjected to preliminary tests, such as AFM and WCA measurements, to investigate the topography and the roughness before printing on them. Due to the difference in hydrophobicity and wettability, the evaporation time of the printed drugs on SAMF was faster than those on the LE15 slide.

Raman spectra of the selected APIs printed on SAMF show clear and good intense peaks, which enable easy differentiation between polymorphs. Although the LE15 slide exhibits higher WCA than SAMF, the printed spots show noisy Raman spectra due to the interactions between the glass material and the spot spectrum, which gives a fluorescent background, although the spots spectra show sharp and high intense peaks, especially in the molecular region (400 cm^{-1} -1800 cm^{-1}). However, the identification of peaks in the phonon region can easily be achieved.

The limitations that can be involved in this screening approach are the range of adoptable solvents, the cost of nozzle and maintenance, and the quality of surfaces to be used and the automation for analysing the printed samples.

6.2. Future work

Many different adaptations, tests, and experiments have been left for the future due to lack of time. There are some ideas that I would have liked to try during the working on the nano-quantities polymorph screening of APIs. In chapter three, for example, it could be interesting to study the effect of the humidity and the temperature during and after printing of APIs and investigate the possibility of appearance of different polymorphs.

To adapt the 2D inkjet printing technique in a largely experimental pharmaceutical field, further optimisations should be done. For any new synthesised candidates, it can be speculated that the current scope it is not to produce a product but to screen or pre-screen APIs and excipients for their stability, polymorph tendency and so on. Therefore, it is important to subject the

APIs to optimisation processes in order to confirm the optimal form for the subsequent formulation. These optimisations need to extend the range of APIs used with different BCS classes, use wide range of solvents as they have an important effect of appearing of new polymorphs. Also, these processes include choosing the suitable concentration which not causing direct crystallisation due to saturation or supersaturation.

Viscosity of the prepared pharmaceutical solution should be monitored, thus, it is important to study the effect of humectants on the properties of the prepared pharmaceutical solution.

The effect of the humidity should be studied, either during the printing process or after keeping the printed slides inside a close and controllable humidity system, to investigate the possibility of appearing different polymorphs.

For supporting and assessing the resulting Raman data, it is advisable to use another spectroscopic technique such as XRPD, as it uses in characterisation of the polymorphs, to give further evidence about formation and/or appearing different polymorphs as well as comparing the findings (Raman and XRPD data) with most certified and documented references like in Cambridge Structural database

Furthermore, using two types of thiols with different functional group to create SAMs as substrates for solid form screening of APIs in chapter four was studied from the structural point of view, while the study of the effect of the acidity and the basicity of these compounds has not dealt with so far, this encourages studying the effect of pH on the appearance of different polymorphs after printing.

Creating of highly-hydrophobic surfaces using fluorinated materials might be hazardous, therefore, it is advisable to find new possible hydrophobization agents such as non fluor-containing silanes.

References

1. Vilegave K, Vidyasagar G, Chandankar P. Preformulation Studies of Pharmaceutical New Drug Molecule & Products: An Overview. American journal of pharmacy and health research. 2013;1(3):1-20.
2. Yadav A, Shete A, Dabke A, Kulkarni P, Sakhare S. Co-crystals: A novel approach to modify physicochemical properties of active pharmaceutical ingredients. Indian journal of pharmaceutical sciences. 2009;71(4):359.
3. Qiu Y, Chen Y, Zhang GG, Liu L, Porter W. Developing solid oral dosage forms: pharmaceutical theory & practice: Academic Press; 2009.
4. Yu L. Amorphous pharmaceutical solids: preparation, characterization and stabilization. Advanced drug delivery reviews. 2001;48(1):27-42.
5. Hilfiker R. Polymorphism: in the pharmaceutical industry: John Wiley & Sons; 2006.
6. Vaidya S. Clathrates—An exploration of the chemistry of caged compounds. Resonance. 2004;9(7):18-31.
7. Peterson ML, Hickey MB, Zaworotko MJ, Almarsson Ö. Expanding the scope of crystal form evaluation in pharmaceutical science. J Pharm Pharm Sci. 2006;9(3):317-26.
8. Shiraki K, Takata N, Takano R, Hayashi Y, Terada K. Dissolution improvement and the mechanism of the improvement from cocrystallization of poorly water-soluble compounds. Pharmaceutical research. 2008;25(11):2581-92.
9. Haleblian J, McCrone W. Pharmaceutical applications of polymorphism. Journal of Pharmaceutical Sciences. 1969;58(8):911-29.
10. Khoshkhoo S, Anwar J. Crystallization of polymorphs: the effect of solvent. Journal of Physics D: Applied Physics. 1993;26(8B):B90.
11. Lee EH, Boerrigter SX, Rumondor AC, Chamarthy SP, Byrn SR. Formation and solid-state characterization of a salt-induced metastable polymorph of flufenamic acid. Crystal Growth and Design. 2008;8(1):91-7.
12. Allegrini P, Vladiskovic C. Polymorphism of Active Pharmaceutical Ingredients The border between a real quality issue and an effective patent tool. Chimica OGGI-Chemistry today. 2013;31(5):30-3.

13. Pirttimäki J, Laine E, Ketolainen J, Paronen P. Effects of grinding and compression on crystal structure of anhydrous caffeine. International journal of pharmaceutics. 1993;95(1):93-9.
14. Di Martino P, Guyot-Hermann A, Conflant P, Drache M, Guyot J. A new pure paracetamol for direct compression: the orthorhombic form. International journal of pharmaceutics. 1996;128(1):1-8.
15. Nichols G, Frampton CS. Physicochemical characterization of the orthorhombic polymorph of paracetamol crystallized from solution. Journal of pharmaceutical sciences. 1998;87(6):684-93.
16. Suihko E, Lehto V-P, Ketolainen J, Laine E, Paronen P. Dynamic solid-state and tableting properties of four theophylline forms. International Journal of pharmaceutics. 2001;217(1):225-36.
17. Byrn SR, Sutton PA, Tobias B, Frye J, Main P. Crystal structure, solid-state NMR spectra, and oxygen reactivity of five crystal forms of prednisolone tert-butylacetate. Journal of the American Chemical Society. 1988;110(5):1609-14.
18. Guo Y, Byrn SR, Zografi G. Physical characteristics and chemical degradation of amorphous quinapril hydrochloride. Journal of pharmaceutical sciences. 2000;89(1):128-43.
19. Savjani KT, Gajjar AK, Savjani JK. Drug solubility: importance and enhancement techniques. ISRN pharmaceutics. 2012;2012.
20. Threlfall TL. Analysis of organic polymorphs. A review. Analyst. 1995;120(10):2435-60.
21. Amidon GL, Lennernäs H, Shah VP, Crison JR. A theoretical basis for a biopharmaceutic drug classification: the correlation of in vitro drug product dissolution and in vivo bioavailability. Pharmaceutical research. 1995;12(3):413-20.
22. Chemburkar SR, Bauer J, Deming K, Spiwek H, Patel K, Morris J, et al. Dealing with the impact of ritonavir polymorphs on the late stages of bulk drug process development. Organic Process Research & Development. 2000;4(5):413-7.
23. Kahela P, Aaltonen R, Lewing E, Anttila M, Kristoffersson E. Pharmacokinetics and dissolution of two crystalline forms of carbamazepine. International Journal of Pharmaceutics. 1983;14(1):103-12.

24. Meyer MC, Straughn AB, Jarvi EJ, Wood GC, Pelsor FR, Shah VP. The bioinequivalence of carbamazepine tablets with a history of clinical failures. Pharmaceutical research. 1992;9(12):1612-6.
25. Thun J, Seyfarth L, Senker J, Dinnebier RE, Breu J. Polymorphism in Benzamide: Solving a 175-Year-Old Riddle. Angewandte Chemie International Edition. 2007;46(35):6729-31.
26. Stahly GP. Diversity in single-and multiple-component crystals. The search for and prevalence of polymorphs and cocrystals. Crystal Growth & Design. 2007;7(6):1007-26.
27. Davey RJ. Crystallization: How come you look so good? Nature. 2004;428(6981):374-5.
28. Dunitz JD. Are crystal structures predictable? Chemical Communications. 2003 (5):545-8.
29. Raw AS, Yu LX. Pharmaceutical solid polymorphism in drug development and regulation. Advanced Drug Delivery Reviews. 2004;56(3):235-6.
30. Datta S, Grant DJ. Crystal structures of drugs: advances in determination, prediction and engineering. Nature Reviews Drug Discovery. 2004;3(1):42-57.
31. Gu CH, Young V, Grant DJ. Polymorph screening: Influence of solvents on the rate of solvent-mediated polymorphic transformation. Journal of pharmaceutical sciences. 2001;90(11):1878-90.
32. Miller J, Collman B, Greene L, Grant D, Blackburn A. Identifying the Stable Polymorph Early in the Drug Discovery-Development Process. Pharmaceutical Development and Technology. 2005;10(2):291-7.
33. Grant DJ. Theory and origin of polymorphism. Drugs and the pharmaceutical sciences. 1999;95:1-33.
34. Newman A. Specialized solid form screening techniques. Org Process Res Dev. 2013;17(3):457-71.
35. Maiwald M. Examining the range of methods available to derive numerous polymorphic forms. Am Pharm Rev. 2006;9(4):95-9.
36. Aaltonen J, Allesø M, Mirza S, Koradia V, Gordon KC, Rantanen J. Solid form screening–a review. European Journal of Pharmaceutics and Biopharmaceutics. 2009;71(1):23-37.

37. Morissette SL, Almarsson Ö, Peterson ML, Remenar JF, Read MJ, Lemmo AV, et al. High-throughput crystallization: polymorphs, salts, co-crystals and solvates of pharmaceutical solids. Advanced drug delivery reviews. 2004;56(3):275-300.
38. Morissette SL, Soukasene S, Levinson D, Cima MJ, Almarsson Ö. Elucidation of crystal form diversity of the HIV protease inhibitor ritonavir by high-throughput crystallization. Proceedings of the National Academy of Sciences. 2003;100(5):2180-4.
39. Park A, Chyall LJ, Dunlap J, Schertz C, Jonaitis D, Stahly BC, et al. New solid-state chemistry technologies to bring better drugs to market: knowledge-based decision making. Expert opinion on drug discovery. 2007;2(1):145-54.
40. McNevin M, Higgins J. Strategies and Methods for Drug Candidate Phase Optimization in Discovery Space. Discovering and Developing Molecules with Optimal Drug-Like Properties: Springer; 2015. p. 209-40.
41. Peterson ML, Morissette SL, McNulty C, Goldsweig A, Shaw P, LeQuesne M, et al. Iterative high-throughput polymorphism studies on acetaminophen and an experimentally derived structure for form III. Journal of the American Chemical Society. 2002;124(37):10958-9.
42. Dai W-G, Pollock-Dove C, Dong LC, Li S. Advanced screening assays to rapidly identify solubility-enhancing formulations: high-throughput, miniaturization and automation. Advanced drug delivery reviews. 2008;60(6):657-72.
43. Kojima T, Tsutsumi S, Yamamoto K, Ikeda Y, Moriwaki T. High-throughput cocrystal slurry screening by use of in situ Raman microscopy and multi-well plate. International journal of pharmaceutics. 2010;399(1):52-9.
44. Manin AN, Voronin AP, Drozd KV, Manin NG, Bauer-Brandl A, Perlovich GL. Cocrystal screening of hydroxybenzamides with benzoic acid derivatives: a comparative study of thermal and solution-based methods. European Journal of Pharmaceutical Sciences. 2014;65:56-64.
45. Katstra W, Palazzolo R, Rowe C, Giritlioglu B, Teung P, Cima M. Oral dosage forms fabricated by Three Dimensional Printing™. Journal of controlled release. 2000;66(1):1-9.

46. Voura C, Gruber M, Schroedl N, Strohmeier D, Eitzinger B, Bauer W, et al. Printable medicines: a microdosing device for producing personalised medicines. Pharm Tech Eur. 2011;23:32-6.
47. Sandler N, Määttänen A, Ihalainen P, Kronberg L, Meierjohann A, Viitala T, et al. Inkjet printing of drug substances and use of porous substrates-towards individualized dosing. Journal of pharmaceutical sciences. 2011;100(8):3386-95.
48. Boland T, Xu T, Damon B, Cui X. Application of inkjet printing to tissue engineering. Biotechnology journal. 2006;1(9):910-7.
49. Gbureck U, Hölzel T, Doillon CJ, Mueller FA, Barralet JE. Direct printing of bioceramic implants with spatially localized angiogenic factors. Advanced Materials. 2007;19(6):795-800.
50. Zhu X, Zheng Q, Yang H, Cai J, Huang L, Duan Y, et al. Recent advances in inkjet dispensing technologies: applications in drug discovery. Expert opinion on drug discovery. 2012;7(9):761-70.
51. Lemmo AV, Rose DJ, Tisone TC. Inkjet dispensing technology: applications in drug discovery. Current opinion in biotechnology. 1998;9(6):615-7.
52. Shiu S, Borevitz J. The next generation of microarray research: applications in evolutionary and ecological genomics. Heredity. 2006;100(2):141-9.
53. Rose D. Microdispensing technologies in drug discovery. Drug discovery today. 1999;4(9):411-9.
54. Le HP. Progress and trends in ink-jet printing technology. Journal of Imaging Science and Technology. 1998;42(1):49-62.
55. Arrabito G, Pignataro B. Inkjet printing methodologies for drug screening. Analytical chemistry. 2010;82(8):3104-7.
56. Zheng Q, Lu J, Chen H, Huang L, Cai J, Xu Z. Application of inkjet printing technique for biological material delivery and antimicrobial assays. Analytical biochemistry. 2011;410(2):171-6.
57. Davies MC, Alexander MR, Hook AL, Yang J, Mei Y, Taylor M, et al. High throughput surface characterization: a review of a new tool for screening prospective biomedical material arrays. Journal of drug targeting. 2010;18(10):741-51.

58. Austin J, Holway AH. Contact printing of protein microarrays. Protein Microarrays: Springer; 2011. p. 379-94.
59. Scoutaris N, Alexander MR, Gellert PR, Roberts CJ. Inkjet printing as a novel medicine formulation technique. Journal of Controlled Release. 2011;156(2):179-85.
60. Tarcha PJ, Verlee D, Hui HW, Setesak J, Antohe B, Radulescu D, et al. The application of ink-jet technology for the coating and loading of drug-eluting stents. Annals of biomedical engineering. 2007;35(10):1791-9.
61. Attinger D, Zhao Z, Poulikakos D. An experimental study of molten microdroplet surface deposition and solidification: transient behavior and wetting angle dynamics. Journal of Heat Transfer. 2000;122(3):544-56.
62. Di Risio S, Yan N. Piezoelectric Ink-Jet Printing of Horseradish Peroxidase: Effect of Ink Viscosity Modifiers on Activity. Macromolecular Rapid Communications. 2007;28(18-19):1934-40.
63. Yun YH, Kim JD, Lee BK, Cho YW, Lee HY. Polymer inkjet printing: Construction of three-dimensional structures at micro-scale by repeated lamination. Macromolecular research. 2009;17(3):197-202.
64. Meléndez PA, Kane KM, Ashvar CS, Albrecht M, Smith PA. Thermal inkjet application in the preparation of oral dosage forms: Dispensing of prednisolone solutions and polymorphic characterization by solid-state spectroscopic techniques. Journal of pharmaceutical sciences. 2008;97(7):2619-36.
65. Desai S, Perkins J, Harrison BS, Sankar J. Understanding release kinetics of biopolymer drug delivery microcapsules for biomedical applications. Materials Science and Engineering: B. 2010;168(1):127-31.
66. Buanz AB, Saunders MH, Basit AW, Gaisford S. Preparation of personalized-dose salbutamol sulphate oral films with thermal ink-jet printing. Pharmaceutical research. 2011;28(10):2386.
67. Pardeike J, Strohmeier DM, Schrödl N, Voura C, Gruber M, Khinast JG, et al. Nanosuspensions as advanced printing ink for accurate dosing of poorly soluble drugs in personalized medicines. International journal of pharmaceutics. 2011;420(1):93-100.

68. Scoutaris N, Hook AL, Gellert PR, Roberts CJ, Alexander MR, Scurr DJ. ToF-SIMS analysis of chemical heterogenities in inkjet micro-array printed drug/polymer formulations. Journal of Materials Science: Materials in Medicine. 2012;23(2):385-91.
69. Lee BK, Yun YH, Choi JS, Choi YC, Kim JD, Cho YW. Fabrication of drug-loaded polymer microparticles with arbitrary geometries using a piezoelectric inkjet printing system. International journal of pharmaceutics. 2012;427(2):305-10.
70. Iwanaga S, Saito N, Sanae H, Nakamura M. Facile fabrication of uniform size-controlled microparticles and potentiality for tandem drug delivery system of micro/nanoparticles. Colloids and Surfaces B: Biointerfaces. 2013;109:301-6.
71. Genina N, Janßen EM, Breitenbach A, Breitkreutz J, Sandler N. Evaluation of different substrates for inkjet printing of rasagiline mesylate. European Journal of Pharmaceutics and Biopharmaceutics. 2013;85(3):1075-83.
72. Genina N, Fors D, Palo M, Peltonen J, Sandler N. Behavior of printable formulations of loperamide and caffeine on different substrates—Effect of print density in inkjet printing. International journal of pharmaceutics. 2013;453(2):488-97.
73. Raijada D, Genina N, Fors D, Wisaeus E, Peltonen J, Rantanen J, et al. A step toward development of printable dosage forms for poorly soluble drugs. Journal of pharmaceutical sciences. 2013;102(10):3694-704.
74. Vakili H, Nyman JO, Genina N, Preis M, Sandler N. Application of a colorimetric technique in quality control for printed pediatric orodispersible drug delivery systems containing propranolol hydrochloride. International journal of pharmaceutics. 2016;511(1):606-18.
75. Varan C, Wickström H, Sandler N, Aktaş Y, Bilensoy E. Inkjet printing of antiviral PCL nanoparticles and anticancer cyclodextrin inclusion complexes on bioadhesive film for cervical administration. International Journal of Pharmaceutics. 2017.
76. Wickström H, Nyman JO, Indola M, Sundelin H, Kronberg L, Preis M, et al. Colorimetry as quality control tool for individual inkjet-printed pediatric formulations. AAPS PharmSciTech. 2017;18(2):293-302.

77. Palo M, Kogermann K, Laidmäe I, Meos A, Preis M, Heinämäki J, et al. Development of Oromucosal Dosage Forms by Combining Electrospinning and Inkjet Printing. Molecular Pharmaceutics. 2017;14(3):808-20.
78. Vakili H, Wickström H, Desai D, Preis M, Sandler N. Application of a handheld NIR spectrometer in prediction of drug content in inkjet printed orodispersible formulations containing prednisolone and levothyroxine. International journal of pharmaceutics. 2017;524(1):414-23.
79. Chan KA, Kazarian SG. Fourier transform infrared imaging for high-throughput analysis of pharmaceutical formulations. Journal of combinatorial chemistry. 2005;7(2):185-9.
80. Liberski AR, Tizzard GJ, Diaz-Mochon JJ, Hursthouse MB, Milnes P, Bradley M. Screening for polymorphs on polymer microarrays. Journal of combinatorial chemistry. 2008;10(1):24-7.
81. Taresco V, Louzao I, Scurr D, Booth J, Treacher K, McCabe J, et al. Rapid nano-gram scale screening method of micro-arrays to evaluate drug-polymer blends using high-throughput printing technology. Molecular Pharmaceutics. 2017.
82. Brillante A, Bilotti I, Della Valle RG, Venuti E, Girlando A. Probing polymorphs of organic semiconductors by lattice phonon Raman microscopy. CrystEngComm. 2008;10(8):937-46.
83. Bosch ME, Sanchez A, Rojas FS, Ojeda CB. Determination of paracetamol: Historical evolution. Journal of pharmaceutical and biomedical analysis. 2006;42(3):291-321.
84. Hinz B, Cheremina O, Brune K. Acetaminophen (paracetamol) is a selective cyclooxygenase-2 inhibitor in man. The FASEB journal. 2008;22(2):383-90.
85. Lindenberg M, Kopp S, Dressman JB. Classification of orally administered drugs on the World Health Organization Model list of Essential Medicines according to the biopharmaceutics classification system. European Journal of Pharmaceutics and Biopharmaceutics. 2004;58(2):265-78.
86. Naumov DY, Vasilchenko M, Howard J. The monoclinic form of acetaminophen at 150K. Acta Crystallographica Section C: Crystal Structure Communications. 1998;54(5):653-5.

87. Perrin M-A, Neumann MA, Elmaleh H, Zaske L. Crystal structure determination of the elusive paracetamol Form III. Chemical Communications. 2009 (22):3181-3.
88. Di MART1N0 P, Palmieri GF, Martelli S. Molecular mobility of the paracetamol amorphous form. Change. 2000;1:1.495.
89. Haisa M, Kashino S, Kawai R, Maeda H. The monoclinic form of p-hydroxyacetanilide. Acta Crystallographica Section B: Structural Crystallography and Crystal Chemistry. 1976;32(4):1283-5.
90. Welton JM, McCarthy GJ. X-Ray Powder Data for Acetaminophen (C 8 H 9 NO 2). Powder Diffraction. 1988;3(02):102-3.
91. Haisa M, Kashino S, Maeda H. The orthorhombic form of p-hydroxyacetanilide. Acta Crystallographica Section B: Structural Crystallography and Crystal Chemistry. 1974;30(10):2510-2.
92. Di Martino P, Conflant P, Drache M, Huvenne J-P, Guyot-Hermann A-M. Preparation and physical characterization of forms II and III of paracetamol. Journal of thermal analysis. 1997;48(3):447-58.
93. Burley JC, Duer MJ, Stein RS, Vrcelj RM. Enforcing Ostwald's rule of stages: Isolation of paracetamol forms III and II. European journal of pharmaceutical sciences. 2007;31(5):271-6.
94. Sander J. Overview of established antiepileptic drugs. Epilepsy 2009. 2009.
95. Tian F, Zeitler J, Strachan C, Saville D, Gordon K, Rades T. Characterizing the conversion kinetics of carbamazepine polymorphs to the dihydrate in aqueous suspension using Raman spectroscopy. Journal of pharmaceutical and biomedical analysis. 2006;40(2):271-80.
96. Gilpin R, Zhou W. Infrared studies of the polymorphic states of the fenamates. Journal of pharmaceutical and biomedical analysis. 2005;37(3):509-15.
97. Modi S, Patel N. Development and evaluation of self emulsifying drug delivery of a poorly water soluble NSAID. World J Pharm Pharm Sci. 2015;4:462-79.
98. Panchagnula R, Sundaramurthy P, Pillai O, Agrawal S, Raj YA. Solid-state characterization of mefenamic acid. Journal of pharmaceutical sciences. 2004;93(4):1019-29.

99. SeethaLekshmi S, Guru Row TN. Conformational polymorphism in a non-steroidal anti-inflammatory drug, mefenamic acid. Crystal Growth & Design. 2012;12(8):4283-9.
100. Ibolya F, Gyeresi A, Szabó-Révész P, Aigner Z. Solid dispersions of flufenamic acid with PEG 4000 and Peg 6000. Farmacia. 2011;59(1):60-9.
101. López-Mejías V, Kampf JW, Matzger AJ. Nonamorphism in flufenamic acid and a new record for a polymorphic compound with solved structures. Journal of the American Chemical Society. 2012;134(24):9872-5.
102. Schwartz DK. Mechanisms and kinetics of self-assembled monolayer formation. Annual Review of Physical Chemistry. 2001;52(1):107-37.
103. Boneva MP, Danov KD, Christov NC, Kralchevsky PA. Attraction between particles at a liquid interface due to the interplay of gravity-and electric-field-induced interfacial deformations. Langmuir. 2009;25(16):9129-39.
104. Indian J. A new radiation. Indian J Phys. 1928;2:387-98.
105. Maiman TH. Ruby laser systems. Google Patents; 1967.
106. Vankeirsbilck T, Vercauteren A, Baeyens W, Van der Weken G, Verpoort F, Vergote G, et al. Applications of Raman spectroscopy in pharmaceutical analysis. TrAC trends in analytical chemistry. 2002;21(12):869-77.
107. Zeitler JA, Taday PF, Newnham DA, Pepper M, Gordon KC, Rades T. Terahertz pulsed spectroscopy and imaging in the pharmaceutical setting-a review. Journal of Pharmacy and Pharmacology. 2007;59(2):209-23.
108. Ayala AP. Polymorphism in drugs investigated by low wavenumber Raman scattering. Vibrational Spectroscopy. 2007;45(2):112-6.
109. Alkhalil A, Babu Nanubolu J, Burley JC. Analysis of phase transitions in molecular solids: quantitative assessment of phonon-mode vs intra-molecular spectral data. RSC Advances. 2012;2(1):209-16.
110. Hédoux A, Guinet Y, Descamps M. The contribution of Raman spectroscopy to the analysis of phase transformations in pharmaceutical compounds. International journal of pharmaceutics. 2011;417(1):17-31.
111. Bellows JC, Chen FP, Prasad PN. Determination of drug polymorphs by laser Raman Spectroscopy. I. Ampicillin and Griseofulvin. Drug Development and Industrial Pharmacy. 1977;3(5):451-8.

112. Al-Dulaimi S, Aina A, Burley J. Rapid polymorph screening on milligram quantities of pharmaceutical material using phonon-mode Raman spectroscopy. CrystEngComm. 2010;12(4):1038-40.
113. Tres F, Patient JD, Williams PM, Treacher K, Booth J, Hughes LP, et al. Monitoring the dissolution mechanisms of amorphous bicalutamide solid dispersions via real-time Raman mapping. Molecular pharmaceutics. 2015;12(5):1512-22.
114. Binnig G, Quate CF, Gerber C. Atomic force microscope. Physical review letters. 1986;56(9):930.
115. Jalili N, Laxminarayana K. A review of atomic force microscopy imaging systems: application to molecular metrology and biological sciences. Mechatronics. 2004;14(8):907-45.
116. Carlton RA. Polarized light microscopy: Springer; 2011.
117. Bracco G, Holst B. Surface science techniques: Springer Science & Business Media; 2013.
118. Schneller T, Waser R, Kosec M, Payne D. Chemical solution deposition of functional oxide thin films: Springer; 2013.
119. Rahaman M, Rahaman MN. Ceramic processing: CRC press; 2006.
120. Van Eerdenbrugh B, Stuyven B, Froyen L, Van Humbeeck J, Martens JA, Augustijns P, et al. Downscaling drug nanosuspension production: processing aspects and physicochemical characterization. Aaps Pharmscitech. 2009;10(1):44-53.
121. Mullins JDaM, T. J. Some pharmaceutical properties of novobiocin. Journal of the American Pharmaceutical Association. 1960;49(4):245-8.
122. Szelagiewicz M, Marcolli C, Cianferani S, Hard A, Vit A, Burkhard A, et al. In situ characterization of polymorphic forms: the potential of Raman techniques. Journal of Thermal Analysis and Calorimetry. 1999;57(1):23-43.
123. Roy S, Chamberlin B, Matzger AJ. Polymorph discrimination using low wavenumber Raman spectroscopy. Organic process research & development. 2013;17(7):976-80.
124. Bettini R, Bonassi L, Castoro V, Rossi A, Zema L, Gazzaniga A, et al. Solubility and conversion of carbamazepine polymorphs in supercritical

carbon dioxide. European journal of pharmaceutical sciences. 2001;13(3):281-6.

125. Otsuka M, Nishizawa Ji, Shibata J, Ito M. Quantitative evaluation of mefenamic acid polymorphs by terahertz–chemometrics. Journal of pharmaceutical sciences. 2010;99(9):4048-53.

126. Lefebvre C, Guyot-Hermann A, Draguet-Brughmans M, Bouché R, Guyot J. Polymorphic transitions of carbamazepine during grinding and compression. Drug Development and Industrial Pharmacy. 1986;12(11-13):1913-27.

127. Hu Y, Liang JK, Myerson AS, Taylor LS. Crystallization monitoring by Raman spectroscopy: simultaneous measurement of desupersaturation profile and polymorphic form in flufenamic acid systems. Industrial & engineering chemistry research. 2005;44(5):1233-40.

128. Boldyreva E, Shakhtshneider T, Ahsbahs H, Sowa H, Uchtmann H. Effect of high pressure on the polymorphs of paracetamol. Journal of thermal analysis and calorimetry. 2002;68(2):437-52.

129. Romero S, Escalera B, Bustamante P. Solubility behavior of polymorphs I and II of mefenamic acid in solvent mixtures. International journal of pharmaceutics. 1999;178(2):193-202.

130. Nuzzo RG, Allara DL. Adsorption of bifunctional organic disulfides on gold surfaces. Journal of the American Chemical Society. 1983;105(13):4481-3.

131. Ivanov V, Todorov N, Petrov L, Ritacco T, Giocondo M, Vlakhov E, editors. Strong surface enhanced Raman scattering from gold nanoarrays obtained by direct laser writing. Journal of Physics: Conference Series; 2016: IOP Publishing.

132. Wu T, Sun Y, Li N, de Villiers MM, Yu L. Inhibiting surface crystallization of amorphous indomethacin by nanocoating. Langmuir. 2007;23(9):5148-53.

133. McKim A, Strub R. Dimethyl sulfoxide USP, PhEur in approved pharmaceutical products and medical devices. Pharmaceutical Technology. 2008;32(5):74.

134. Alonzo DE, Zhang GG, Zhou D, Gao Y, Taylor LS. Understanding the behavior of amorphous pharmaceutical systems during dissolution. Pharmaceutical research. 2010;27(4):608-18.
135. Cunha VR, Izumi CM, Petersen PA, Magalhaes A, Temperini ML, Petrilli HM, et al. Mefenamic acid anti-inflammatory drug: probing its polymorphs by vibrational (IR and Raman) and solid-state NMR spectroscopies. The Journal of Physical Chemistry B. 2014;118(16):4333-44.
136. Lee IS, Lee AY, Myerson AS. Concomitant polymorphism in confined environment. Pharmaceutical research. 2008;25(4):960-8.
137. O'Brien LE, Timmins P, Williams AC, York P. Use of in situ FT-Raman spectroscopy to study the kinetics of the transformation of carbamazepine polymorphs. Journal of pharmaceutical and biomedical analysis. 2004;36(2):335-40.
138. Strachan CJ, Howell SL, Rades T, Gordon KC. A theoretical and spectroscopic study of carbamazepine polymorphs. Journal of Raman Spectroscopy. 2004;35(5):401-8.
139. Baird JA, Van Eerdenbrugh B, Taylor LS. A classification system to assess the crystallization tendency of organic molecules from undercooled melts. Journal of pharmaceutical sciences. 2010;99(9):3787-806.
140. Nanubolu JB, Burley JC. Investigating the recrystallization behavior of amorphous paracetamol by variable temperature Raman studies and surface Raman mapping. Molecular pharmaceutics. 2012;9(6):1544-58.
141. Frostman LM, Bader MM, Ward MD. Nucleation and growth of molecular crystals on self-assembled monolayers. Langmuir. 1994;10(2):576-82.
142. Meldrum FC, Flath J, Knoll W. Chemical deposition of PbS on self-assembled monolayers of 16-mercaptohexadecanoic acid. Langmuir. 1997;13(7):2033-49.
143. Lee AY, Ulman A, Myerson AS. Crystallization of amino acids on self-assembled monolayers of rigid thiols on gold. Langmuir. 2002;18(15):5886-98.
144. Kang JF, Zaccaro J, Ulman A, Myerson A. Nucleation and growth of glycine crystals on self-assembled monolayers on gold. Langmuir. 2000;16(8):3791-6.

145. Franklin B, Brownrigg W, Farish M. Of the stilling of waves by means of oil. Extracted from Sundry Letters between Benjamin Franklin, LL. DFRS William Brownrigg, MDFRS and the Reverend Mr. Farish. Philosophical Transactions. 1774;64:445-60.
146. Pockels A. On the relative contamination of the water surface by equal quantities of different substances. Nature. 1892;46(1192):418-9.
147. Pockels A. Relations between the surface tension and relative contamination of water surfaces. Nature. 1893;48:152.
148. Pockels A. On the spreading of oil upon water. Nature. 1894;50:223-4.
149. Rayleigh L. XXXVI. Investigations in Capillarity:—The size of drops.—The liberation of gas from supersaturated solutions.—Colliding jets.—The tension of contaminated water-surfaces. The London, Edinburgh, and Dublin Philosophical Magazine and Journal of Science. 1899;48(293):321-37.
150. Langmuir I. The constitution and fundamental properties of solids and liquids. II. Liquids. 1. Journal of the American Chemical Society. 1917;39(9):1848-906.
151. Blodgett KB. Films built by depositing successive monomolecular layers on a solid surface. Journal of the American Chemical Society. 1935;57(6):1007-22.
152. Gracias DH, Tien J, Breen TL, Hsu C, Whitesides GM. Forming electrical networks in three dimensions by self-assembly. Science. 2000;289(5482):1170-2.
153. Sellers H, Ulman A, Shnidman Y, Eilers JE. Structure and binding of alkanethiolates on gold and silver surfaces: implications for self-assembled monolayers. Journal of the American Chemical Society. 1993;115(21):9389-401.
154. Love JC, Estroff LA, Kriebel JK, Nuzzo RG, Whitesides GM. Self-assembled monolayers of thiolates on metals as a form of nanotechnology. Chemical reviews. 2005;105(4):1103-70.
155. Sagiv J. Organized monolayers by adsorption. 1. Formation and structure of oleophobic mixed monolayers on solid surfaces. Journal of the American Chemical Society. 1980;102(1):92-8.

156. Gun J, Iscovici R, Sagiv J. On the formation and structure of self-assembling monolayers: II. A comparative study of Langmuir—Blodgett and adsorbed films using ellipsometry and IR reflection—absorption spectroscopy. Journal of Colloid and Interface Science. 1984;101(1):201-13.
157. Gun J, Sagiv J. On the formation and structure of self-assembling monolayers: III. Time of formation, solvent retention, and release. Journal of colloid and interface science. 1986;112(2):457-72.
158. Strong L, Whitesides GM. Structures of self-assembled monolayer films of organosulfur compounds adsorbed on gold single crystals: electron diffraction studies. Langmuir. 1988;4(3):546-58.
159. Laibinis PE, Whitesides GM, Allara DL, Tao YT, Parikh AN, Nuzzo RG. Comparison of the structures and wetting properties of self-assembled monolayers of n-alkanethiols on the coinage metal surfaces, copper, silver, and gold. Journal of the American Chemical Society. 1991;113(19):7152-67.
160. Ye S, Li G, Noda H, Uosaki K, Osawa M. Characterization of self-assembled monolayers of alkanethiol on GaAs surface by contact angle and angle-resolved XPS measurements. Surface science. 2003;529(1):163-70.
161. Troughton EB, Bain CD, Whitesides GM, Nuzzo RG, Allara DL, Porter MD. Monolayer films prepared by the spontaneous self-assembly of symmetrical and unsymmetrical dialkyl sulfides from solution onto gold substrates: structure, properties, and reactivity of constituent functional groups. Langmuir. 1988;4(2):365-85.
162. Allara DL, Nuzzo RG. Spontaneously organized molecular assemblies. 1. Formation, dynamics, and physical properties of n-alkanoic acids adsorbed from solution on an oxidized aluminum surface. Langmuir. 1985;1(1):45-52.
163. Schlotter N, Porter MD, Bright T, Allara DL. Formation and structure of a spontaneously adsorbed monolayer of arachidic on silver. Chemical physics letters. 1986;132(1):93-8.
164. Vericat C, Vela M, Benitez G, Carro P, Salvarezza R. Self-assembled monolayers of thiols and dithiols on gold: new challenges for a well-known system. Chemical Society Reviews. 2010;39(5):1805-34.

165. Brovelli D, Hähner G, Ruiz L, Hofer R, Kraus G, Waldner A, et al. Highly oriented, self-assembled alkanephosphate monolayers on tantalum (V) oxide surfaces. Langmuir. 1999;15(13):4324-7.
166. Bain CD, Troughton EB, Tao YT, Evall J, Whitesides GM, Nuzzo RG. Formation of monolayer films by the spontaneous assembly of organic thiols from solution onto gold. Journal of the American Chemical Society. 1989;111(1):321-35.
167. Reed MA, Tour JM. Computing with molecules. Scientific American. 2000;282(6):86-93.
168. Schreiber F, Eberhardt A, Leung T, Schwartz P, Wetterer S, Lavrich D, et al. Adsorption mechanisms, structures, and growth regimes of an archetypal self-assembling system: Decanethiol on Au (111). Physical Review B. 1998;57(19):12476.
169. Poirier G. Coverage-dependent phases and phase stability of decanethiol on Au (111). Langmuir. 1999;15(4):1167-75.
170. Peterlinz KA, Georgiadis R. In situ kinetics of self-assembly by surface plasmon resonance spectroscopy. Langmuir. 1996;12(20):4731-40.
171. Buck M, Himmelhaus M. Vibrational spectroscopy of interfaces by infrared–visible sum frequency generation. Journal of Vacuum Science & Technology A: Vacuum, Surfaces, and Films. 2001;19(6):2717-36.
172. Mrksich M. Mass spectrometry of self-assembled monolayers: a new tool for molecular surface science. Acs Nano. 2008;2(1):7-18.
173. Himmelhaus M, Eisert F, Buck M, Grunze M. Self-Assembly of n-Alkanethiol Monolayers. A Study by IR− Visible Sum Frequency Spectroscopy (SFG). The Journal of Physical Chemistry B. 2000;104(3):576-84.
174. Camillone N, Leung T, Schwartz P, Eisenberger P, Scoles G. Chain length dependence of the striped phases of alkanethiol monolayers self-assembled on Au (111): An atomic beam diffraction study. Langmuir. 1996;12(11):2737-46.
175. Hähner G, Wöll C, Buck M, Grunze M. Investigation of intermediate steps in the self-assembly of n-alkanethiols on gold surfaces by soft X-ray spectroscopy. Langmuir. 1993;9(8):1955-8.

176. Karpovich D, Blanchard G. Direct measurement of the adsorption kinetics of alkanethiolate self-assembled monolayers on a microcrystalline gold surface. Langmuir. 1994;10(9):3315-22.
177. Dannenberger O, Wolff JJ, Buck M. Solvent dependence of the self-assembly process of an endgroup-modified alkanethiol. Langmuir. 1998;14(17):4679-82.
178. Yamada R, Sakai H, Uosaki K. Solvent effect on the structure of the self-assembled monolayer of alkanethiol. Chemistry letters. 1999;28(7):667-8.
179. Bensebaa F, Voicu R, Huron L, Ellis TH, Kruus E. Kinetics of formation of long-chain n-alkanethiolate monolayers on polycrystalline gold. Langmuir. 1997;13(20):5335-40.
180. Wartewig S. IR and Raman spectroscopy: fundamental processing: John Wiley & Sons; 2006.
181. Love JC, Wolfe DB, Haasch R, Chabinyc ML, Paul KE, Whitesides GM, et al. Formation and structure of self-assembled monolayers of alkanethiolates on palladium. Journal of the American Chemical Society. 2003;125(9):2597-609.
182. Schoenfisch MH, Pemberton JE. Air stability of alkanethiol self-assembled monolayers on silver and gold surfaces. Journal of the American Chemical Society. 1998;120(18):4502-13.
183. Graham D, Dingman S. A Step-by-Step Guide for Solution Based Self-Assembly. Material Matters. 2006;1(2):18.
184. Faucheux N, Schweiss R, Lützow K, Werner C, Groth T. Self-assembled monolayers with different terminating groups as model substrates for cell adhesion studies. Biomaterials. 2004;25(14):2721-30.
185. Chandra S, Di Marzo M, Qiao Y, Tartarini P. Effect of liquid-solid contact angle on droplet evaporation. Fire Safety Journal. 1996;27(2):141-58.
186. Shintani H, Tanaka H. Universal link between the boson peak and transverse phonons in glass. Nature materials. 2008;7(11):870-7.
187. Kachrimanis K, Braun DE, Griesser UJ. Quantitative analysis of paracetamol polymorphs in powder mixtures by FT-Raman spectroscopy and PLS regression. Journal of pharmaceutical and biomedical analysis. 2007;43(2):407-12.

188. Al-Zoubi N, Koundourellis J, Malamataris S. FT-IR and Raman spectroscopic methods for identification and quantitation of orthorhombic and monoclinic paracetamol in powder mixes. Journal of pharmaceutical and biomedical analysis. 2002;29(3):459-67.
189. Jabeen S, Dines TJ, Leharne SA, Chowdhry BZ. Raman and IR spectroscopic studies of fenamates–conformational differences in polymorphs of flufenamic acid, mefenamic acid and tolfenamic acid. Spectrochimica Acta Part A: Molecular and Biomolecular Spectroscopy. 2012;96:972-85.
190. Dolbier WR. Fluorine chemistry at the millennium. Journal of Fluorine Chemistry. 2005;126(2):157-63.
191. Banks R. Fluorocarbons and their Derivatives (2nd edn.) MacDonald. London; 1970.
192. Banks RE, Smart BE, Tatlow J. Organofluorine chemistry: principles and commercial applications: Springer Science & Business Media; 2013.
193. O'Hagan D. Understanding organofluorine chemistry. An introduction to the C–F bond. Chemical Society Reviews. 2008;37(2):308-19.
194. Krafft MP, Riess JG. Chemistry, physical chemistry, and uses of molecular fluorocarbon− hydrocarbon diblocks, triblocks, and related compounds・ unique “apolar” components for self-assembled colloid and interface engineering. Chemical reviews. 2009;109(5):1714-92.
195. Mukerjee P. Fluorocarbon—hydrocarbon interactions in micelles and other lipid assemblies, at interfaces, and in solutions. Colloids and Surfaces A: Physicochemical and engineering aspects. 1994;84(1):1-10.
196. Holmberg K, Jönsson B, Kronberg B, Lindman B. Surfactants and polymers in aqueous solution: Wiley Online Library; 2002.
197. Ma M, Hill RM. Superhydrophobic surfaces. Current opinion in colloid & interface science. 2006;11(4):193-202.
198. Scarratt LR, Steiner U, Neto C. A review on the mechanical and thermodynamic robustness of superhydrophobic surfaces. Advances in Colloid and Interface Science. 2017.

199. Liu H, Feng L, Zhai J, Jiang L, Zhu D. Reversible wettability of a chemical vapor deposition prepared ZnO film between superhydrophobicity and superhydrophilicity. Langmuir. 2004;20(14):5659-61.
200. Shiu J-Y, Kuo C-W, Chen P, editors. Fabrication of tunable superhydrophobic surfaces. Proceedings of SPIE-The International Society for Optical Engineering; 2005.
201. Teshima K, Sugimura H, Inoue Y, Takai O, Takano A. Transparent ultra water-repellent poly (ethylene terephthalate) substrates fabricated by oxygen plasma treatment and subsequent hydrophobic coating. Applied Surface Science. 2005;244(1):619-22.
202. Jin M, Feng X, Xi J, Zhai J, Cho K, Feng L, et al. Super-hydrophobic PDMS surface with ultra-low adhesive force. Macromolecular rapid communications. 2005;26(22):1805-9.
203. Qian B, Shen Z. Fabrication of superhydrophobic surfaces by dislocation-selective chemical etching on aluminum, copper, and zinc substrates. Langmuir. 2005;21(20):9007-9.
204. Podsiadlo P, Michel M, Lee J, Verploegen E, Wong Shi Kam N, Ball V, et al. Exponential growth of LBL films with incorporated inorganic sheets. Nano letters. 2008;8(6):1762-70.
205. Amigoni S, Taffin de Givenchy E, Dufay M, Guittard F. Covalent Layer-by-Layer Assembled Superhydrophobic Organic− Inorganic Hybrid Films. Langmuir. 2009;25(18):11073-7.
206. Wang H, Ishihara S, Ariga K, Yamauchi Y. All-metal layer-by-layer films: bimetallic alternate layers with accessible mesopores for enhanced electrocatalysis. Journal of the American Chemical Society. 2012;134(26):10819-21.
207. Li Y, Wang X, Sun J. Layer-by-layer assembly for rapid fabrication of thick polymeric films. Chemical Society Reviews. 2012;41(18):5998-6009.
208. Zhai L, Cebeci FÇ, Cohen RE, Rubner MF. Stable superhydrophobic coatings from polyelectrolyte multilayers. Nano letters. 2004;4(7):1349-53.
209. Zarzycki J. Past and present of sol-gel science and technology. Journal of Sol-Gel Science and Technology. 1997;8(1):17-22.

210. Hikita M, Tanaka K, Nakamura T, Kajiyama T, Takahara A. Super-liquid-repellent surfaces prepared by colloidal silica nanoparticles covered with fluoroalkyl groups. Langmuir. 2005;21(16):7299-302.
211. Ganesh VA, Raut HK, Nair AS, Ramakrishna S. A review on self-cleaning coatings. Journal of Materials Chemistry. 2011;21(41):16304-22.
212. Khorasani M, Mirzadeh H, Kermani Z. Wettability of porous polydimethylsiloxane surface: morphology study. Applied Surface Science. 2005;242(3):339-45.
213. Ma M, Hill RM, Lowery JL, Fridrikh SV, Rutledge GC. Electrospun poly (styrene-block-dimethylsiloxane) block copolymer fibers exhibiting superhydrophobicity. Langmuir. 2005;21(12):5549-54.
214. Zhao N, Xie Q, Weng L, Wang S, Zhang X, Xu J. Superhydrophobic surface from vapor-induced phase separation of copolymer micellar solution. Macromolecules. 2005;38(22):8996-9.
215. Jarvis N, Zisman W. Surface chemistry of fluorochemicals. NAVAL RESEARCH LAB WASHINGTON DC, 1965.
216. Shiu J-Y, Kuo C-W, Chen P, Mou C-Y. Fabrication of tunable superhydrophobic surfaces by nanosphere lithography. Chemistry of materials. 2004;16(4):561-4.
217. Zhang J, Li J, Han Y. Superhydrophobic PTFE surfaces by extension. Macromolecular Rapid Communications. 2004;25(11):1105-8.
218. Yabu H, Shimomura M. Single-step fabrication of transparent superhydrophobic porous polymer films. Chemistry of materials. 2005;17(21):5231-4.
219. Lu X, Zhang C, Han Y. Low-density polyethylene superhydrophobic surface by control of its crystallization behavior. Macromolecular Rapid Communications. 2004;25(18):1606-10.
220. Jiang L, Zhao Y, Zhai J. A lotus-leaf-like superhydrophobic surface: a porous microsphere/nanofiber composite film prepared by electrohydrodynamics. Angewandte Chemie. 2004;116(33):4438-41.
221. Feng X, Feng L, Jin M, Zhai J, Jiang L, Zhu D. Reversible super-hydrophobicity to super-hydrophilicity transition of aligned ZnO nanorod films. Journal of the American Chemical Society. 2004;126(1):62-3.

222. Florey K. Profiles of drug substances, excipients and related methodology: Academic press; 1983.
223. Alvarez AJ, Singh A, Myerson AS. Polymorph screening: comparing a semi-automated approach with a high throughput method. Crystal Growth and Design. 2009;9(9):4181-8.
224. Everall N. Quantitative study of self-absorption in near-infrared Fourier transform Raman spectroscopy. Journal of Raman Spectroscopy. 1994;25(10):813-9.
225. Wang H, Mann CK, Vickers TJ. Effect of powder properties on the intensity of Raman scattering by crystalline solids. Applied spectroscopy. 2002;56(12):1538-44.
226. Cochain B, Neuville D, Henderson G, Pinet O, Richet P, Bagnols-sur-cèze F, editors. Determination of iron redox ratio in borosilicate glasses and melts from Raman spectra. Proceedings of ATALANTE; 2008.
227. Hemley R, Mao H, Bell P, Mysen B. Raman Spectroscopy of Si O 2 Glass at High Pressure. Physical Review Letters. 1986;57(6):747.
228. Quist F, Kakkar A. Self-assembled monolayers: Influence of complementarity between chemisorbed and crystallizing molecules in polymorph selection. Journal of colloid and interface science. 2007;313(1):378-82.

Appendix A
Supplementary information

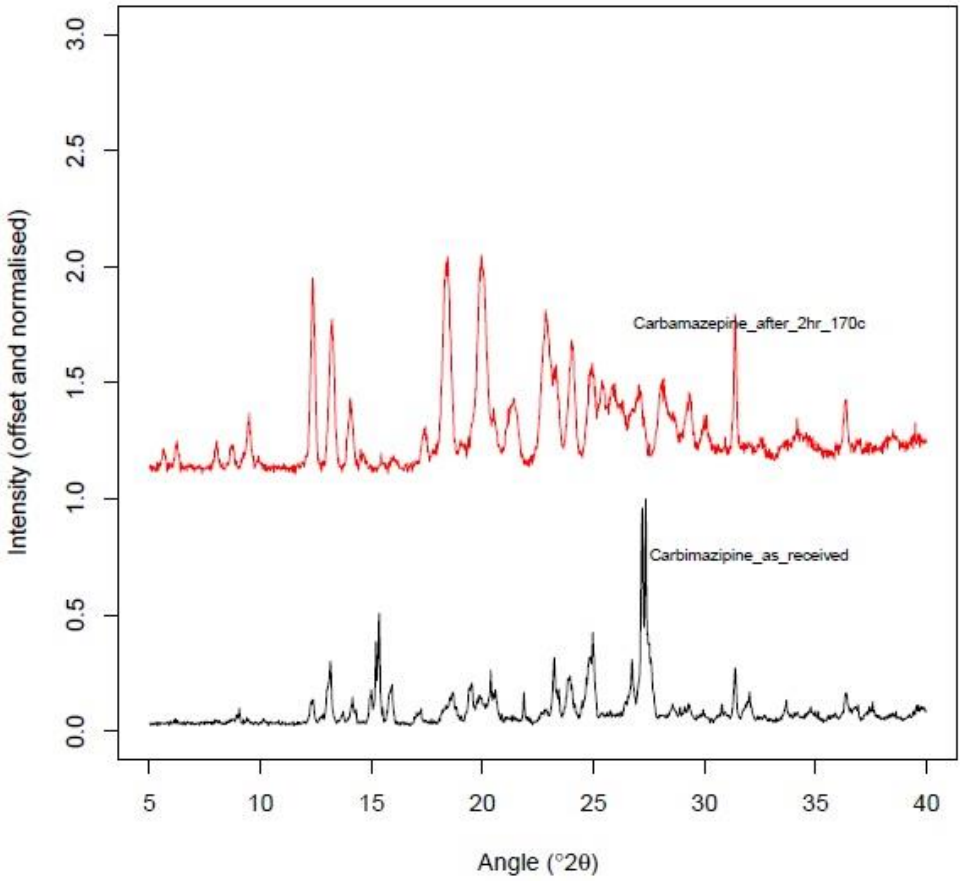

Figure A. 1. XRPD diffractograms of Carbamazepine polymorphs

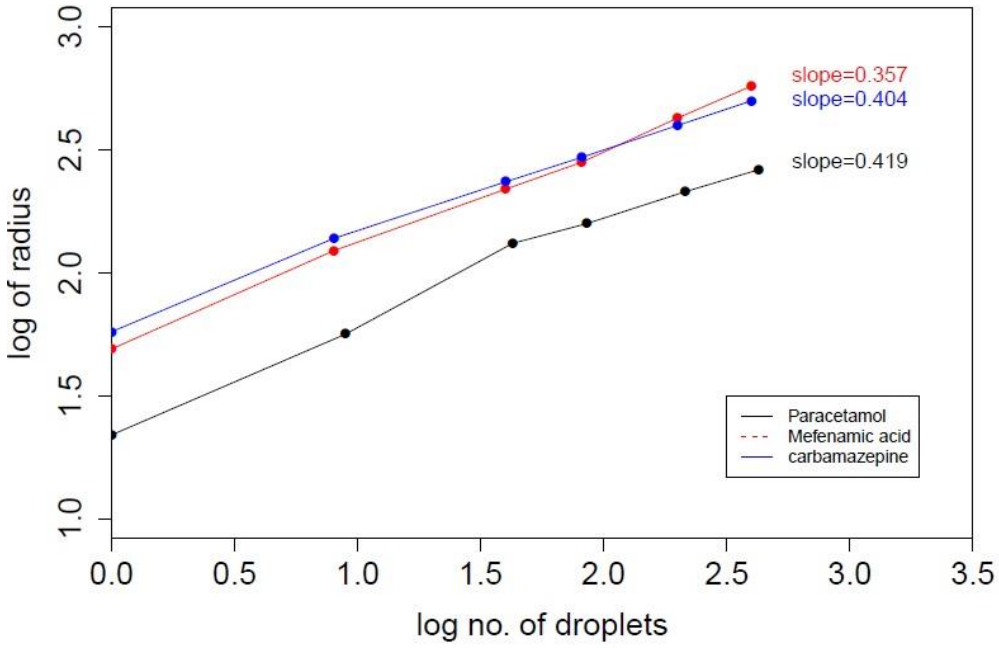

Figure A. 2. The behaviour of the drugs on the gold coated slide

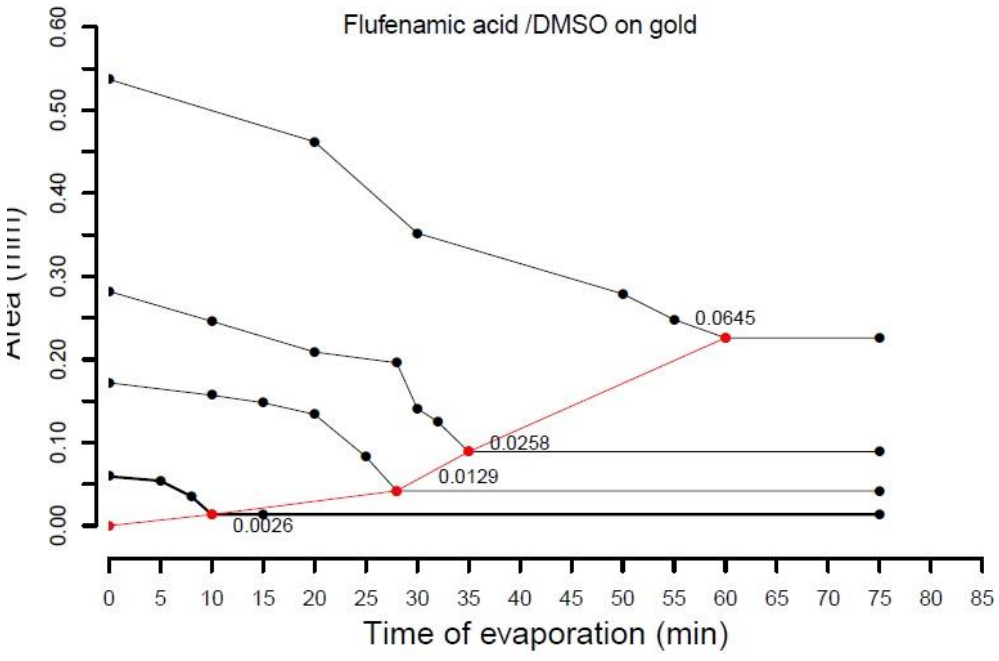

Figure A. 3. The evaporation time of different printed quantities of FLUF/DMSO on gold coated slide

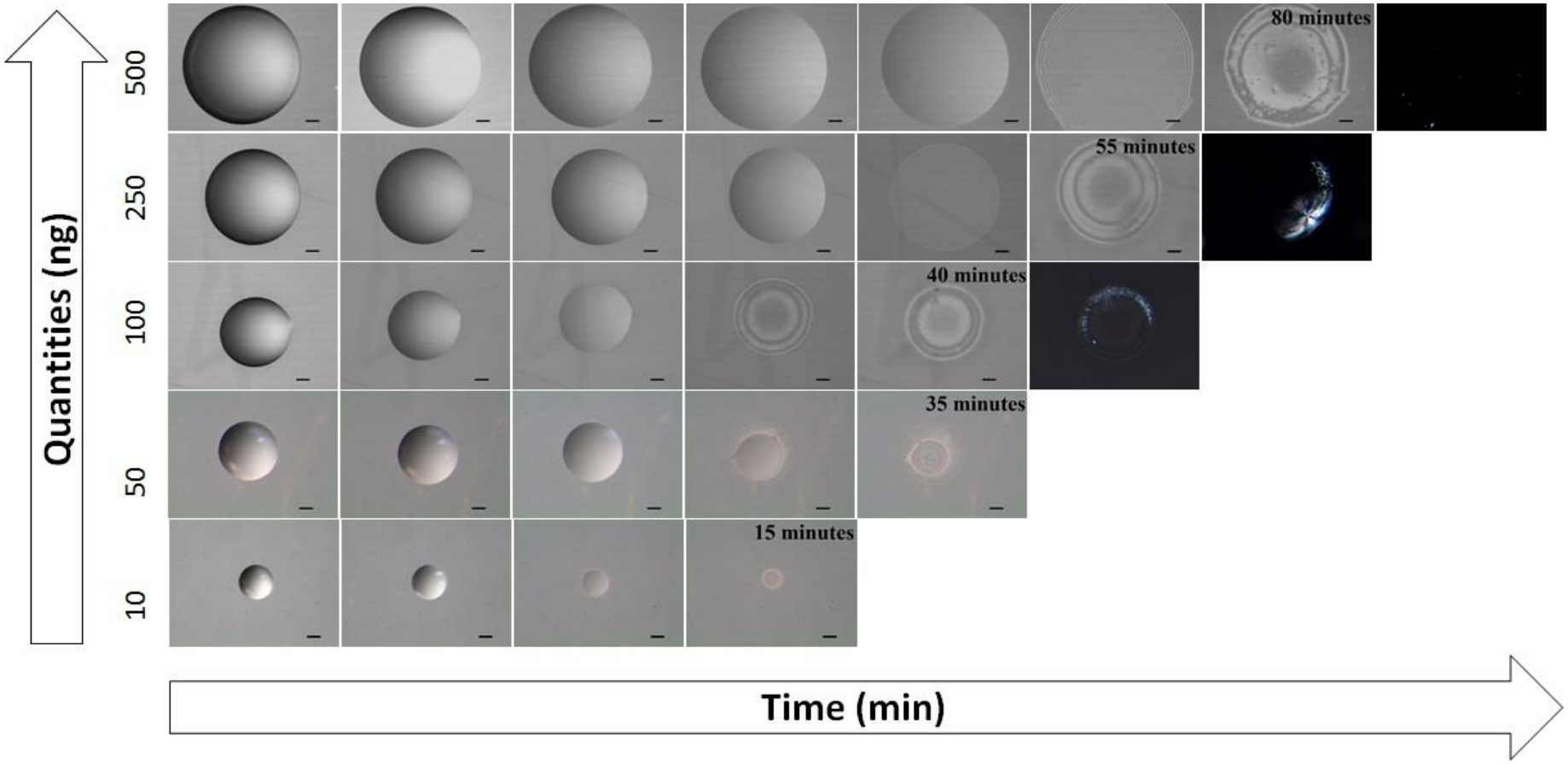

Figure A. 4. The optical micrographs of all the quantities of the printed dots of FLUF/DMSO on gold-coated slide, scale bar: 0.1 mm

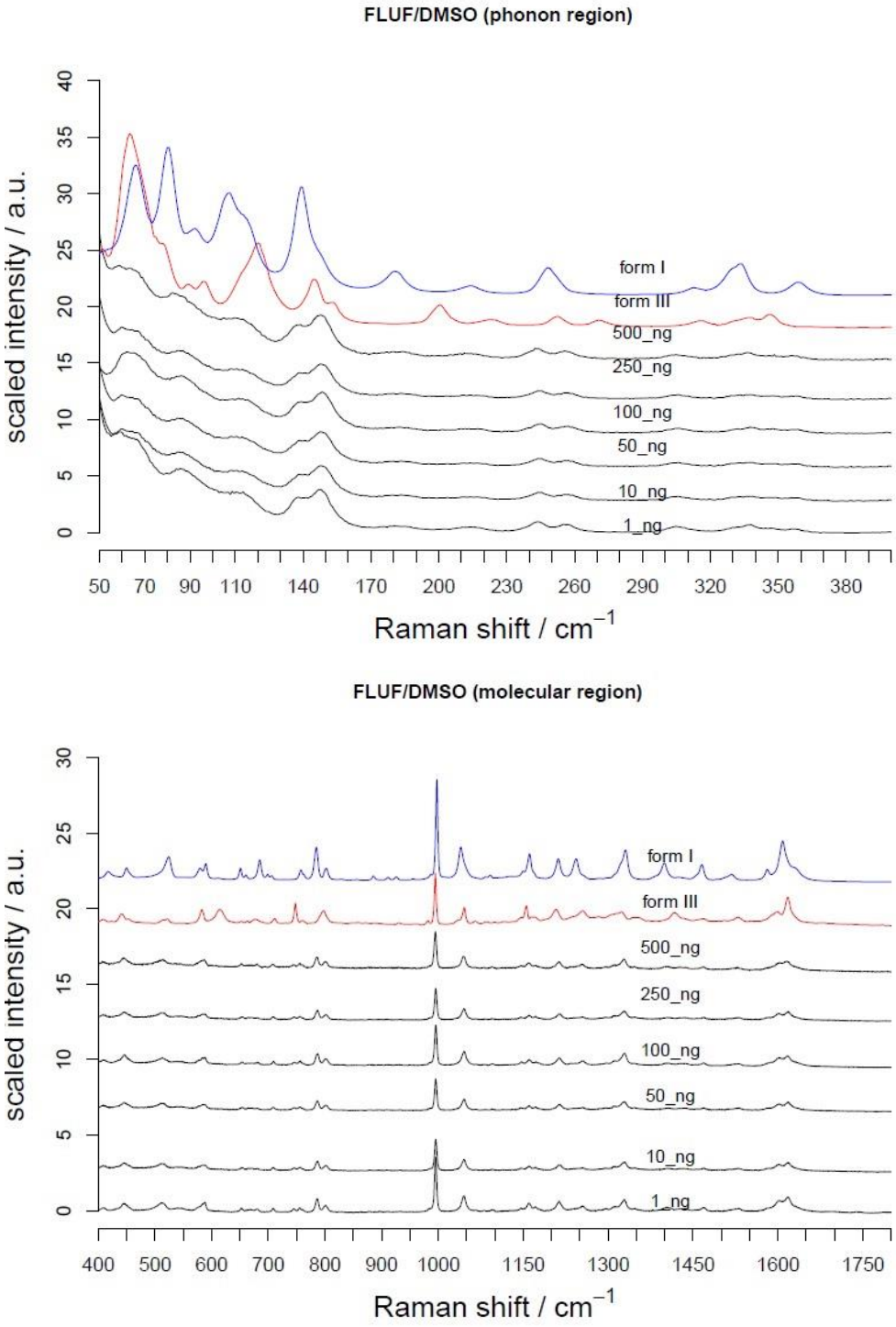

Figure A. 5. Raman spectra for phonon region (top) and molecular region (bottom) of different printed quantities of paracetamol printed on SAM-CH_3 ,with reference spectra of PAR (as received) (blue) and the prepared substrate (red).y-axis offsets were employed for presenting the differences between panels.

Appendix B
Supplementary information

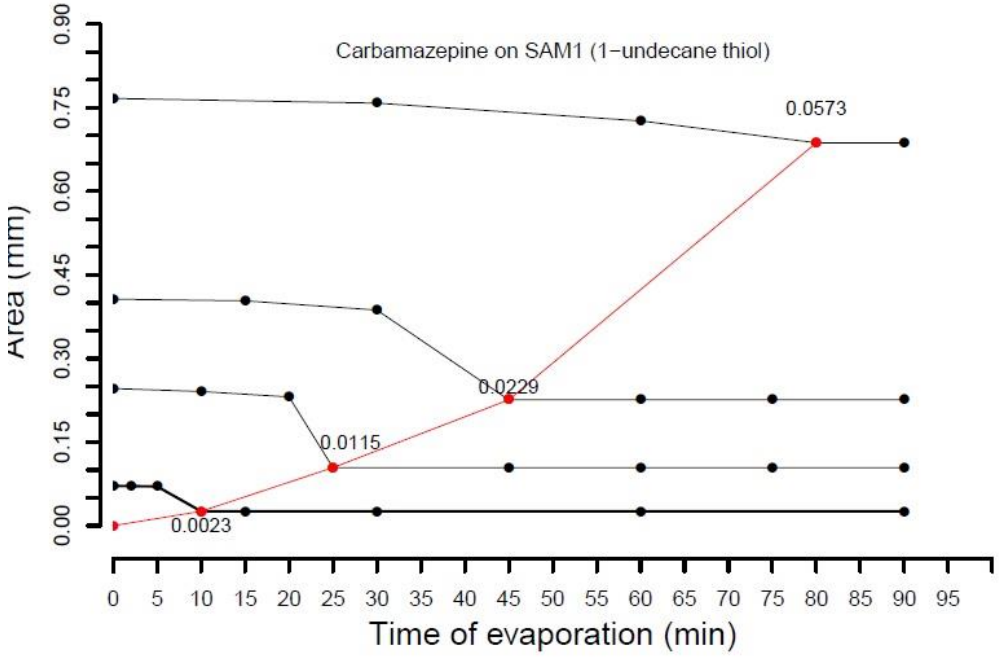

Figure B. 1. The evaporation time of different printed quantities of CBZ/DMSO on SAM-CH_3

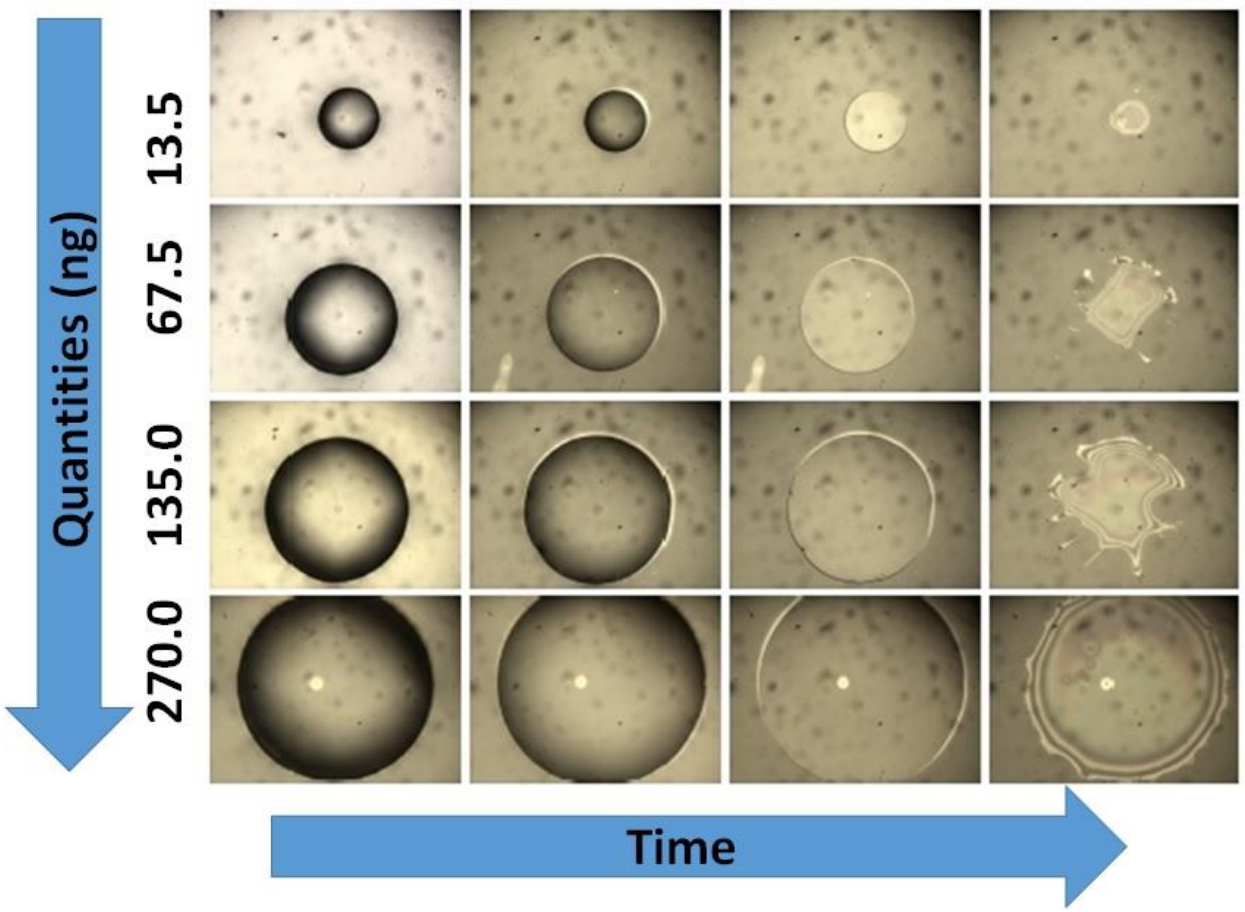

Figure B. 2. Optical micrographs of CBZ/ DMSO on SAM-CH_3

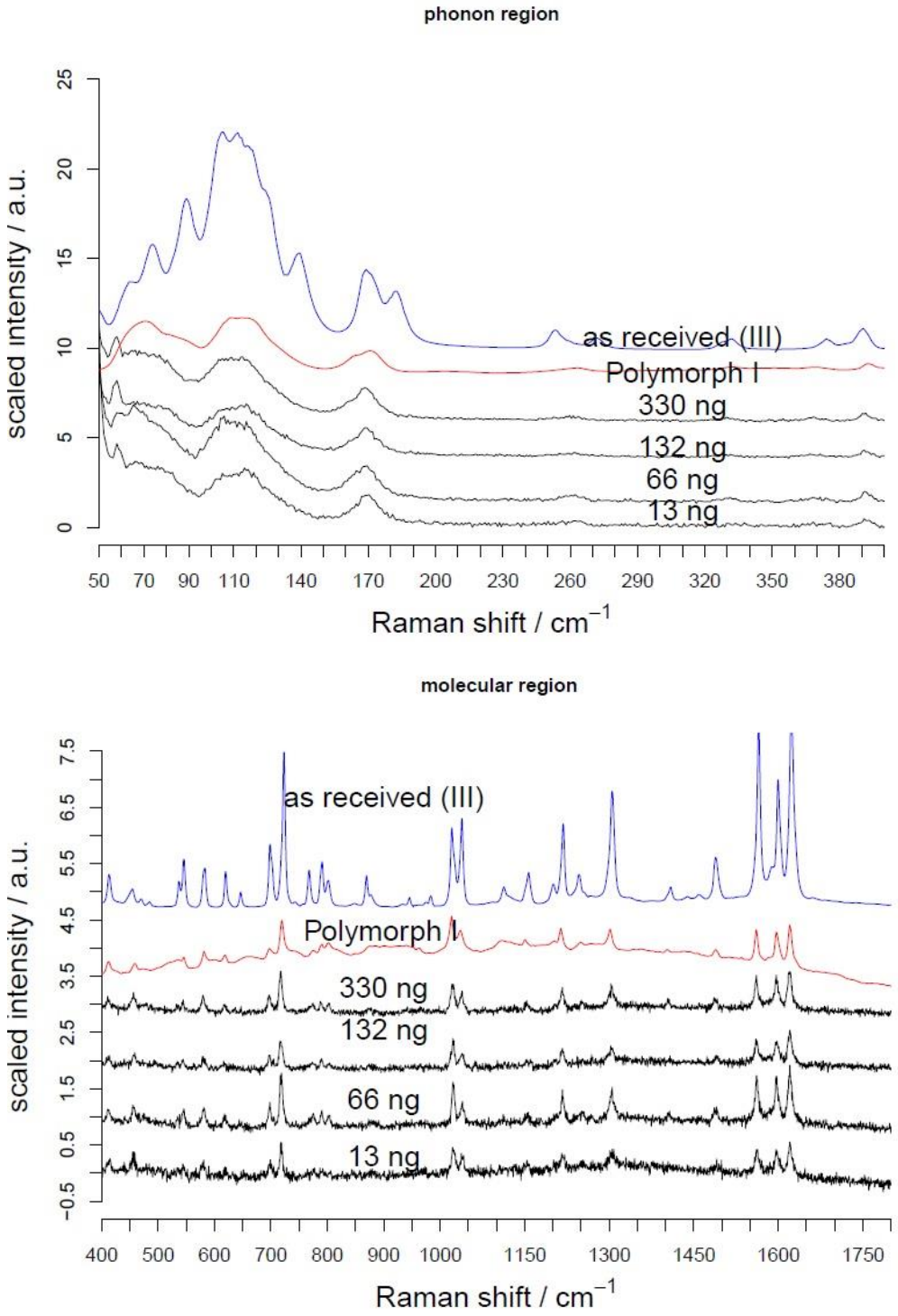

Figure B. 3. Raman spectra for phonon region (top) and molecular region (bottom) of different printed quantities of CBZ/DMSO on SAM-CH_3 ,with reference spectra of CBZ III (as received) (blue) and the prepared polymorph I (red).y-axis offsets were employed for presenting the differences between panels.

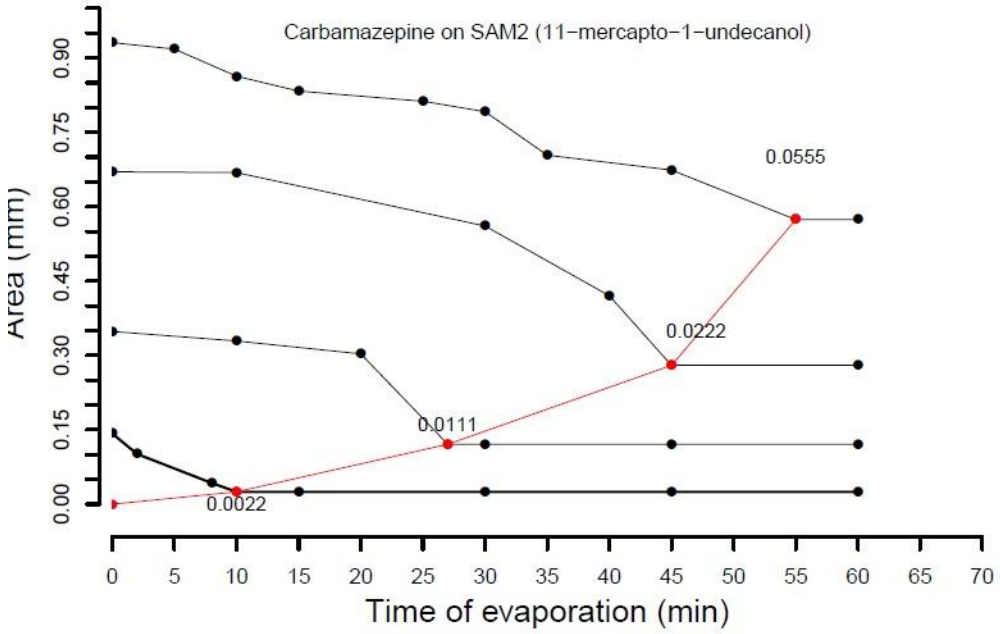

Figure B. 4. The evaporation time of different printed quantities of CBZ/DMSO on SAM-CH_2OH

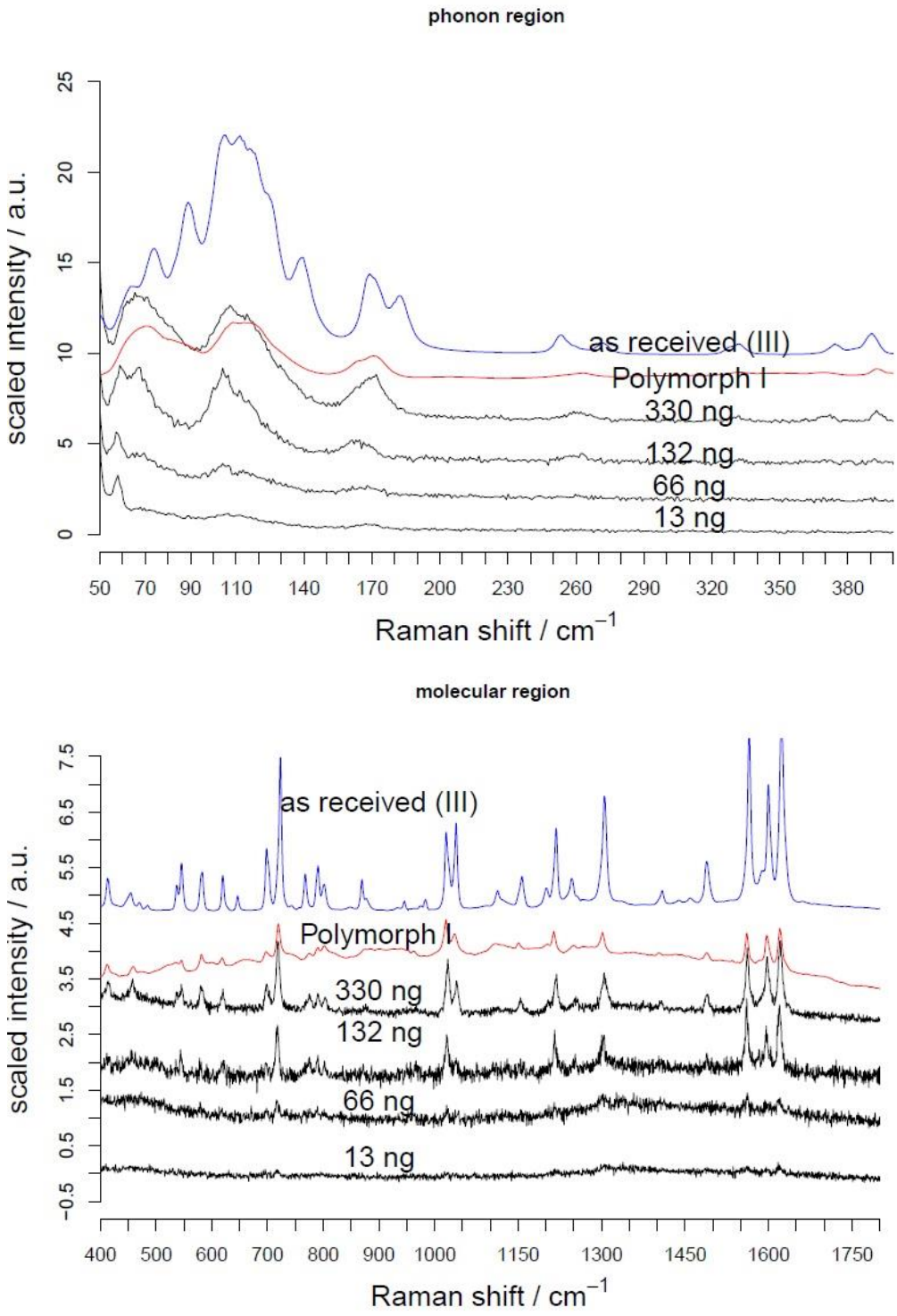

Figure B. 5. Raman spectra for phonon region (top) and molecular region (bottom) of different printed quantities of CBZ/DMSO on SAM-CH_2OH ,with reference spectra of CBZ III (as received) (blue) and the prepared polymorph I (red).y-axis offsets were employed for presenting the differences between panels.

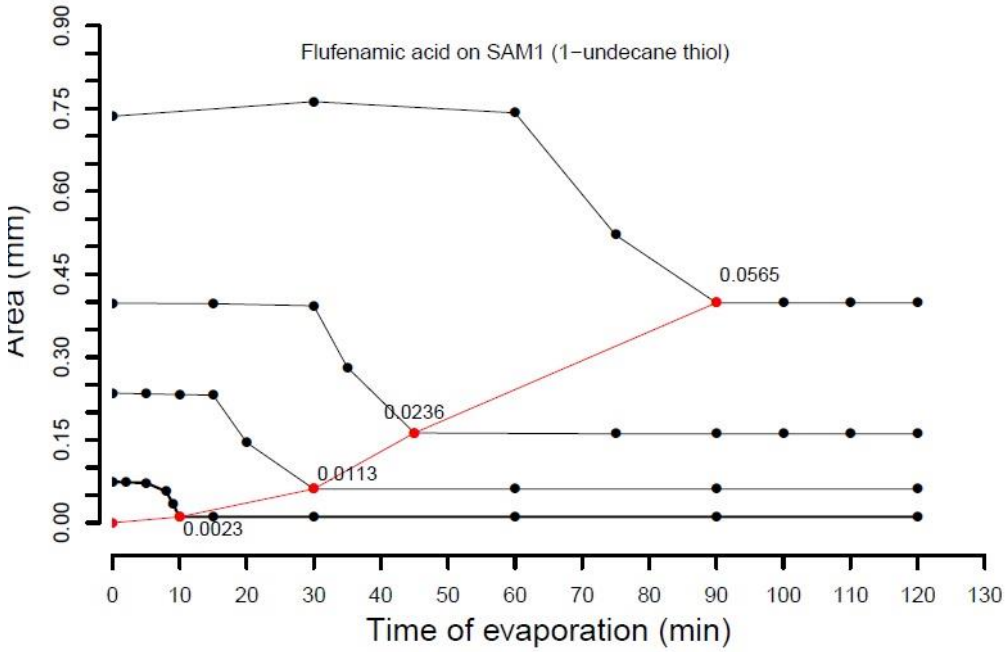

Figure B. 6. The evaporation time of different printed quantities of FLUF/DMSO on SAM-CH_3

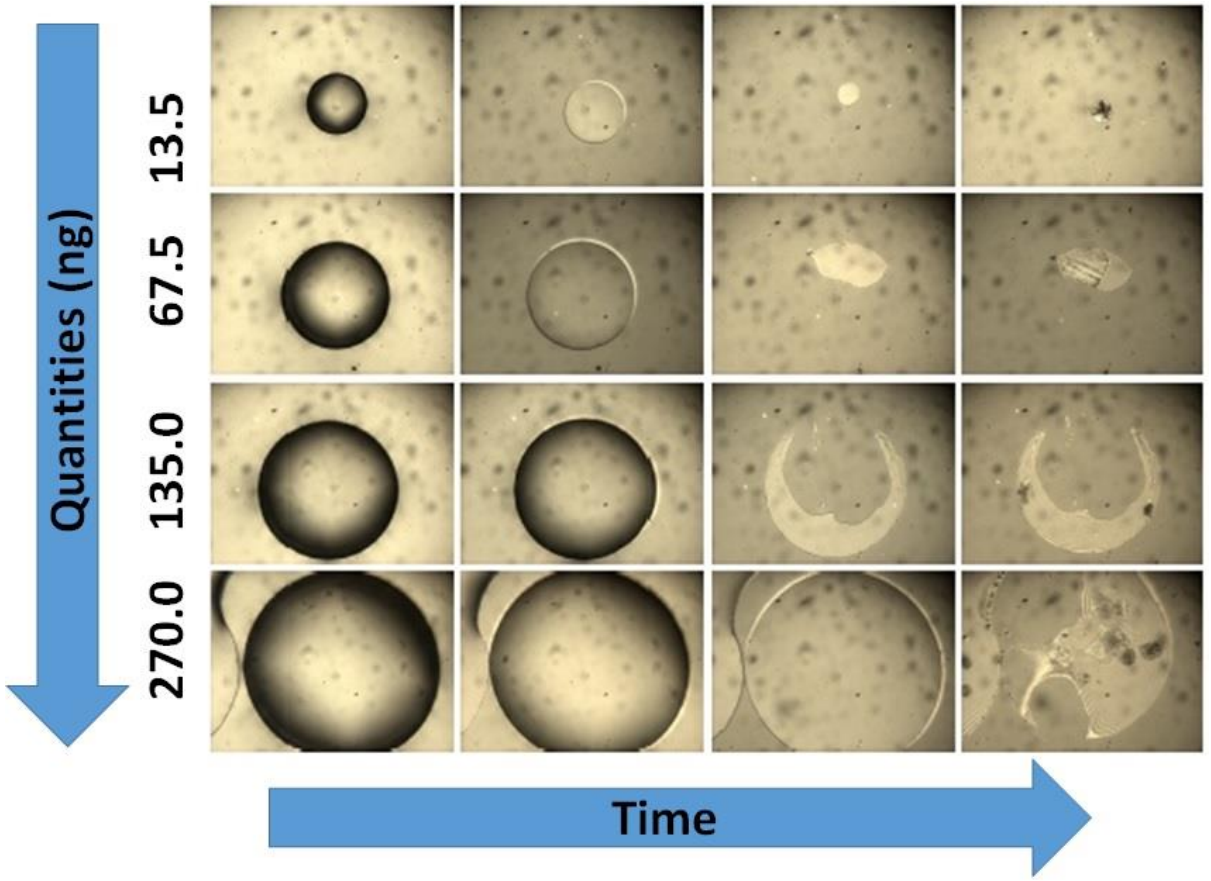

Figure B. 7. Optical micrographs of FLUF/ DMSO SAM-CH_3

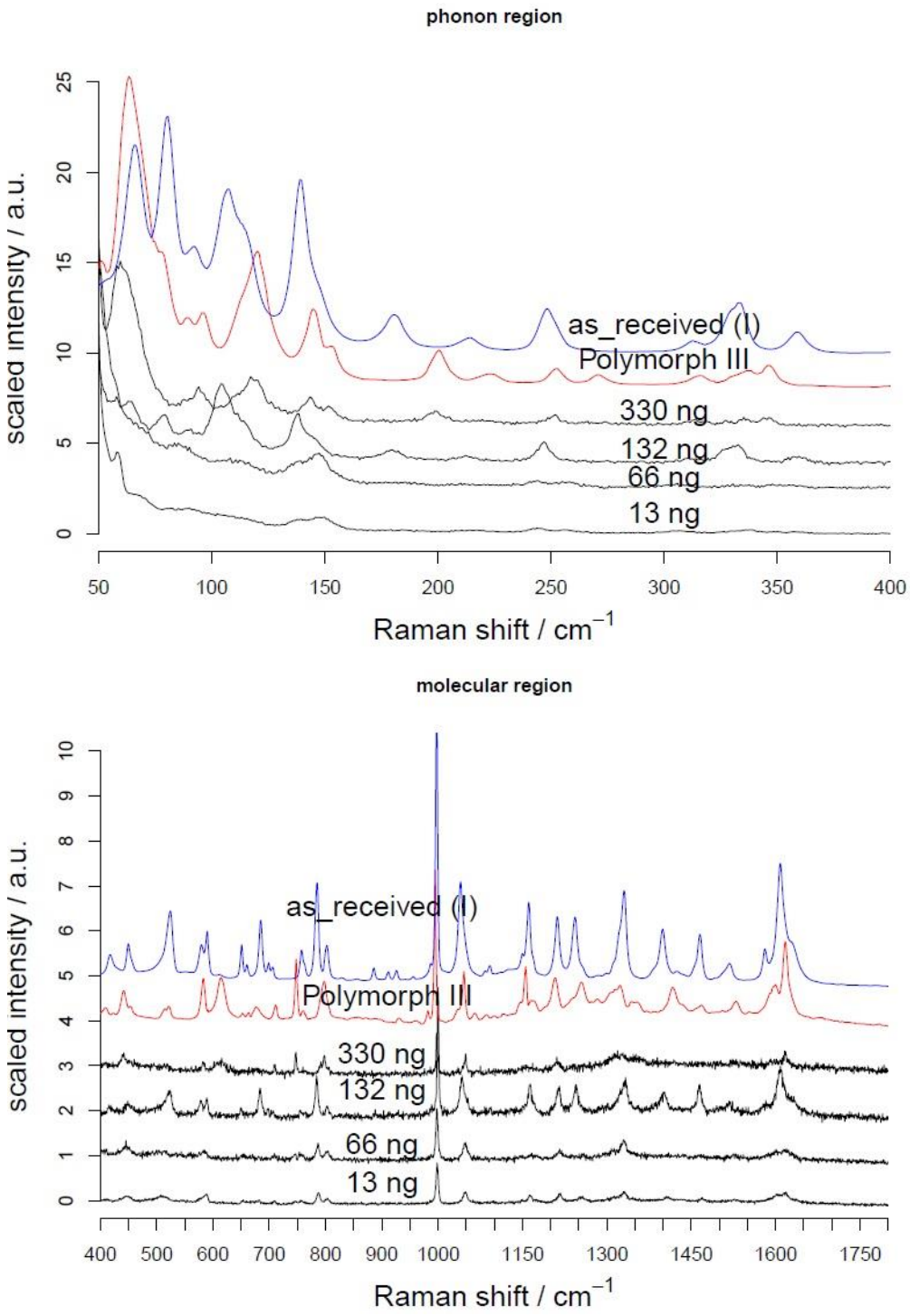

Figure B. 8. Raman spectra for phonon region (top) and molecular region (bottom) of different printed quantities of FLUF/DMSO on SAM-CH_3 ,with reference spectra of FLUF I (as received) (blue) and the prepared polymorph III (red).y-axis offsets were employed for presenting the differences between panels.

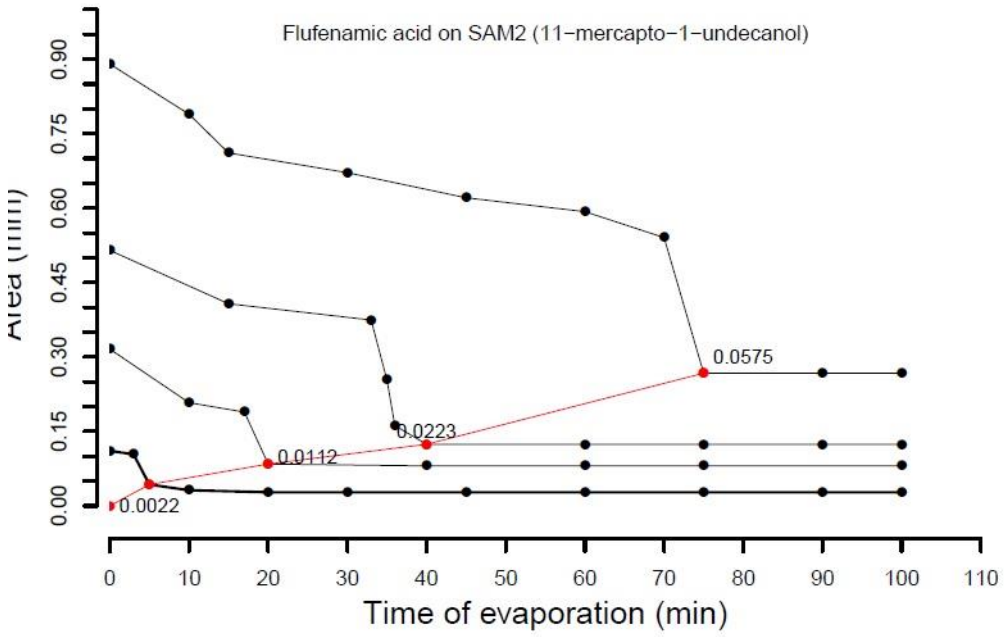

Figure B. 9. The evaporation time of different printed quantities of FLUF/DMSO on SAM-CH_2OH

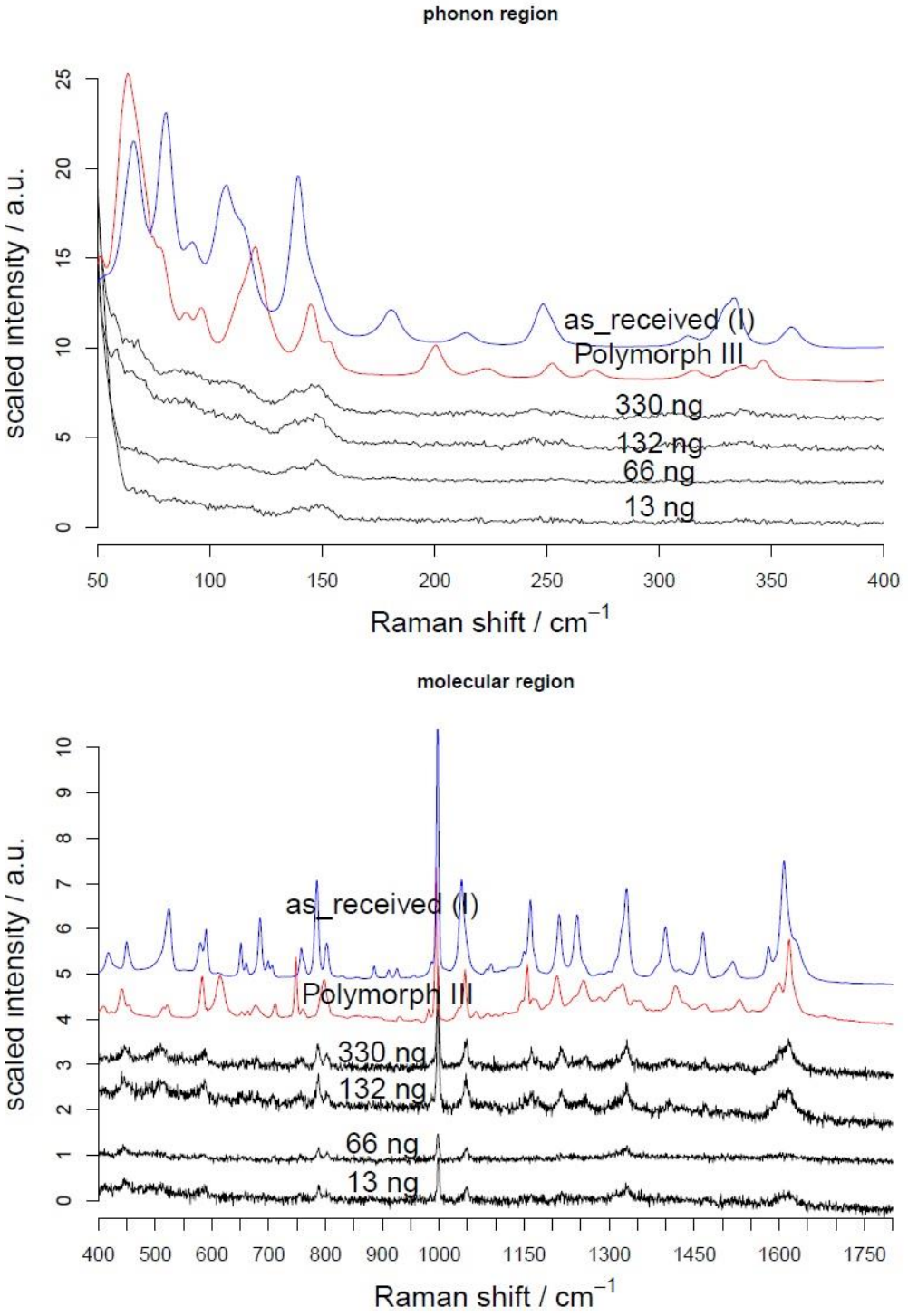

Figure B. 10. Raman spectra for phonon region (top) and molecular region (bottom) of different printed quantities of FLUF/DMSO on SAM-CH_2OH ,with reference spectra of FLUF I (as received) (blue) and the prepared polymorph III (red).y-axis offsets were employed for presenting the differences between panels.

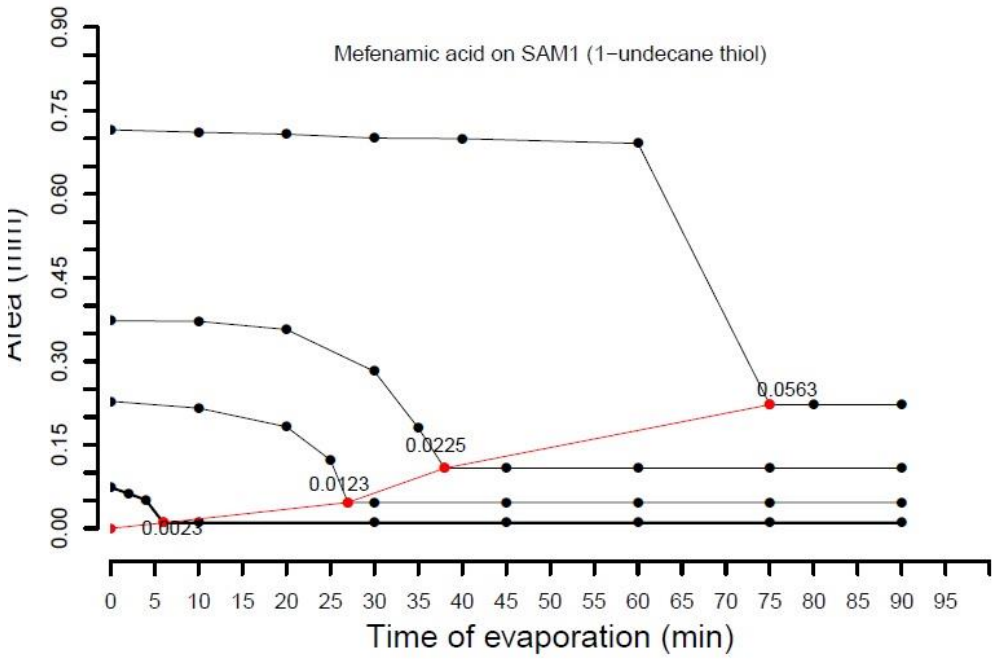

Figure B. 11. The evaporation time of different printed quantities of MEF/DMSO on SAM-CH_3

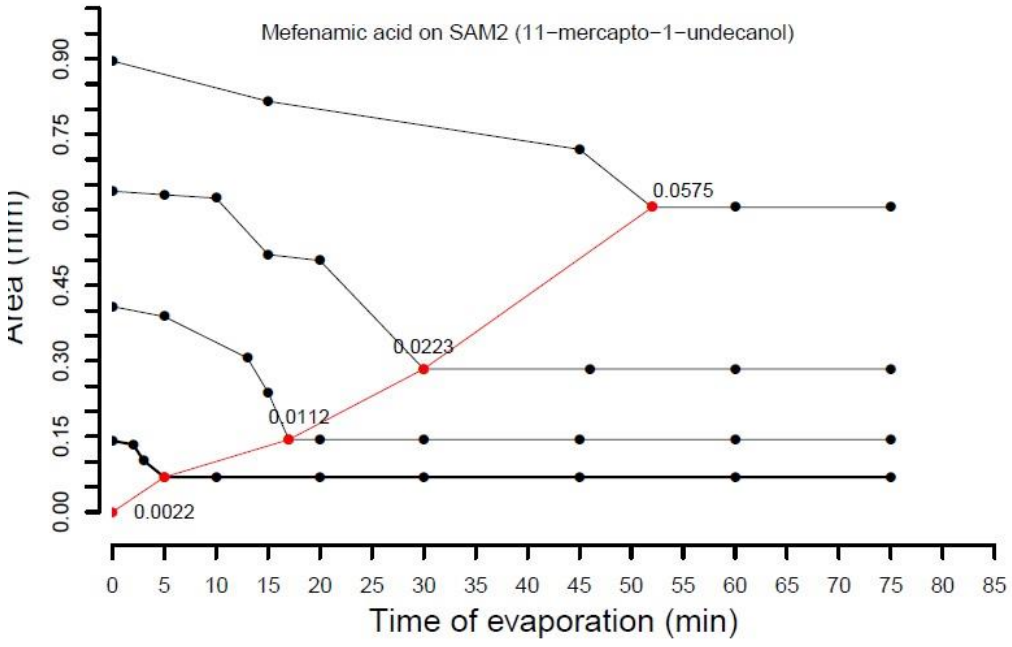

Figure B. 12. The evaporation time of different printed quantities of MEF/DMSO on SAM-CH_2OH

Appendix C
Supplementary information

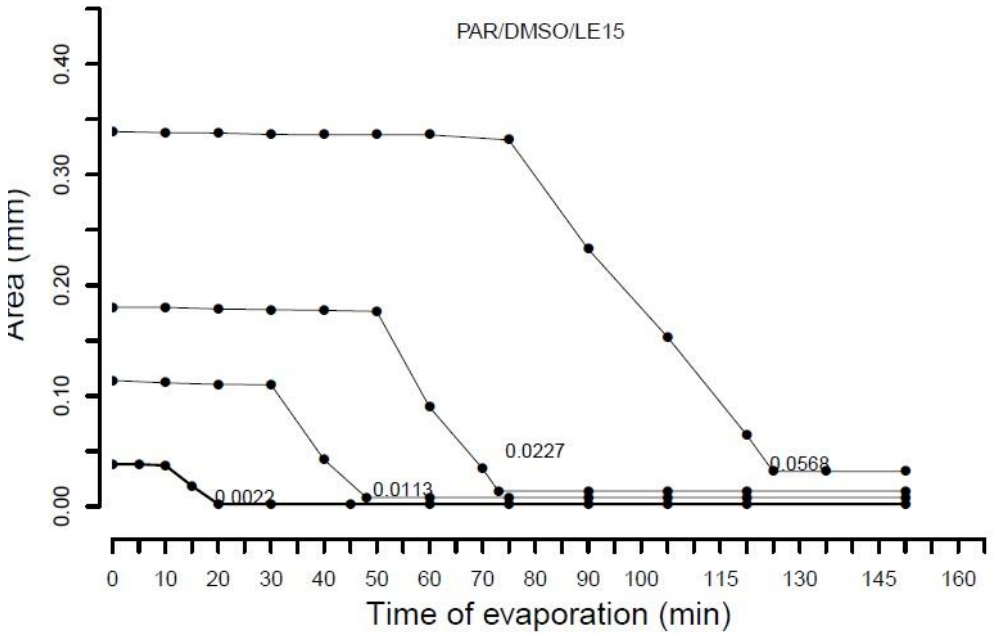

Figure C. 1. The evaporation time of different printed quantities of PAR/DMSO on LE15

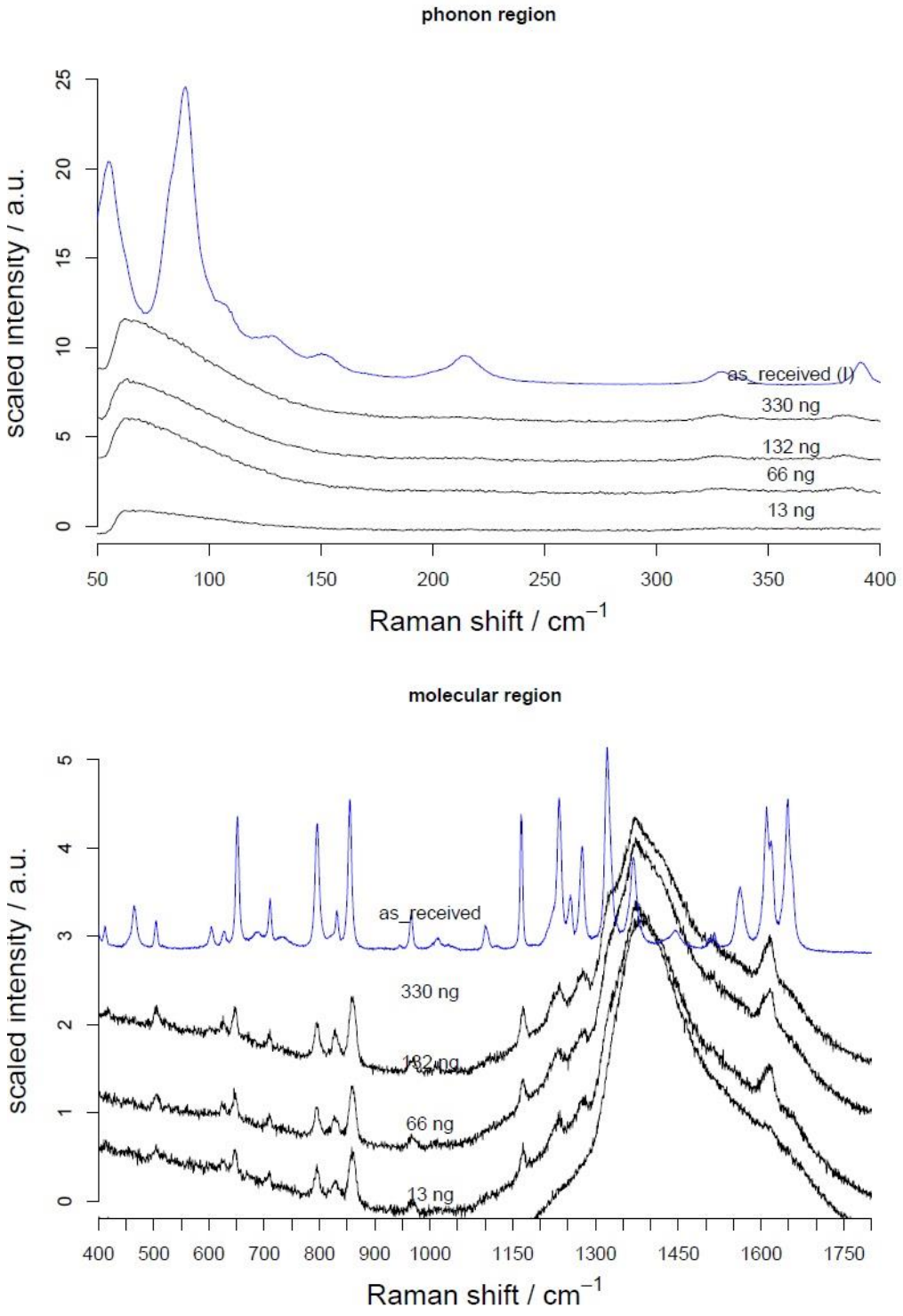

Figure C. 2. Raman spectra for phonon region (top) and molecular region (bottom) of different printed quantities of PAR/DMSO on LE15, with reference spectra of PAR I (as received) (blue). Y-axis offsets were employed for presenting the differences between panels.

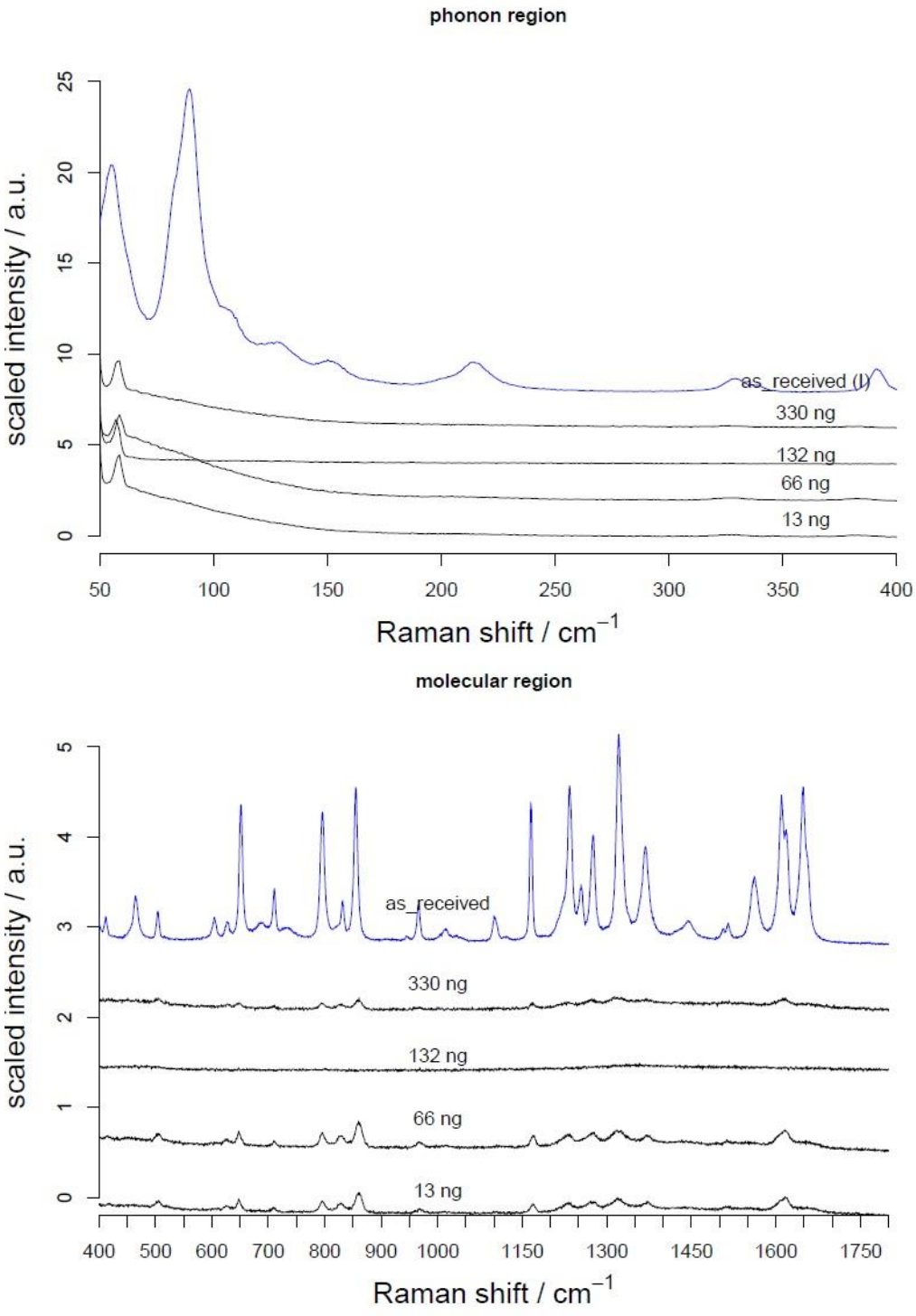

Figure C. 3. Raman spectra for phonon region (top) and molecular region (bottom) of different printed quantities of PAR/DMSO on SAMF, with reference spectra of PAR I (as received) (blue). Y-axis offsets were employed for presenting the differences between panels.